

# Droplet behaviour and thermal separation in Ranque-Hilsch vortex tubes

**Citation for published version (APA):**

Liew, R. (2013). *Droplet behaviour and thermal separation in Ranque-Hilsch vortex tubes*. [Phd Thesis 1 (Research TU/e / Graduation TU/e), Applied Physics and Science Education]. Technische Universiteit Eindhoven. <https://doi.org/10.6100/IR756973>

**DOI:**

[10.6100/IR756973](https://doi.org/10.6100/IR756973)

**Document status and date:**

Published: 01/01/2013

**Document Version:**

Publisher's PDF, also known as Version of Record (includes final page, issue and volume numbers)

**Please check the document version of this publication:**

- A submitted manuscript is the version of the article upon submission and before peer-review. There can be important differences between the submitted version and the official published version of record. People interested in the research are advised to contact the author for the final version of the publication, or visit the DOI to the publisher's website.
- The final author version and the galley proof are versions of the publication after peer review.
- The final published version features the final layout of the paper including the volume, issue and page numbers.

[Link to publication](#)

**General rights**

Copyright and moral rights for the publications made accessible in the public portal are retained by the authors and/or other copyright owners and it is a condition of accessing publications that users recognise and abide by the legal requirements associated with these rights.

- Users may download and print one copy of any publication from the public portal for the purpose of private study or research.
- You may not further distribute the material or use it for any profit-making activity or commercial gain
- You may freely distribute the URL identifying the publication in the public portal.

If the publication is distributed under the terms of Article 25fa of the Dutch Copyright Act, indicated by the "Taverne" license above, please follow below link for the End User Agreement:

[www.tue.nl/taverne](http://www.tue.nl/taverne)

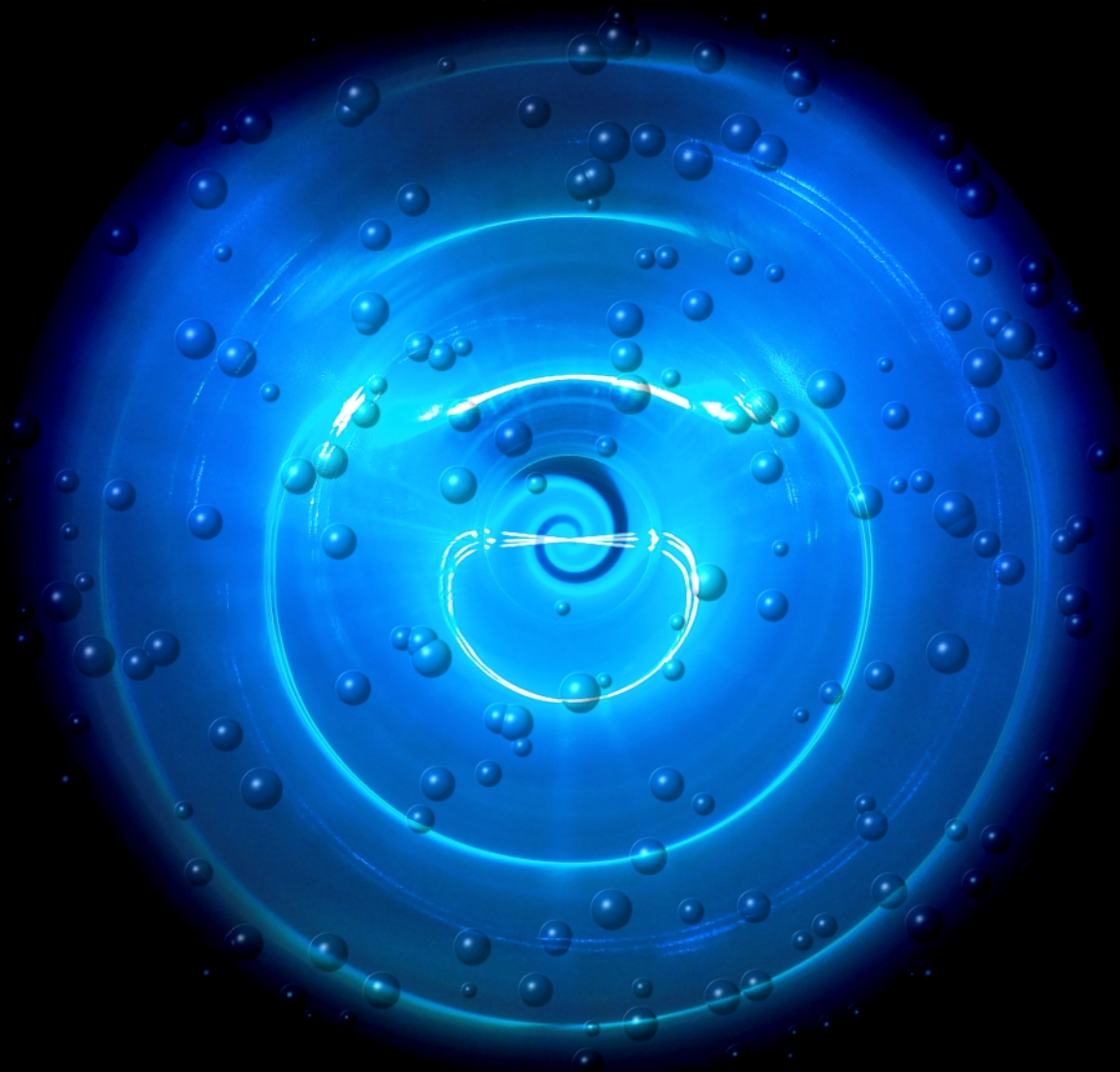
**Take down policy**

If you believe that this document breaches copyright please contact us at:

[openaccess@tue.nl](mailto:openaccess@tue.nl)

providing details and we will investigate your claim.

**Droplet Behaviour  
and Thermal Separation in  
Ranque-Hilsch Vortex Tubes**



**Raoul Liew**

DROPLET BEHAVIOUR  
AND THERMAL SEPARATION IN  
RANQUE-HILSCH VORTEX TUBES

Copyright © 2013 R. Liew  
Cover design by R. Liew  
Printed by Ridderprint, Ridderkerk, The Netherlands

CIP-DATA LIBRARY TECHNISCHE UNIVERSITEIT EINDHOVEN

Liew, Raoul

Droplet Behaviour and Thermal Separation in Ranque-Hilsch Vortex Tubes / by R. Liew.  
- Eindhoven: Technische Universiteit Eindhoven, 2013. - Proefschrift.

A catalogue record is available from the Eindhoven University of Technology Library

ISBN: 978-90-386-3416-6

NUR: 924

Subject headings: Ranque-Hilsch vortex tube; droplets; evaporation; condensation; thermal separation; Phase Doppler Particle Analysis; Laser Doppler Anemometry; frequency analysis; gas separation

DROPLET BEHAVIOUR  
AND THERMAL SEPARATION IN  
RANQUE-HILSCH VORTEX TUBES

PROEFSCHRIFT

ter verkrijging van de graad van doctor aan de  
Technische Universiteit Eindhoven, op gezag van de  
rector magnificus, prof.dr.ir. C.J. van Duijn, voor een  
commissie aangewezen door het College voor  
Promoties in het openbaar te verdedigen  
op maandag 16 september 2013 om 16.00 uur

door

Raoul Liew

geboren te 's Hertogenbosch

Dit proefschrift is goedgekeurd door de promotoren:

prof.dr. A.A. Darhuber  
en  
prof.dr. J.G.M. Kuerten

Copromotor:  
dr.ir. J.C.H. Zeegers

This research is supported by the Dutch Technology Foundation STW, which is part of the Netherlands Organisation for Scientific Research (NWO), and which is partly funded by the Ministry of Economic Affairs.







# Contents

<b>1</b>	<b>Introduction</b>	<b>1</b>
1.1	Background	1
1.1.1	Cyclone separators	1
1.1.2	The rotational particle separator	3
1.1.3	The Twister supersonic gas separator	4
1.2	The Ranque-Hilsch Vortex Tube	4
1.2.1	The RHVT as a cooler or heater	6
1.2.2	The RHVT as a separator	7
1.3	Motivation and objective of the research	8
1.4	Preview of this thesis	9
<b>2</b>	<b>Theoretical analysis of droplet behaviour in the RHVT</b>	<b>11</b>
2.1	Equation of motion for small droplets	11
2.2	Phase change model	13
2.2.1	Humidity	15
2.2.2	Energy balance	17
2.2.3	Evaluation of the phase change model	18
2.3	Numerical method	19
2.4	Droplet behaviour in the vortex chamber	21
2.4.1	Model parameters of gas in the vortex chamber	21
2.4.2	Results of droplet behaviour in the vortex chamber	23
2.5	Droplet behaviour in the main tube	26
2.5.1	Model parameters of the gas in the main tube	26
2.5.2	Results of droplet behaviour in the main tube	28
2.5.3	Steady state liquid concentration in the main tube	35
2.6	Conclusions	38
<b>3</b>	<b>Experimental methods and equipment</b>	<b>41</b>
3.1	The experimental Ranque-Hilsch Vortex Tube	41
3.1.1	The design of the swirl generator	41
3.1.1.1	Compressible flow through a nozzle	43
3.1.1.2	Application to the swirl generator	45
3.2	Phase Doppler Particle Analysis	48
3.2.1	LDA	48
3.2.2	PDPA	50

3.2.3	Hardware . . . . .	50
3.2.4	Optical configuration . . . . .	52
3.2.5	Transparent measurement sections . . . . .	54
3.3	CPT method . . . . .	60
3.4	Gas conditioning . . . . .	62
3.4.1	Droplet generators . . . . .	67
3.5	Process Scheme . . . . .	68
3.5.1	Nitrogen supply section . . . . .	68
3.5.2	Humidifier section . . . . .	70
3.5.3	Sensing section . . . . .	71
3.5.4	Mass flow control section . . . . .	71
3.6	Conclusions . . . . .	72
<b>4</b>	<b>Experimental study of flow and droplet behaviour in the RHVT</b>	<b>75</b>
4.1	Water droplets as seeding particles . . . . .	75
4.1.1	The sizes of droplets entering the RHVT . . . . .	78
4.1.2	Liquid collection in the vortex chamber . . . . .	80
4.2	Velocity statistics . . . . .	82
4.3	Test case for LDA . . . . .	82
4.4	PDPA results . . . . .	83
4.4.1	Mean velocity . . . . .	85
4.4.2	Velocity fluctuations . . . . .	86
4.4.3	Influence of the cold fraction . . . . .	88
4.4.4	Comparison between different mass flows . . . . .	89
4.4.5	Influence of the type of swirl generator . . . . .	91
4.4.6	Frequency analysis . . . . .	94
4.4.7	Vortex wobbling . . . . .	95
4.4.8	Droplet behaviour . . . . .	101
4.5	Conclusions . . . . .	108
<b>5</b>	<b>Energy Separation in the RHVT</b>	<b>111</b>
5.1	A selection of existing RHVT theories . . . . .	111
5.2	Energy separation model . . . . .	113
5.2.1	Process I: Energy transfer . . . . .	113
5.2.2	Process II: Decay of the vortex . . . . .	116
5.2.3	The overall process . . . . .	118
5.3	Determination of $Ma_0$ . . . . .	119
5.3.1	The Mach number in the vortex chamber . . . . .	120
5.3.2	A model for $Ma_0$ . . . . .	121
5.3.3	The static cold exit pressure . . . . .	121
5.4	Experimental Study . . . . .	123
5.4.1	Results . . . . .	124
5.5	Summary and conclusions . . . . .	129

---

<b>6 Preliminary study of the RHVT as a separator</b>	<b>133</b>
6.1 Measuring the water content in a gas/droplet mixture . . . . .	133
6.2 Preliminary results of water vapour separation . . . . .	138
6.3 A theoretical example of the RHVT as a gas cleaner . . . . .	138
6.4 Conclusions . . . . .	143
<b>7 Conclusions and recommendations</b>	<b>145</b>
7.1 Conclusions . . . . .	145
7.1.1 Theoretical analysis of droplet behaviour in the RHVT . . . . .	145
7.1.2 Experimental methods and equipment . . . . .	146
7.1.3 Experimental study of flow and droplet behaviour in the RHVT . . . . .	146
7.1.4 Energy separation in the RHVT . . . . .	147
7.1.5 Preliminary study of the RHVT as separator . . . . .	148
7.2 Recommendations . . . . .	148
<b>A Properties of water and nitrogen</b>	<b>151</b>
<b>B Ray tracing analysis</b>	<b>153</b>
<b>C Uncertainty analysis mixing ratio</b>	<b>157</b>
<b>References</b>	<b>159</b>
<b>Nomenclature</b>	<b>169</b>
<b>Abstract</b>	<b>175</b>
<b>Samenvatting</b>	<b>177</b>
<b>List of publications</b>	<b>179</b>
<b>Acknowledgements</b>	<b>181</b>
<b>Curriculum vitae</b>	<b>183</b>



# 1 | Introduction

## 1.1 Background

Natural gas is one of the fossil fuels and represents approximately 25% of world's energy supply (BP, 2012). In 2012, the total usage of natural gas in the world was about  $3.17 \cdot 10^{12}$  Nm<sup>3</sup>, which is 468 Nm<sup>3</sup> per capita (Nm<sup>3</sup> = Normal cubic meter, representing 1 m<sup>3</sup> of gas at a temperature of 0°C and a pressure of 1.01325 bar), and the world's reserve of natural gas is estimated to be  $2.08 \cdot 10^{14}$  Nm<sup>3</sup> (CIA, 2012). With the current rate of consumption, there is enough natural gas for the the next 60 years to power our world.

The natural gas reserves in the earth not only contain methane (CH<sub>4</sub>, the main product), but also other components, like other higher hydrocarbons, carbon dioxide (CO<sub>2</sub>), oil, water, and hydrogen sulfide (H<sub>2</sub>S). Some of the contaminants, e.g. H<sub>2</sub>S, are the cause for corrosion problems. The presence of water and CO<sub>2</sub> in natural gas lowers the heating value of the fuel and from a mixture of water and CO<sub>2</sub> hydrates can be formed, which may contaminate or clog transporting equipment like pipe lines, valves, and compressors. Furthermore, equipment that is operated with the gas, for example domestic boilers at home, require that the quality and composition of the gas is maintained. These are optimized to work efficiently at specific gas compositions. The use of gas that has a composition different from the specified composition may lead to lower burner efficiencies, the formation of hazardous combustion products (e.g. carbon monoxide), or failure of the burner. For these reasons, natural gas is cleaned from the contaminants before it is transported to the user.

While the world exploits natural gas fields, the amount of contaminants in the natural gas increases over time. The reason for this is that the most clean gas fields are produced first, thereby leaving highly contaminated gas fields, which are currently not economically beneficial enough to exploit, for future generations (Mondt, 2005; Willems, 2009). This leads to the demand for high efficiency separators, which separate the contaminants from the product gas, for the production of clean natural gas in the future and thus to a continuous development of separation techniques.

### 1.1.1 Cyclone separators

There are several techniques available that are currently used to remove liquid and solid contaminants from (natural) gas. Among these are cyclone separators, which are based on inertial (centrifugal or gravitational) separation. In this type of separators, particles in the gas are forced towards collecting walls by means of the centrifugal force.

Two cyclone separators are shown in Fig. 1.1. For both designs, the inlet of the separator

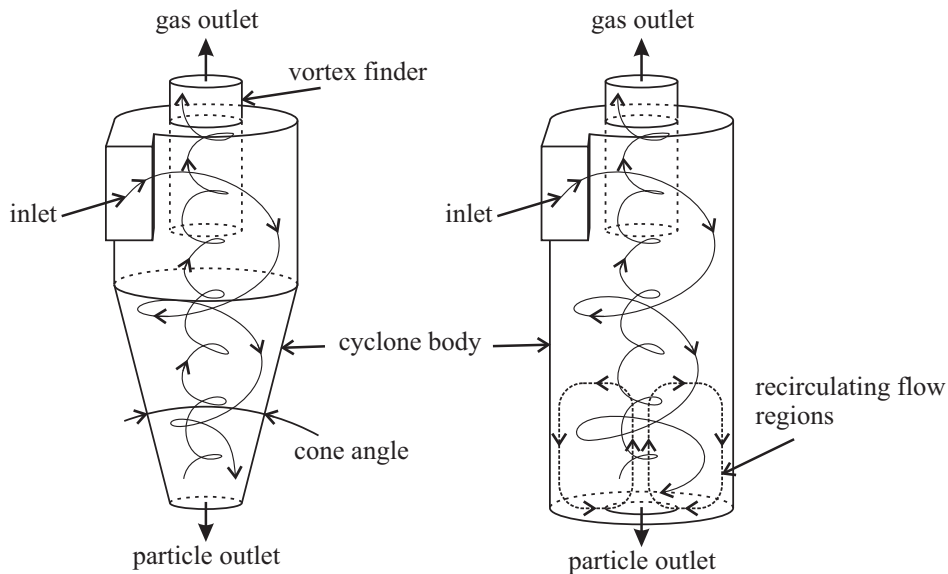


Figure 1.1: Schematic drawing of a conical cyclone separator (left) and a flat bottom cyclone (right).

is tangentially attached to a cyclone body, where the particles are centrifuged towards the walls while the carrier fluid is moved radially inward. Due to the velocity field inside the cyclone, the particles are transported towards the (in this picture) bottom of the device, where they are removed from the gas. The clean gas moves up and leaves the cyclone through a smaller diameter tube, i.e. the vortex finder, that is inserted from the top into the cyclone body. The vortex finder prevents short circuit flow from the inlet towards the gas outlet.

The cyclone body often has a conical shape with a certain angle, as shown in the left drawing in Fig. 1.1. This cone angle is a main design parameter because it has a fundamental effect on the flow in the cyclone body. Because of the conical shape, the loss of angular momentum while the gas moves down is compensated, leading to a similarity in swirl and axial velocity profiles along the axis. Additionally, the conical shape allows the discharge of particles to be more efficient (Bradley, 1965; Svarovsky, 1984).

If the cyclone body is cylindrical (the cone angle is  $180^\circ$ , as shown in the right drawing in Fig. 1.1), there is a strong radial velocity inward at the bottom of the separator and recirculation zones are present in the flow (Peng *et al.*, 2002). Because of this, particles that are initially swirled towards the cylinder wall can be re-entrained in the gas, reducing the efficiency of the separation process. The advantage of large cone angles is that the cyclone can be used for sorting applications (Svarovsky, 1984).

The performance of cyclones is measured by collection efficiency (the efficiency at which the particles are separated from the gas) and pressure drop. Most theories of predicting the collection efficiency are based on particle size, particle mass density, gas velocity, as well as the cyclone geometry (Hoekstra *et al.*, 1999).

A measure for the collection efficiency is the cut size, which is the size of particles at which the chance of separation is 50%, i.e. the  $d_{p50}$ . If  $D_c$  is the cyclone diameter,  $\Delta p$  the pressure drop over the cyclone, and  $Q_c$  the volume flow, the cut size typically scales

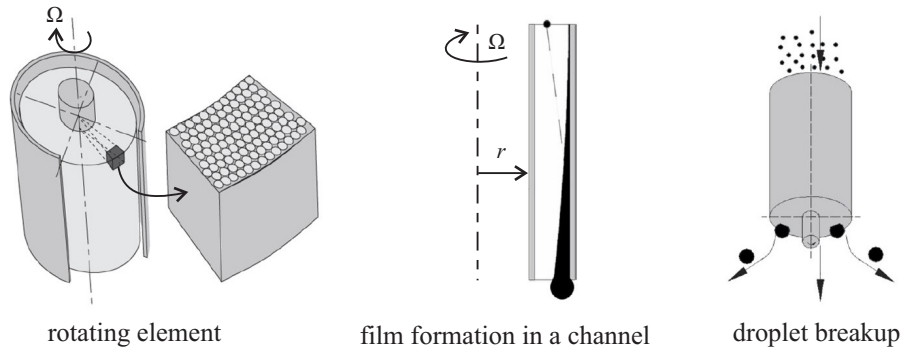


Figure 1.2: Schematic drawing of an RPS element and its working principle (Kroes, 2012).

according to  $d_{p50} \propto \Delta p^{-1/4}$ , the pressure drop scales with  $\Delta p \propto Q_c^{5/2}$ , and the cyclone diameter with  $D_c \propto Q_c^{1/2}$  (Bradley, 1965). For small cut sizes, the cyclone diameter must be small, which is at the expense of a higher pressure drop (resulting in higher operating cost). This is the reason why, instead one large cyclone separator, the use of multiple small cyclones is considered to be an optimum (economical) trade-off between pressure drop and collection efficiency.

### 1.1.2 The rotational particle separator

The techniques that are most commonly used to remove  $\text{CO}_2$  are absorption, adsorption, membranes, and cryogenics (Olajire, 2010). In the latter process, condensable components are removed by first cooling the gas (by means of refrigeration or expansion) in order to condense some of the components, thereby forming small droplets that are suspended in the gas. These droplets can then be removed with, e.g., cyclones. However, most of the droplets created during this process are small, typically  $1 - 20 \mu\text{m}$  (Bansal *et al.*, 2011), and separation of micron-sized particles by means of cyclones requires unconventional large pressure drops.

A device that is able to remove small particles from gas, having a relatively low pressure drop, is the rotational particle separator (Brouwers, 1996). This separator, which is able to remove solid or liquid particles of  $0.1 \mu\text{m}$  and larger from a gas phase, has a high separation efficiency ( $> 90\%$ ) for particles of  $1 \mu\text{m}$  (Brouwers, 1997). The driving force of the separation process is the centrifugal force that is induced by a rotating stack of small (typically a few millimeter in diameter) channels through which the gas/particle mixture flows, as shown in Fig. 1.2. Because of the small size of the channels, the time it takes for particles to reach the channel walls is much smaller compared to a conventional cyclone separator. Additionally, the channels are so small that it is more easy to have laminar flow in the channels. Therefore, turbulent dispersion, which counteracts the centrifugal separation and lowers the separation efficiency (Kroes, 2012), is minimized. Consequently, the apparatus has a higher separation efficiency than a conventional cyclone when it is operated at similar conditions and having a comparable size (Van Wissen *et al.*, 2007). It is however, just as for a cyclone separator, required that the feed stream already contains droplets or particles that are to be separated.

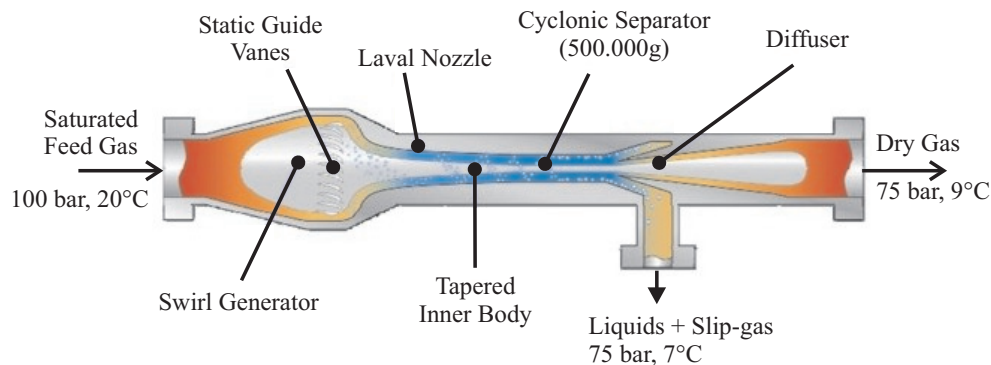


Figure 1.3: A Twister Supersonic Gas Separator (image courtesy of Twister B.V.)

### 1.1.3 The Twister supersonic gas separator

The production of droplets by means of condensation, followed by the separation of these droplets, is combined in the Twister Supersonic Gas Separator (Twister, 2013), shown in Fig. 1.3. The gas is first brought into rotation via stationary guide vanes, after which it is accelerated to supersonic speeds through a Laval nozzle. During the acceleration, the temperature decreases rapidly and homogeneous condensation occurs. During this process, micron-sized droplets are formed, which are swirled towards the outer wall due to the centrifugal force and are eventually separated from the gas.

## 1.2 The Ranque-Hilsch Vortex Tube

In this thesis, we will focus on a relatively simple device in which gas rotates at a very high swirl velocity ( $> 300$  m/s) while a part of the gas is cooled and the remaining part is heated: the Ranque-Hilsch Vortex Tube, or simply vortex tube. Additional to the cooling of gas due to expansion and acceleration, internal heat transfer is present that produces even lower temperatures. This means that higher condensate fractions can be reached compared to a conventional expansion process. The advantages of the local cooling and the high swirl velocity (large centrifugal force that can be used for centrifugal separation) are combined in the device, making it suitable to remove condensable contaminants from the gas.

The cooling and heating effect that a gas undergoes when it is expanded through the vortex tube was discovered by Ranque (1933). A year later, the first US patent on the device appeared (Ranque, 1934). At that time, the vortex tube was not thermodynamically efficient enough to be of commercial interest. Later, Hilsch (1947) systematically studied the effect of the inlet pressure and the geometry on the cooling performance and managed to improve the cooling power. The latter study introduced the vortex tube in the scientific and commercial world. Because of Hilsch's significant contributions to the invention of Ranque, the device is now known as the Ranque-Hilsch vortex tube (RHVT).

The RHVT, which is shown in Fig. 1.4, consists of a main tube, which has a typical length to diameter ratio of 20 – 50, connected to a vortex chamber, which has one or more tangentially oriented nozzles through which pressurized gas is expanded to generate a highly swirling motion, i.e., the main vortex. At one side of the vortex chamber, there is an opening



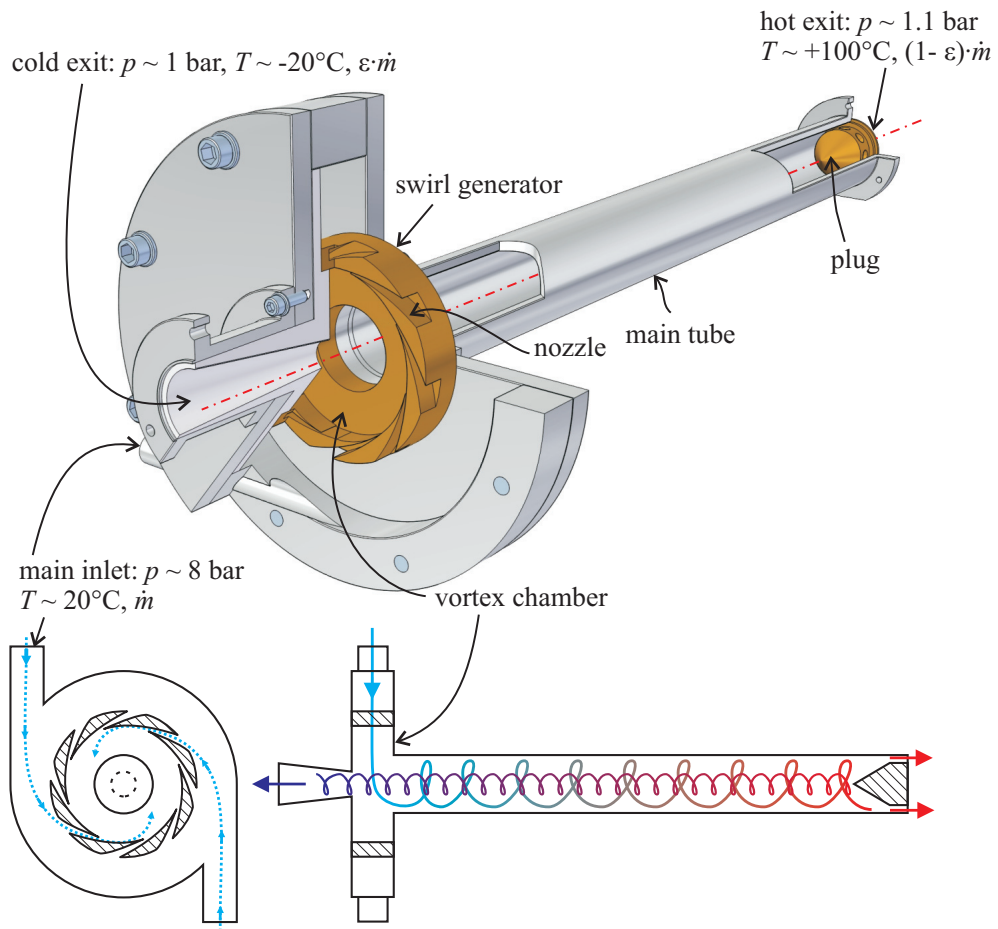


Figure 1.4: The Ranque-Hilsch Vortex Tube. Typical pressures  $p$  temperatures  $T$  are indicated in the figure. The mass flow through the device is  $\dot{m}$  and the cold fraction is  $\varepsilon$ .

that has a smaller diameter than the main tube. A fraction of the gas leaves the device through this opening at a lower temperature than at the inlet. Therefore, this opening is referred to as the cold exit. The remaining part of the gas has a higher temperature and leaves the RHVT via the hot exit, located at the end of the main tube. The ratio of both flows is usually controlled via a control valve located in the hot exit. The ratio of the cold to total mass flow, the cold fraction, is an important parameter to control the exit temperatures and cooling or heating powers and is defined as

$$\varepsilon = \frac{\dot{m}_c}{\dot{m}}, \quad (1.1)$$

where  $\dot{m}_c$  and  $\dot{m}$  are the cold-, respectively, total mass flow rates.

### 1.2.1 The RHVT as a cooler or heater

The RHVT has no moving parts, does not contain any refrigerants, is cheap to produce, and requires little maintenance. Therefore, vortex tubes are mostly used for low temperature applications, for example, to cool electronics, for solvent free cooling of cutting tools and work pieces, and at other places where pressurized air (gas) is at the disposal to generate local cooling (AirTx, 2013; Exair, 2013; ITW-Vortec, 2013).

Many attempts were made to explain and describe the mechanism that causes the temperature differences, or the energy separation. Hilsch (1947) explained the energy separation mechanism by means of internal friction, causing transport of heat from gas in the core (near axis region) to gas in the periphery (the near wall region). Schultz-Grunow (1951) addressed theories of heat transfer in the atmosphere and explained that, because of the existence of a pressure gradient caused by the centrifugal force, there is a temperature difference between the core and peripheral region. Van Deemter (1952) and Deissler & Perlmutter (1960) explained that turbulent eddies transport gas from the core region towards the peripheral region and vice-versa. The compression and expansion cycles of gas in these eddies, which are subjected to a radial pressure gradient, are the cause for the energy transport. Linderstrøm-Lang (1971) showed that there is turbulent transport of both heat and kinetic energy. Kurosaka (1982) has measured frequency spectra of generated sound by the gas in the RHVT and found that the magnitude of the acoustic power is related to the difference in temperatures. He proposes that acoustic streaming is the main source for the energy separation. Ahlborn *et al.* (1994) found that the radial pressure gradient inside the RHVT is important for the energy separation process. Later, Ahlborn *et al.* (1998) developed a semi-incompressible model that is based on a heat pump in the RHVT.

Although there are numerous (complex) theories and models available from literature, most of the theories are not validated or are impossible to validate. The models that are validated by experimental results, e.g. (Ahlborn *et al.*, 1998), are questionable because some inconsistent approximations are made. For example, the compressibility of the gas and the kinetic energy are not consistently used in the model of Ahlborn *et al.* (1998).

Since the last decades, it has become popular to study the flow field and the energy separation processes in the vortex tube by means of numerical simulations. Fröhlingdorf & Unger (1999) published results that were computed using a 2D axisymmetric numerical simulation. They concluded that energy separation is the result of mechanical energy transfer via friction in combination with cooling due to expansion of gas. Kazantseva *et al.* (2005) performed a 3D simulation, showing that multiple large scale vortices are present in the main tube, which were also observed by, among others, Farouk & Farouk (2007), Secchiaroli *et al.* (2009), and

Xue *et al.* (2011).

Most numerical computations have shown to be able to capture (some of) the energy separation phenomenon, however, do not provide a full understanding of the energy separation processes inside the RHVT. More extensive reviews of the available literature are found in Eiamsa-ard & Promvonge (2008b), Yilmaz *et al.* (2009), Xue *et al.* (2010).

### 1.2.2 The RHVT as a separator

Since its invention, many scientists have focused on the energy separation process in the RHVT or have tried to increase its efficiency by optimizing the geometry of the vortex tube (Nimbalkar & Muller, 2009; Takahama & Yokosawa, 1981). Less attention was paid, however, to a second possible use for the RHVT: separation of gases or removal of undesired condensable components from a gas stream.

Comparing the RHVT to a conventional cyclone separator reveals that there are some agreements. First of all, gas (and possibly particles/droplets) is tangentially injected to create a fast rotating flow. Secondly, the device has also two exits, one close to the inlet and the other at the end of a cylindrical body. Empirical correlations that are used to estimate the collection efficiency and required pressure drop of cyclones are widely available (see e.g. Cortes & Gil (2007)). Unfortunately, assumptions that are often made, e.g. no axial variation of the swirl velocity, no re-circulation, and incompressibility of the medium, do generally not hold for the flow in the vortex tube, making the correlations less (or not) applicable.

The typical pressure drop over a RHVT is orders of magnitude larger than that of cyclone separators in order to have the cooling and heating effect. This makes the RHVT less practical as solely particle separator. However, by utilizing the cooling effect the advantage of the RHVT becomes more clear.

The local cooling effect can be used to liquify undesired condensable components in a gas mixture, thereby forming small droplets that are suspended in the gas. The large centrifugal force (the centrifugal force can reach values of over  $10^6$  times the earth's gravitational force in an RHVT with a main tube of 1 cm in diameter) that acts on these droplets in combination with the higher mass density of the droplets compared to that of the gas, cause them to be transported away from the tube axis towards the main tube wall. At the wall, a liquid film, which can easily be removed from the gas stream, can be formed. After removing the liquid film, the gas stream is (partially) cleaned from the undesired components. Therefore, the high swirl velocity in combination with the cooling effect, which acts in addition to the cooling due to expansion of the gas, and the simplicity of the design make the RHVT suitable for, e.g., the removal of CO<sub>2</sub> from natural gas.

Linderstrøm-Lang (1964) has studied the enrichment or depletion of gaseous components in the hot or cold streams. He has performed experiments with oxygen (O<sub>2</sub>) and nitrogen (N<sub>2</sub>), O<sub>2</sub> and CO<sub>2</sub>, and O<sub>2</sub> and helium, and showed that there is separation of the components, however, the separation effect is fairly small ( $< 0.01\%$ ). Hellyar (1979) reports several potential applications of the RHVT in (natural) gas processing. Dependent on the types of prototypes, the condensables were separated from the cold or from the hot stream. Hajdik *et al.* (1997) have shown that the separation of condensate from natural gas is improved by using a RHVT, compared to a conventional (Joule-Thompson valve) system. The advantage of the RHVT is that the system is less complex and less costly compared to an isentropic system, such as a turboexpander. They have shown that liquid removal with RHVT's is successful, even when liquid concentrations up to 5% are present at the inlet feed. A single

phase gas at the inlet is therefore not essential. FILTAN (2013) has produced vortex tube separators for gas flows of  $140.000 \text{ Nm}^3/\text{h}$  that are used for natural gas dehydration or liquid hydrocarbon recovery (in operation for RWE since 2001 as a separation unit for the cavern storage in Epe, Germany). They state that a 15 – 20% (by weight) additional condensate recovery may be expected compared to a conventional Joule-Thompson process. According to FILTAN (2013), the most important advantages of the RHVT as a separator are

- Less downtime (the time that the device is out of operation);
- A short start up phase;
- Lower capital and operation costs;
- Minimal maintenance is required because of the lack of rotating parts;
- Small volume occupation.

The main disadvantages of the RHVT are that the device requires a significant pressure drop (the pressure ratio must be at least 1.3 or higher (FILTAN, 2013)) and that the thermodynamic efficiency is much lower than, e.g., a turboexpander (approximately a factor 3 lower), or a conventional cooler (approximately a factor 10 lower).

### 1.3 Motivation and objective of the research

For the design of an effective separator, we would like to know where droplets are present in the RHVT, how large they are, and what their velocities and trajectories are, in short: we would like to know the behaviour of droplets in the RHVT.

Local heating and cooling in the device influence the droplet behaviour. Dependent on local conditions, like temperature, pressure, and gas composition, the droplets change in size due to condensation or evaporation. By understanding the thermodynamics of the RHVT and how the energy transfer is related to the dimensions of the vortex tube and its operating conditions, one is able to optimize the geometry of the RHVT, both as a cooler (heater) and as a separator.

A second important subject of this project, which is the topic of a second PhD thesis, involves a Large Eddy Simulation (LES) of a droplet-laden RHVT. In this numerical study, the flow in a vortex tube, having similar dimensions as in the experiments, is simulated. Droplets are added to the flow and their behaviour is simulated. The results of the numerical simulation will be used as a tool for future design optimizations, thermodynamical predictions, and to estimate the performance of the RHVT as a separator.

The knowledge gained from the - both experimental and theoretical - study presented in this thesis will be used to validate results of the numerical simulations of the flow and droplet behaviour in the RHVT.

Performing experiments with a gas mixture that is equivalent to natural gas, e.g., a mixture of  $\text{CH}_4$  and  $\text{CO}_2$ , is very expensive and requires elaborate safety measures. To reduce safety risks and the running costs of the experiments, we have utilized a laboratory scale experimental RHVT that is operated with a gas mixture consisting of nitrogen gas as the main fluid, and water (in liquid and gaseous state) as the contaminant.

## 1.4 Preview of this thesis

In chapter 2 we theoretically investigate the droplet behaviour in a vortex tube from which the temperature, pressure, and velocity distributions are known from a previous study (Gao, 2005). Based on the equation of motion for droplets and a phase change model, droplet velocities, trajectories, and sizes are computed. The influences of the humidity of the gas mixture and the size of droplets on the droplet behaviour are evaluated. The main aims of this chapter are to provide a first insight into the behaviour of droplets in the RHVT and to determine criteria and specifications for the laboratory equipment that is used during the experimental studies.

Details of the experimental RHVT and all the sensing/controlling equipment are listed in chapter 3. The physics behind the utilized experimental techniques, such as Phase Doppler Particle Analysis (PDPA), which is used to measure droplet velocities and sizes, and a Cylindrical Pitot Tube method (CPT), which is used to measure gas velocities, are described. The calculations and designs of crucial components in the experimental setup, such as the swirl generator, measurement sections, and the gas conditioning system are provided.

Chapter 4 discusses experimental results that are obtained from PDPA measurements in the RHVT. We provide an estimation what sizes of droplets we may expect to measure, based on the geometry of the swirl generators and the operating conditions. The definitions of the velocity statistics are given, and results of a test case, which are used to verify measured velocities, are presented. Various PDPA experiments were performed. Operating conditions were varied in order to investigate individual influences of, e.g., mass flow and cold fraction, on the droplet behaviour. The measured droplet velocities, velocity moments, and droplet sizes are reported and an extensive analysis of the results is given.

In chapter 5 we present an energy separation model that we have developed. The model is used to predict the temperatures in the exits of the RHVT, its cooling power, and thermodynamic efficiency. Various experiments have been performed to validate the model. The type of swirl generator, the mass flow, and the operating pressures were varied to cover a wide range of experimental conditions.

Preliminary results of water vapour separation from a gas mixture with the vortex tube are provided in chapter 6. Additionally, we utilize the developed energy separation model in order to model the thermodynamics when the RHVT is operated with a mixture of methane and carbon dioxide. Based on this model, the cold and hot exit temperatures are computed and predictions are made regarding the enrichment of methane in the exit streams of the RHVT.

Finally, the conclusions and recommendations are listed in chapter 7.



## 2 | Theoretical analysis of droplet behaviour in the RHVT

In the experiments described in this thesis, water droplets are used for two different reasons. The first is the use of water droplets as contaminants that need to be separated from the gas. The second is the use as ‘tracers’ to measure flow velocities in the RHVT. It is important to have an indication how droplets behave and whether they are detectable during experiments, because this knowledge is crucial to determine specifications for expensive laboratory equipment that will be used for the experimental study.

In this chapter, we theoretically investigate the behaviour of water droplets that are injected, together with a carrier gas (nitrogen and water vapour), into the RHVT. When the gas is unsaturated with water vapour, the droplets will evaporate after they are injected. Due to their small sizes, the process of evaporation can be very fast and takes place within a few milliseconds. Another possibility is that the gas is already saturated or even supersaturated. In the latter case, water vapour will condense onto the droplets, which then increase in size.

It will be shown that the droplet size is an important parameter in the equation of motion for droplets. To compute the droplet size while a droplet is moving through the RHVT, we have included a phase change model in the description of the droplet behaviour. Using a discretized equation of motion and the phase change model, we have simulated droplet velocities, trajectories, sizes (in short the droplet behaviour), and we computed droplet concentrations in the vortex tube.

In §2.1, the simplified equation that describes the motion of small spherical particles is provided. In §2.2, the phase change model that is utilized to simulate condensation or evaporation is described. Details of the numerical method are provided in §2.3. Gas conditions and results of the simulated droplet behaviour in the vortex chamber and in the main tube are shown in §2.4 and §2.5, respectively.

### 2.1 Equation of motion for small droplets

Droplets are assumed to be spherical, having a typical diameter of  $\mathcal{O}(1)$   $\mu\text{m}$ , and are considered as point particles with a volume fraction so low, that their effect on the fluid flow is negligible and that droplet-droplet interactions play no role (Elghobashi, 1994). Therefore, only the forces exerted by the fluid on the droplets have to be taken into account. The ratio of the mass densities of water droplets and gas is so high that the added mass force, lift force, and history force are considered to be negligible. The force due to gravity is much smaller than the drag or centrifugal force and is, therefore, also neglected. The only forces acting on

Type of force	Order of magnitude [N]
Added mass force	$10^{-11}$
Lift force	$10^{-11}$
History force	$10^{-12}$
Drag force	$10^{-8}$
Centrifugal force	$10^{-8}$
Gravitational force	$10^{-14}$

Table 2.1: The types of forces and their order of magnitudes based on a particle diameter of  $2 \mu\text{m}$ , a density ratio between the droplet material and the gas of  $10^3$ , and typical velocities and velocity gradients that are measured in the vortex tube (Gao, 2005).

the droplets, which are considered, are the viscous friction of the fluid upon the droplets and the centrifugal force due to the swirl velocity. An order of magnitude estimate of the forces is provided in Table 2.1.

Taking all these assumptions into account, the equation of motion for droplets (Maxey & Riley, 1983) in cylindrical coordinates is given by

$$\frac{d\mathbf{u}}{dt} = \frac{\mathbf{v} - \mathbf{u}}{\tau_p} (1 + 0.15\text{Re}_p^{0.687}) + \mathbf{f}, \quad (2.1)$$

where  $\mathbf{u} = [U_r, U_\theta, U_z]^T$  is the velocity of a droplet with diameter  $d_p$ , and  $\mathbf{v} = [V_r, V_\theta, V_z]^T$  is the fluid velocity at the droplet position  $\mathbf{x} = [r, \theta, z]^T$ . The equation is valid for droplet Reynolds numbers  $\text{Re}_p < 800$  (Schiller & Naumann, 1933). The droplet inertial response time  $\tau_p$  is given by (Crowe *et al.*, 2012, p. 24)

$$\tau_p = \frac{\rho_p d_p^2}{\rho_f 18 \nu_f} C_c, \quad (2.2)$$

where  $\rho_f$  and  $\rho_p$  are the mass densities of the fluid and droplet material, respectively,  $\nu_f = \mu_f / \rho_f$  is the kinematic viscosity of the fluid, which is the ratio of the dynamic viscosity  $\mu_f$  and the mass density of the fluid, and  $C_c$  is the slip factor. Subscripts  $f$  and  $p$  are used to indicate fluid or droplet properties. The slip factor is important when the droplet size becomes of the same order of magnitude as the molecular mean free path length of the fluid (Cunningham, 1910). The slip factor is computed according to (Davies, 1945)

$$C_c \approx 1 + \frac{2.514 \lambda_m}{d_p}. \quad (2.3)$$

The molecular mean free path length,  $\lambda_m$ , is given by (Bird *et al.*, 2007, p. 24)

$$\lambda_m = \frac{kT}{\pi \sqrt{2} d_m^2 p}, \quad (2.4)$$

where  $k \approx 1.38 \cdot 10^{-23} \text{ J/K}$  is the Boltzmann constant,  $p$  is the pressure, and  $d_m$  is the molecular collision diameter of, in this case, nitrogen molecules ( $d_m \approx 0.3789 \text{ nm}$  (Poling *et al.*, 2001, p. B2)). At room temperature and atmospheric pressure  $\lambda_m \approx 63 \text{ nm}$ . The Reynolds number is the ratio of inertial forces to viscous forces (Kundu & Cohen, 2008, p. 166) and is defined as

$$\text{Re}_p \equiv \frac{|\mathbf{v} - \mathbf{u}| d_p}{\nu_f}. \quad (2.5)$$



The flow is considered to be axisymmetric, and in combination with the cylindrical coordinate system, the centrifugal acceleration reads

$$\mathbf{f} = [f_c, 0, 0]^T, \quad (2.6)$$

where  $f_c = U_\theta^2/r$ , and  $U_\theta$  is the swirl velocity of the particle.

## 2.2 Phase change model

In the experiments, nitrogen was used as the carrier gas to which water droplets were added. The nitrogen gas itself is dry, i.e., the water vapour content is zero. If water vapour is added to the nitrogen gas, a gas mixture is formed. Dependent on the amount of water vapour in the gas mixture, the mixture can be unsaturated, saturated or supersaturated. Except for the case that the gas mixture is saturated, there is a non-equilibrium between the partial pressures of water vapour and nitrogen. When droplets are introduced in the gas mixture, phase changes tend to bring the system back to equilibrium (which is the saturated state). If the gas mixture is unsaturated, droplets evaporate, thereby increasing the water vapour content and decreasing the droplet size. In the other case, when the gas mixture is supersaturated, water vapour condenses onto the droplets and the water vapour content decreases while droplets grow.

The droplet size is an important parameter in the equation of motion for droplets (see previous section). To determine what droplet sizes we may expect in different regions of the vortex tube, we have modeled the phase change process using the analysis given by Kuo (2005, pp. 572-578), which is based on Spalding's approach (Spalding, 1953). The model is valid for a single droplet, present in a quiescent atmosphere of a given temperature and pressure, where the mass density of water vapour  $\rho_v$  and the diffusion coefficient  $\mathcal{D}$  (Appendix A) are assumed to be independent of the radial coordinate  $r$ , which is the radial coordinate with respect to the droplet center (Fig. 2.1, not to be confused with the coordinate system in the RHVT). In our case, the gas mixture contains two species: water vapour and nitrogen gas.

When a droplet evaporates or water vapour condenses onto the droplet, the water vapour that surrounds the droplet has a velocity normal to the droplet surface. Because one phase changes into another phase, having different mass densities, the normal velocity of the surface of the droplet differs from the velocity of the water vapour at the droplet surface. The ratio of both velocities is equal to the mass density ratio between both phases. In the case of water, the density ratio between liquid and water vapour is  $\mathcal{O}(10^3)$ , so the velocity of the droplet surface is much smaller than the normal velocity of water vapour at the droplet surface. Therefore, we may neglect the surface velocity, and the distributions of water vapour mass fraction and temperature around the droplet can be considered to be quasi-steady.

The water vapour mass fraction  $Y$  is defined as the ratio of the partial density of water vapour  $\rho_{\text{H}_2\text{O}}$  over the mass density of the gas mixture  $\rho$  according to  $Y = \rho_{\text{H}_2\text{O}}/\rho$ . The steady-state continuity equation of the water vapour mass fraction in the gas that surrounds the droplet is

$$r^2 v \frac{dY}{dr} = \frac{d}{dr} \left( r^2 \mathcal{D} \frac{dY}{dr} \right), \quad (2.7)$$

where  $v$  is the velocity normal to the droplet surface (Fig. 2.1). It is assumed that nitrogen does not dissolve into the liquid water. Therefore, there is no mass flux of nitrogen (Faeth,

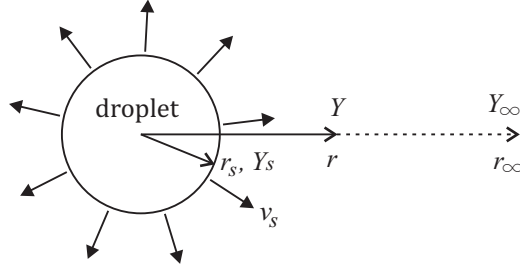


Figure 2.1: Droplet coordinate system and the most relevant parameters.

1977), and the water vapour mass flux at the droplet surface (subscript  $s$ ) is

$$\rho_v v_s = Y_s \rho_v v_s - \rho_v \mathcal{D} \left( \frac{dY}{dr} \right)_s. \quad (2.8)$$

$Y_s$  is the mass fraction of water vapour at the surface and can be determined (this will be described in §2.2.1) by making the assumption that the gas mixture in the vicinity of the water droplet is always saturated (Sazhin, 2005). The first term at the right-hand-side of Eq. (2.8) is due to bulk convective motion of gaseous mixture at the surface (mass transfer driven), the second term represents the mass flux caused by a water vapour concentration gradient above the droplet surface (diffusion driven).

From Eq. (2.8) we derive the velocity of water vapour leaving the surface

$$v_s = \frac{\mathcal{D}}{Y_s - 1} \left( \frac{dY}{dr} \right)_s. \quad (2.9)$$

Spalding then defined

$$b \equiv \frac{Y}{Y_s - 1}. \quad (2.10)$$

Because  $Y_s$  does not depend on the radial coordinate, Eq. (2.9) can be rewritten by using Eq. (2.10) to become

$$v_s = \mathcal{D} \left( \frac{db}{dr} \right)_s. \quad (2.11)$$

Applying conservation of mass ( $r^2 v = r_s^2 v_s$ ) the species continuity equation, which is described by Eq. (2.7), becomes

$$r^2 v b = \mathcal{D} r^2 \frac{db}{dr} + C_1, \quad (2.12)$$

where the constant  $C_1$  is found with Eq. (2.11) to be  $C_1 = r_s^2 v_s (b_s - 1)$ . Substituting this in the species continuity equation leads to

$$\frac{r_s^2 v_s}{r^2 \mathcal{D}} dr = \frac{db}{b - b_s + 1}. \quad (2.13)$$

Integration of this equation yields

$$-\frac{r_s^2 v_s}{r \mathcal{D}} = \ln(b - b_s + 1) + C_2, \quad (2.14)$$

The integration constant  $C_2$  is determined by the boundary condition  $b|_{r=r_\infty} = b_\infty$ , and found to be  $C_2 = -\ln(b_\infty - b_s + 1)$ . The subscript  $\infty$  is used to indicate a quantity or condition ‘far away from the droplet surface’. The final solution of Eq. (2.7) is given by

$$\frac{r_s^2 v_s}{r \mathcal{D}} = \ln \left( \frac{b_\infty - b_s + 1}{b - b_s + 1} \right). \quad (2.15)$$

At the droplet surface  $r = r_s$ , we have

$$r_s v_s = \mathcal{D} \ln(b_\infty - b_s + 1) = \mathcal{D} \ln(1 + B_M), \quad (2.16)$$

where the Spalding mass transfer number,  $B_M \equiv b_\infty - b_s$ , is ‘‘a convenient driving potential for the definition of a mass transfer coefficient for the diffusion of one gas through a stagnant gas’’ (Faeth, 1977). In terms of water vapour mass concentration, the Spalding mass number is

$$B_M \equiv \frac{Y_\infty - Y_s}{Y_s - 1}. \quad (2.17)$$

$Y_s$  and  $Y_\infty$  are the water vapour mass fractions at the droplet surface and far away from the droplet in the gas mixture, respectively, and will be defined in the next section.

With Eq. (2.16),  $2r_s = d_p$ , and the mass transfer rate per unit area, which is defined as  $\frac{dm_p}{dt} / 4\pi r_s^2 = -\rho_v v_s$ , the change of mass of a droplet in time is

$$\frac{dm_p}{dt} = -2\pi \rho_v d_p \mathcal{D} \ln(1 + B_M). \quad (2.18)$$

The change of the droplet diameter is related to Eq. (2.18),  $d_p$ , and the mass density of liquid water,  $\rho_p$ , according to

$$\frac{dd_p}{dt} = \frac{2}{\pi d_p^2 \rho_p} \frac{dm_p}{dt} = -4 \frac{\rho_v}{\rho_p} \frac{\mathcal{D}}{d_p} \ln(1 + B_M). \quad (2.19)$$

In case of constant  $B_M$ , pressure, diffusion coefficient, and mass densities, the droplet diameter as a function of time can easily be found to be

$$d_p(t) = \sqrt{d_{p,0}^2 - 8t \frac{\rho_v}{\rho_p} \mathcal{D} \ln(1 + B_M)}, \quad (2.20)$$

where  $d_{p,0}$  is the initial droplet diameter and  $t$  is the time. The time it takes for the droplet to completely evaporate,  $t_{life} \equiv t|_{d_p=0}$ , is the droplet lifetime

$$t_{life} = \frac{\rho_p d_{p,0}^2}{8\rho_v \mathcal{D} \ln(1 + B_M)}. \quad (2.21)$$

The equation shows that the lifetime depends quadratically on the initial droplet diameter. This is the reason that Spalding’s model is often referred to as the d-squared law.

### 2.2.1 Humidity

When the water vapour fraction near the surface of the droplet equals the water vapour fraction in the gas mixture, i.e.  $Y_s = Y_\infty$ , the Spalding mass transfer number is zero. In

this case, the gas mixture is saturated and there will be no net condensation or evaporation. When  $Y_s > Y_\infty$ , the Spalding mass transfer number is  $B_M > 1$  resulting in  $dm_p/dt < 0$ : droplets evaporate. If  $Y_s < Y_\infty$  the Spalding mass transfer number is  $B_M < 1$  resulting in  $dm_p/dt > 0$ : the water vapour present in the gas mixture condenses onto the droplets, which means that they grow in time. The water vapour mass fraction in the gas mixture is therefore an important parameter in the phase change process.

The mass fraction of a species,  $Y_i$ , is defined as the ratio of the partial and total mass densities. Assuming that the gas is ideal, the partial mass density can be found by using the ideal gas law

$$\rho_i = \frac{p_i M_i}{\mathcal{R}T}, \quad (2.22)$$

where  $p_i$  is the partial pressure,  $\mathcal{R} = 8.314 \text{ J/mol K}$  is the universal gas constant,  $M_i$  is the molar mass of the species, and  $T$  is the temperature. The total mass density is defined as  $\rho = \sum \rho_i$ . The mass fraction of water vapour in a mixture of water vapour and nitrogen is found to be

$$Y = \frac{\rho_{\text{H}_2\text{O}}}{\rho} = \frac{p_{\text{H}_2\text{O}} M_{\text{H}_2\text{O}}}{p_{\text{H}_2\text{O}} M_{\text{H}_2\text{O}} + p_{\text{N}_2} M_{\text{N}_2}} = \left[ 1 + \left( \frac{p}{p_{\text{H}_2\text{O}}} - 1 \right) \frac{M_{\text{N}_2}}{M_{\text{H}_2\text{O}}} \right]^{-1}, \quad (2.23)$$

where  $M_{\text{N}_2}$  and  $M_{\text{H}_2\text{O}}$  are the molar masses of nitrogen and water, respectively, and  $p_{\text{H}_2\text{O}}$  is the partial pressure of water vapour.

As mentioned above, the gas mixture in the vicinity of the water droplet is assumed to be saturated. This means that the partial pressure of water vapour in this region equals the saturation vapour pressure of water,  $p_{sat}$ , which depends on the temperature (Appendix A). The ratio of the partial pressure and the saturation pressure of water vapour is defined as the relative humidity RH:

$$\text{RH} \equiv \frac{p_{\text{H}_2\text{O}}}{p_{sat}(T)}. \quad (2.24)$$

If  $\text{RH} < 1$ , water droplets evaporate, and if  $\text{RH} = 1$ , the gas mixture is saturated and there are no phase changes. For  $\text{RH} > 1$ , the gas mixture is supersaturated and water vapour condenses onto the droplets. Rewriting Eq. (2.23) by using Eq. (2.24), leads to the following equations for the mass fractions of water vapour near the surface and in the ambient gas mixture

$$Y_s = \left[ 1 + \left( \frac{p}{p_{sat}(T_p)} - 1 \right) \frac{M_{\text{N}_2}}{M_{\text{H}_2\text{O}}} \right]^{-1}, \quad (2.25a)$$

$$Y_\infty = \left[ 1 + \left( \frac{p}{\text{RH} \cdot p_{sat}(T_\infty)} - 1 \right) \frac{M_{\text{N}_2}}{M_{\text{H}_2\text{O}}} \right]^{-1}. \quad (2.25b)$$

In the RHVT, the local relative humidity changes as a function of the local temperature and pressure. The change in overall water vapour content (or humidity) due to the phase change processes, can safely be neglected if the total mass of all droplets that are suspended in the gas is small compared to  $Y_\infty$ . For larger amounts of liquid water, however, the change in water vapour content may be significant and needs to be taken into account. This, however, is computationally very expensive.

For simplicity, we assume that the mole fraction of water vapour,  $\Gamma \equiv \frac{p_{\text{H}_2\text{O}}}{p}$ , in the RHVT is not affected by the phase changes. This means that the mole fraction of water vapour in the RHVT is equal to the conditions in the plenum (before the gas enters the vortex tube,

indicated with subscript  $pl$ ). The properties of the gas mixture in the plenum are considered to be known quantities that are used to compute the local humidity according to

$$\text{RH} = \frac{p(z, r)}{p_{\text{sat}}(T(z, r))} \Gamma_{pl}, \quad (2.26)$$

in which  $\Gamma_{pl}$  is the mole fraction in the plenum, defined as

$$\Gamma_{pl} = \frac{p_{\text{sat}}(T_{pl})}{p_{pl}} \text{RH}_{pl}. \quad (2.27)$$

### Notes on supersaturation

In some regions of the RHVT, the relative humidity might be larger than one (which will be shown in §2.5.1), and the water vapour in the gas mixture is supersaturated. When there are no condensation nuclei present, and the humidity reaches a critical value, homogeneous condensation occurs. The condition  $\text{RH} > 1$  is generally known as supersaturation. The critical value of the supersaturation to have homogeneous condensation is referred to as the onset supersaturation. For water vapour at room temperature the onset supersaturation is approximately  $\text{RH} = 3.5$  (Heist & Reiss, 1973; Miller *et al.*, 1983). The homogeneous condensation process is fast, typically  $\mathcal{O}(10^{-3})$  s, and causes the supersaturation to relax to saturation, i.e.  $\text{RH} = 1$ . During this process, small droplets are first formed by nucleation, which is then followed by condensation.

The theory that describes homogeneous nucleation and accompanying droplet growth during condensation is complex and is not considered here. Therefore, we have assumed that homogeneous condensation does not take place and that the relative humidity (supersaturation) may exceed the onset supersaturation.

### 2.2.2 Energy balance

Heat exchange between the droplets and their surrounding gas plays an important role in the phase change process. Latent heat of vaporization is absorbed or released during evaporation or condensation, respectively. For both processes, the temperatures of both the droplet and the fluid are important.

Internal heat transfer in the droplet material is much faster than heat transfer in the water vapour, due to its higher thermal conductivity (neglecting convection). Therefore, we may assume that the droplet temperature is uniform. Thermal energy for the phase change process is initially delivered by the heat capacity of the droplet. In the case of evaporation, the temperature of the droplet  $T_p$  drops below the temperature of the ambient gas  $T_\infty$ . The now existing temperature difference causes heat transfer  $Q$  from the ambient gas to the droplet. The general equation for the heat transfer is

$$Q = \bar{h} A \Delta T, \quad (2.28)$$

where  $\bar{h}$  is the overall heat transfer coefficient,  $A$  is the surface area through which the heat is transferred, and  $\Delta T$  the temperature difference between the surface and fluid at large distance from the surface. The energy that is required for the phase change process is

$$Q_{fg} = \frac{dm_p}{dt} h_{fg}, \quad (2.29)$$

where  $h_{fg}$  is the specific enthalpy of vaporization of water.

The change in droplet temperature in time is given by the thermal energy balance

$$m_p c_w \frac{dT_p}{dt} = Q + Q_{fg}, \quad (2.30)$$

where  $c_w$  is the heat capacity of liquid water. After some time, the phase change process becomes steady:  $m_p c_w \frac{dT_p}{dt} = Q + Q_{fg} = 0$ , and the droplet reaches an equilibrium temperature, i.e., the so-called wet bulb temperature (Holterman, 2003).

The heat transfer coefficient in Eq. (2.28) is found with a Nusselt correlation. This empirical correlation is a dimensionless heat transfer coefficient and is defined as the ratio of convective heat transfer and conductive heat transfer across a boundary according to

$$\text{Nu} \equiv \bar{h}\mathcal{L}/\lambda_f, \quad (2.31)$$

where  $\mathcal{L} = d_p$  is a characteristic length scale, which is in this case the droplet diameter, and  $\lambda_f$  is the thermal conductivity of the gas mixture. Empirical correlations have been determined for a variety of heat transfer situations (Janna, 2000). The Nusselt number for a single sphere in a fluid is given by the Ranz-Marshall correlation (Ranz & Marshall, 1952)

$$\text{Nu} = 2 + 0.6\text{Re}_p^{1/2}\text{Pr}^{1/3}, \quad (2.32)$$

where the Reynolds number is  $\text{Re} = |\mathbf{v} - \mathbf{u}|d_p/\nu_f$  (defined in §2.1), and  $\text{Pr} = \nu_f/\alpha_f$  is the Prandtl number of the gas, which is the ratio of kinematic viscosity  $\nu_f$  to thermal diffusivity  $\alpha_f$  of the fluid ( $\text{Pr} \approx 0.7$  for nitrogen gas). The above correlation is valid for  $0 \leq \text{Re}_p < 200$  and  $0 \leq \text{Pr} < 250$ .

For Reynolds numbers  $\text{Re}_p \ll 1$ , the Nusselt correlation is  $\text{Nu} \approx 2$ . In that case, the dominant heat transfer mechanism is conduction. Because the droplets are small ( $\mathcal{O}(1)\mu\text{m}$ ), it is assumed that  $\text{Re}_p \ll 1$ . Therefore, by applying the approximation  $\text{Nu} \approx 2$ , the heat transfer between the droplet and its surrounding gas becomes

$$Q = 2\pi d_p \lambda_f (T_\infty - T_p). \quad (2.33)$$

With the energy balance and the phase change model, the temperature of the droplet can be computed. This temperature is used in Eq. (2.25a) to determine the water vapour mass fraction at the droplet surface, which is required to compute the Spalding Mass number.

### 2.2.3 Evaluation of the phase change model

The phase change model will now be evaluated. It is assumed that a single water droplet is present in a large volume of quiescent gas mixture of nitrogen gas and water vapour. Therefore, the relative humidity, the diffusion coefficient, and the temperature of the gas far away from the droplet are not affected by the phase changes and are taken to be constant. The initial temperature of the droplets equals that of the gas, and the initial droplet diameter is  $d_{p,0} = 20 \mu\text{m}$ . Table 2.2 shows some of the computed lifetimes and the corresponding droplet temperatures for different humidities and ambient temperatures. The time it takes for the  $d_{p,0} = 20 \mu\text{m}$  droplet to reach the equilibrium temperature is  $\mathcal{O}(10)$  ms.

Other models that describe droplet vaporization, which are found in literature, are valid for droplets in air at atmospheric pressure, e.g. Ferron & Soderholm (1990), or are derived

$T_\infty$ [°C]	RH [%]	$T_p$ [°C]	$t_{life}$ [s]
10	0.00	1.77	0.62
	0.10	2.66	0.70
	0.50	6.07	1.31
	0.90	9.24	6.81
20	0.00	7.55	0.41
	0.10	9.00	0.46
	0.50	14.31	0.89
	0.90	18.94	4.80
50	0.00	20.58	0.16
	0.10	25.27	0.20
	0.50	38.96	0.44
	0.90	48.12	2.62

Table 2.2: The droplet lifetime and droplet temperature for a  $d_{p,0} = 20 \mu\text{m}$  water droplet in a quiescent nitrogen-water vapour mixture at atmospheric pressure.

for droplets that have a certain velocity with respect to the carrier gas, e.g. Holterman (2003). Nevertheless, values of the lifetimes computed with the Spalding model agree within 15% with the values found in the literature.

The dependencies of the lifetime on the ambient temperature, droplet size, pressure, and relative humidity are plotted in Fig. 2.2. Fig. 2.2a shows the lifetimes for three ambient temperatures as functions of the relative humidity. Fig. 2.2b shows the lifetimes as functions of the initial droplet size for an ambient temperature of  $T_\infty = 20^\circ\text{C}$ . Larger droplets have a longer lifetime than smaller droplets, and the lifetime increases with increasing humidity. Results shown in Fig. 2.2c were obtained for evaporating droplets at atmospheric pressure. Fig. 2.2d shows results that were obtained with an ambient pressure of 10 bars. The ambient temperature was kept constant at  $20^\circ\text{C}$  for both pressures. Increasing the pressure thus increases the lifetime of droplets.

## 2.3 Numerical method

The equation of motion of droplets, which is described by Eq. (2.1), was solved numerically (partially based on the Crank-Nicolson method (Crank & Nicolson, 1947), which is a second order method and implicit in time). The discretized equation of motion is

$$\frac{\mathbf{u}_i - \mathbf{u}_{i-1}}{\Delta t} = \frac{\mathbf{v}_i^* - \mathbf{u}_i^*}{\tau_{p,i-1}} (1 + 0.15\text{Re}_p^{0.687}) + \mathbf{f}_{i-1}, \quad (2.34)$$

where indices  $i$  and  $i - 1$  denote the current and the previous time step, respectively, and  $\Delta t$  is the size of the time interval.  $\mathbf{v}_i^*$  and  $\mathbf{u}_i^*$  are estimations of the fluid and droplet velocities at time step  $i - \frac{1}{2}$  according to

$$\mathbf{v}_i^* = \frac{\mathbf{v}_{i-1} + \mathbf{v}_e}{2}, \quad \mathbf{u}_i^* = \frac{\mathbf{u}_{i-1} + \mathbf{u}_i}{2}. \quad (2.35)$$

The fluid velocity in the main tube region of the RHVT was measured by Gao (2005) and is therefore considered to be known at every position vector  $\mathbf{x}$ . It is assumed that the flow is

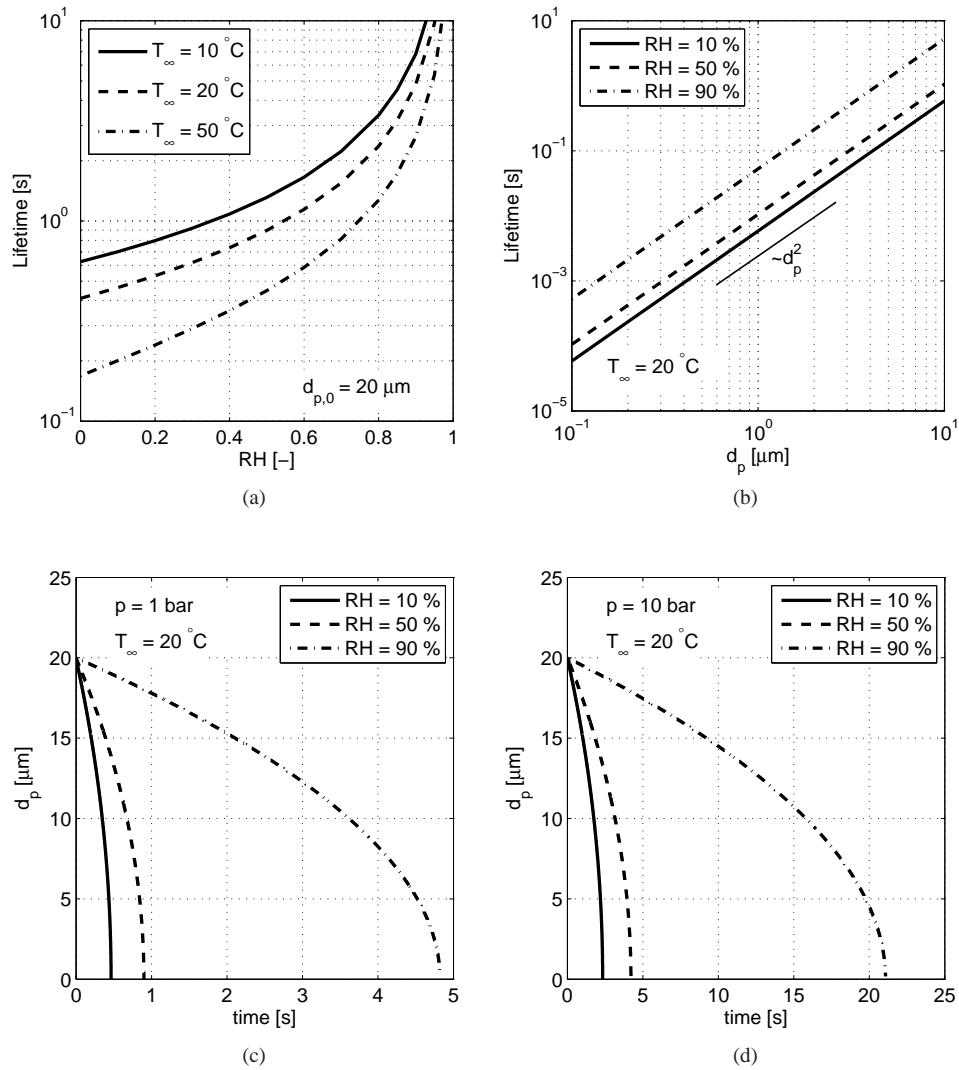


Figure 2.2: (a) The lifetime of a  $d_{p,0} = 20 \mu\text{m}$  droplet as a function of the ambient relative humidity; (b) droplet lifetime as a function of the droplet size for  $T_\infty = 20^\circ\text{C}$ ; (c) droplet size as a function of time at atmospheric pressure (1 bar absolute) and  $T_\infty = 20^\circ\text{C}$ ; (d) droplet size as a function of time at high pressure (10 bar absolute) and  $T_\infty = 20^\circ\text{C}$ .



axisymmetric and that the only relevant coordinates are the radial and axial coordinates. The position vector of the droplet,  $\mathbf{x}$ , is not known a priori, however, it can be estimated by using information from the previous time step:  $\mathbf{x}_e = [r_e, z_e] = \mathbf{x}_{i-1} + \Delta t \mathbf{u}_{i-1}$ , where subscript  $e$  stands for ‘estimated’. From this, we determine the estimated fluid velocity at current time step  $\mathbf{v}_e = \mathbf{v}(\mathbf{x}_e)$ . Substitution of Eq. (2.35) into Eq. (2.34) results in

$$\frac{\mathbf{u}_i - \mathbf{u}_{i-1}}{\Delta t} = \frac{\mathbf{v}_{i-1} + \mathbf{v}_e - \mathbf{u}_{i-1} - \mathbf{u}_i}{2\tau_{p,i-1}} (1 + 0.15\text{Re}_p^{0.687}) + \mathbf{f}_{i-1}. \quad (2.36)$$

Rearranging this equation to find the particle velocity at current time step leads to

$$\mathbf{u}_i = \frac{\frac{\Delta t}{2\tau_{p,i-1}} (\mathbf{v}_{i-1} + \mathbf{v}_e - \mathbf{u}_{i-1}) (1 + 0.15\text{Re}_p^{0.687}) + \Delta t \mathbf{f}_{i-1} + \mathbf{u}_{i-1}}{1 + \frac{\Delta t}{2\tau_{p,i-1}} (1 + 0.15\text{Re}_p^{0.687})}. \quad (2.37)$$

The new position vector is computed with the trapezoidal rule (Spiegelman & Katz, 2006)

$$\mathbf{x}_i = \mathbf{x}_{i-1} + \frac{\Delta t}{2} (\mathbf{u}_{i-1} + \mathbf{u}_i). \quad (2.38)$$

The equations for the droplet velocity and position were combined with the Spalding model (§ 2.2) to compute the droplet size at each time step (which is important for  $\tau_p$ ). The numerical scheme of the simulation is schematically represented in Fig. 2.3. The simulation stopped when the droplet size  $d_p < 0.01d_{p,0}$ , when the droplet hits the RHVT wall ( $r \geq R - d_p/2$ ), the hot exit ( $z \geq L$ ), or when the droplet exits the domain at  $z < 0$ , where  $R$  and  $L$  are the radius and length of the main tube, respectively.

The appropriate size of the time interval depends on the particle relaxation time  $\tau_p$ . We have simulated droplet behaviour with different interval sizes to study the effect on the stability of the solutions and on the accuracy. Stable solutions were found as long as  $\Delta t \leq \tau_p/4$ . Further decreasing the interval size did not result in any significant changes in the solution. This  $\Delta t$  is therefore considered to be sufficiently small to have accurate results.

In practice, large droplet volume fractions may be reached (which is desired in a separator). Consequently, droplet collisions or coalescence are inevitable, thereby forming larger droplets. These large droplets may again break up due to shear stresses in the gas. Because these complex processes are computationally expensive to model, they are neglected to keep the model tractable. For the same reason, turbulence is not accounted for and the flow is assumed to be steady.

## 2.4 Droplet behaviour in the vortex chamber

### 2.4.1 Model parameters of gas in the vortex chamber

The computational domain that was used for the simulation of droplet behaviour in the vortex chamber is shown in Fig. 2.4. The simulation is performed on a cross sectional plane that is located in the middle of the vortex chamber. The radial coordinate  $r$  is made dimensionless with the radius of the vortex chamber  $R_{vc}$ , which is  $R_{vc} = 2R$ .

The flow is considered to be axisymmetric, isothermal, incompressible, and having a radial component  $V_r$  and an azimuthal, or swirl, component  $V_\theta$ . Fluctuations of the velocity are not taken into account. In this region of the vortex tube, there was no temperature data

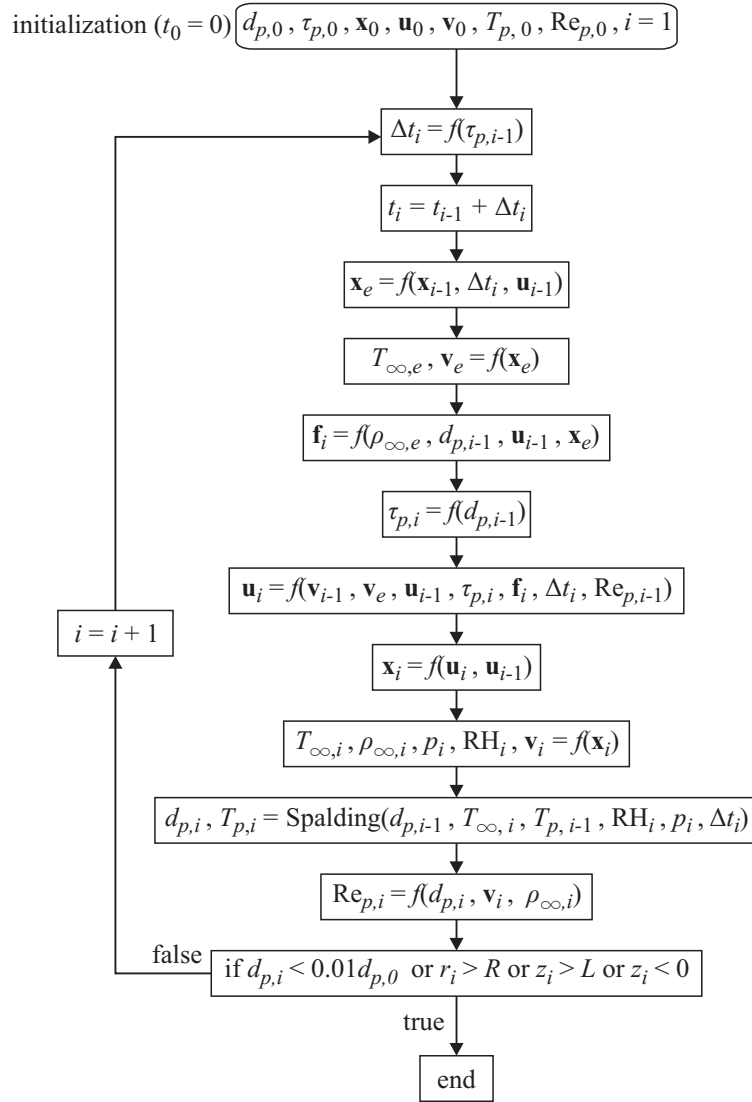


Figure 2.3: Numerical scheme that was used to simulate droplet behaviour in the RHVT.

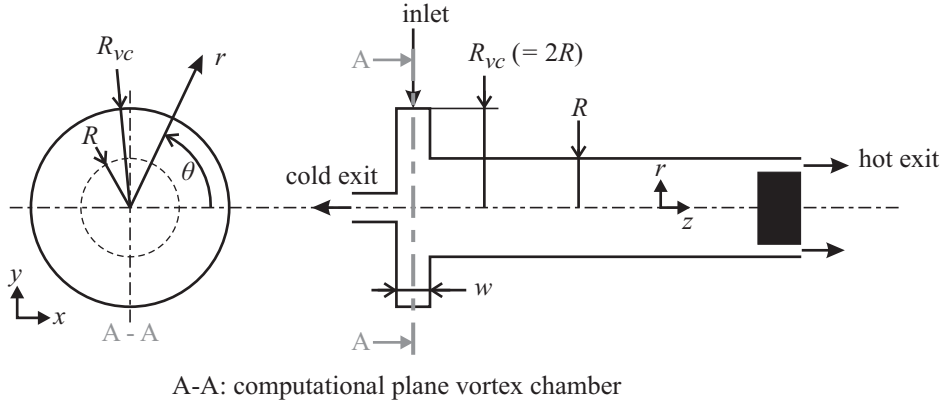


Figure 2.4: Schematic RHVT where the droplet behaviour in the vortex chamber is simulated on the cross sectional plane in the vortex chamber.

available. Therefore, phase changes are not considered in the vortex chamber. The mass flow of nitrogen is 69.5 g/s and the cold fraction is  $\varepsilon = 0.28$ .

The radial and swirl velocity components that were used to simulate droplet behaviour in the vortex chamber are shown in Fig. 2.5. There was no experimental data available for the radial velocity in the vortex chamber. Therefore, we have assumed the following velocity distribution.

The radial velocity is proportional to  $1/r$  in the region  $0.5 \leq rR_{vc}^{-1} \leq 1$  (which equals  $1 \leq rR^{-1} \leq 2$ ), because of conservation of mass. In the region  $0 \leq rR_{vc}^{-1} < 0.5$  (which equals  $0 \leq rR^{-1} < 1$ ), the radial velocity magnitude is taken to be proportional to  $r$ . The maximum radial velocity is  $V_r(r = R) = -15.4$  m/s and is based on the mass flow of 69.5 g/s, a temperature of 20°C, a pressure of 2.25 bar, a thickness of the vortex chamber of  $w = 14$  mm, and a main tube radius of  $R = 20$  mm.

The swirl velocity of the continuous phase in the vortex chamber was measured by Gao (2005) and is proportional to  $r$  in the region  $0 \leq rR_{vc}^{-1} < 0.5$ . Because of conservation of angular momentum, the swirl velocity is proportional to  $1/r$  in the region  $0.5 \leq rR_{vc}^{-1} \leq 1$ . This type of swirl velocity distribution is referred to as a Rankine vortex (Kundu & Cohen, 2008, p. 71), where the swirl velocity in the vortex core is dominated by viscous forces, while in the outer region, the inertial forces are dominant and viscosity can be neglected. The maximum swirl velocity is  $V_\theta(r = R) = 300$  m/s.

## 2.4.2 Results of droplet behaviour in the vortex chamber

Droplets were released in the vortex chamber in the region  $0 \leq rR_{vc}^{-1} \leq 1$ . The radial droplet positions are shown for two droplet sizes as functions of time in Fig. 2.6. Some interesting droplet behaviour can be observed from these figures.

The  $d_p = 0.5$   $\mu\text{m}$  droplets are so small, that the centrifugal force is everywhere in the vortex chamber smaller than the radial drag force (except at the axis) that results from the negative radial velocity of the gas. Therefore, these droplets move towards the axis of the RHVT (Fig. 2.6a). Fig. 2.6b shows the dimensionless radial coordinates as functions of

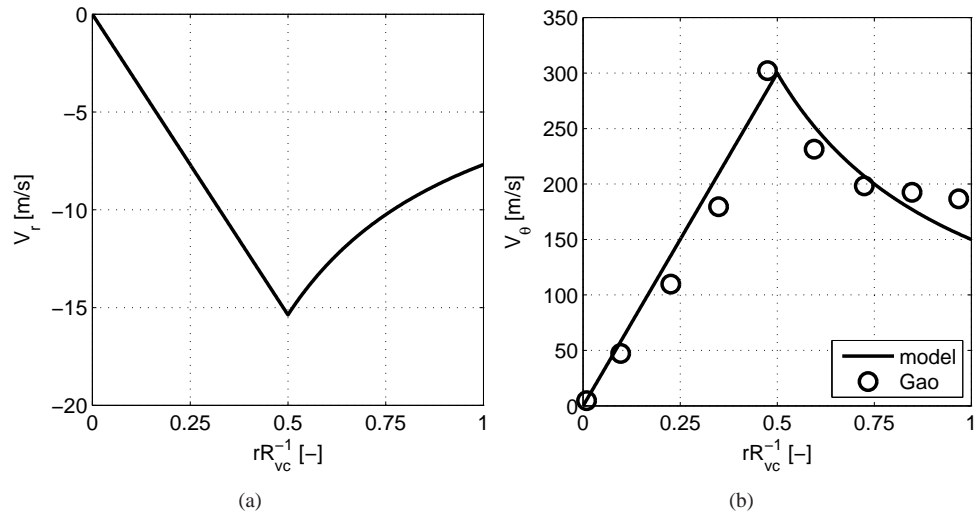


Figure 2.5: Velocity components as functions of the dimensionless radial coordinate in the vortex chamber. (a) Radial velocity; (b) swirl velocity. The symbols are experimental values measured by Gao (2005).

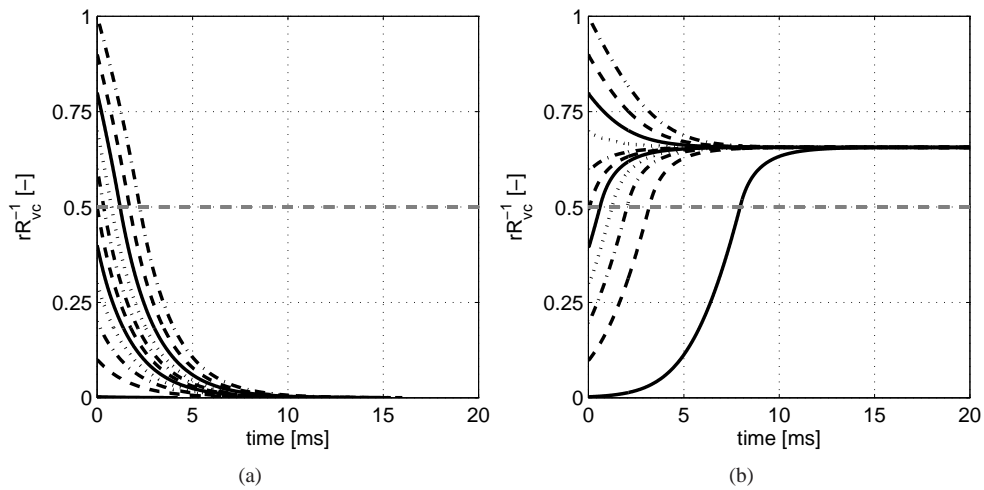


Figure 2.6: Dimensionless radial droplet positions in the vortex chamber as functions of time. (a)  $d_p = 0.5 \mu\text{m}$ ; (b)  $d_p = 1.5 \mu\text{m}$ . Different black lines belong to droplets that were released from different initial radial coordinates. The dashed grey line indicates the radius of the main tube.

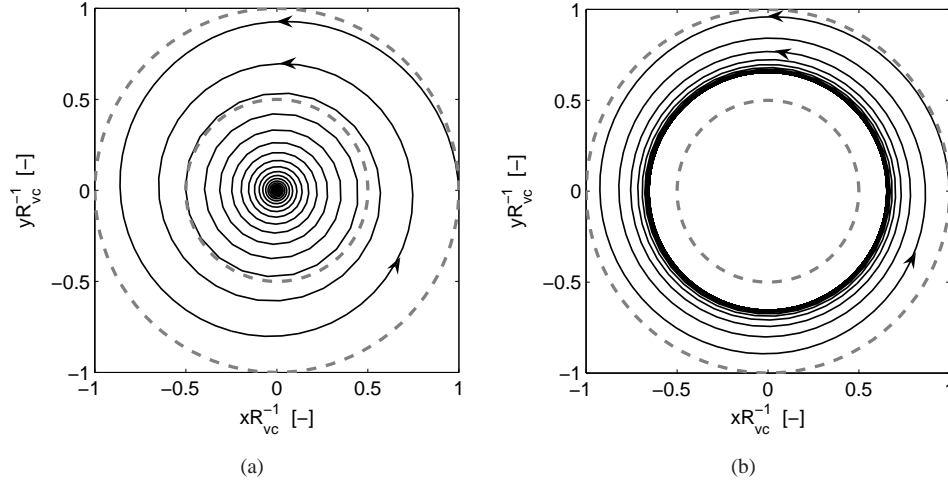


Figure 2.7: Droplet trajectory in the vortex chamber for (a)  $d_p = 0.5 \mu\text{m}$  and (b)  $d_p = 1.5 \mu\text{m}$ . The initial radius is  $r_0 = R_{vc}$ . The outer dashed circle indicates the inner wall of the vortex chamber, the inner dashed circle indicates the main tube wall.

time for  $d_p = 1.5 \mu\text{m}$  droplets. The figure shows that after some time, all droplets are located at a certain radial coordinate. This is the radial coordinate at which the radial drag force is equal to the centrifugal force and is referred to as the equilibrium radius  $r_e$ . For the  $d_p = 0.5 \mu\text{m}$  droplets, the equilibrium radius is  $r_e R_{vc}^{-1} = 0$ . Because  $r_e R_{vc}^{-1} < 0.5$ , they are able to enter the main tube. The equilibrium radius of the  $d_p = 1.5 \mu\text{m}$  droplets, however, is  $r_e R_{vc}^{-1} > 0.5$  and these droplets will not be able to enter the main tube (not simulated here because the simulation is 2D at a plane that is perpendicular to the  $z$  coordinate). This is more clearly seen by plotting the droplet trajectories in the vortex chamber.

Droplet trajectories in the vortex chamber are computed with the angular velocity of a droplet with respect to the axis of the vortex tube,  $\Omega = \dot{\theta} = U_\theta/r$ . The position angle  $\theta$  (see Fig. 2.4) is computed by numerically integrating the angular velocity over time. The corresponding coordinates for a droplet in a cross sectional  $xy$ -plane in the vortex chamber are  $[x, y]^T = [r \cos \theta, r \sin \theta]^T$ .

Results of two droplet trajectories are shown in Fig. 2.7. Both results are obtained from droplets released from  $r_0 R_{vc}^{-1} = 1$  ( $\theta_0 = 0$ ). The first result is obtained for a droplet having size  $d_p = 0.5 \mu\text{m}$  (Fig. 2.7a), and the second result belongs to a  $d_p = 1.5 \mu\text{m}$  droplet (Fig. 2.7b). As can be observed from Fig. 2.6, the  $d_p = 0.5 \mu\text{m}$  droplet finally reaches the axis of the vortex chamber, while the  $d_p = 1.5 \mu\text{m}$  droplet eventually remains suspended in the gas at a non-zero equilibrium radius.

To investigate which droplet sizes are eventually able to enter the main tube for the corresponding operating conditions, the simulation was repeated for many droplet sizes. In experiments, water droplets enter the RHVT close to  $r = R_{vc}$ , through the nozzles (see Fig. 1.4). Therefore, in the simulation, the droplets are released close to the exit of the nozzles, at  $r R_{vc}^{-1} = 0.9875$ . The dimensionless equilibrium radius as a function of the droplet

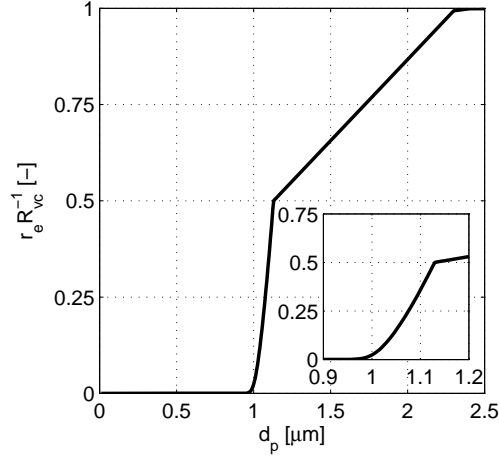


Figure 2.8: Dimensionless equilibrium radius of droplets in the vortex chamber as a function of the droplet size. A zoom into the region  $0.9 \leq d_p \leq 1.2$  is presented in the inset.

size is shown in Fig. 2.8. Apparently, droplets with sizes  $1.1 < d_p < 2.3 \mu\text{m}$  are not able to enter the main tube, but are trapped in a region between the main tube radius and the outer wall of the vortex chamber, based on the velocity distributions of the gas as shown in Fig. 2.5.

Because of the accumulation of droplets in the vortex chamber, the droplet concentration increases and droplet collisions or coalescence will be inevitable. When droplets are (or become) larger than  $d_p \approx 2.3 \mu\text{m}$ , they will eventually hit the outer wall of the vortex chamber.

From these results we may conclude that, under the stated circumstances (velocity distributions of the gas), it seems to be highly unlikely that droplets larger than  $d_p \approx 1.1 \mu\text{m}$  enter the main tube. The vortex chamber appears to act as a pre-separator that separates the larger droplets from the gas. These large droplets will eventually reach the outer or side walls of the vortex chamber where they form a liquid film that transports water into the main tube. Only the smaller droplets are able to enter the main tube. The following section, therefore, discusses how small droplets ( $d_p \leq 2 \mu\text{m}$ ) behave after they are introduced in the main tube.

## 2.5 Droplet behaviour in the main tube

### 2.5.1 Model parameters of the gas in the main tube

The computational domain that was used for the simulation of droplet behaviour in the main tube of the RHVT is shown in Fig. 2.9, where  $z$  and  $r$  are the axial and radial coordinates (2D simulation), respectively. The coordinates are made dimensionless with the diameter,  $D = 2R$ , and the radius of the main tube  $R$  ( $= 20\text{mm}$ ). The experimental RHVT of Gao (2005) had a length of  $L \approx 65D$ .

The temperature, pressure, and velocity distributions (except for the radial velocity component) of the gas in the main tube were measured by Gao (2005). The experimental data are simplified and are used as gas conditions to simulate the droplet behaviour in the main tube.

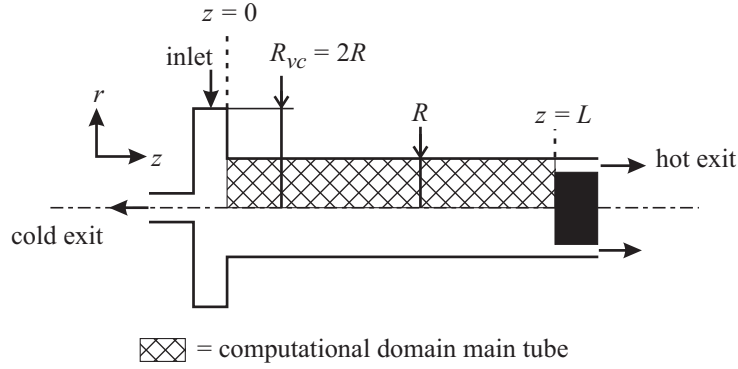


Figure 2.9: Schematic RHEVT where the hatched area is the computational domain as used in the simulation of droplet behaviour in the main tube.

The mass flow of nitrogen is 69.5 g/s and the cold fraction is  $\varepsilon = 0.28$ . The relative humidity and the temperature of the continuous phase are assumed to be time independent and are not affected by the phase change processes.

The radial velocity field can be computed based on the measured axial velocity, assuming a constant mass density and an axisymmetric flow. The continuity equation in cylindrical coordinates then reduces to

$$\frac{\partial V_r}{\partial r} = - \left( \frac{\partial V_z}{\partial z} + \frac{V_r}{r} \right). \quad (2.39)$$

The term  $\frac{\partial V_z}{\partial z}$  can be obtained from the measurements. We have first computed  $V_r(r, z)$  by applying the boundary condition  $V_r(r = 0) = 0$ . There is, however, a problem to determine  $\frac{\partial V_z}{\partial z}$  at small  $z$ , because there was no measurement data available for  $zD^{-1} < 7$ . To overcome this problem, we have extrapolated the velocity field into this region. The computed radial velocity appeared to be very small ( $\ll 1$  m/s) and is therefore, at least in the major part of the main tube, neglected. That the radial velocity is very small, was confirmed by the same analysis on measurements of the velocity field by means of laser Doppler anemometry in the region  $2 < zD^{-1} < 4.5$  (results are provided in §4.4.1).

Despite the results described above, there must be a finite radial velocity, because nitrogen gas is injected into the RHEVT. Due to the lack of experimental data close to the entrance of the main tube, we have assumed the following radial velocity distribution, which is shown in Fig. 2.10a. At  $zD^{-1} = 0$ , the radial velocity is proportional to  $r$  and is equal to that as used in the simulation of the vortex chamber (§2.4.1). Because the radial velocity is approximately zero in the measured region of the main tube ( $zD^{-1} > 2$ ), we assume that the radial velocity magnitude decreases rapidly (as a Gaussian function) with  $z$  according to

$$V_r(r, z) = V_r(R, 0) \frac{r}{R} \exp \left( -\frac{z^2}{2s^2} \right), \quad (2.40)$$

where  $V_r(R, 0) = -15.4$  m/s (see §2.4.1). The shape parameter  $s = 0.01$  m is chosen in such a way that at  $zD^{-1} \geq 1$ , there is no noticeable radial velocity.

Gao (2005) has measured the swirl velocity and the axial velocity by means of a cylindrical pitot tube (see §3.3). He has also measured the static pressure and static temperature

in the RHVT. The experimental data was approximated by functions that were implemented in the model. The swirl velocity  $V_\theta$  is shown in Fig. 2.10b for 3 axial positions. Because of viscous effects, the maximum swirl velocity decreases with  $z$ . The axial velocity  $V_z$ , shown in Fig. 2.10c, is negative in the core region due to the flow through the cold exit and is positive in the peripheral region. The static pressure increases from the axis towards the wall due to the high swirl velocity and is shown in Fig. 2.11a. The corresponding temperature distribution of the gas is shown in Fig. 2.11b (Gao, 2005).

The static pressures and temperatures are used together with the plenum humidity to determine the local humidity. The derivation of the local humidity is given in § 2.2.1. The local humidities in the RHVT are shown in Fig. 2.12 for plenum humidities  $\text{RH}_{pl} = 0.2$  and  $\text{RH}_{pl} = 1$ . The red and white lines in the figures represent  $\text{RH} = 1$  and  $\text{RH} = 3.5$  (i.e. the onset humidity), respectively. Note that the local relative humidity reaches very high values ( $\text{RH} \gg 1$ ) in both cases. Obviously, the region where condensation takes place is larger for higher plenum humidities.

## 2.5.2 Results of droplet behaviour in the main tube

Droplet properties as a function of the dimensionless axial coordinate  $zD^{-1}$  were computed for three initial droplet coordinates. As can be observed from Fig. 2.10c, the axial velocity is negative in the core region of the main tube. The initial axial coordinate of droplets was  $z_0D^{-1} = 0$ , and at this location, the axial velocity is positive for  $rR^{-1} > 0.5$ .

It appeared that only the droplets that were released from  $r_0R^{-1} > 0.65$  were actually able to enter the main tube. For smaller  $r_0$ , the droplets eventually exit the computational domain at the left side (see Fig. 2.9), because the radial fluid velocity forces them towards the region with negative axial velocity. Therefore, we have chosen only to show results for initial radial coordinates  $r_0R^{-1} = 0.75, 0.85, \text{ and } 0.95$ .

Results for the case that  $\text{RH}_{pl} = 0$  are shown in Figs. 2.13 and 2.14. The simulation is carried out for initial droplet sizes  $d_{p,0} = 0.1, 0.5, 1$  and  $2 \mu\text{m}$ . Droplet trajectories are shown in Fig. 2.13. Due to negative radial flow near the inlet, the droplets first move towards the axis of the RHVT. When the centrifugal force becomes larger than the radial drag force, the droplets move towards the wall. For small droplets ( $d_{p,0} = 0.1$  and  $0.5 \mu\text{m}$ ), the trajectories suddenly end. At these points, the droplets are evaporated completely. Fig. 2.14 shows the corresponding evolution of the droplet sizes. The droplet size decreases while droplets travel towards the hot exit. Only the  $d_{p,0} = 2 \mu\text{m}$  droplets (Fig. 2.14d) survive the evaporation process and are able to reach the tube wall. The other droplets evaporate in a very short time, which is shorter than 5 ms.

Instead of decreasing in size due to evaporation, the droplets can grow due to condensation if the local gas is supersaturated. For the next results, the plenum humidity is  $\text{RH}_{pl} = 0.5$ . The local relative humidity, however, varies as a function of the local temperature and pressure. The droplet trajectories and the corresponding local humidities are shown in Fig. 2.15. Isolines of constant local humidity are shown as the thin grey lines, where the numbers denote its value. In a certain region of the RHVT, the gas mixture is supersaturated. In this region, the water vapour condenses onto the droplets, which therefore grow. This can be observed from the droplet sizes as shown in Fig. 2.16. Because of the larger centrifugal force, the droplets move faster towards the wall. The thick grey line is the isoline of  $\text{RH} = 1$ . When droplets cross this line, they start to evaporate. Because of this, the two smallest droplets eventually evaporate while the larger droplets hit the wall with a larger diameter than initially.



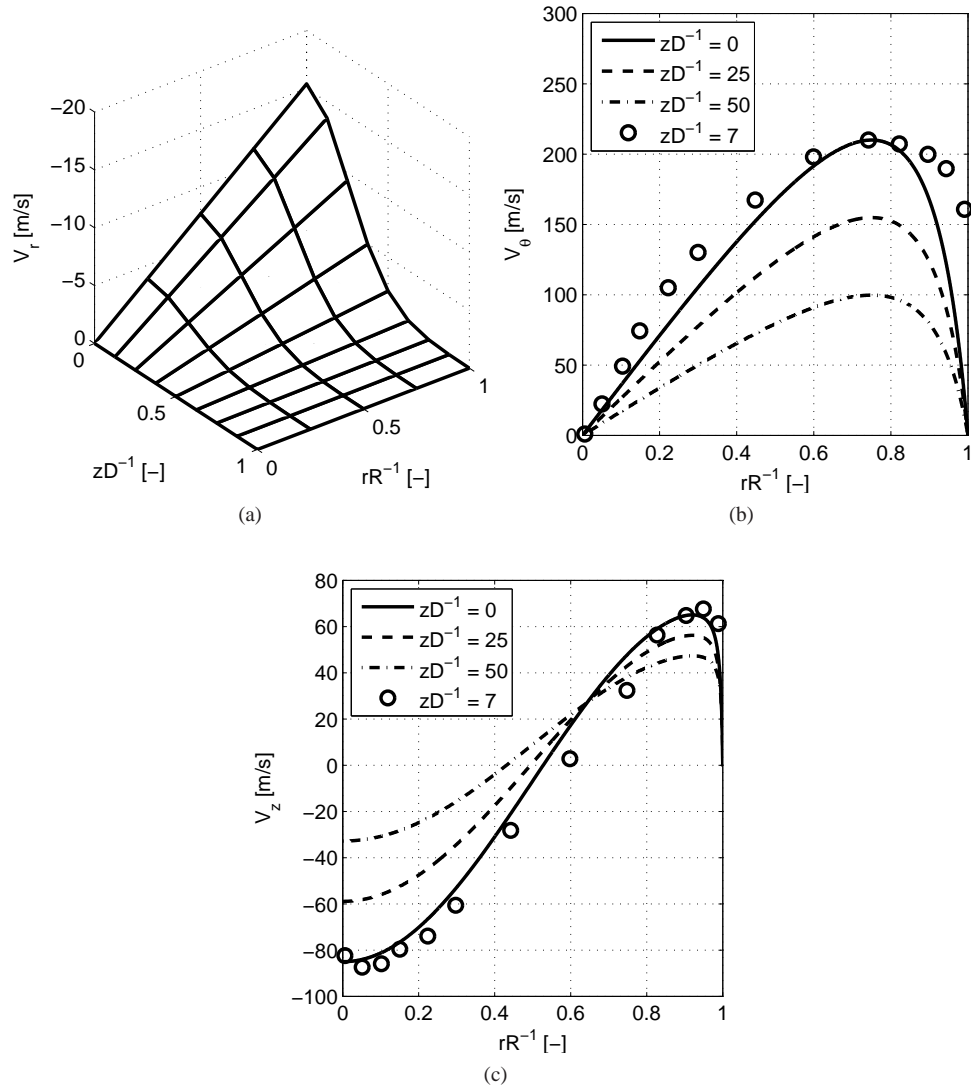


Figure 2.10: Velocity distributions in the main tube. (a) Radial velocity component; (b) swirl velocity component; (c) axial velocity component. The symbols are experimental values measured by Gao (2005). The radial velocity component is plotted as function of the dimensionless axial and radial coordinates, the swirl and axial velocity components are plotted as functions of the dimensionless radial coordinate.

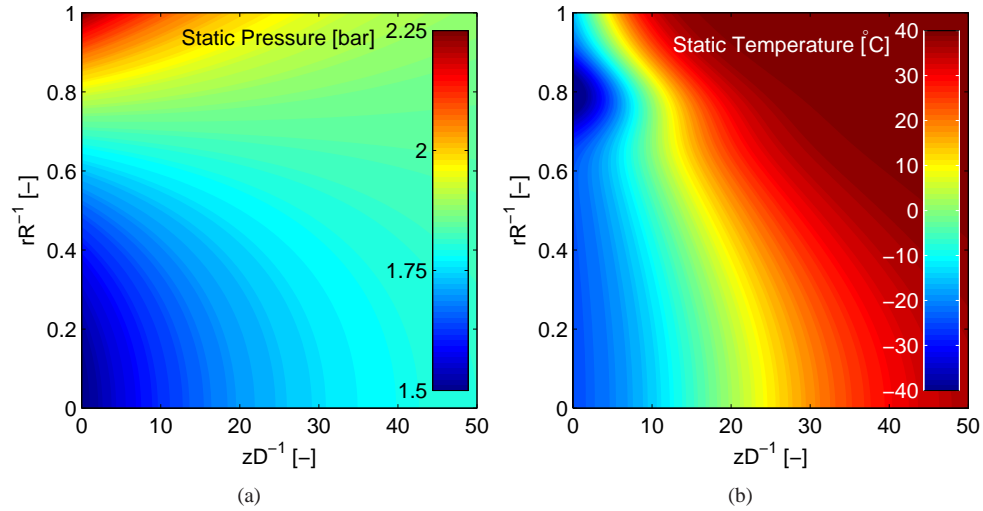


Figure 2.11: Static pressure distribution (a) and static temperature distribution (b) in the main tube as functions of the dimensionless radial and axial coordinates.

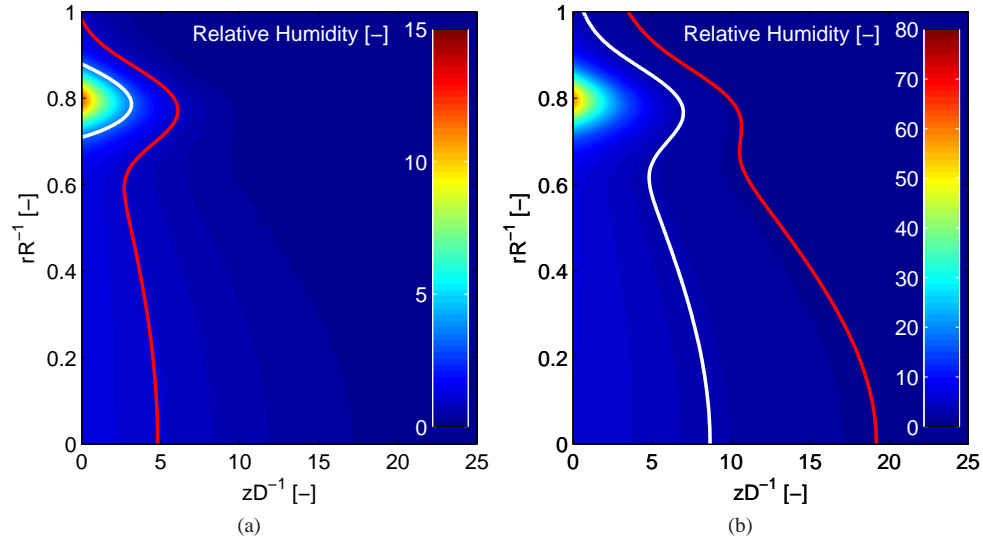


Figure 2.12: Local relative humidity in the main tube as a function of the dimensionless radial and axial coordinates. (a)  $RH_{pl} = 0.2$ ; (b)  $RH_{pl} = 1$ . The white lines in the plots represent the condition  $RH = 3.5$ , i.e., the homogeneous nucleation threshold, and the red lines represent the condition  $RH = 1$ , i.e., gas mixture is saturated. Note that the relative humidity is plotted for  $0 \leq zD^{-1} \leq 25$ . For larger  $zD^{-1}$ , the contours are insignificant.

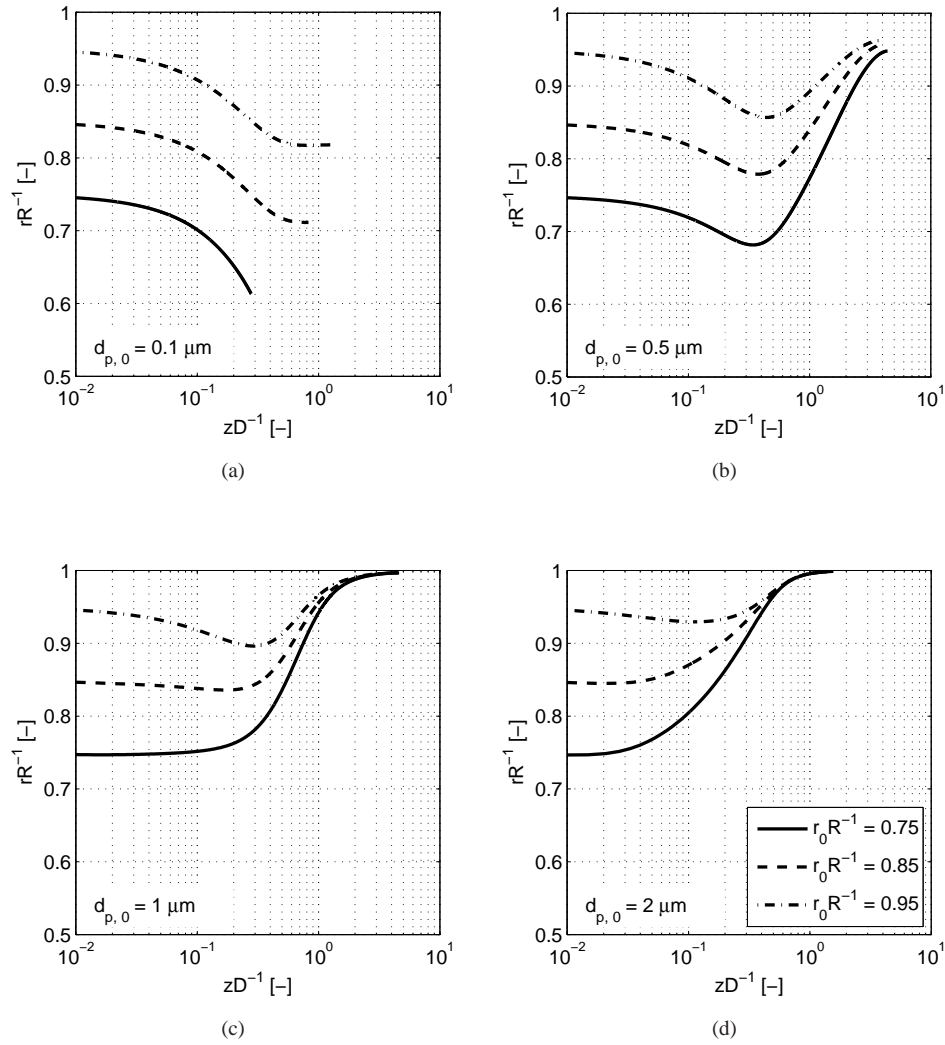


Figure 2.13: Droplet trajectories for  $RH_{pl} = 0$  (droplets move from left to right). (a)  $d_{p,0} = 0.1 \mu\text{m}$ ; (b)  $d_{p,0} = 0.5 \mu\text{m}$ ; (c)  $d_{p,0} = 1 \mu\text{m}$ ; (d)  $d_{p,0} = 2 \mu\text{m}$ . All are plotted as functions of the dimensionless axial and radial coordinate. Different lines belong to droplets that were released from different radial positions. For legend see Fig. (d).

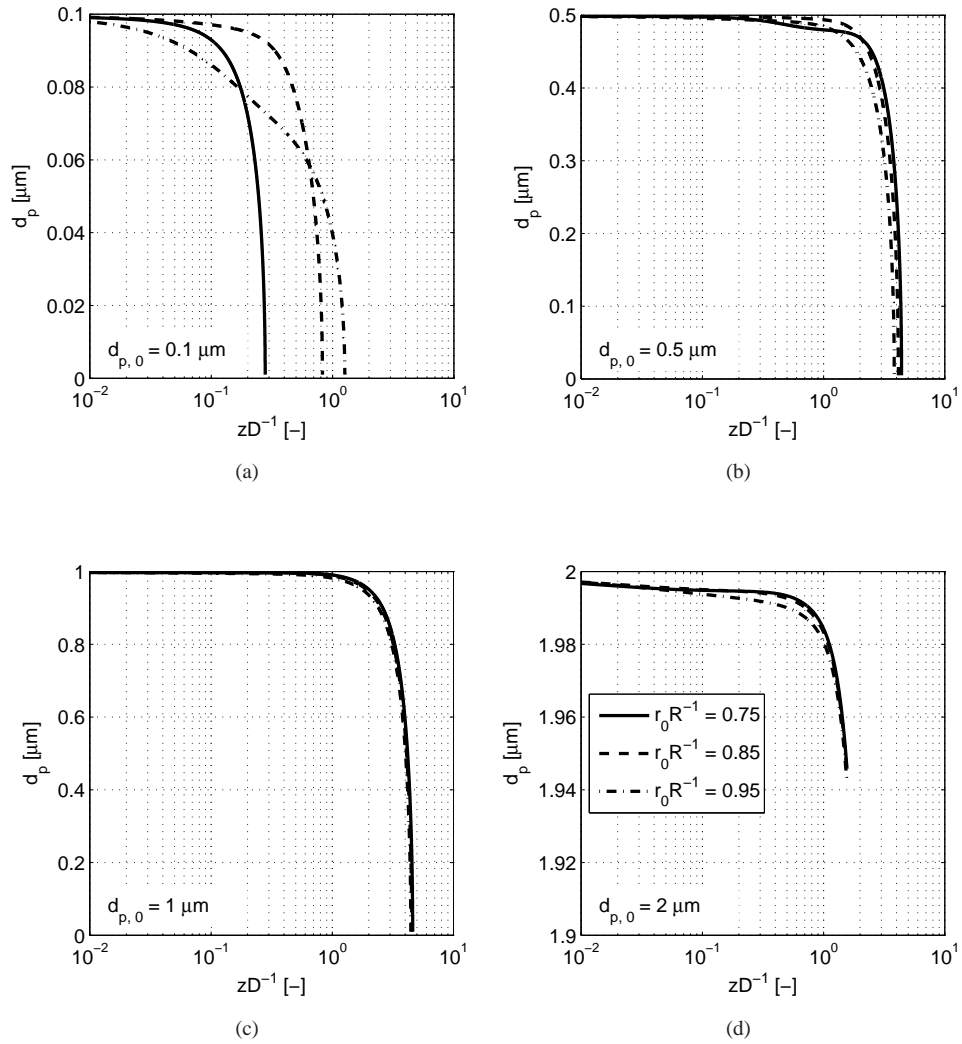


Figure 2.14: Droplet sizes for  $RH_{pl} = 0$ . (a)  $d_{p,0} = 0.1 \mu\text{m}$ ; (b)  $d_{p,0} = 0.5 \mu\text{m}$ ; (c)  $d_{p,0} = 1 \mu\text{m}$ ; (d)  $d_{p,0} = 2 \mu\text{m}$ . All are plotted as functions of the dimensionless axial coordinate. For legend see Fig. (d).

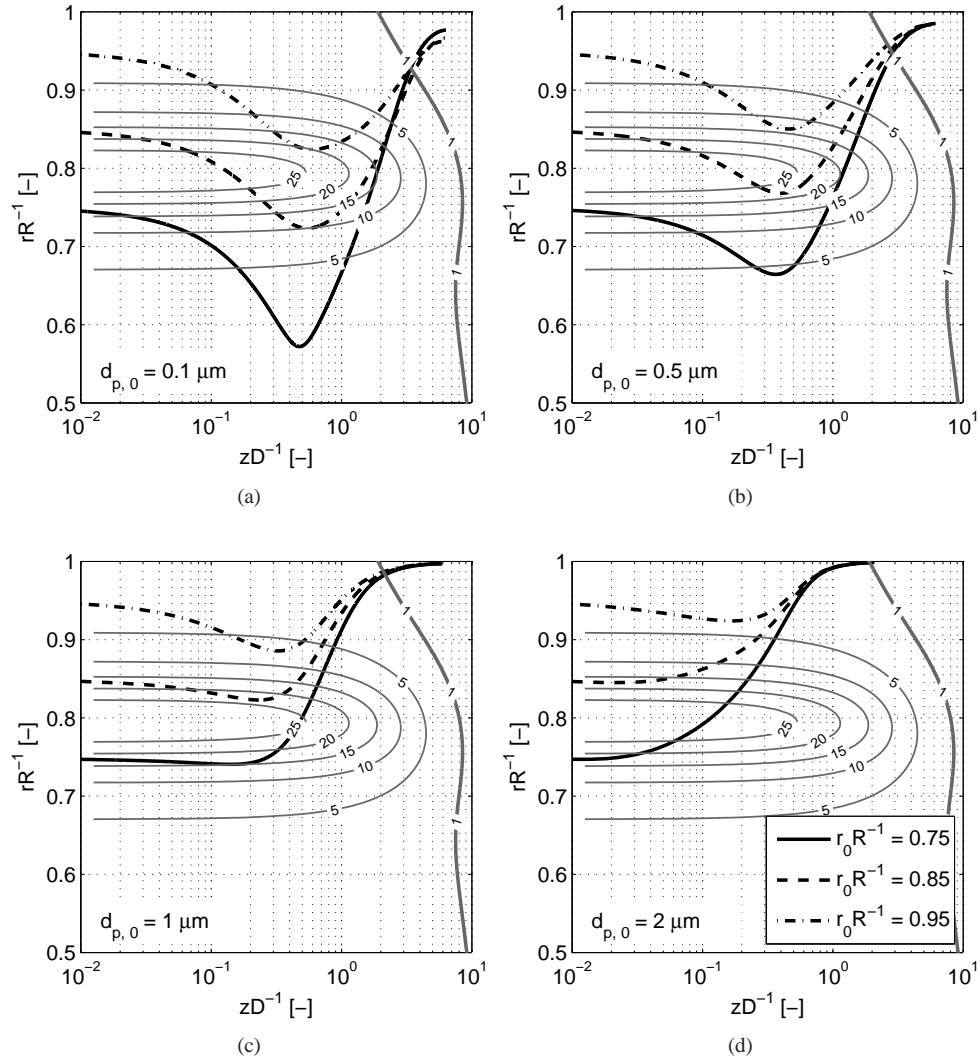


Figure 2.15: Droplet trajectories (black) and isolines of the local relative humidity (thin grey lines) for  $RH_{pl} = 0.5$  (droplets move from left to right). (a)  $d_{p,0} = 0.1 \mu\text{m}$ ; (b)  $d_{p,0} = 0.5 \mu\text{m}$ ; (c)  $d_{p,0} = 1 \mu\text{m}$ ; (d)  $d_{p,0} = 2 \mu\text{m}$ . All are plotted as functions of the dimensionless axial and radial coordinate. The thick grey line is the isoline of  $RH = 1$ . Different black lines belong to droplets that were released from different radial positions. For legend see Fig. (d).

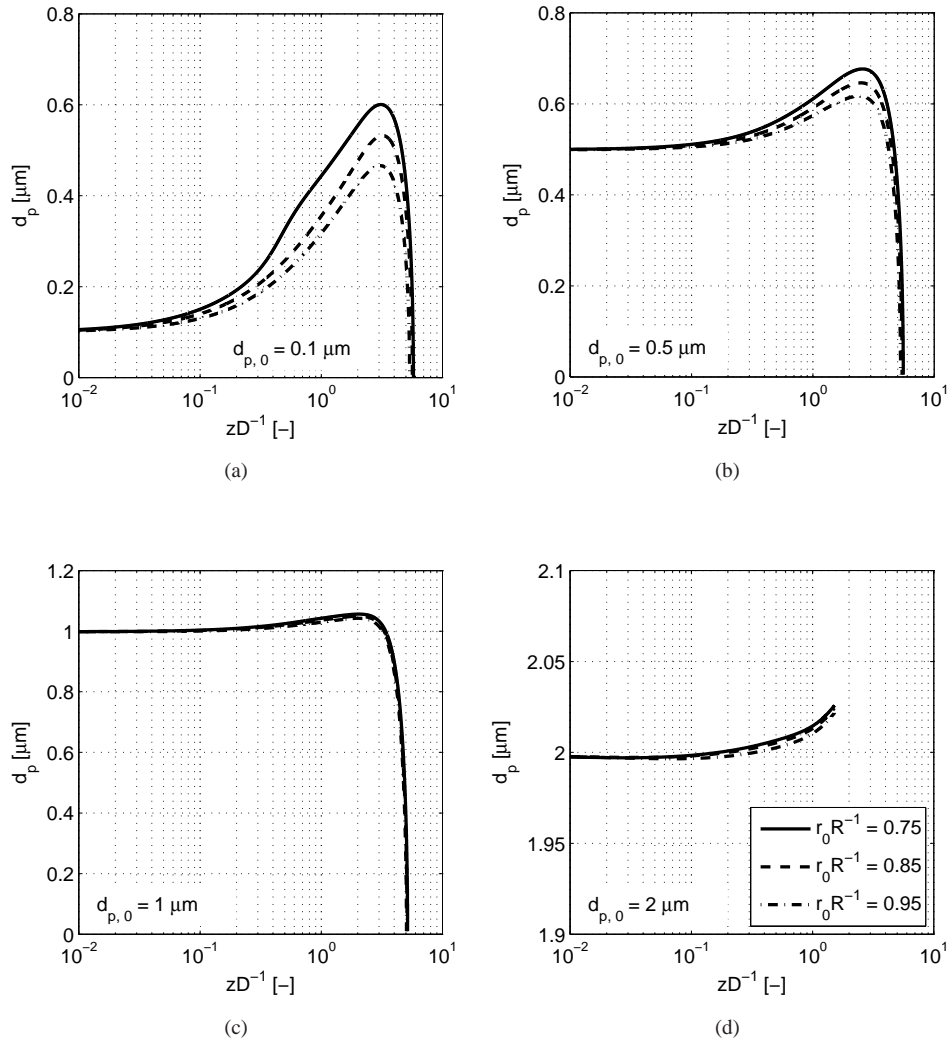


Figure 2.16: Droplet sizes for  $RH_{pl} = 0.5$ . (a)  $d_{p,0} = 0.1 \mu\text{m}$ ; (b)  $d_{p,0} = 0.5 \mu\text{m}$ ; (c)  $d_{p,0} = 1 \mu\text{m}$ ; (d)  $d_{p,0} = 2 \mu\text{m}$ . All are plotted as functions of the dimensionless axial coordinate. For legend see Fig. (d).

To study the effect of the plenum humidity and the initial droplet size on the droplet behaviour in more detail, we compare droplet trajectories and sizes of several cases. The initial radial coordinates of the droplets is taken to be  $r_0 R^{-1} = 0.75$ . Figs. 2.17a and 2.17b show droplet trajectories for droplets with  $d_{p,0} = 0.5$  and  $2 \mu\text{m}$ , respectively. For each droplet size, the plenum humidities are  $\text{RH}_{pl} = 0, 0.5$ , and  $1$ .

When condensation takes place, droplets grow and the centrifugal force becomes relatively larger compared to the drag force. Therefore, the trajectories of the droplets shift towards the wall with increasing plenum humidity. This is, however, more evident for the small droplets compared to the larger droplets. The reason for this is that the relative increase in diameter (see Figs. 2.17c and 2.17d) due to condensation of a small droplet is much larger than that of larger droplets. Hence, the mass of a small droplet and the related centrifugal force increase relatively faster compared to those of a large droplet, what results in larger differences between trajectories at different humidities. Phase change processes are, therefore, less important for the trajectories of large droplets. Large droplets are able to reach the RHVT wall, no matter the plenum humidity.

### 2.5.3 Steady state liquid concentration in the main tube

In order to compute local concentrations of liquid water in the main tube, which is due to the presence of droplets, the simulation is repeated with a size distribution of droplets. The droplets are released from  $zD^{-1} = 0$ , between  $rR^{-1} = 0$  and  $rR^{-1} = 1$ , having intervals of  $\Delta r R^{-1} = 0.005$ . As shown in §2.4.2, it is highly unlikely that droplets larger than  $1 \mu\text{m}$  enter the main tube. Therefore, the distribution is chosen to have a mean initial droplet diameter of  $\langle d_{p,0} \rangle = 0.5 \mu\text{m}$  and a standard deviation of  $\sigma_{d_p} = 0.2 \mu\text{m}$ .

The computational domain is axisymmetric and is divided into cells of size  $\Delta z_i \times \Delta r_j$ , having a volume  $\mathcal{V}_{i,j} = 2\pi r_{cell} \Delta z_i \Delta r_j$ , a radial coordinate  $r_{cell}$ , and an index  $(i, j)$ . If the mass density of the liquid water is constant, the steady state liquid concentration  $C_{i,j}$  is determined as

$$C_{i,j} = \frac{1}{\mathcal{V}_{i,j}} \sum_{n=1}^{N_p} (d_p^3 \varpi)_n, \quad (2.41)$$

where  $n$  is the droplet index and  $N_p$  is the total number of droplets found in cell  $(i, j)$ . For each droplet that is released in the domain, a weighting factor  $\varpi$  is assigned that depends on the droplet size, its position, and its velocity.

The probability to have a droplet with a size  $d_p$ , which is  $\varpi_{d_p}$ , is given by a normal distribution having the mean droplet size  $\langle d_{p,0} \rangle$  and the standard deviation  $\sigma_{d_p}$  according to

$$\varpi_{d_p} = \frac{1}{\sigma_{d_p} \sqrt{2\pi}} \exp \left[ -\frac{(d_p - \langle d_{p,0} \rangle)^2}{2\sigma_{d_p}^2} \right]. \quad (2.42)$$

The sizes  $\Delta z_i$  and  $\Delta r_j$  are constant in the analysis. Therefore, cells located at larger radii have a larger volume. Without correction, the liquid concentration would be lower for cells located at larger radii. The droplet volume is therefore weighted with  $r_0/R$ . Additionally, there is another weighting factor that relates the velocity of the gas at the droplet release position,  $|\mathbf{v}(\mathbf{x}_0)|$ , to the velocity of a droplet while it moves through the domain,  $|\mathbf{u}(\mathbf{x})|$ , reading  $|\mathbf{v}(\mathbf{x}_0)|/|\mathbf{u}(\mathbf{x})|$ . Combination of the above weights gives an overall weighting factor

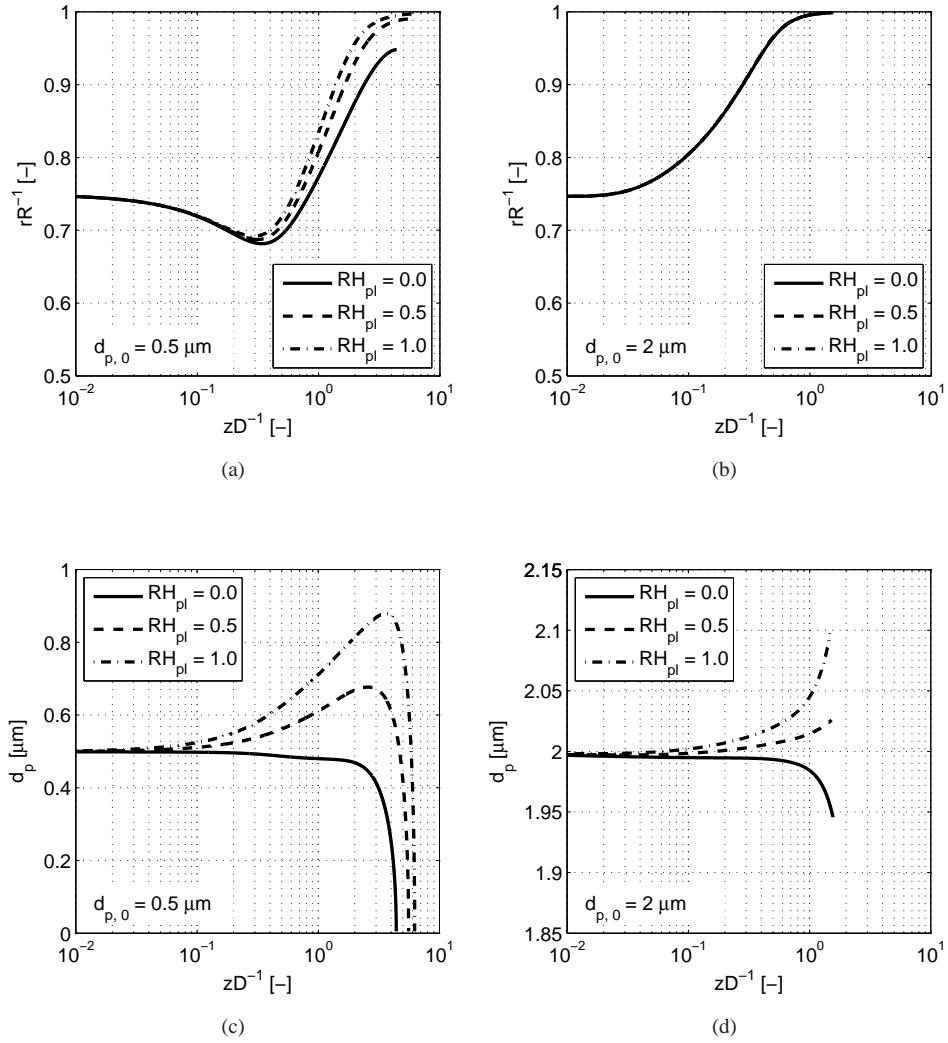


Figure 2.17: (a, b) Droplet trajectories (droplets move from left to right) for plenum humidities  $RH_{pl} = 0, 0.5,$  and  $1$  as functions of the dimensionless axial and radial coordinates. (c, d) Droplet diameters as functions of the dimensionless axial coordinate. (a, c)  $d_{p,0} = 0.5 \mu\text{m}$ ; (b, d)  $d_{p,0} = 2 \mu\text{m}$ . All droplets were released from  $r_0 R^{-1} = 0.75$ . For legend see Fig. (d).



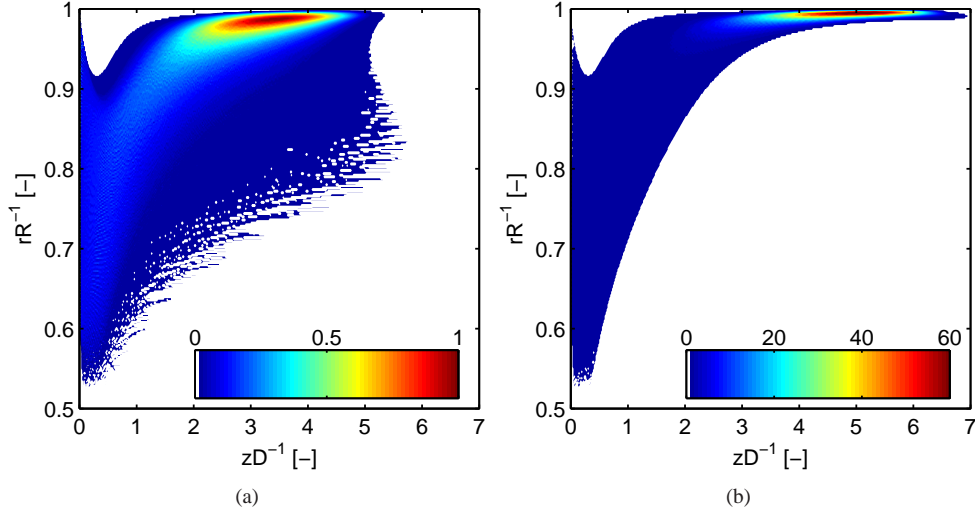


Figure 2.18: Steady state liquid concentration for water droplets in the main tube. The results are scaled with the maximum liquid concentration for  $\text{RH}_{pl} = 0$ . (a)  $\text{RH}_{pl} = 0$ ; (b)  $\text{RH}_{pl} = 0.5$ . Note that the scaling of the y-axis starts at  $rR^{-1} = 0.5$ .

that is unique for each individual droplet:

$$\varpi = \varpi_{d_p} \frac{r_0}{R} \frac{|\mathbf{v}(\mathbf{x}_0)|}{|\mathbf{u}(\mathbf{x})|} \quad (2.43)$$

When a droplet reaches the wall ( $r \geq R$ ) it is removed from the computational domain. Therefore, the liquid concentration at the wall is not computed.

Liquid concentrations of two plenum humidities,  $\text{RH}_{pl} = 0$  and  $\text{RH}_{pl} = 0.5$ , have been computed and are shown in Fig. 2.18 as functions of the radial and axial coordinates. The results are scaled with the maximum liquid concentration for  $\text{RH}_{pl} = 0$ . White regions in the graphs indicate a liquid concentration of less than 1% of the maximum value.

The figures show that the maximum liquid concentration increases with increasing plenum humidity. The reason for this is that a higher humidity results in larger droplets and, consequently, a larger centrifugal force. Thus, droplets move faster towards the wall, resulting in a higher liquid concentration. Because of this, the domain in which droplets are present is smaller and located closer to the wall than for cases with lower plenum humidities. Both the results shown here demonstrate that the maximum axial distance droplets travel before they evaporate or hit the wall is less than  $7D$ .

This study reveals that PDPA measurements can only take place in a region that is close to the entrance of the RHVT. Humidifying the gas has the disadvantage that PDPA measurements in the core region of the RHVT are more difficult, because there is less seeding available. On the other hand, it has the advantage that droplets are larger and, therefore, better detectable.

## 2.6 Conclusions

A model has been developed and solved numerically to simulate the droplet behaviour in the vortex chamber and the main tube of the RHVT. The model allows to calculate the droplet velocity  $\mathbf{u}(t)$ , its position  $\mathbf{x}(t)$ , and size  $d_p(t)$  if the velocity, pressure, and temperature fields are known from measurements. The model neglects droplet break up, droplet coalescence, and the flow is considered to be steady and laminar.

We have separated the RHVT into two computational domains. The first domain covers the vortex chamber, the second domain covers the main tube. Phase changes due to condensation and evaporation are not considered in the simulation of the droplets in the vortex chamber, because the temperature of the gas is unknown here. Furthermore, the flow in the vortex chamber is assumed to be two dimensional, having a radial and swirl velocity component (the axial velocity component is unknown). The pressure, temperature, and axial and swirl velocities of the gas in the main tube are known from measurements. The radial velocity is taken to be proportional to  $r$  and decreases as a Gaussian function of  $z$ . This means that only the droplet velocities, trajectories, and sizes are modeled.

Results from the simulation in the vortex chamber show that droplets smaller than  $d_p < 1.1 \mu\text{m}$  are able to enter the main tube when they are injected through the swirl generator of the RHVT. Larger droplets, having sizes between  $1.1 \leq d_p \leq 2.3 \mu\text{m}$ , are trapped in the vortex chamber. It is expected that these droplets collide with each other, forming larger droplets that are swirled towards the outer walls of the vortex chamber. For droplets larger than  $d_p > 2.3 \mu\text{m}$ , the radial drag force (which is directed towards the axis) is always smaller than the centrifugal force. These droplets will be swirled towards the outer walls of the vortex chamber, immediately after they are injected into the vortex chamber. In this way, the vortex chamber acts as a pre-separator that separates the largest droplets from the carrier gas.

The droplet trajectories in the main tube show that droplets first move towards the tube axis, after which the centrifugal force becomes larger than the radial drag force, and droplets move towards the tube wall. Due to evaporation or condensation, droplets change in size. This has a significant effect on the trajectories of small droplets. Trajectories of larger droplets, however, are less affected by the plenum humidity.

The plenum humidity has influence on the droplet size and the liquid concentration. A higher plenum humidity leads to larger droplets. If the droplets are meant to be used as seeding particles for PDPA measurements, it is convenient (in terms of signal quality) if droplets are larger and have longer lifetimes. Furthermore, a higher humidity results in larger and heavier droplets, which can more easily be separated from the carrier medium.

A drawback of a higher humidity is that the domain in which droplets are expected to be found, is smaller than in the case of lower humidities. This is undesirable for the PDPA measurements. In that case, there is less seeding available in the core region of the RHVT, making PDPA measurements more difficult. Another drawback is that larger droplets have a velocity that is less representative for the gas velocity (will be discussed in more detail in §4.1), making it more difficult to estimate the velocity of the gas by using PDPA results.

From this study we conclude that it is very important to be able to control the humidity of the carrier gas, because it appears to have an important influence on the trajectories, sizes, and concentration of droplets.

The computed liquid concentrations show that we may expect droplets only in a small region of the main tube. According to the model, no droplets are found for  $zD^{-1} > 7$ . This means that the length of the domain, in which we can perform PDPA measurements, is

---

approximately 280 mm based on  $R = 20$  mm. The PDPA equipment must be able to detect droplets that have sizes in the order of  $1\ \mu\text{m}$  and at the same time velocities in the order of  $\mathcal{O}(10^2)$  m/s.

In the next chapter, we will provide a detailed overview of the equipment that was used during the experiments.



## 3 | Experimental methods and equipment

In this chapter, we provide an overview of the measurement methods and the equipment used in the experimental study. Because of the complexity of the devices, we will focus on their most important working principles and features. The heart of the experimental setup is the Ranque-Hilsch vortex tube. We will first provide a detailed description of the experimental RHVT and its main components. In §3.2, the working principles of LDA and PDPA are explained and the main components of the system and their properties are listed. As discussed in chapter. 2, the droplet sizes are affected by the humidity of the carrier gas. In §3.4, we discuss the gas conditioning system that was used to humidify the nitrogen. Details of the process scheme and the equipment involved are provided in §3.5.

### 3.1 The experimental Ranque-Hilsch Vortex Tube

The RHVT that was used in the experiments is shown in Fig. 3.1. The main components are indicated in the figure. Pressurized plenum gas enters the RHVT via two inlets, which are attached to an outer ring. The gas expands and accelerates through nozzles in a swirl generator after which it flows into the vortex chamber. Here, a fast rotating vortex is formed. While rotating, the gas enters the main tube. Gas is allowed to exit via an orifice in the vortex chamber or at the other side of the main tube, where it passes through a conical plug. The first exit has a smaller diameter, and the leaving gas has a lower temperature than that of the gas in the plenum. Hence, this exit is referred to as the cold exit. Gas that flows through the other exit has a higher temperature. This exit is referred to as the hot exit. A (conical) plug, which allows gas at the periphery of the main tube to leave at the hot exit, is placed concentric with the main tube. In commercial vortex tubes, this plug is also used to regulate the ratio of hot and cold mass flows. In our study, however, external valves were used to control the mass flows. A detailed cross section including the main dimensions of the experimental RHVT are shown in Fig. 3.2. The diameter of the main tube was  $2R = 40$  mm and had a length up to  $L = 2.50$  m. The diameter of the cold exit was fixed to be  $2R_c = 15.75$  mm.

#### 3.1.1 The design of the swirl generator

The swirl generator is a very important component in the RHVT and induces rotation and acceleration of the gas. The swirl generator contains converging slot nozzles (rectangular shape) through which the gas is accelerated. Among other parameters, such as the plenum

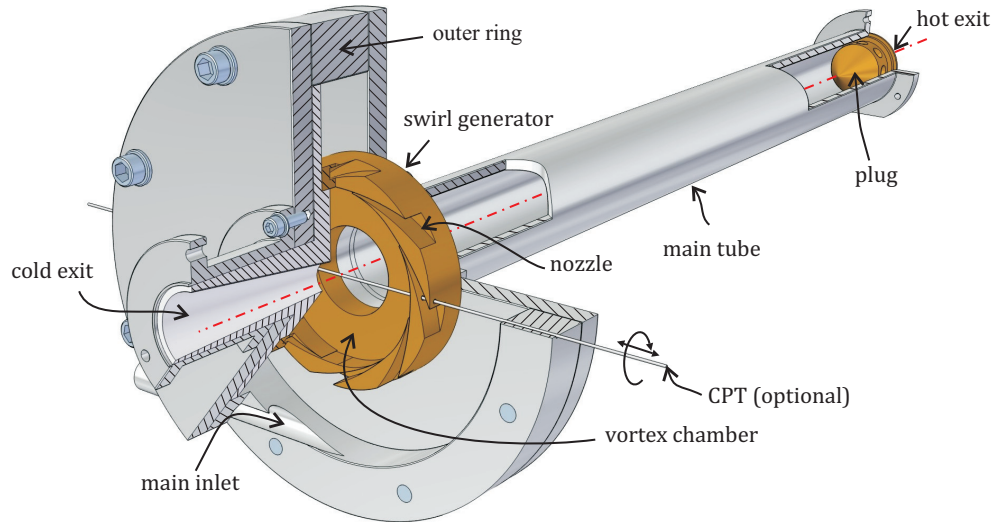


Figure 3.1: The Ranque-Hilsch Vortex Tube that was used in the experiments.

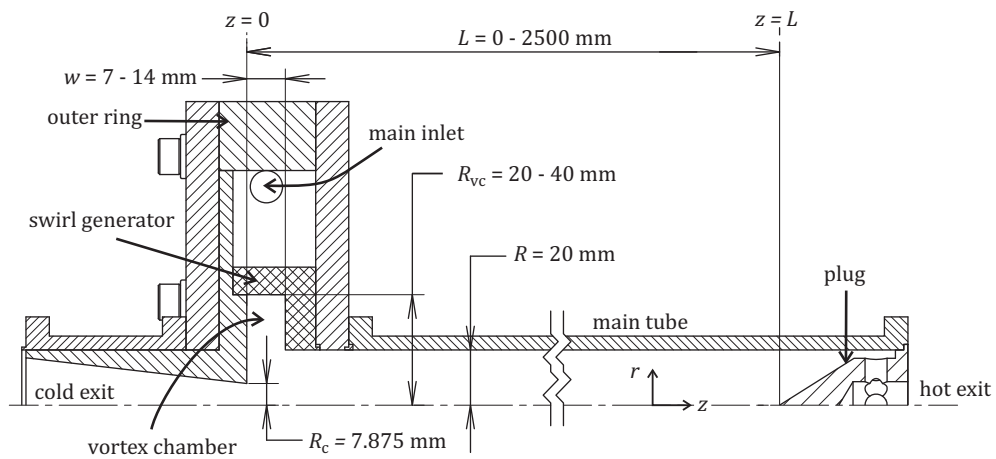


Figure 3.2: Section of the Ranque-Hilsch Vortex Tube and its main dimensions.

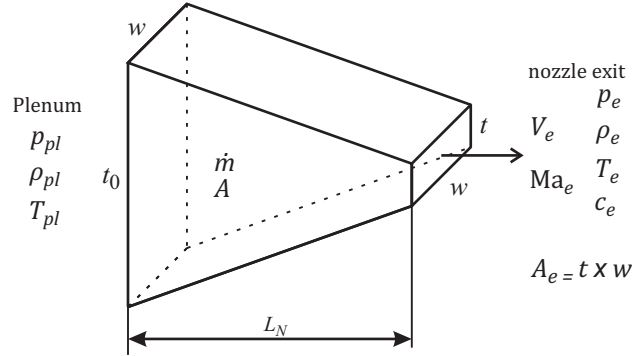


Figure 3.3: Illustration of a converging nozzle through which pressurized gas is expanded.

pressure and mass flow, the cross sectional area of the exit of a nozzle determines the initial swirl velocity of the gas that is injected into the vortex chamber.

To optimize the nozzle geometry for the characteristics of the nitrogen supply system in our laboratory, we have computed the mass flow and velocity in a nozzle as functions of its minimum cross sectional area by using the one-dimensional isentropic gas equations (Kundu & Cohen, 2008, pp. 724-729). Assuming that there are no friction losses and heat transfer from the gas to the surroundings, the flow is isentropic. Furthermore, the flow is considered to be one-dimensional, and the mass flow is constant through the nozzle (continuity). Fig. 3.3 shows a cross section of a converging nozzle through which pressurized gas is expanded. We are mainly interested in the velocity at which the gas exits the nozzle as a function of the plenum properties (subscript  $pl$ ), the mass flow  $\dot{m}$  and the cross sectional area  $A$  of the nozzle.

### 3.1.1.1 Compressible flow through a nozzle

In compressible gas dynamics, the Mach number is an important dimensionless velocity and is defined as

$$Ma \equiv \frac{V}{c}, \quad (3.1)$$

where  $V$  is the velocity and  $c$  is the speed of sound. The local velocity in the nozzle  $V$  is found by applying conservation of mass

$$V = \frac{\dot{m}}{\rho A}. \quad (3.2)$$

The speed of sound for an ideal gas is  $c \equiv \left. \frac{\partial p}{\partial \rho} \right|_s$  is

$$c = \sqrt{\gamma \overline{\mathcal{R}} T}, \quad (3.3)$$

where  $\overline{\mathcal{R}} = \frac{\mathcal{R}}{M}$  is the specific gas constant.

During deceleration of the gas, which is adiabatic because there are no heat interactions, the total enthalpy of the gas is conserved, and the corresponding energy balance is

$$h_{pl} = h + \frac{V^2}{2}. \quad (3.4)$$

With the enthalpy defined as  $h \equiv c_p T$ , where  $c_p$  can be written as  $c_p = \gamma \bar{\mathcal{R}} / (\gamma - 1)$ , we rewrite Eq. (3.4) to become

$$T_{pl} = T \left( 1 + \frac{\gamma - 1}{2} \text{Ma}^2 \right), \quad (3.5)$$

where  $\gamma \equiv c_p / c_v$  is the adiabatic exponent, which is the ratio of the specific heat capacities at constant pressure  $c_p$  and constant volume  $c_v$ .

Using the isentropic gas relation  $T \propto p^{\gamma / (\gamma - 1)}$ , the local pressure  $p$  is

$$p = p_{pl} \left( 1 + \frac{\gamma - 1}{2} \text{Ma}^2 \right)^{\frac{\gamma}{1 - \gamma}} \quad (3.6)$$

According to the ideal (perfect) gas law  $p = \rho \bar{\mathcal{R}} T$ , the mass density is

$$\rho = \frac{p_{pl}}{\bar{\mathcal{R}} T_{pl}} \left( 1 + \frac{\gamma - 1}{2} \text{Ma}^2 \right)^{\frac{1}{1 - \gamma}}, \quad (3.7)$$

and the velocity becomes

$$V = \frac{\dot{m} \bar{\mathcal{R}} T_{pl}}{p_{pl} A} \left( 1 + \frac{\gamma - 1}{2} \text{Ma}^2 \right)^{\frac{1}{\gamma - 1}}. \quad (3.8)$$

The local speed of sound in the nozzle is, by using Eq. (3.5),

$$c = \sqrt{\gamma \bar{\mathcal{R}} T} = \sqrt{\gamma \bar{\mathcal{R}} T_{pl}} \left( 1 + \frac{\gamma - 1}{2} \text{Ma}^2 \right)^{-1/2}, \quad (3.9)$$

and the mass flux  $\Psi$  as a function of the plenum gas properties and the local Mach number becomes

$$\Psi \equiv \frac{\dot{m}}{A} = p_{pl} \text{Ma} \sqrt{\frac{\gamma}{\bar{\mathcal{R}} T_{pl}}} \left( 1 + \frac{\gamma - 1}{2} \text{Ma}^2 \right)^{\frac{1 + \gamma}{2(1 - \gamma)}}. \quad (3.10)$$

For a known mass flow and cross sectional area of the exit of a nozzle  $A_e$ , the Mach number in the exit of the nozzle,  $\text{Ma}_e$ , is given by

$$\text{Ma}_e \left( 1 + \frac{\gamma - 1}{2} \text{Ma}_e^2 \right)^{\frac{1 + \gamma}{2(1 - \gamma)}} = \frac{\dot{m}}{p_{pl} A_e} \sqrt{\frac{\bar{\mathcal{R}} T_{pl}}{\gamma}}. \quad (3.11)$$

$\Psi$  is plotted as a function of the Mach number for  $p_{pl} = 5$  bar and  $T_{pl} = 293$  K in Fig. 3.4, from which we see that the mass flux has a maximum at  $\text{Ma} = 1$ . For a constant  $p_{pl}$ ,  $T_{pl}$ , and  $\dot{m}$ , the condition  $\text{Ma} = 1$  can only be reached at the location where  $\Psi$  has its maximum value. According to Eq. (3.10) this can be achieved at the location in the nozzle, where the cross sectional area has its minimum.

In our experiments, we have used converging nozzles. In that case, the exit of the nozzle has the smallest cross sectional area. This means that the maximum velocity is found in the exit of the nozzle and is equal to  $\text{Ma}_e$ . Further decreasing the pressure in the nozzle exit does not increase the mass flow or velocity: the flow is choked.

With the converging nozzle, it is impossible to reach  $\text{Ma} > 1$ . Higher Mach numbers can, however, be reached in a convergent-divergent nozzle (a Laval nozzle). In such a nozzle,  $\text{Ma} = 1$  is found in the throat, i.e., the location where the cross sectional area is the smallest, and supersonic velocities ( $\text{Ma} > 1$ ) can be reached in the diverging section of the nozzle.



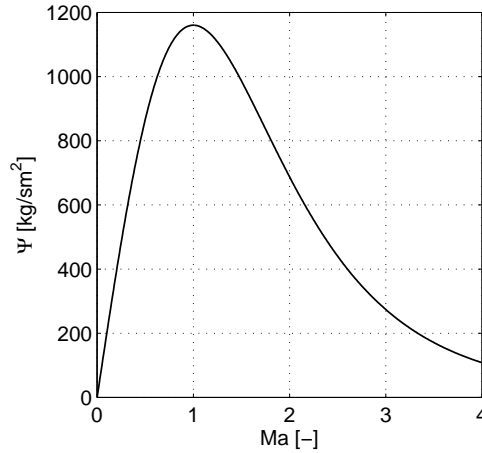


Figure 3.4: Mass flux as a function of the Mach number. Mach numbers larger than  $Ma > 1$  can only be reached in convergent-divergent nozzles. For the nozzle in the swirl generator (which is only converging) the maximum Mach number that can be reached is  $Ma = 1$ .

### 3.1.1.2 Application to the swirl generator

Nitrogen gas that was used during the experiments was provided by a nitrogen supply system, consisting of a liquid nitrogen tank, evaporators, and a pressure controller (details of the system are provided in §3.5.1). The system had a maximum capacity of approximately 87 g/h. However, because of friction losses in supply tubes and connections, the mass flow is related to the pressure via a system characteristic. We have measured the mass flow as a function of the plenum pressure at the place where the RHVT is located by replacing the RHVT with a mass flow meter and a pressure sensor. In that way, all the pressure losses in the tubing and valves upstream of the RHVT were included.

Fig. 3.5 shows the mass flow as a function of the plenum pressure. The experimental values are shown as the symbols, and dashed lines are drawn to guide the eye. In between  $1 \leq p_{pl} \leq 4$  bar,  $\dot{m}$  increases with  $p_{pl}$ , here the plenum pressure was controlled with the pressure controller and the mass flow resulted from the pressure drop over the system. At some point (at approximately  $p_{pl} = 4$  bar), the valve of the pressure controller was fully opened. At the corresponding pressure, the maximum mass flow that the nitrogen system was able to deliver was reached. Higher pressures ( $p_{pl} > 4$ ) were reached by decreasing the mass flow by means of gradually closing a valve that is located downstream of the pressure sensor.

According to the above, there is a specific relation between  $\dot{m}$  and  $p_{pl}$  of the nitrogen supply system. Together with the cross sectional area of the nozzle exit and the plenum temperature, they determine the Mach number in the nozzle exit. Two types of swirl generators were used during the experiments. Both swirl generators are shown in Fig. 3.6. The swirl generators consist of two segments, which fit into each other, thereby forming the openings through which the nitrogen is expanded (the nozzles). The width  $w$ , thickness  $t$ , and number  $N$  of slots, as well as the inner radius of the vortex chamber  $R_{vc}$ , were different to be able to study the (energy) separation process. The geometrical details of the swirl generators are listed in Table 3.1.

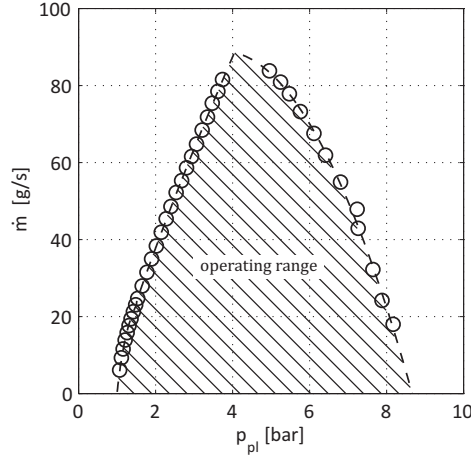


Figure 3.5: The maximum mass flow as a function of the plenum pressure ( $T_{pl} = 288$  K). Symbols are experimental values and the dashed line is added to guide the eye. The hatched area indicates the operating range of the supply system.

Type	$R_{vc}$	$L_N$ [mm]	$N$ [-]	$t_0$ [mm]	$t$ [mm]	$w$ [mm]	$A_{e,tot}$ [mm <sup>2</sup> ]
1	40	25	8	4	1	14	112
2	20	40	12	11	0.7	7	58.8

Table 3.1: Details of the swirl generators that were used in the experimental study. The nozzle dimensions  $L_N$ ,  $t_0$ ,  $t$ , and  $w$  are indicated in Fig. 3.3.

The first swirl generator (type 1), also used by Gao (2005), contained  $N = 8$  nozzles with dimensions  $t \times w = 1 \times 14$  mm. The diameter of the vortex chamber was  $2R_{vc} = 80$  mm. For example, to have a nitrogen mass flow of  $\dot{m} = 70$  g/s,  $p_{pl}$  should be at least  $p_{pl} = 3.25$  bar (Fig. 3.5). The corresponding Mach number in the exit of the nozzle is, according to Eq. (3.11),  $Ma_e = 0.57$ . The pressure in the nozzle exit is, according to Eq. (3.6),  $p_e = 2.61$  bar. In practice however,  $Ma_e$  and  $\dot{m}$  are lower than computed. This is because the previous analysis does not take account of friction in the nozzle and the rotation of the gas in the vortex chamber. The latter effect is much more pronounced, and it will be explained in chapter 5 that because of the high swirl velocity, there is a strong positive radial pressure gradient. The pressure in the exits of the nozzles  $p_e$  is therefore higher than without rotation of the gas. This higher back pressure has a similar effect on the mass flow as closing a valve: it reduces the mass flow. The only way to increase the mass flow, is to increase  $p_{pl}$ . For the type 1 nozzle, the plenum pressure should be  $p_{pl} = 4.65$  bar, rather than  $p_{pl} = 3.25$  bar, to have  $\dot{m} = 0.070$  kg/s (experimentally determined). The corresponding Mach number is in that case  $Ma_e = 0.36$ .

The second swirl generator (type 2) was fabricated in order to be able to reach  $Ma_e = 1$ , i.e. sonic conditions in the exits of the nozzles, at a mass flow of  $\dot{m} = 70$  g/s and a plenum pressure that is within the operating range of the nitrogen supply system. Using the radial momentum balance and the velocity distribution in the vortex chamber (to be discussed in §5.3), we have computed the required plenum pressure and surface area of the nozzles. We

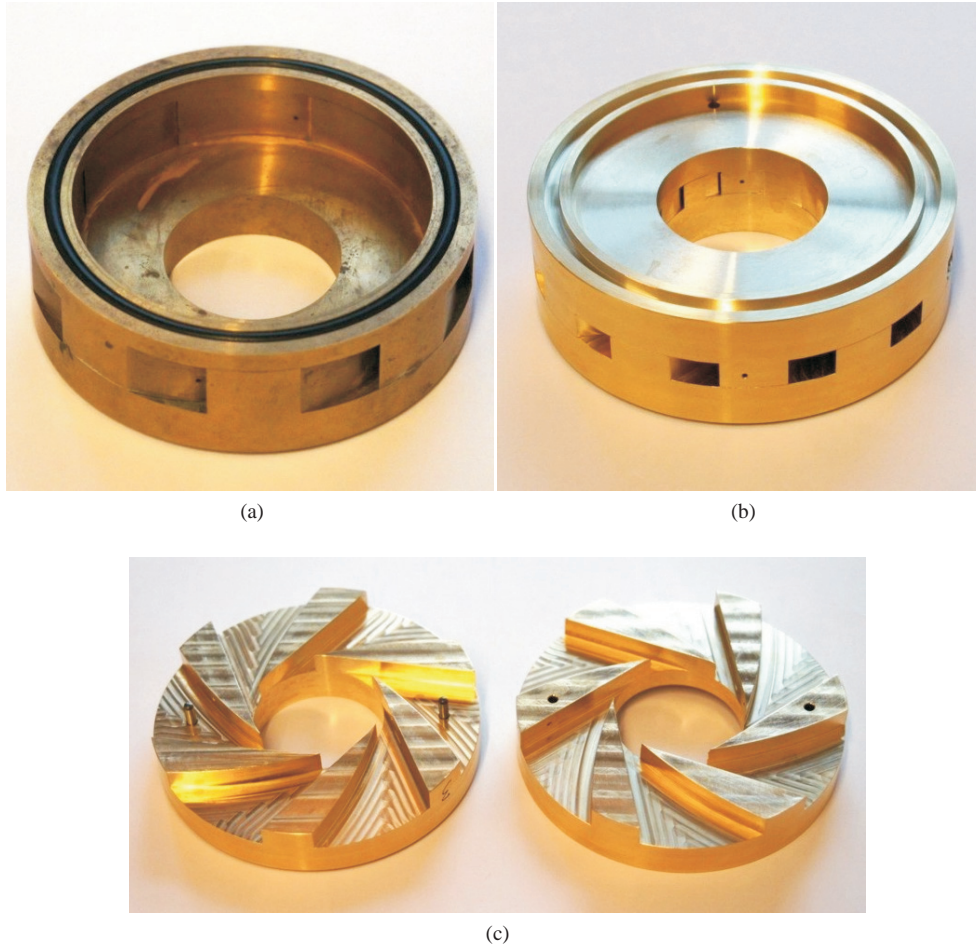


Figure 3.6: (a) Swirl generator type 1:  $R_{vc} = 40$ ,  $N \times t \times w = 8 \times 1 \text{ mm} \times 14 \text{ mm}$ ; (b) swirl generator type 2:  $R_{vc} = 20$ ,  $N \times t \times w = 12 \times 0.7 \text{ mm} \times 7 \text{ mm}$ ; (c) two segments that form the type 2 swirl generator. The nozzle dimensions  $t$  and  $w$  are indicated in Fig. 3.3.

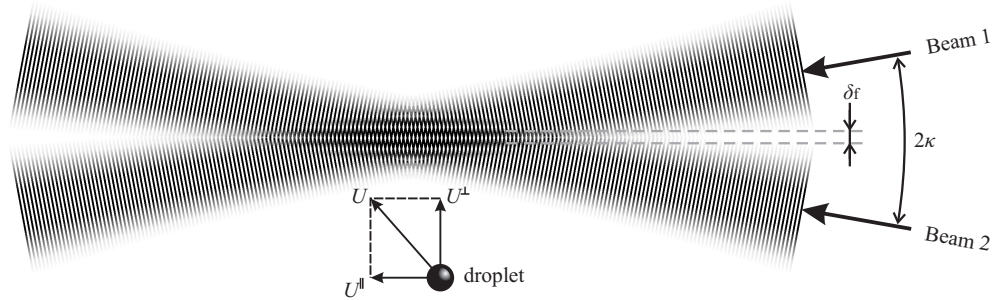


Figure 3.7: Illustration of an interference pattern created by two crossing laser beams.  $U$  is the droplet velocity, which is decomposed into a perpendicular velocity  $U^\perp$ , and a parallel velocity  $U^\parallel$ , with respect to the fringes.  $2\kappa$  is the crossing angle between the two beams, and  $\delta_f$  is the fringe spacing.

have based the computation on a swirl generator with  $2R_{vc} = 40$  mm. Because of the smaller diameter of the vortex chamber, the pressure near the nozzle exit due to the rotation of the gas is lower compared to the previous swirl generator, allowing higher Mach numbers to be reached. This second swirl generator contained  $N = 12$  nozzles with dimensions  $t \times w = 0.7 \times 7$  mm. The computed required plenum pressure to have  $Ma_e = 1$  is in this case  $p_{pl} = 5.13$  bar, which is in the operating range of the nitrogen supply system (see Fig. 3.5).

## 3.2 Phase Doppler Particle Analysis

Droplet velocities and sizes were measured by means of Phase Doppler Particle Analysis, PDPA (Bachalo & Houser, 1984). PDPA uses the same principle as Laser Doppler Anemometry (LDA) to measure velocities of particles. Additionally to the velocity of a particle, PDPA provides the particle size. First, we will explain the basic principle of LDA and will then continue with PDPA.

### 3.2.1 LDA

Laser Doppler anemometry (Albrecht, 2003) is an optical, non intrusive measurement method that makes use of two (or more) laser beams that intersect each other, having a crossing angle  $2\kappa$ . In the crossing volume of the laser beams, there are alternate ‘bright’ and ‘dark’ bands, resulting from constructive and destructive interference, respectively. These bands are called fringes, and a schematic representation of such an interference pattern is illustrated in Fig. 3.7. Each beam is shown as a set of parallel lines, which represent light waves. In the volume where the waves of both beams overlap, there are fringes present that have a mutual spacing  $\delta_f$ , also referred to as the fringe spacing. In the beam crossing volume, the frequency of scattered light from particles, which is a measure for the particle velocity, is in a measurable range. Hence, this volume is called the measurement volume, MV.

When a water droplet with a velocity  $U$  enters the MV, it scatters light in all directions, but, with an intensity that depends on its location in the MV. Therefore, when the absolute droplet velocity perpendicular to the fringes  $|U^\perp| > 0$ , the droplet scatters light from which

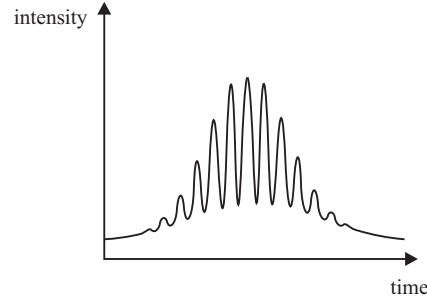


Figure 3.8: Intensity of scattered light in time, i.e., the Doppler Burst.

its intensity fluctuates in time. Because of the Gaussian intensity distribution of the laser beams, the intensity of the fringes is strongest in the center of the measurement volume. The intensity of scattered light in time is the Doppler burst, shown in Fig. 3.8.

The scattered light is captured by a light sensitive sensor (a Photomultiplier Tube, or PMT) that converts the optical signal to an electrical signal. The frequency of this signal is the Doppler frequency  $f_D$  and is related to the absolute velocity perpendicular to the fringes and fringe spacing according to

$$f_D = \frac{|U^\perp|}{\delta_f}. \quad (3.12)$$

The fringe spacing is related to the half beam crossing angle  $\kappa$  and the wavelength of the laser light  $\lambda$  according to

$$\delta_f = \frac{\lambda}{2 \sin \kappa}. \quad (3.13)$$

Eqs. (3.12) and (3.13) show that, for a fixed wavelength and beam crossing angle, the Doppler frequency depends on the droplet velocity perpendicular to the fringes. One pair of laser beams is, consequently, used to determine one velocity component.

According to Eq. (3.12), only the magnitude of the perpendicular velocity component is known. Its sign, however, is generally not known. Also, if the droplet has only a parallel velocity component ( $U = U^\parallel$ ) or zero velocity  $U = 0$ , there will be no useful signal at all. This problem is solved by introducing a frequency shift in one of the laser beams. The frequency of one beam is shifted by an acousto-optic modulator, i.e., a Bragg cell, operating at a frequency of 40 MHz. Because of the frequency shift, the fringes move at this frequency in the measurement volume. When a droplet crosses the MV, its scattered signal has a frequency either above or below 40 MHz, depending on the direction of motion. If the PMT receives a signal with a frequency less than 40 MHz, the velocity is negative. Oppositely, when the frequency is higher, the velocity is positive. In the case that there is only parallel flow or zero velocity, the measured frequency is exactly 40 MHz, that is  $U_\perp = 0$ . The Doppler frequency is the frequency shift subtracted from the measured frequency  $f_m$ , and the velocity perpendicular to the MV becomes

$$U_\perp = \frac{f_D}{\delta_f} = \frac{f_m - 40 \text{ MHz}}{\delta_f}. \quad (3.14)$$

Each velocity component requires one pair of laser beams. In the case of 3D measurements, three beam pairs and three PMTs are therefore required. To distinguish between the

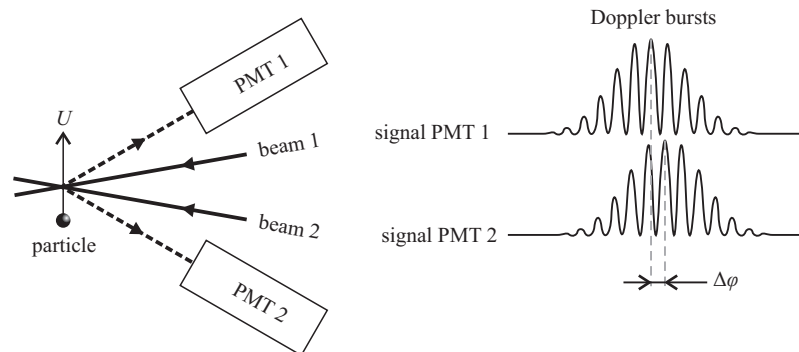


Figure 3.9: Principle of Phase Doppler Particle Analysis. There is a phase difference  $\Delta\phi$  between signals from the PMTs that depends on the droplet size and the location of the PMTs.

three velocity components, each beam pair has its unique laser wavelength (colour). Narrow band filters are placed in front of the PMTs and are used to distinguish between the optical signals with different colours.

### 3.2.2 PDPA

Phase Doppler Particle Analysis is an extension of LDA that additionally provides the size of spherical droplets (Bachalo & Houser, 1984). When a droplet crosses the MV, it scatters light in all directions. As in LDA, the frequency of the scattered light is used to determine the velocity of the droplet. The main difference between PDPA and LDA is that instead of one PMT for a velocity component, multiple light sensitive sensors are used that capture the optical signal from different angles. Because of the positioning of the PMTs with respect to the MV and the scattering properties of droplets, there exists a phase shift  $\Delta\phi$  between the recorded signals (Fig. 3.9). This phase shift is approximately linearly related to the droplet size and can, therefore, in combination with the droplet velocity, be used to determine the droplet size.

The smallest droplet size that can be measured with PDPA depends on the amount of light captured and the wavelength of the laser. Measuring small droplets requires a high laser power and large light collecting optics. Especially when small droplets have high velocities, the combination of low intensity signals and high frequencies makes accurate measurements more difficult.

### 3.2.3 Hardware

The PDPA setup (TSI, 2013) that was used for the droplet size and velocity measurements consisted of the following main components:

#### Laser

A Spectra-Physics Stabilite 2017 Argon-Ion laser (single line, output 7 W) was used as the light source for the PDPA measurements. The laser light was split by a prism into three laser

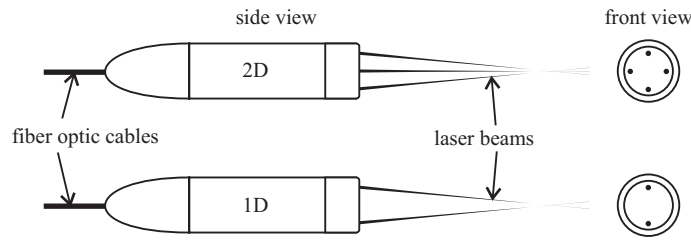


Figure 3.10: 2D transceiver probe (top) and 1D transceiver probe (bottom).

beams having wavelengths 514.5 nm (green), 488 nm (light blue), and 476.5 nm (dark blue). Each single wavelength beam was split into two laser beams from which one was phase-shifted by the Bragg cell. The unshifted and shifted beams were transmitted via optical fibers to transceiver probes. The green laser beam has the highest power. Therefore, this wavelength is generally used for droplet size measurements.

### Transceiver Probes

Both the shifted and unshifted laser beams were transmitted through optical fibers to transceiver probes. These probes focussed the beams in such a way that they crossed each other and form the measurement volume. The transceiver probes are not only used to transmit the laser beams, but are also used as light collecting optics that receive scattered light back from droplets. The received scattered light is transmitted via optical fibers to the PMTs.

Two types of transceiver probes were used in the study. A 2D probe (TSI TR260) transmitted the green and light blue laser beams (Figs. 3.10 and 3.11a) and was used to measure velocity components  $U_1$  and  $U_2$ . A 1D probe (TSI TR160) transmitted the dark blue beams and was used to measure  $U_3$ . The focal distance of the front lenses that were used was 250 mm (the focal length was 261.3 mm). This resulted in a half beam crossing angle of  $\kappa = 5.49^\circ$ , and an MV of approximately  $62 \times 650 \mu\text{m}$  (diameter  $\times$  length).

Pictures of the probes and their transmitted laser beams are shown in Fig. 3.11a, where the laser beams are made visible with a fog of small water droplets. A close up of all the six crossing laser beams (three beam pairs) is shown in Fig. 3.11b. A pin-hole having a diameter of  $50 \mu\text{m}$  was used to align the laser beams to ensure that they cross each other in the same point in space.

### PDPA Receiver Probe

The sizes of droplets were measured with a 3D PDPA receiver probe (TSI RV3070). This probe contains a mask that has several slits, allowing scattered light to pass under different angles with respect to the measurement volume. Each slit has its own optical fiber, connected to a PMT. In this way, there is a phase difference between the optical signals received by the PMTs. Together with the known position of the slits and the measured velocity, the droplet diameter can be computed. The probe can also be used as a receiver probe for 3D velocimetry.

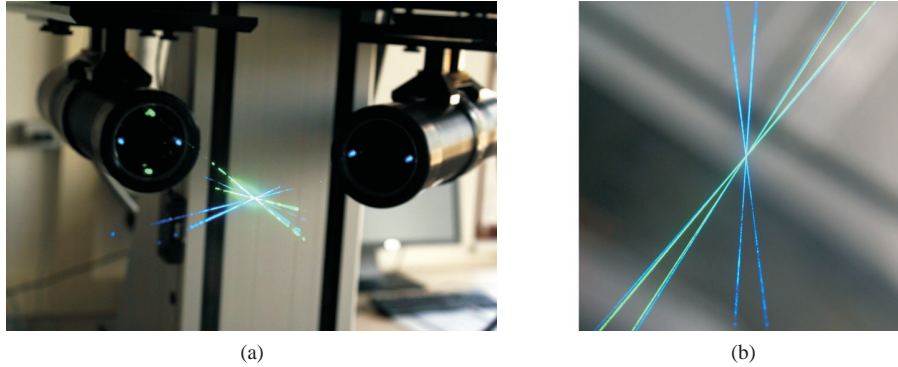


Figure 3.11: (a) Transceiver probes. The left probe measures two velocity components, the right probe measures the third; (b) close up of the overlapping laser beams. The laser beams are visualized by a fog of small water droplets.

### Traverse system

The PDPA probes were mounted onto an xyz-translation stage (the traverse system), which is shown in Fig. 3.12. The traverse system has three axes that are controlled by a computer. Its positioning accuracy is  $10\ \mu\text{m}$  and the travel range is  $600 \times 600 \times 600\ \text{mm}$ .

### Burst Analyzer

The signals from the PMTs were analyzed by the TSI FSA4000 multibit digital burst correlator. The maximum Doppler frequency that can be analyzed by this burst correlator is 175 MHz, having a sampling rate of 800 MHz (for  $\kappa = 5.49^\circ$  and  $\lambda = 514.5\ \text{nm}$ , the maximum measurable velocity is 470 m/s). All data were collected by TSI FlowSizer<sup>TM</sup> software. The uncertainty in the measured droplet sizes was determined by TSI to be 3% for droplets of size  $d_p < 10\ \mu\text{m}$  and 0.5% for larger droplets.

## 3.2.4 Optical configuration

Light that is scattered by the droplets is captured by the transceiver and receiver probes. There are two main modes of capturing the scattered light. The first is the backward scattering mode, in which the transceiver collects the reflected light from the droplets, which is originally transmitted from the same transceiver. The second mode involves forward scattering, where refracted light from droplets is collected by a second receiver probe that is located at the opposite side of the MV. Another mode is side scattering, but, because of the low intensity of the scattered light, this mode is usually not applied. An example of the intensity of scattered light from a spherical droplet is shown in Fig. 3.13, where the intensity is shown as a function of the angle with respect to the incident light beam. Note that the intensity is plotted in logarithmic scale.

The forward and backward scattering modes have their advantages and disadvantages. The advantage of the backward scattering mode is that the measurement volume created by



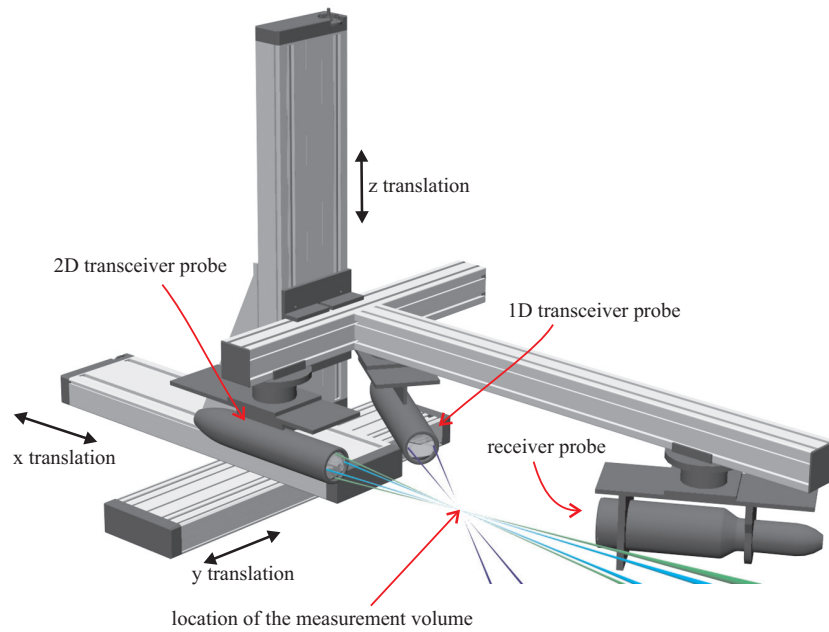


Figure 3.12: 3D Traverse system with the mounted PDPA probes.

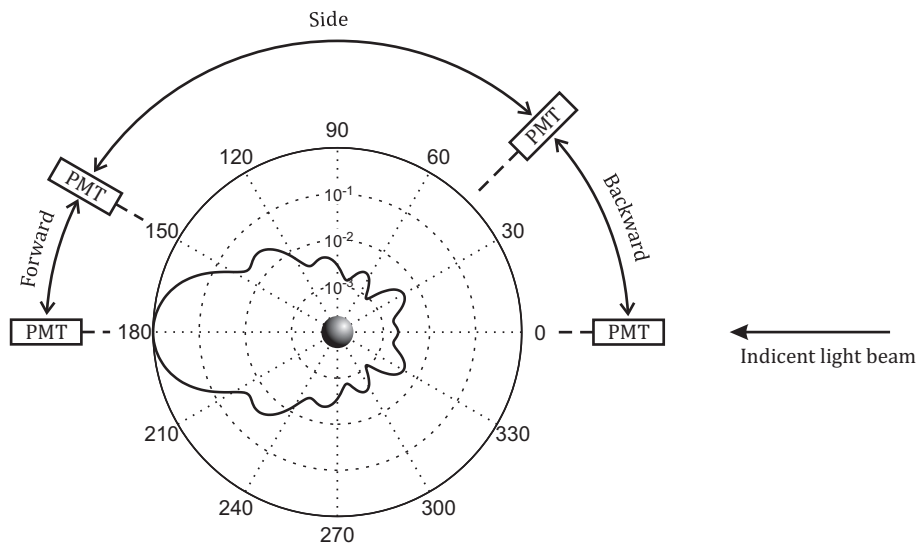


Figure 3.13: Intensity of the scattered light from a spherical droplet as a function of the scattering angle. Several possible locations of the PMTs are shown, indicating forward-, side-, and backward scattering mode.

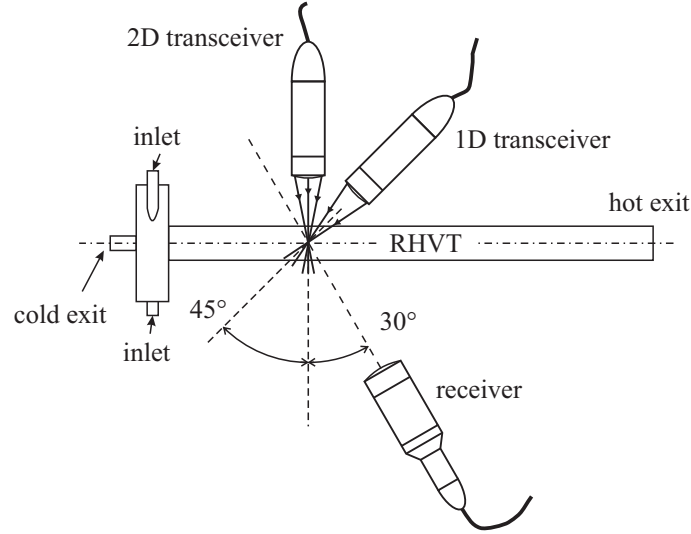


Figure 3.14: Optical layout of the PDPA probes with respect to the RHVT.

the laser beams is located exactly in the focal point of the lens of the probe. Therefore, there is no additional alignment required, even when the beams are refracted through a window. Forward scattering has the advantage that the intensity of the refracted light is orders of magnitude higher than for backward scattering (Fig. 3.13). Because of this, the obtained signals contain less noise and are of better quality. However, forward scattering requires the measurement volumes of both probes to be precisely aligned.

Deuss (2012) found that the optimum scattering mode is the backscattering mode for the 1D probe (dark blue) and forward scattering, by using the PDPA probe, for the green and light blue scattering signals. The corresponding optical configuration of the probes with respect to the RHVT is shown in Fig. 3.14. Using this configuration, the velocities measured by the probes are transformed to the velocities in cylindrical coordinates with respect to the RHVT according to

$$\begin{bmatrix} U_r \\ U_\theta \\ U_z \end{bmatrix} = \begin{bmatrix} 0 & 1 & \sqrt{2} \\ 1 & 0 & 0 \\ 0 & 1 & 0 \end{bmatrix} \cdot \begin{bmatrix} U_1 \text{ (green)} \\ U_2 \text{ (light blue)} \\ U_3 \text{ (dark blue)} \end{bmatrix} \quad (3.15)$$

### 3.2.5 Transparent measurement sections

All optical measurements were performed through transparent sections (windows) of the main tube. The sections were partially fabricated from brass supports and transparent plastic (Polymethyl-Methacrylate or PMMA) and provided an optically accessible domain. A picture of one of the sections is shown in Fig. 3.15.

To be able to have an indication of the shear stresses in the fluid and to determine instantaneous droplet velocities and their sizes, it is required that the velocity components are obtained from a single droplet. This can only be achieved if there is an overlap of the three measurement volumes. Due to astigmatism induced by the refraction of the laser beams

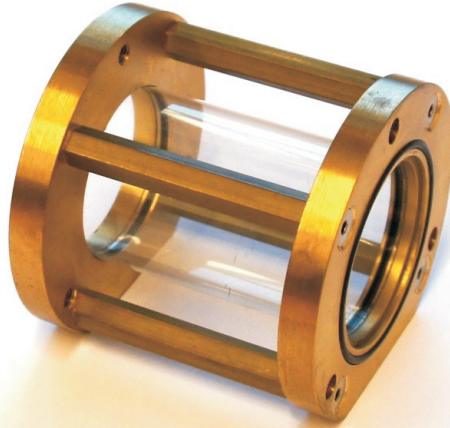


Figure 3.15: A transparent segment of the main tube that was used for the PDPA measurements.

through the cylindrical windows, the overlap of the measurement volumes of the three velocity components varies with the radial position inside the RHVT (Zhang & Eisele, 1996). At the same time, the MV does not exactly follow the displacement of the transmitting probes, because of the cylindrical shape of the windows, and the beam crossing angle varies with the radial coordinate.

When a light beam crosses an interface between two materials with different refractive indices, the refracted angle  $\theta_r$  differs from that of the incident angle  $\theta_i$ , schematically represented in Fig. 3.16. The refracted and incident angles are defined as the absolute angles between the surface normal and the light beam. The relation between the incident and re-

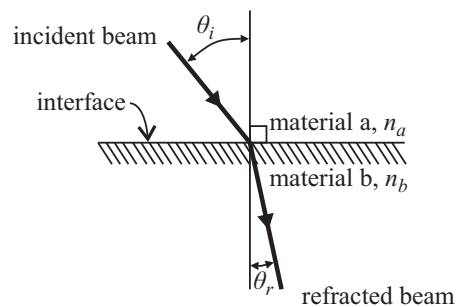


Figure 3.16: Refraction of a laser beam through an interface.  $\theta_i$  is the incident angle,  $\theta_r$  is the angle of the refracted beam, and  $n_a$  and  $n_b$  are the refractive indices of material  $a$  and  $b$ , respectively.

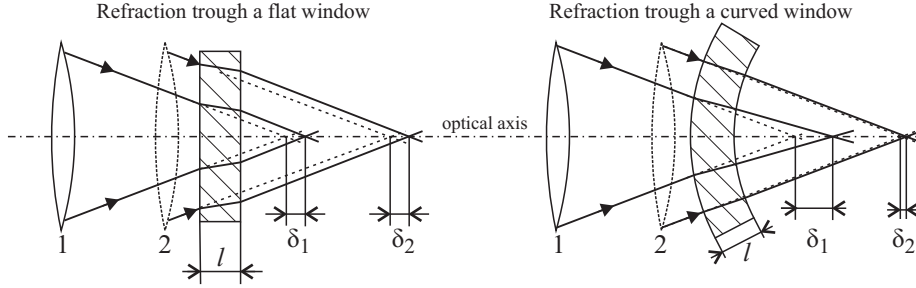


Figure 3.17: Refraction of laser beams through a flat (left) or curved (right) window. Non-refracted laser beams are indicated with dashed lines.

refracted angles is given by Snell's law

$$n_a \sin \theta_i = n_b \sin \theta_r, \quad (3.16)$$

where  $n_a$  and  $n_b$  are the refractive indices of materials  $a$  and  $b$ , respectively.

Figure 3.17 shows how laser beams are refracted through a flat and a curved window. There are two lens positions shown with respect to the window (indicated with 1 and 2). Because of the refraction, there is a difference  $\delta$  between the actual location of MV and the location it would have if there is no window present (the non-refracted case). For a flat window, having a refractive index  $n_b$ , which is placed in a medium with refractive index  $n_a$ ,  $\delta$  is related to the incident and refracted angles and the window thickness  $l$  according to

$$\delta_{flat} = \frac{l \sin(\theta_i - \theta_r)}{\sin \theta_i \cos \theta_r}, \quad (3.17)$$

where  $\theta_r$  is found using Eq. (3.16). As long as  $\theta_i$  is constant,  $\delta_{flat}$  is constant, which means that the relative distance of the LDA probe with respect to the window does not affect  $\delta_{flat}$ .

For a curved window, however, the analysis is more complex. To estimate how large  $\delta$  is for a curved window and how it depends on  $l$  and the position of the LDA probe, we have performed a ray tracing analysis in Matlab. During the analysis, the variation in  $\kappa$  (which is the half of the beam crossing angle, see §3.2.1 and Fig. 3.7) was also computed. Details of the ray tracing analysis are provided in Appendix B. Additionally, we have performed an experiment where we have measured  $\delta$  as a function of the location of the MV in the non-refracted case. The results of the experiment are compared with the values computed with the ray tracing method.

Figure 3.18 schematically shows how the crossing point of the two laser beams is determined. Two laser beams were transmitted from an LDA probe and were focussed into a glass tube. The MV was moved by translating the LDA probe that was mounted onto a manual translation stage. A diffuse reflecting surface was placed inside the glass tube on which two laser spots were formed. The surface was positioned with a second manual translation stage inside the tube and was moved along the optical axis of the LDA probe. With a digital camera, pictures were taken from the laser spots at coordinates  $x_a$  and  $x_b$ . From the pictures, the distances between the two spots,  $d_a$  and  $d_b$ , were determined. If the MV lies in between  $x_a$  and  $x_b$ , its position is

$$x_{MV} = \frac{d_a (x_b - x_a)}{d_a - d_b} + x_a, \quad (3.18)$$

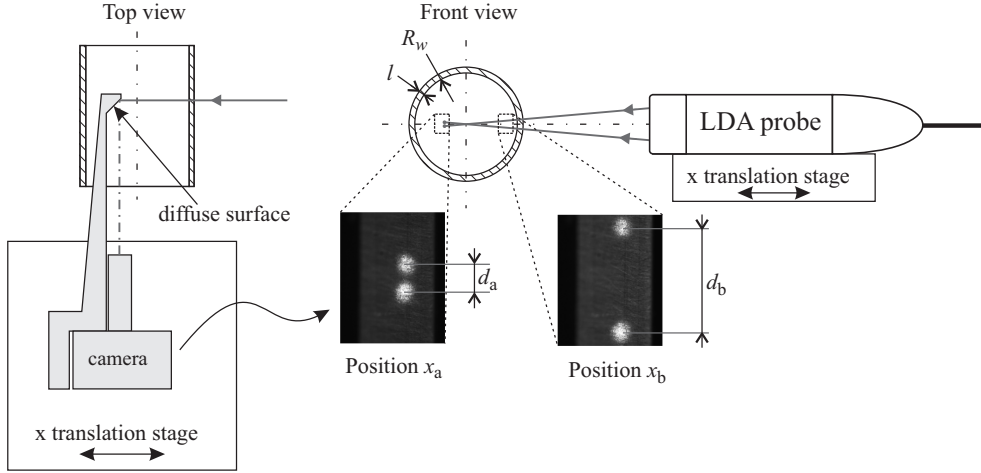


Figure 3.18: Experiment to determine the beam crossing position in a cylindrical window.

otherwise, the position is

$$x_{MV} = \frac{d_a (x_b - x_a)}{d_a + d_b} + x_a. \quad (3.19)$$

With the displacement of the LDA probe with respect to the tube axis  $x_{LDA}$ , which equals  $x_{MV}$  in the non-refracted case, the discrepancy between the actual position of the MV and the non-refracted case becomes for the cylindrical window

$$\delta_{cyl} = x_{LDA} - x_{MV}. \quad (3.20)$$

Results of the experiment are shown in Fig. 3.19 for two cylindrical glass tubes, having wall thicknesses  $l = 0.65$  mm and  $l = 3.6$  mm, respectively. For both tubes, the inner radius was  $R_w = 20.2$  mm. The results are plotted as functions of the displacement of the LDA probe with respect to the tube axis ( $= x_{LDA}$ ). The symbols in the graphs are the experimental values and the solid lines are the results from the ray tracing analysis. A remarkably good agreement is found between the computed and experimental values. Results for refraction through flat windows, computed with Eq. (3.17) and having the same thicknesses as the cylindrical cases, are added to the graphs as the dashed lines.

$\delta_{cyl}$  is zero at the axis of the tube ( $x = 0$ ), because the beams are in that case positioned normal to the window surface. Therefore, the differences between  $\delta_{flat}$  and  $\delta_{cyl}$ , i.e., the astigmatism, are the largest at the axis of the tube, but when  $x \rightarrow R_w$ ,  $\delta_{cyl} \rightarrow \delta_{flat}$ . In general, also seen from Eq. (3.17),  $\delta$  is much smaller for the thin walled tubes. Therefore, it is important to minimize the wall thickness.

The 2D transceiver probe has one pair of laser beams that is used to measure the axial velocity and a second pair that is used to measure the swirl velocity. The first beam pair forms a plain that includes the axis of the cylindrical window, while the second beam pair is positioned orthogonally to the axis. This is shown in Fig. 3.20, where the light blue and green planes are formed by the 2D probe, and the dark blue plane is formed by the 1D probe. The light- and dark blue beam pairs are refracted as if the window is flat. Because of this, their overlap is constant with  $r$ . The green beam pair, however, experiences refraction through a

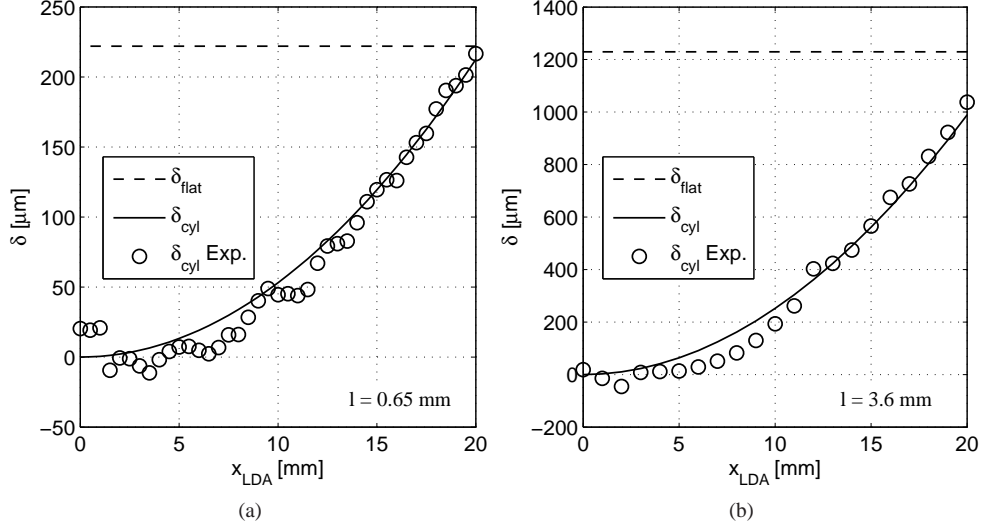


Figure 3.19: The distance between the focal point of the LDA probe and the position of the measurement volume as a function of the displacement of the LDA probe with respect to the tube axis. Symbols are experimental values, dashed lines are computed with Eq. (3.17), and the solid line is computed with a ray tracing analysis.

cylindrical window, so there will be a varying overlap between the green MV and the light- and dark blue MV's.

According to the above, the astigmatism  $A = \delta_{flat} - \delta_{cyl}$ , is largest at the axis of the window. Here, at  $x = 0$ , we have  $\delta_{cyl} = 0$ , so the maximum astigmatism is equal to  $\delta_{flat}$ . The variation in beam crossing angle of the green beam pair has its maximum when the MV is close to the wall. We have computed the astigmatism and the variation in beam crossing angle ( $\Delta\kappa$ ) based on the properties of the 2D transceiver, the window, and the inside and outside media (taken to be nitrogen). The maximum astigmatism,  $A_{max}$ , and the change in crossing angle  $\Delta\kappa$  are plotted as functions of the window thickness for  $R_w = 20$  mm in Fig. 3.21a. It is obvious from Eq. (3.17) that both  $A_{max}$  and  $\Delta\kappa$  are proportional to  $l$ .

From the above, we conclude that the window material should be as thin as possible. The minimum wall thickness, however, is limited by the maximum allowable deformation of PMMA under pressure and by its fabrication process. State of the art lathes were able to make windows with a minimum wall thickness of  $l = 350$   $\mu\text{m}$  while maintaining optical quality (surface roughness is  $\mathcal{O}(10^{-8})$  m). When the wall thickness is much smaller than the tube radius, the material stress  $\sigma$  due to the pressure  $p$  can be approximated with

$$\sigma = \frac{pR_w}{l}. \quad (3.21)$$

The strain in the window material is  $\epsilon = \sigma/E$ , where  $E \approx 2.5 \cdot 10^9$  Pa is Young's modulus of PMMA (Matbase, 2012). At a pressure of  $p = 2.5 \cdot 10^5$  Pa, which is a typical pressure in the RHVT, a wall thickness of  $350$   $\mu\text{m}$ , and a radius of  $R_w = 0.02$  m, the strain is  $\epsilon \approx 0.5\%$ . This

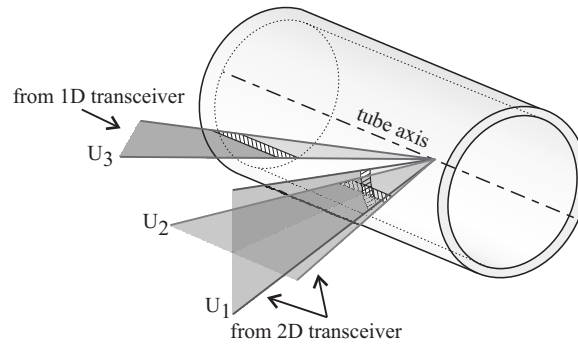


Figure 3.20: Measurement planes created by the LDA probes. The hatched areas are shown to indicate how the measurement planes cross the window.

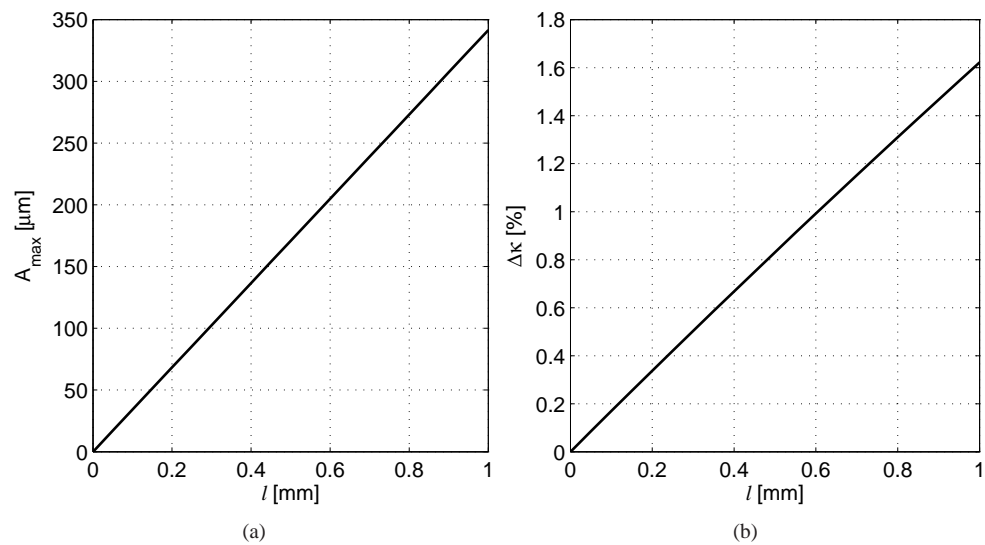


Figure 3.21: (a) Maximum astigmatism between the green MV and the light- and dark blue MV's. The values shown here represent the astigmatism at the axis of the cylindrical window; (b) maximum relative variation in beam crossing angle, which occurs close to the wall. Results are plotted as functions of the wall thickness. The inner radius of the window is  $R_w = 20$  mm and the window material is PMMA. The outside and inside media are taken to be nitrogen gas.

has only a minor influence on the refraction and is therefore considered to be an acceptable value.

To have an estimation of the possible measurement errors using a window with  $l = 350 \mu\text{m}$ , we have assumed that the pressure gradient, the temperature gradient, and the humidity inside the RHVT have no influence on the refractive index of nitrogen gas. The maximum astigmatism between the green and light blue MV's was computed to be  $116 \mu\text{m}$ , which was roughly 15% of the length of one measurement volume ( $650 \mu\text{m}$ ). In this case, the astigmatism had only minor influence on the size of the measurement volume (when properly aligned). The variation in the swirl velocity due to the change in the beam crossing angle is for small beam crossing angles approximately equal to  $\Delta\kappa$  and was computed to be an acceptable 0.6%.

Close to the wall, internal scattering of the laser light in the windows caused the signal quality to drop, making it more difficult to measure close to the wall. Because of its fabrication process, the window surface can never be perfectly smooth, but contained extremely small scratches (which are not visible by the eye) that caused additional scattering. This problem existed especially for the 1D transceiver, which was placed under a  $45^\circ$  angle (see Fig. 3.14). Because of this, the radial velocity component contained more noise. It is, however, impossible to give a quantitative value of the noise and the corresponding errors, because it depends on the local surface quality of the window. During the experiments, care has been taken to optimize the signal to noise (SNR) ratio to minimize the additional errors due to surface imperfections.

### 3.3 CPT method

A cylindrical Pitot tube (Ahlborn & Groves, 1997; Gao *et al.*, 2005), or CPT, was used to measure Mach numbers in the vortex chamber. The advantage of the CPT versus a standard Pitot tube is that the probe can be much smaller, and is therefore less disturbing to the flow. The CPT, shown in Fig. 3.22, consists of a cylindrical capillary or tube in which a small hole is drilled. The tube is closed at one end and is connected to a pressure sensor at the other end. The CPT can be rotated and translated in order to measure the pressure distribution around the capillary, at different locations in the fluid. The CPT that we have used consisted of a cylindrical tube, having a diameter of 1 mm in which a small hole of 0.1 mm diameter was drilled.

A measured pressure distribution around the CPT is shown in Fig. 3.23. When the hole faces the flow direction, the measured pressure has its maximum value, which is equal to the total pressure  $p_t$ . This corresponding angle is the flow angle  $\beta$ . When the CPT is rotated, the measured pressure  $p_\alpha$  changes as a function of the inclination angle  $\alpha$ .

It has been shown that the pressure distribution depends mainly on the Mach number (Zeegers *et al.*, 2011). When the flow around the CPT is isentropic, the Mach number is related to the total and static pressures according to

$$\text{Ma} = \left( \frac{2}{\gamma - 1} \left[ \left( \frac{p_t}{p} \right)^{\frac{\gamma-1}{\gamma}} - 1 \right] \right)^{1/2}. \quad (3.22)$$

The static pressure  $p$  is measured at an angle  $\alpha_s$ . This angle, i.e., the static angle, is known



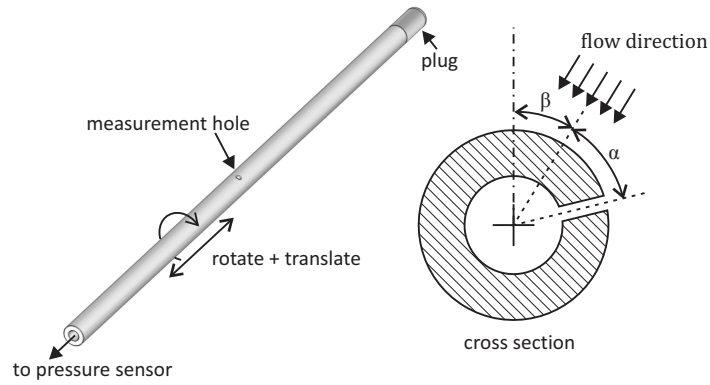


Figure 3.22: A cylindrical Pitot tube and a cross section at the location of the measurement hole, where  $\alpha$  is the inclination angle and  $\beta$  is the flow angle. The angle of measurement is  $\alpha + \beta$ .

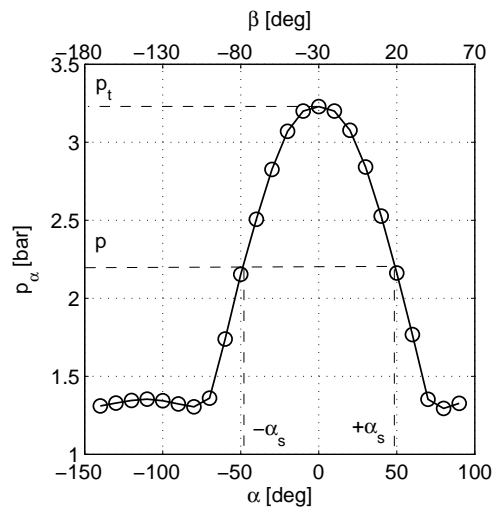


Figure 3.23: Pressure distribution around the CPT as a function of the inclination angle  $\alpha$  and the flow angle  $\beta$ . In this example, the flow direction is  $-30^\circ$ . The resulting Mach number is  $Ma = 0.763$ .

from calibration measurements and is related to the Mach number according to

$$\alpha_s = 37.81 + 0.285 \exp\left(\frac{\text{Ma}}{0.209}\right) \quad (\text{Ma} < 0.8). \quad (3.23)$$

The Mach number is found iteratively by measuring  $p$  and  $p_t$  in combination with Eqs. (3.22) and (3.23).

Because of the positioning of the CPT in the experimental RHVT (Fig. 3.1), it was not possible to determine a radial Mach number. However, the radial velocity is much smaller than the swirl and axial velocities and has only minor influence on the measured pressures (Ahlborn & Groves, 1997; Gao *et al.*, 2005) and is, therefore, neglected. Ma is decomposed into a swirl Mach number  $\text{Ma}_\theta$  and an axial Mach number  $\text{Ma}_z$  according to

$$\text{Ma}_\theta = \text{Ma} \cdot \cos \beta; \quad \text{Ma}_z = \text{Ma} \cdot \sin \beta, \quad (3.24)$$

where the direction of the flow  $\beta$ , shown in Fig. 3.22, is found at the angle at which the maximum pressure is found.

### 3.4 Gas conditioning

The humidity of the plenum gas has a major influence on the lifetime and size of the water droplets, as discussed in Chapter 2. To be able to control the humidity of the plenum gas, a humidifier was utilized in which small water droplets were injected into the nitrogen. The details of the humidifier itself will be provided in §3.5.2. In the humidifier, time was given for the droplets to evaporate, thereby humidifying the gas. Dependent on the amount of water injected, the gas pressure, the temperature, and the mass flow of nitrogen, the gas could be unsaturated, saturated, or saturated with droplets suspended in the gas. In the latter case, the droplets can be used as seeding for the PDPA measurements or as contaminant which needs to be separated from the gas.

The main component of the humidifier, a pressure vessel, in which small water droplets are injected into the nitrogen, requires a certain volume, based on the mass flow of nitrogen through the humidifier, to provide time for the injected droplets to evaporate. To estimate this volume, the evaporation process of droplets in the vessel was simulated based on the model described in §2.2. At the start of the simulation, a fixed control volume contains nitrogen and water droplets having a specified size distribution, schematically represented in Fig. 3.24. The model simulates the evaporation process and the humidification of gas in the control volume as a function of time until there exists a steady state. This means that all droplets evaporate, if the total amount of liquid water in the volume is less than the amount when the gas is saturated. If the amount of liquid water is higher, the droplets evaporate until  $\text{RH} = 1$  (in the simulation until  $\text{RH} = 0.99$ ) and the droplets that not fully evaporate remain suspended in the gas.

The maximum amount of water vapour per unit volume, i.e., the maximum absolute humidity  $\chi$  in  $\text{kg/m}^3$ , that can be reached in the vessel is equal to the partial density water vapour, which is determined by the saturation vapour pressure of water  $p_{sat}$  and the temperature in the vessel  $T$  according to

$$\chi = \frac{p_{sat}(T)M_{\text{H}_2\text{O}}}{\mathcal{R}T}, \quad (3.25)$$

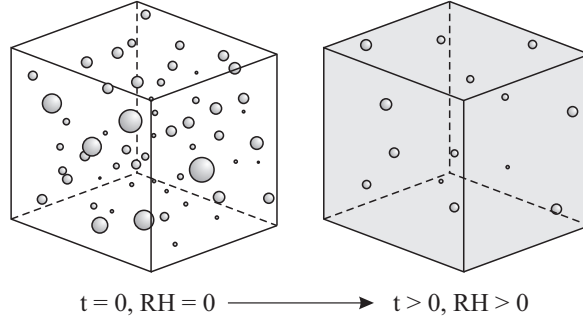


Figure 3.24: Control volume of gas containing water droplets, before and after humidification.

where  $\mathcal{R}$  is the universal gas constant and  $M_{\text{H}_2\text{O}}$  is the molar mass of water.

Using Spalding's model (§ 2.2), the time needed to reach a specified humidity, i.e. the residence time  $\tau = t|_{\text{RH}=\text{RH}_{\text{specified}}}$ , was computed. With the mass flow of nitrogen  $\dot{m}$  in kg/s, the plenum pressure  $p_{pl}$ , and the average temperature in the vessel, which is approximated by the plenum temperature  $T_{pl}$ , the minimum volume of the pressure vessel is given by

$$\mathcal{V}_{min} \simeq \frac{\dot{m}}{\rho_{pl}} \tau = \dot{m} \frac{\mathcal{R} T_{pl}}{M_{\text{N}_2} p_{pl}} \tau, \quad (3.26)$$

where it is assumed that the added volume of water vapour can be neglected with respect to the volume of nitrogen.

Because of the evaporation process, which requires thermal energy from the gas, the temperature of the control volume  $T_\infty$  decreases in time. The temperature change of the control volume is the result of the heat transferred from the gas to the droplets and is computed with

$$\rho_f c_p \frac{dT_\infty}{dt} = - \sum Q, \quad (3.27)$$

where  $\sum Q$  is the total heat transferred from the nitrogen to all the droplets, which is described by Eq. (2.33), in the control volume. Here,  $\rho_f$  and  $c_p$  are the mass density and the heat capacity at constant pressure of the gas, respectively.

The initial size distribution of the droplets, which is a normal distribution having a mean and a standard deviation, is an input parameter for the simulation. In that way, we can study the influence of the initial droplet size distribution on the time it takes to reach a specified humidity, i.e. on the minimum volume  $\mathcal{V}_{min}$  of the pressure vessel. Two initial droplet size distribution, which are shown in Fig. 3.25, are chosen for the simulation. The first droplet size distribution corresponds to a typical size distribution of droplets that are generated by means of ultrasonic atomizers, which can be estimated using the correlation of Lang (1962)

$$d_p = 0.34 \left( \frac{8\pi\gamma_p}{\rho_p f^2} \right)^{1/3}, \quad (3.28)$$

where  $\gamma_p$  and  $\rho_p$  are the surface tension and mass density of the liquid, respectively, and  $f$  is the frequency of the ultrasonic transducer. Atomizing water ( $\gamma_p = 0.07$  N/m and  $\rho =$

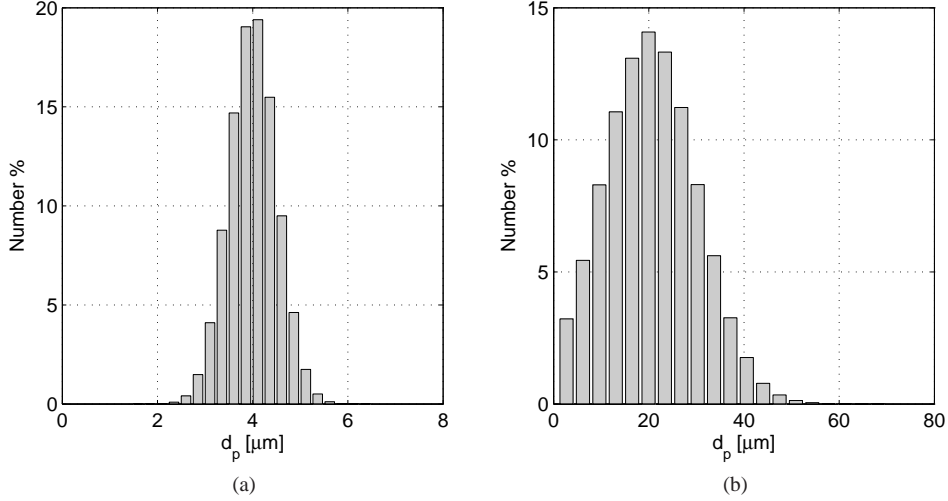


Figure 3.25: Two initial droplet size distributions used in the humidifier simulations. Both the droplet size distributions are Gaussian. Here the distributions are plotted with  $n = 20$  droplet size intervals. (a)  $d_{p,0} = (4 \pm 0.5) \mu\text{m}$ , and (b)  $d_{p,0} = (20 \pm 10) \mu\text{m}$ , where the minimum droplet size is  $d_p = 0 \mu\text{m}$ .

998 kg/m<sup>3</sup>) at a frequency of  $f = 1$  MHz, results in  $d_p = 4 \mu\text{m}$  droplets. Because of non-uniformities in droplet break up and collisions and agglomeration of droplets, the droplets are not uniform in size. However, the size distributions of ultrasonically generated droplets are narrow banded. Therefore, the first droplet size distribution was taken to be  $d_{p,0} = (4 \pm 0.5) \mu\text{m}$ . The second size distribution is taken to be  $d_{p,0} = (20 \pm 10) \mu\text{m}$ , which is typical for droplets generated with high pressure nozzles (see e.g. Chaker *et al.* (2002)).

Initially, there are a number of droplets present per unit volume. The amount of droplets depends on their size distribution and the total amount of water per unit volume ( $\equiv \phi_{\text{H}_2\text{O}}$ ), which is initially in the liquid phase. When the droplets evaporate, the absolute humidity  $x_v$  (not to be confused with the *maximum* absolute humidity  $\chi$ ), increases in time. The process is discretized in time, allowing us to compute the total mass transfer from all the droplets during a time interval. The size distribution of droplets is divided into  $n$  size intervals (in Fig. 3.25, the distributions are divided into  $n = 20$  intervals for clarity, while in the simulation  $n = 100$  intervals were used). The index of a size interval is  $i$ , and the change in absolute humidity during a time interval  $\Delta t$  is

$$\Delta x_v = \sum_{i=1}^n \Delta m_i, \quad (3.29)$$

where  $\Delta m_i$  is the total mass transfer from all the droplets that belong to size interval  $i$ , per unit volume. The absolute humidity at the new time becomes  $x_{v,new} = x_{v,old} + \Delta x_v$ , and the corresponding relative humidity in the control volume becomes

$$\text{RH}_{new} = \frac{x_{v,new}}{\chi} \quad (\text{RH} \leq 1). \quad (3.30)$$

For both simulations, the gas and the droplets have the same initial temperature (20 °C). Furthermore, there was no velocity difference between the droplets and the gas. The required volume of the pressure vessel was computed for the case that the initial mass of the droplets per unit volume is equal to  $\phi_{\text{H}_2\text{O}} = \chi$  and the mass flow of nitrogen is 0.070 g/s. The initial humidity is  $\text{RH} = 0$ , and the simulation stopped when the humidity reached  $\text{RH} = 0.99$ .

Results of the simulations are shown in Fig. 3.26 and are obtained for a gas pressure of 6 bar. The relative humidities as functions of time are shown in Figs. 3.26a and 3.26b. Initially, the evaporation process of the droplets is very rapid because of the low ambient gas humidity. During the evaporation process however, the humidity increases, thereby decreasing the mass flux from the droplets to the gas. Consequently, the increase in humidity per unit time decreases. Comparing the results of the two initial droplet size distributions reveals that  $\text{RH} = 0.99$  is much faster achieved by injecting the small droplets ( $d_{p,0} = (4 \pm 0.5) \mu\text{m}$ ) instead of the larger droplets ( $d_{p,0} = (20 \pm 10) \mu\text{m}$ ). For the latter, the time it takes to reach  $\text{RH} = 0.99$  is  $\tau = 43$  s, while for the small droplets  $\tau = 1$  s. According to Eq. (3.26), the required volume of the pressure vessel is, under the above conditions,  $\mathcal{V}_{\text{min}} = 0.01 \text{ m}^3$  for the small droplets and  $\mathcal{V}_{\text{min}} = 0.44 \text{ m}^3$  for the large droplets. The amount of water that needs to be injected is for both cases approximately 0.5 kg/h.

Because of the evaporation process, the temperature of the droplets and the gas decreases in time. The corresponding mean droplet temperature and gas temperature are shown in Figs. 3.26c and 3.26d. The temperature difference between the droplets and the gas results from an equilibrium between convective heat transfer from the gas to the droplets and the heat required for vaporization (see § 2.2.2).

The differences in the required volume of the vessel between small and large droplets can be explained as follows: for an equal amount of liquid water per unit volume, the small droplets have a larger combined surface area from which water evaporates. Therefore, under the same other operating conditions, the humidification process is faster for the small droplets than for the large droplets. Thus,  $\tau$  is influenced by the total surface area of the droplets suspended in the gas.

To decrease  $\tau$  or the volume of the vessel, we can simply inject more droplets. By doing so, remaining droplets will be suspended in the gas. To see what effect this has on  $\tau$  and to estimate the size distribution of the remaining droplets, we have repeated the simulation with the  $d_{p,0} = (20 \pm 10) \mu\text{m}$  droplets, but with a mass flow of water of 1 kg/h, which is  $\phi_{\text{H}_2\text{O}} = 2\chi$ . The results are shown in Fig. 3.27. Compared to the previous situation, there are now twice as many droplets that evaporate. Therefore, the time it takes to reach  $\text{RH} = 0.99$  is significantly reduced (Fig. 3.27a). The droplets that remain after the evaporation process, have a size distribution as shown as the solid line in Fig. 3.27b. For convenience, the initial droplet size distribution is included in the graph.

When high pressure spray nozzles are used, the water droplets have a high initial velocity. Due to this, numerous droplets will hit the walls of the vessel where they form big droplets that fall down to the bottom. This means that less droplets are suspended in the gas than is assumed above. Also, due to the high initial velocity of the droplets, the nitrogen gas will obtain a higher velocity and recirculates in the vessel. Therefore, the effective vessel volume is larger than estimated by Eq. (3.26). To ensure that the plenum humidity can be controlled over the full range ( $0 \leq \text{RH}_{\text{pl}} \leq 1$ ), we have used the results from the simulation where  $\phi_{\text{H}_2\text{O}} = \chi$  and  $d_{p,0} = (20 \pm 10) \mu\text{m}$  as design criteria for the pressure vessel, resulting in  $\mathcal{V}_{\text{min}} = 0.44 \text{ m}^3$ . In this way, the vessel can be used as humidifier in combination with the ultrasonic atomizers (small droplets) or the high pressure spray nozzles (large droplets).

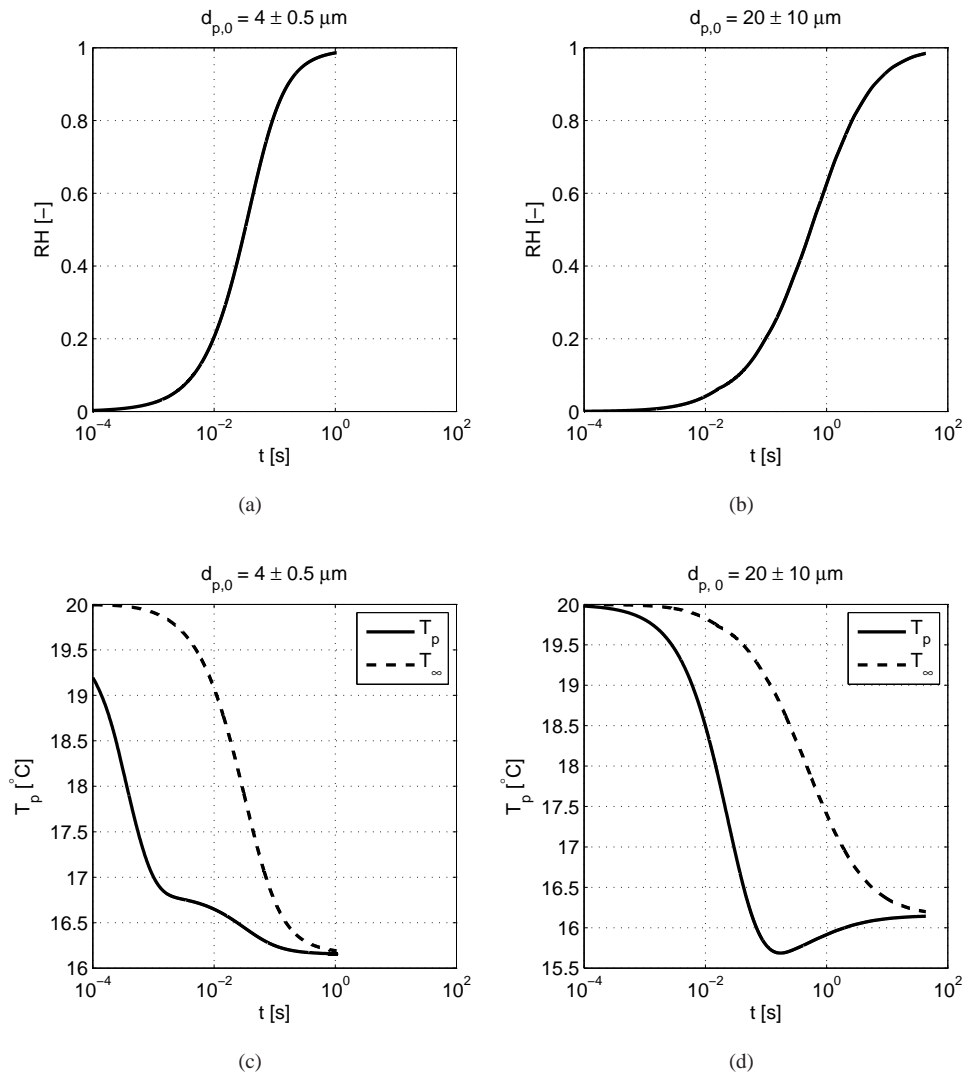


Figure 3.26: Results of two simulations of evaporating water droplets in nitrogen, having two different initial droplet size distributions, indicated in the graphs. (a, b) Relative humidity; (b, c) droplet and gas temperatures. All results are plotted as functions of time. The initial amount of liquid water equals  $\phi_{\text{H}_2\text{O}} = \chi$ , the initial temperatures of both the droplets and the gas is 20°C and the ambient pressure is 6 bar. The simulation was stopped at  $\text{RH} = 0.99$ .

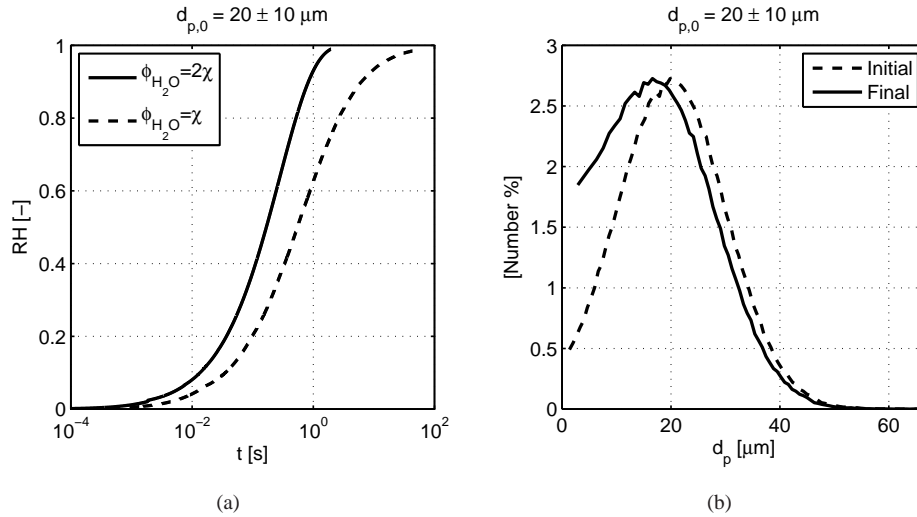


Figure 3.27: Results of a simulation of evaporating water droplets in a control volume of nitrogen. (a) Relative humidity as a function of time for  $\phi_{\text{H}_2\text{O}} = \chi$  and  $\phi_{\text{H}_2\text{O}} = 2\chi$ ; (b) initial (for  $\phi_{\text{H}_2\text{O}} = \chi$  and  $\phi_{\text{H}_2\text{O}} = 2\chi$ ) and final (for  $\phi_{\text{H}_2\text{O}} = 2\chi$ ) droplet size distributions. The pressure in the vessel is 6 bar. The simulation was stopped at  $\text{RH} = 0.99$ .

More details of the pressure vessel are given in § 3.5.2.

### 3.4.1 Droplet generators

The initial idea was to use two industrial ultrasonic atomizers (UCAN-K42) as droplet generators, which would be placed inside the pressure vessel. The main advantage of these type of atomizers is that, according to literature, the ultrasonic atomization process is independent of ambient pressure (Avvaru *et al.*, 2005; Lang, 1962; Rajan & Pandit, 2001). Additionally, the generated droplets are very small and have no significant initial velocity. Because of the small droplet size, the required volume of the vessel is also small. Although the ultrasonic atomization process would be independent of the ambient pressure, the supplier could not guarantee that these humidifiers would work under higher ambient pressures.

What we have tested first after the pressure vessel was manufactured and the ultrasonic atomizers were mounted, was if the ambient pressure has indeed no influence on the output of the humidifier. Figure 3.28 shows the production of droplets per unit of time as a function of the pressure in the vessel. At atmospheric pressure,  $p = 1$  bar, the humidifier output is approximately 3.7 kg/h, which is close to its specification (4 kg/h). Increasing the pressure, however, leads to a significant reduction in output. It appears that the output can be approximated by an exponential function of the pressure (dashed line). At the operating pressure of the RHVT, which is about 6 bar, almost no droplets are produced.

To ensure that this effect is not the result of influences of the pressure on the electronics of the device, we have performed an experiment used a different ultrasonic atomizer (Liquifog<sup>®</sup>). We have mounted this atomizer to a small pressure vessel through which pres-

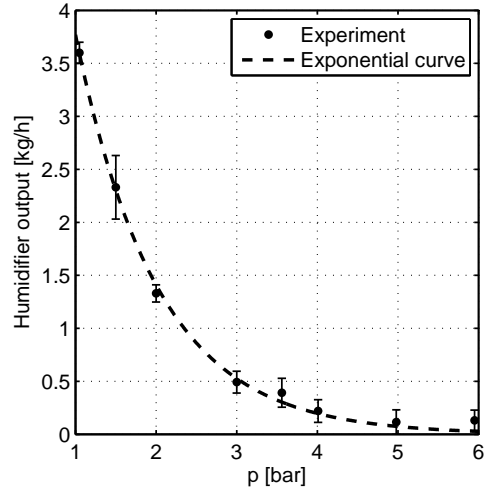


Figure 3.28: The humidifier output as a function of pressure for the ultrasonic atomizers.

surized nitrogen gas flowed. We have constructed the experimental setup in such way that the electronics and the piezoelectric element, which generates the ultrasound, were operated under atmospheric pressure while the water was under higher pressure. The result was the same as above: the higher pressure reduces the production of droplets. This means that the reduction in droplet production must be caused by an additional effect that was not noted before.

The poor droplet production of the ultrasonic humidifiers under high pressure was unexpectedly, however, the humidifier vessel was designed for the worse case scenario, i.e., when high pressure water nozzles are used. These were finally used to generate droplets in the vessel. Details of the water nozzles and the pressure vessel are provided in § 3.5.2.

## 3.5 Process Scheme

The process scheme of the experimental setup is shown in Fig. 3.29. The scheme is separated into four sections: the nitrogen supply, the humidifier section, the sensing section, and the mass flow controller. We will discuss each section separately.

### 3.5.1 Nitrogen supply section

Nitrogen was supplied from a liquid nitrogen tank ( $\text{LN}_2$ ). The pressure of the nitrogen was controlled by means of a pressure controller. Because the liquid nitrogen tank was placed outside the building, the temperature of the supplied nitrogen varied in time (the nitrogen supply tube is exposed to the weather). Therefore, we have used a temperature controller (Julabo F32 with a 2 kW heater and cooler) to control the nitrogen temperature. Downstream of the temperature controller, the total mass flow was measured with a mass flow sensor  $F_{pl}$ .



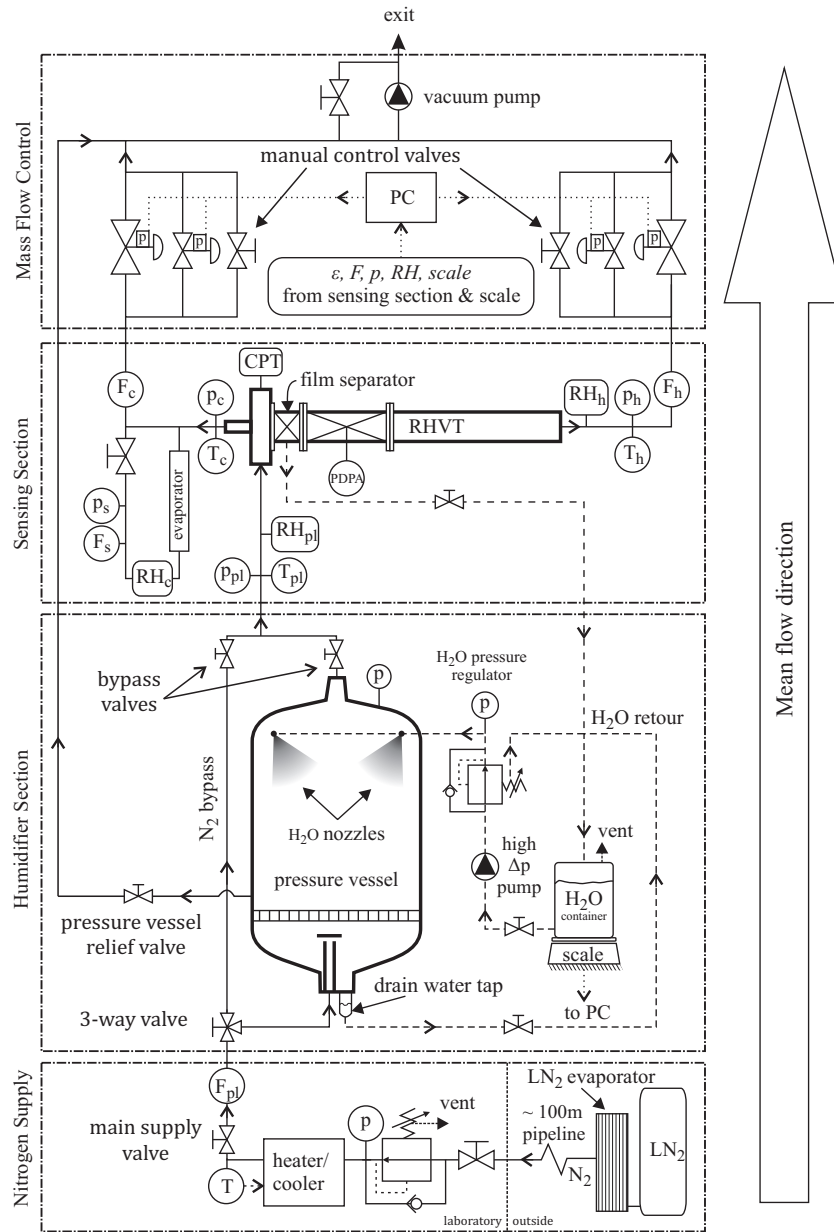


Figure 3.29: The process scheme of the experimental setup. Solid black lines represent gaseous flow, dashed lines indicate water flow, dotted lines are sensing or control signals. The heart of the process scheme, the RHVT, is shown in the sensing section.  $p$ ,  $T$ ,  $F$ , and  $RH$  are used to distinguish for pressure, temperature, mass flow, and humidity sensors, respectively. Indices  $pl$ ,  $c$ ,  $h$ , and  $s$  are used to indicate plenum, cold, hot, and sampling conditions.



Figure 3.30: (a) The pressure vessel; (b) close up of a high pressure water nozzle that was used.

### 3.5.2 Humidifier section

The fabricated pressure vessel had a net volume of  $0.44 \text{ m}^3$ , a diameter of 60 cm, and a height of 1.6 m and is shown in Fig. 3.30a. The vessel consisted of four main segments, containing windows and flanges to which high pressure water nozzles, sensors, and tubing could be mounted.

During the experiments, up to three water nozzles were utilized. The high pressure water nozzles (Danfoss), from which one is shown in Fig. 3.30b, had a exit opening of 0.3 mm and a spray angle of  $45^\circ$ . The flow rate of water at operating pressure (21 bar) was 1.12 kg/h. Water was supplied by means of a high pressure water pump (Nessie Plug&Play™), which had the capacity to pump 75 l/h at a pressure of 100 bar. The pressure (and mass flow) of the water that was injected through the nozzles in the vessel was regulated with a pressure regulator.

A container that was filled with water served as the water source. The container was placed onto a digital scale (Kern FKB36K0.2, max 36.1 kg, reproducibility 0.2 g) that was connected to a computer. Excess water from the pump, which is relieved by the pressure regulator, was fed back to the water reservoir. By logging the weight of the water reservoir

in time, we computed the nett amount of water per unit of time that was suspended in the nitrogen gas.

An automatic drain water trap that is mounted in the bottom of the pressure vessel allows liquid water that is injected in the vessel, but not has been suspended in the gas, to be transported back to the water container.

### 3.5.3 Sensing section

The sensing section was by far the most important part of the experimental setup. It contained the heart of the laboratory, the RHVT, and pressure, temperature, humidity and mass flow sensors. The sensors that were used are:

**Pressure sensors** Digital manometers (Keller) were used to measure the pressures. The range and accuracy of the sensors was 0 – 21 bar and 0.02% FS, respectively. The pressure for the CPT measurements (§3.3) or the pressure used to determine the mole fraction, were measured with a digital manometer, having a range of 0 – 5 bar absolute and an accuracy of 0.02% FS.

**Temperature sensors** Temperatures were measured with pt1000 temperature probes (TempControl, calibrated to have an accuracy of 0.01 K) or with the humidity probes that have a built in temperature sensor (accuracy of 0.5 K).

**Humidity sensors** The relative humidity was measured with capacitive humidity probes (MDR3 General Electric). The accuracy of the probes was 2% for  $0\% \leq RH \leq 90\%$  and 3% for  $90\% < RH \leq 100\%$ .

**Cold stream sampling** The relative humidity in the cold exit was determined from a sample taken from the cold exit stream, which was led through a heated tube (the evaporator) to evaporate droplets that are suspended in the cold gas stream. The mean temperature of the wall of the evaporator was controlled with a temperature controller and could manually be set. The temperature of gas in the exit of the evaporator is different from that of the mean and varies with, among others, the sampling mass flow. At the exit of the heated tube, the humidity, pressure, and temperature were measured.

**Mass flow sensors** Thermal mass flow sensors (Bronkhorst), having an accuracy of 1% FS in the range of 0 – 250 Nm<sup>3</sup>/h (0 – 87 g/s), were used to measure the mass flow through the system and the cold fraction. In the range  $0.2 < \varepsilon < 0.8$ , the uncertainty in the mass flow was determined to be less than 2%. For other cold fractions, the uncertainty in mass flow was less than 3%. The uncertainty in  $\varepsilon$  was  $< 0.01$  for all  $\varepsilon$ . A smaller mass flow sensor (0 – 20 Nm<sup>3</sup>/h or 0 – 4.44 g/s) was utilized to measure the sampling flow (from which the water mole fraction in the cold exit was determined).

### 3.5.4 Mass flow control section

A Labview™ program has been written that was used to control the flow through the system. Based on quantities measured by the mass flow sensors and the input parameters like cold fraction and desired mass flow, control valves in the cold and hot exit tubes were adjusted to maintain the set values. For each hot or cold outlet, two digital control valves (one large and one smaller valve) and one manual valve were used in parallel to be able to accurately control

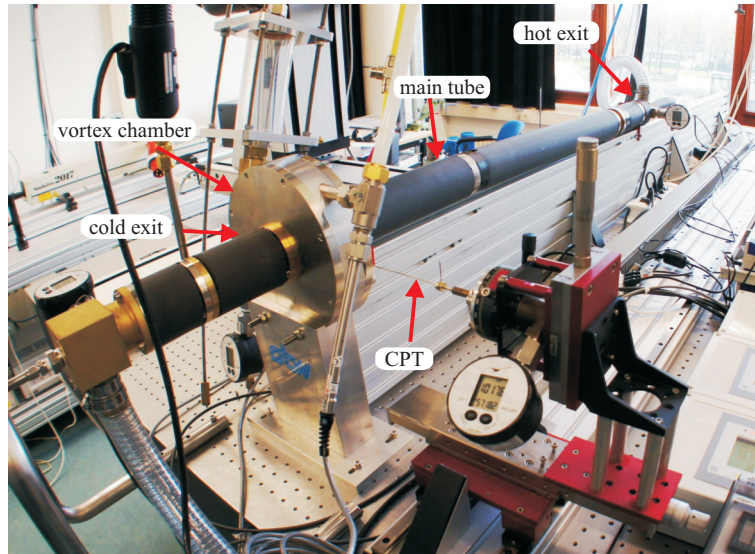


Figure 3.31: The experimental Ranque-Hilsch Vortex Tube. A CPT is inserted into the vortex chamber.

the flow. The valves, water pumps, and water container on the scale are mounted into a mass flow control cabinet, which is shown in Fig. 3.32a.

A vacuum pump (Fig. 3.32b) was utilized to be able to lower the overall pressure in the system. The pump (Gardner Denver™ Liquid-Ring 2SVG.161 pump) had a suction capacity  $480 \text{ Nm}^3/\text{h}$  at 1 bar absolute. At low pressure (0.15 bar absolute) the capacity was approximately  $113 \text{ Nm}^3/\text{h}$ .

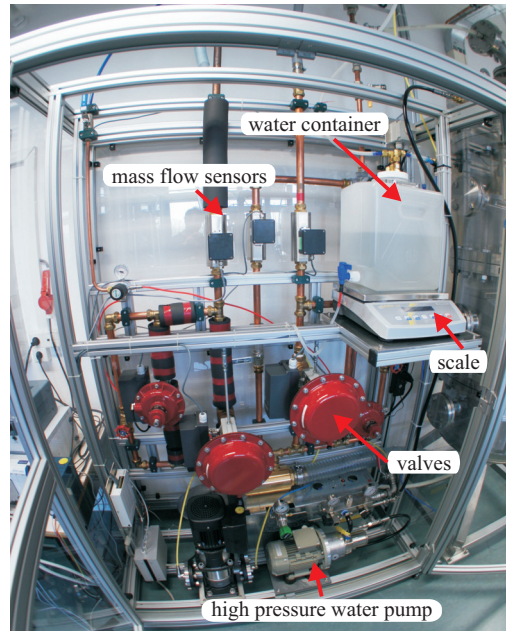
### 3.6 Conclusions

A laboratory has been realized for the experimental studies on the RHVT. The mass flows and cold fraction are controlled via a mass flow control system while pressures, temperatures, and relative humidities are simultaneously recorded.

Details of the experimental RHVT are provided. Two types of swirl generators can be mounted into the vortex chamber to investigate their influences on the flow and temperatures. The latest version swirl generator was designed to maximize the injection velocity, based on 1D compressible gas dynamics and the properties of the nitrogen supply system.

New 3D PDPA equipment has been purchased to measure the velocities and sizes of the water droplets in the RHVT. Specially designed optical transparent measurement sections were produced through which the PDPA measurements can take place. The optical distortion is negligible because of the very thin wall thickness (0.35 mm) of the window material. By means of a ray tracing analysis, we have computed that there is enough overlap of the laser beams to perform the PDPA measurements inside the RHVT.

A gas conditioning system has been developed in order to humidify the nitrogen gas. In a pressure vessel, water is injected via high pressure spray nozzles, creating numerous droplets.



(a)



(b)

Figure 3.32: (a) The mass flow control cabinet; (b) the vacuum pump.

The droplets evaporate, thereby humidifying the nitrogen gas. The humidity of the plenum gas can be varied by changing the mass flow of water, the nitrogen temperature, and the nitrogen mass flow.

## 4 | Experimental study of flow and droplet behaviour in the RHVT

In this chapter, which is based on Liew *et al.* (2013), we experimentally investigate the behaviour of water droplets that are injected, together with a carrier gas (nitrogen and water vapour), in the RHVT. The results are obtained from PDPA measurements, from which the experimental method is provided in §3.2. With PDPA, we have measured the velocities, velocity statistics, and sizes of the droplets. The results of the experiments give insight into the behaviour of droplets, as well as the behaviour of the gas. During the experiments, the gas was humidified and small droplets were suspended in the gas.

In the next section, we discuss the properties of water droplets as seeding particles. Section 4.2 provides details of the velocity statistics. Before we continue with the main results, we show results from a turbulent pipe flow experiment, §4.3, that was done in order to test the laser Doppler equipment. The results of the final PDPA measurements are provided in §4.4.

### 4.1 Water droplets as seeding particles

The velocities of the droplets represent a good approximation of the velocity of the fluid as long as the Stokes number,  $\text{Stk} \ll 1$ , and the centrifugal acceleration is insignificant.  $\text{Stk} \equiv \tau_p/\tau_f$  is the ratio of the droplet relaxation time,  $\tau_p = \rho_p d_p^2 / (18\rho_f \nu_f)$  (see §2.1), and the timescale of the flow  $\tau_f$ , where  $\rho_p$  and  $\rho_f$  are the mass densities of the droplet and the gas respectively,  $d_p$  is the droplet diameter,  $\nu_f$  is the kinematic viscosity of the gas.

The turbulent timescale of the flow, the Kolmogorov timescale, in the RHVT is determined to be  $\tau_\kappa = \mathcal{O}(10^{-6})$  s, based on a numerical simulation, which will be discussed briefly in §4.4.7. Using this as timescale of the fluid, the Stokes number is  $\text{Stk} = \mathcal{O}(1)$  for 1  $\mu\text{m}$  droplets. In this case, the constraint  $\text{Stk} \ll 1$  is not met and droplets are too large to follow all turbulent fluctuations. For measurements of turbulence, droplets of size  $d_p = \mathcal{O}(10^{-1})$   $\mu\text{m}$  or smaller are therefore required. It will be shown in §4.4.8 that droplets are typically larger. This means that can only resolve the larger scale velocity fluctuations.

In order to estimate which velocity scales can be resolved, we have modeled the response of a droplet that is subjected to harmonic velocity fluctuations of its surrounding fluid by solving the equation of motion for droplets (here we assume that the Reynolds number based on the droplet diameter is  $\text{Re} \ll 1$ , i.e. Stokes flow) taking only the drag force as relevant

force (see §2.1) (Maxey & Riley, 1983)

$$\frac{dU}{dt} = \frac{V - U}{\tau_p}, \quad (4.1)$$

where  $U$  is the droplet velocity. The fluid velocity oscillates in time according to  $V(t) = A_f \sin(\omega t)$ , having a certain amplitude  $A_f$  and angular frequency  $\omega$ . The corresponding timescale of the fluid is  $\tau_f = 2\pi/\omega$ . Eq. (4.1) can be solved analytically, and if the initial droplet velocity is  $U(t=0) = 0$ , the expression for the droplet velocity as a function of time is given by

$$U(t) = \frac{A_f}{1 + \tau_p^2 \omega^2} \left( \tau_p \omega [\exp(-t/\tau_p) - \cos(\omega t)] + \sin(\omega t) \right). \quad (4.2)$$

The exponential term in the equation is due to the initial acceleration of the droplet (homogeneous solution). The trigonometric terms result from the sinusoidal behaviour of the gas velocity (the particular solution). For  $t \gg \tau_p$ , the exponential term vanishes and the term between the large parentheses becomes

$$\tau_p \omega [\exp(-t/\tau_p) - \cos(\omega t)] + \sin(\omega t) = \sin(\omega t) - \tau_p \omega \cos(\omega t), \quad (4.3)$$

which can be written, by using the rule  $a \sin(x) + b \cos(x) = \sqrt{a^2 + b^2} \sin(x + \Delta\varphi)$ , as

$$\sin(\omega t) - \tau_p \omega \cos(\omega t) = \sqrt{1 + \tau_p^2 \omega^2} \sin(\omega t + \Delta\varphi), \quad (4.4)$$

where the phase shift  $\Delta\varphi$  is

$$\Delta\varphi = \arccos\left(\frac{a}{\sqrt{a^2 + b^2}}\right) = \arccos\left(\frac{1}{\sqrt{1 + \tau_p^2 \omega^2}}\right). \quad (4.5)$$

The amplitude of the term in between the large parentheses of Eq. (4.2), which is represented by Eq. (4.4), has an amplitude of  $\sqrt{1 + \tau_p^2 \omega^2}$ . Resultantly, the amplitude of the velocity of a droplet,  $A_p$ , is given by

$$A_p = \frac{A_f}{\sqrt{1 + \tau_p^2 \omega^2}}. \quad (4.6)$$

The relative droplet response amplitude is defined as  $\alpha_p = A_p/A_f$  and is related to  $\tau_p$  and  $\omega$  via

$$\alpha_p = \frac{1}{\sqrt{1 + \tau_p^2 \omega^2}}. \quad (4.7)$$

Ideally,  $\alpha_p = 1$  and the droplet velocity equals that of the fluid. This would be the case for  $\tau_p \rightarrow 0$ , i.e. particles without mass (for  $\omega > 0$ ).

Fig. 4.1 shows the Stokes numbers and droplet response amplitudes as functions of the oscillation frequency for three droplet sizes. With increasing  $Stk$ , the droplet response amplitude decreases. For example, at a frequency of 10 kHz, a 2  $\mu\text{m}$  droplet ( $Stk = 0.13$ ) has a relative response amplitude of approximately 76%, while a 5  $\mu\text{m}$  droplet ( $Stk = 0.84$ ) has a relative response amplitude of only 19%. Consequently, droplets that have a small Stokes



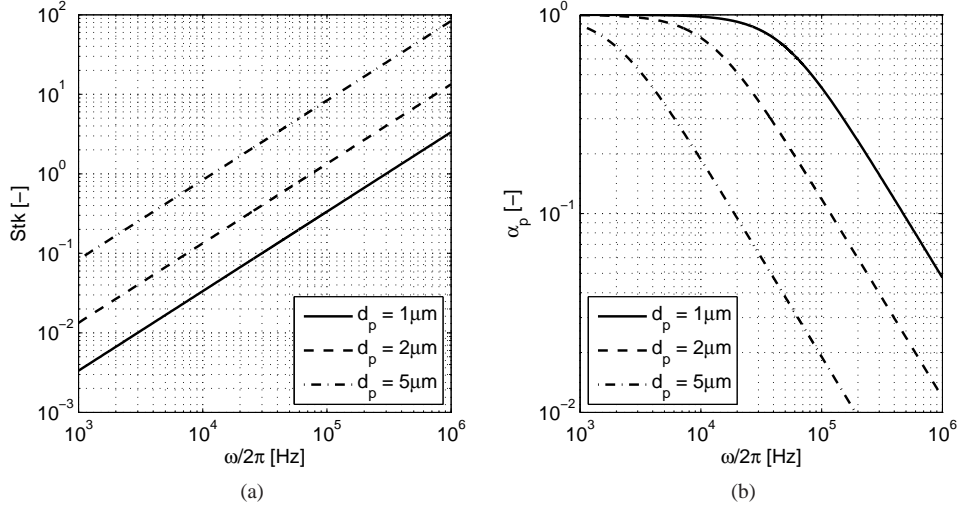


Figure 4.1: (a) Stokes number; (b) relative droplet response amplitude. Both are plotted as functions of the oscillation frequency of the fluid velocity for three droplet sizes.

number follow high frequency velocity fluctuations more accurately than larger, or heavier, droplets. It will be shown later, that the majority of the droplets are typically smaller than  $d_p = 2\mu\text{m}$  and that the maximum frequency that can be measured is approximately 10 kHz. In the measurable frequency range, the Stokes numbers are less than  $\text{Stk} \leq 0.13$ . For the majority of the measurements, the droplets can therefore be considered to be tracer particles.

According to results that are presented in chapter 2, there are no droplets present in the core region of the RHVT. This would be a major problem, because it would be impossible to perform PDDPA measurements in this region. However, due to the cooling effect that occurs in the vortex tube, in combination with the local pressure, the gas mixture (nitrogen and water vapour) becomes locally supersaturated (see for example Fig. 2.12b), causing spontaneous condensation to occur. Therefore, humidifying the nitrogen has a second advantage: local (inside the vortex tube) production of droplets (seeding).

Droplet concentrations in the RHVT were determined with the measured data rate, the dimensions of the measurement volume, and the velocity magnitude. The computed concentrations were used to determine the coincidence uncertainty (i.e., the chance that there are multiple droplets in the measurement volume). We have determined that the coincidence uncertainty was 16% at the axis and 2% near the wall. According to the amount of water injected in the nitrogen gas, the volume fraction of droplets was  $\mathcal{O}(10^{-6})$ . Under the operating conditions, the gas-droplet mixture can be regarded as diluted (Elghobashi, 1994) and it is highly unlikely that droplets affect each other. Therefore, we may neglect inter-particle interactions.

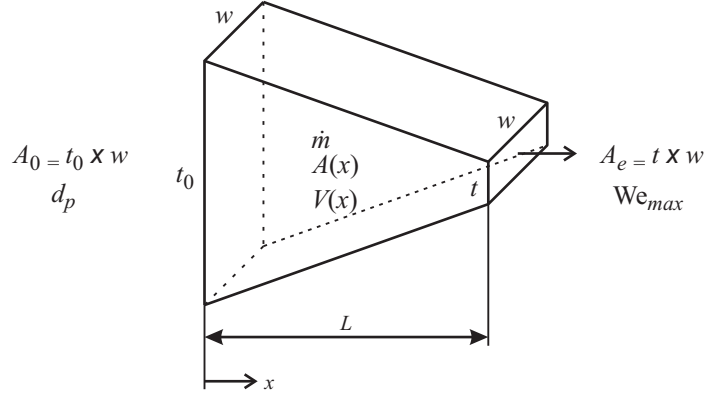


Figure 4.2: A converging nozzle through which gas and droplets accelerate.

#### 4.1.1 The sizes of droplets entering the RHVT

The droplet size distribution upstream of the RHVT, close to the inlet, was determined with PDPA. The mean droplet diameter was approximately  $d_p = 10 \mu\text{m}$ , and the volume mean diameter (will be defined in §4.4.8) was  $21 \mu\text{m}$ . These droplets are relatively large and may break up into smaller droplets due to, among others, inertial effects. A dimensionless number that describes when droplets deform and break up is the Weber number (Oertel, 2010, p. 509). The Weber,  $We$ , number is the ratio of the stagnation pressure and the capillary pressure and is defined as

$$We = \frac{\rho_f (U - V)^2 d_p}{\gamma_p}, \quad (4.8)$$

where  $\gamma_p$  is the surface tension between water and the carrier gas. If  $We > 1$ , the stagnation pressure of the gas is larger than the capillary pressure in the droplet. The droplet will therefore deform, which may lead to droplet break up of the droplet into smaller droplets.

When the gas-droplet mixture is injected into the RHVT, it accelerates through the entrance nozzles. Due to the inertia of a droplets, there will be a velocity difference between the droplet and the accelerating gas. When this velocity difference is large enough, the droplet may break up into smaller droplets. To estimate which droplets might break up due to the acceleration through the nozzles, we have computed the maximum Weber number in the two types of nozzles, from which the details are provided in §3.1.1. Fig. 4.2 schematically shows a converging nozzle as present in the swirl generator. The velocity as a function of the stream-wise coordinate  $x$  is computed with the method and nozzle dimensions provided in §3.1.1. Here, we assume that turbulence has no influence on the breakup phenomena. Furthermore, the flow is considered to be frictionless (inviscid) and reversible (i.e. isentropic flow). This implies that the boundary layer has a zero thickness. Therefore, shear forces, which are due to velocity gradients normal to the nozzle wall, are neglected.

The velocity of the gas as a function of  $x$  is shown in Fig. 4.3a for the nozzles in the two types of swirl generators (see §3.1.1). The corresponding operating conditions are:  $p_{pl} = 5.5 \text{ bar}$ ,  $T_{pl} = 293 \text{ K}$ , and  $\dot{m} = 70 \text{ g/s}$ . The computed gas velocities in the nozzles are used to simulate the motion of a droplet in the nozzle. The basic equation of motion, Eq. (4.1), is solved by using the method as described in §2.3. The computed velocity difference between

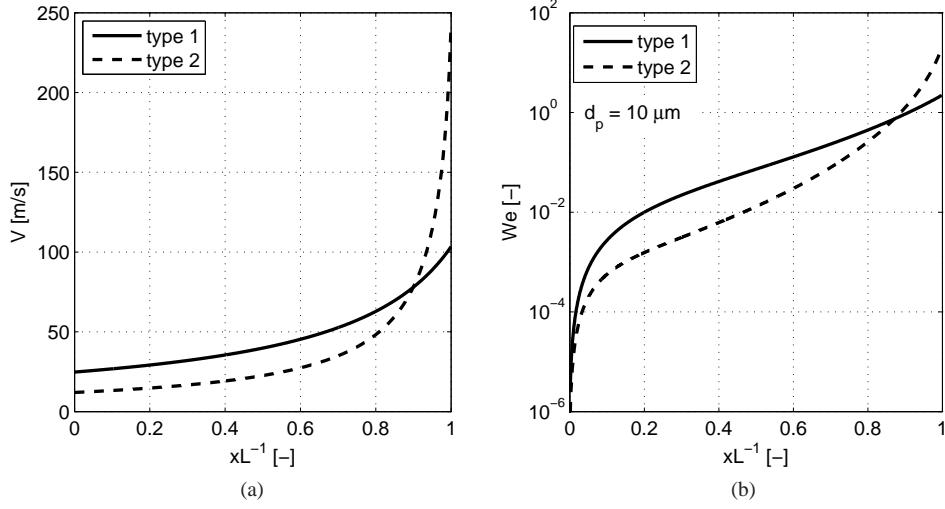


Figure 4.3: Gas velocity (a) and Weber number for a  $10 \mu\text{m}$  droplet (b) in two types of nozzles. Results are plotted as functions of the dimensionless streamwise coordinate for  $p_{pl} = 5.5 \text{ bar}$  and  $\dot{m} = 70 \text{ g/s}$ .

the droplet and the gas is used in Eq. (4.8) to determine the Weber number. An example of the results is shown in Fig. 4.3b, where  $We$  for a  $10 \mu\text{m}$  droplet is plotted.

The maximum Weber number,  $We_{max}$ , is found in the exit of the nozzle, and is plotted as a function of the droplet size in Fig. 4.4a. Additionally, a second analysis is made for a lower plenum pressure and mass flow:  $p_{pl} = 2.75 \text{ bar}$  and  $\dot{m} = 35 \text{ g/s}$ . These results are shown in Fig. 4.4b. For both the high and low mass flows,  $We$  is higher for the type 2 nozzle, indicating that the acceleration of the gas in this nozzle is higher.

It has been experimentally proven that droplets break up due to inertial effects if  $We_{max} > 12$ , and the Ohnesorge number, which relates the viscous forces to the inertial and surface tension forces,  $On = \mu_p / \sqrt{\rho_p d_p \gamma_p}$ , where  $\mu_p$  and  $\rho_p$  are the dynamic viscosity and mass density of the droplet material, is smaller than  $On < 0.1$  (see Pilch & Erdman (1987) and references therein).

For the high pressure case, droplets larger than  $d_p > 28 \mu\text{m}$  or  $d_p > 7 \mu\text{m}$  break up in the type 1 or type 2 nozzle, respectively. As mentioned above,  $We_{max}$  is lower for lower pressures. In that case, droplets break up if  $d_p > 50 \mu\text{m}$  or  $d_p > 11 \mu\text{m}$  in the type 1 or the type 2 nozzles, respectively.

Shear forces and turbulence are not taken into account here, both having an influence on droplet break up. Assuming that these effects enhance the break up, and that droplets break up if  $We_{max} > 1$ , the droplets that will enter the vortex chamber are generally smaller than  $d_p < 10 \mu\text{m}$ .

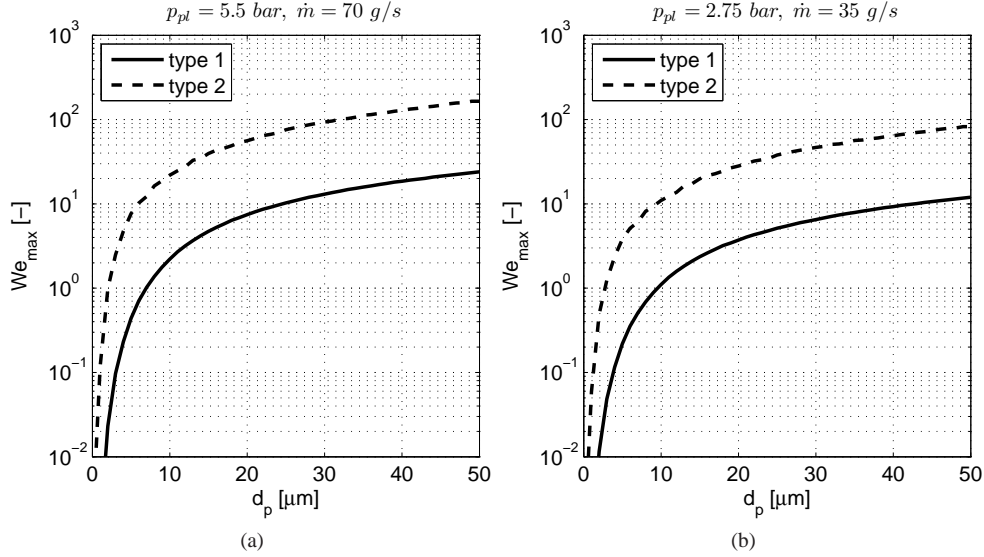


Figure 4.4: The maximum Weber number as a function of the droplet size for the two types of swirl generators. (a)  $p_{pl} = 5.5 \text{ bar}$  and  $\dot{m} = 70 \text{ g/s}$ ; (b)  $p_{pl} = 2.75 \text{ bar}$  and  $\dot{m} = 35 \text{ g/s}$ .

#### 4.1.2 Liquid collection in the vortex chamber

According to the analysis provided in §2.4.2, droplets larger than  $1.1 \mu\text{m}$  would not be able to enter the main tube for the corresponding flow parameters. Large droplets are pre-separated in the vortex chamber, leaving a liquid film on the walls of the swirl generator. This liquid is transported along the walls of the swirl generator into the main tube.

During start up experiments we have observed that, indeed, a liquid film was formed on the walls of the main tube close to the vortex chamber. This film blocked the view through the transparent measurement sections, making PDPA measurements impossible. Therefore, we have constructed film separators that were used to remove the liquid film from the main tube wall. The cross section of a segment of the main tube that contains the film separators is provided in Fig. 4.5. The film separators were formed by two small slots in the circumference of the main tube wall, close to the vortex chamber. The water was drained via plastic tubes and fed back to the water reservoir (§3.5).

After installing the film separators, the transparent sections remained clear of water, while the droplets remained suspended in the gas, allowing us to perform the PDPA measurements. The RHVT with the installed film separators and transparent measurement sections is shown in Fig. 4.6.

From the above observations we have concluded that the liquid film must be formed in the vortex chamber, but also that the suspended droplets are not reaching the tube wall. A possible explanation for this will be provided in §4.4.8.

It has to be noted that these film separators are primarily used to maintain optical properties of the transparent measurement sections, and are not used to study the separation of water from the nitrogen.

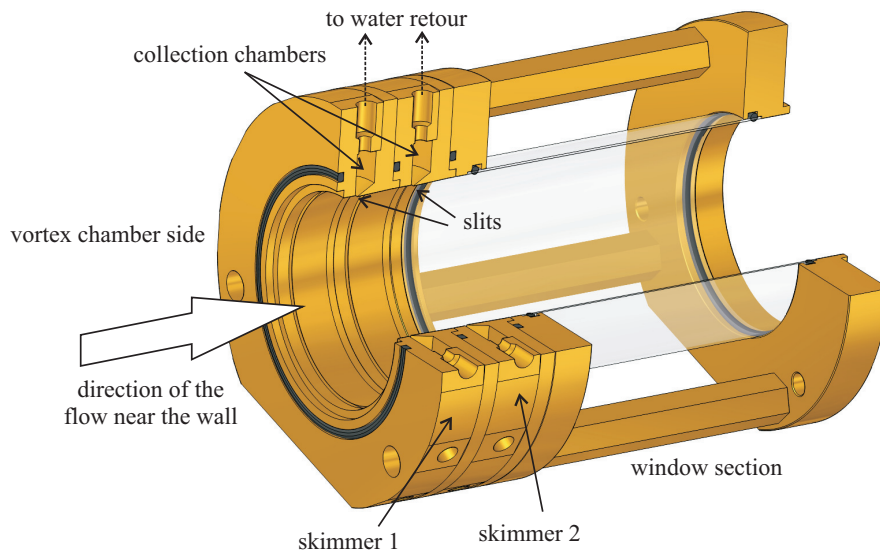


Figure 4.5: Detail of the film separators and a window section.

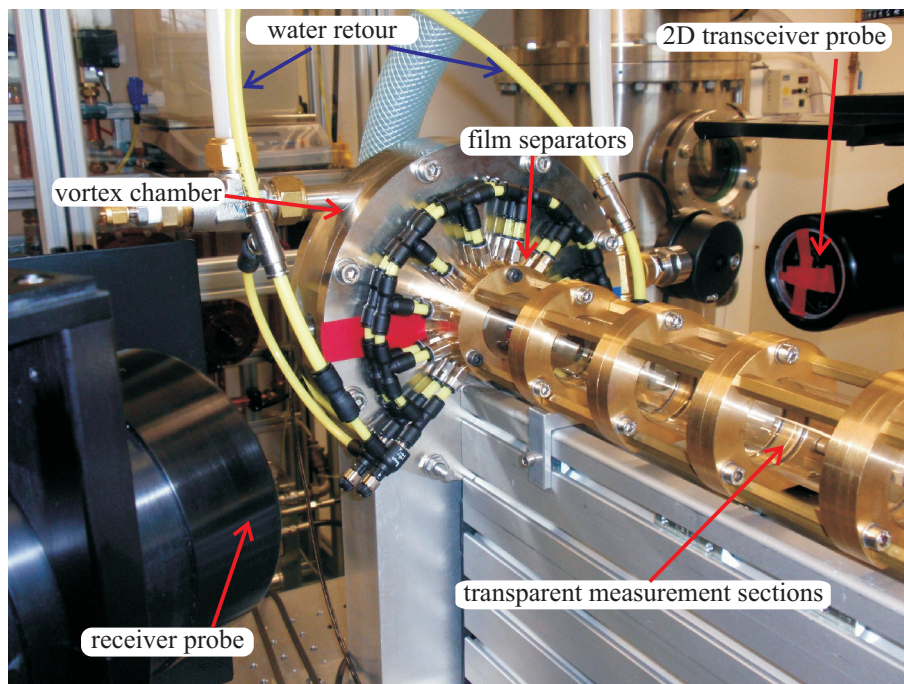


Figure 4.6: The RHVT with the film separators and transparent measurement sections. The 2D transceiver probe and receiver probe are also indicated.

## 4.2 Velocity statistics

PDPA provides samples of the instantaneous velocities of individual droplets. When the rate at which individual measurements are provided is related to the velocity magnitude, there will be a bias in the measured velocity distribution (Hoesel & Rodi, 1977; McLaughlin & Tiederman, 1973). Considering a homogeneous concentration of seeding particles, the amount of particles that cross the measurement volume of the LDA (PDPA) system is proportional to the velocity of the carrier medium. The consequence is that higher velocity magnitudes are measured more frequently than lower velocity magnitudes. Without correction, the mean velocity will therefore be biased towards a higher velocity.

Additionally, there is a bias if the sampling of individual velocities is related to the particle concentration (Barnett & Bentley, 1974; Hoesel & Rodi, 1977). In turbulent flow, heavy particles (with respect to the carrier medium) are preferably located in low-vorticity and high strain rate regions (Squires & Eaton, 1991) (known as preferential concentration), causing a bias in the measured velocity distribution.

To minimize uncertainties caused by the bias, the particle interarrival time was used as weighting factor. This method was described by Barnett & Bentley (1974) and Hoesel & Rodi (1977) and shows to give the most accurate results (Herrin & Dutton, 1993). The time averaged quantity (denoted with chevrons,  $\langle \rangle$ ) of a velocity component,  $\langle U \rangle$ , is

$$\langle U \rangle = \frac{\sum_{i=1}^N U_i \Delta t_i}{\sum_{i=1}^N \Delta t_i}, \quad (4.9)$$

where  $i$  is the index of the individual measurement,  $N$  is the total number of measurements, and  $\Delta t_i$  is the time between two individual measurements. Subscripts  $r, \theta$  and  $z$  denote the radial, swirl, and axial velocity component, respectively. The standard deviation, or rms ( $\sigma$ ), and shear stress ( $\tau$ ) are given by

$$\sigma = \sqrt{\frac{\sum_{i=1}^N u_i^2 \Delta t_i}{\sum_{i=1}^N \Delta t_i}}, \quad \text{and} \quad \tau = \frac{\sum_{i=1}^N u_i v_i \Delta t_i}{\sum_{i=1}^N \Delta t_i}, \quad (4.10)$$

where  $u_i = U_i - \langle U \rangle$  and  $v_i = V_i - \langle V \rangle$  ( $v$  is used here to indicate a second velocity component) are the velocity fluctuations for two components of a sample with respect to their mean. The relative uncertainty in the mean values due to the finite amount of samples (see, e.g. Durst *et al.* (1996)) is defined by  $\varepsilon_m = \sigma / \langle U \rangle \sqrt{N}$  and the uncertainty in rms is  $\varepsilon_\sigma = 1 / \sqrt{2N}$ .

## 4.3 Test case for LDA

The curvature of the windows used in the experiments, introduces additional uncertainties (§ 3.2.5). To verify measured LDA quantities (here, we are mainly interested in the velocity statistics), a classical pipe flow experiment was performed and its results were compared to results obtained from direct numerical simulation (DNS) of single-phase pipe flow (Walpot *et al.*, 2007). The setup used in this experiment is schematically represented in Fig. 4.7. Pressurized nitrogen gas was fed from a nitrogen tank (N<sub>2</sub>) to a droplet generator (DG, [TSI Six Jet Atomizer, model 9306A]). The gas/droplet mixture was injected in the pipe and passed

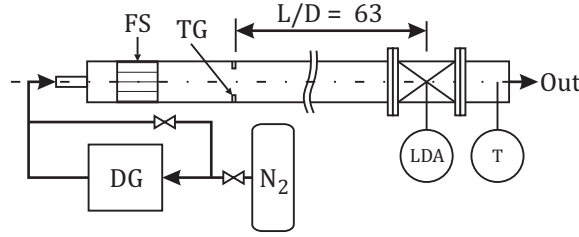


Figure 4.7: Schematic overview of the experimental setup for LDA applied in a turbulent pipe flow. FS: flow straightener, TG: turbulence generator, DG: droplet generator, N<sub>2</sub>: nitrogen supply, T: Temperature sensor, and LDA denotes the measurement location.

a flow straightener (FS) and a turbulence generator (TG) to enhance the development of the flow (Den Toonder & Nieuwstadt, 1997; Eggels *et al.*, 1994; Westerweel *et al.*, 1996). The measurements took place in a transparent pipe section that was mounted near the end of the pipe. The axial velocity at the center of the pipe was matched with that obtained from the DNS for a Reynolds number of  $Re = 10300$  (defined as  $Re = UD/\nu_f$  where  $U$  is the mean velocity,  $D$  the diameter of the tube, and  $\nu_f$  the kinematic viscosity of the gas at the measured temperature in the exit of the pipe).

With PDPA, we have determined the droplet size to be  $d_p = (2.5 \pm 1.5) \mu\text{m}$ , corresponding to a Stokes number of  $Stk < 0.2$ , based on the shear velocity obtained from the DNS. Droplets of this size reflect the behaviour of the gas and were considered as tracers.

Results from this experiment are shown in Figs. 4.8 and 4.9. The mean axial velocity as a function of the dimensionless radial coordinate,  $rR^{-1}$ , is shown in Fig. 4.8, where  $R$  is the radius of the pipe. The rms values of all three velocity components are shown in Fig. 4.9a. The results are normalized with the centerline velocity  $U_c$ . The maximum uncertainty in the mean, due to the finite amount of samples taken, was determined to be  $\varepsilon_m = 1\%$  and the uncertainty in standard deviation  $\varepsilon_\sigma = 2\%$ , both found near the wall. Error bars are not plotted due to their negligible sizes.

For turbulent pipe flow, the only nonzero cross-component in the stress tensor is  $\tau_{rz}$  (Walpot *et al.*, 2007), which is shown in Fig. 4.9b. The measured shear stress is somewhat lower than predicted by the DNS, which is an indication that the flow is not fully developed; the pipe was too short for statistically fully developed pipe flow at this Reynolds number. This is confirmed by the slightly higher measured mean velocity, Fig. 4.8.

The means, standard deviations, and shear stresses of the velocity components for turbulent pipe flow were measured with 3D LDA. The LDA results are comparable with those of the DNS, confirming that optical aberrations caused by the cylindrical window have only minor influence on the results. These results provided the confidence to carry out reliable experiments in the RHVT.

## 4.4 PDPA results

In this section, we present results that we have obtained from experiments in the RHVT. The mass flow of nitrogen was varied between  $\dot{m} = 8.7 \text{ g/s}$  to  $\dot{m} = 69.4 \text{ g/s}$ . The number of samples taken in the experiments varied from 20.000 to 100.000. The maximum standard uncertainty was determined to be less than 1% and is therefore omitted in the results. First,

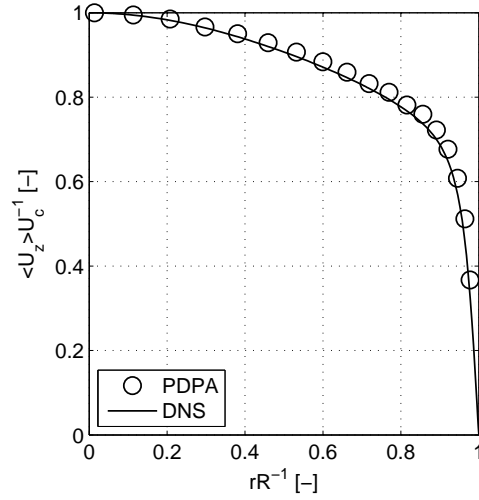


Figure 4.8: Mean axial velocity for  $Re = 10300$  compared to DNS (Walpot *et al.*, 2007). The symbols are the results from LDA and the solid lines are the DNS results. The mean axial velocity is normalized with the centerline velocity  $U_c$  and plotted as a function of the dimensionless radial coordinate.

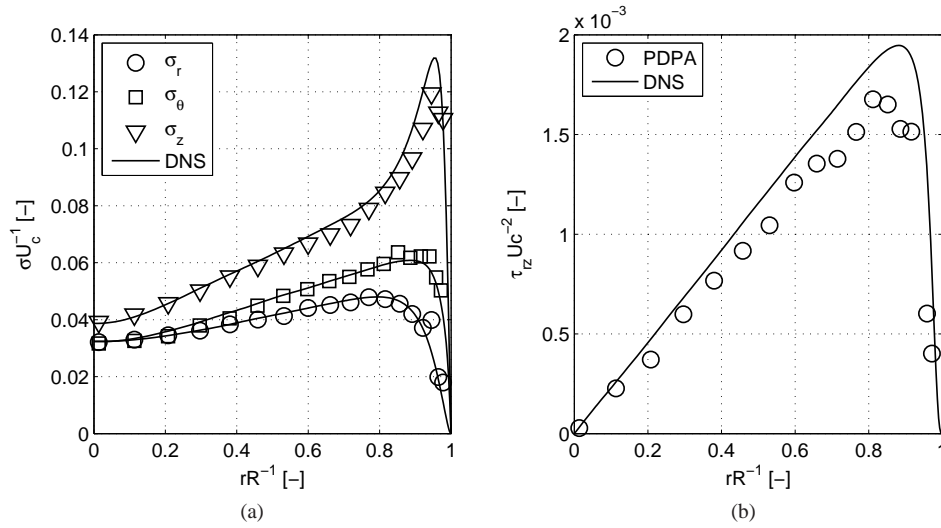


Figure 4.9: (a) Standard deviation of the velocity components and (b)  $\tau_{rz}$  for  $Re = 10300$  compared to DNS (Walpot *et al.*, 2007). The symbols are the results from LDA and the solid lines are the DNS results. The results are normalized with the centerline velocity  $U_c$  and plotted as a function of the dimensionless radial coordinate.



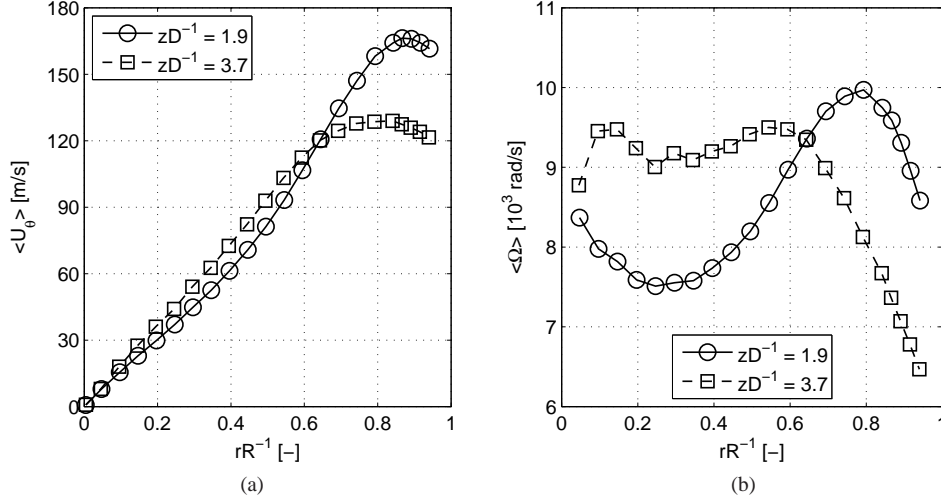


Figure 4.10: (a) Swirl velocity of droplets and (b) angular velocity as a function of the radial coordinate at two axial positions for  $\varepsilon = 0.35$  and  $\dot{m} = 34.7$  g/s.

we show results obtained with a cold fraction of  $\varepsilon = 0.35$ . Later, in § 4.4.3, we will compare these results to those for  $\varepsilon = 0$  and  $\varepsilon = 0.65$ . We have also performed measurements with different mass flows and show that the velocities are scalable. Most of the results shown in this section are obtained for a RHVT having a swirl generator type 1 (see § 3.1.1). However, in § 4.4.5, we compare laser Doppler results obtained with the two types of swirl generators.

A frequency analysis of the velocity will be presented in § 4.4.6 and reveals the motion of the vortex core around the axis, to be discussed in § 4.4.7. Due to this motion, droplets behave differently than predicted (§ 4.4.8). The radial and axial coordinates in the graphs shown in this section,  $r$  and  $z$  respectively, are made dimensionless with the tube radius and tube diameter,  $R$  and  $D = 2R$ , respectively.

#### 4.4.1 Mean velocity

Figure 4.10a shows the mean swirl velocity  $\langle U_\theta \rangle$  of droplets for a cold fraction of  $\varepsilon = 0.35$  measured at two axial positions ( $zD^{-1} = 1.9$  and  $zD^{-1} = 3.7$ ) in the main tube. The mass flow of nitrogen is  $\dot{m} = 34.7$  g/s. Due to viscous effects, the maximum swirl velocity decreases with increasing  $z$ , while in the core region, the vortex spins up. The spin-up is more clearly observed from the angular velocity, which is defined as  $\langle \Omega \rangle = \langle U_\theta \rangle / r$ , plotted in Fig. 4.10b. Due to the shear stresses, some of the angular momentum of gas in the peripheral region is transferred to gas in the core region. Therefore, at  $zD^{-1} = 3.7$ , the gas in the core has a higher angular velocity than at  $zD^{-1} = 1.9$ .

Fig. 4.11a shows the mean radial droplet velocity  $\langle U_r \rangle$  which is an order of magnitude smaller than  $\langle U_\theta \rangle$ . Because of the decrease in swirl velocity (thus the centrifugal force),  $\langle U_r \rangle$  decreases with  $z$ . The radial droplet velocity is positive for all radii, showing that, on average, the droplets move towards the wall. It is expected that the mean radial droplet velocity varies

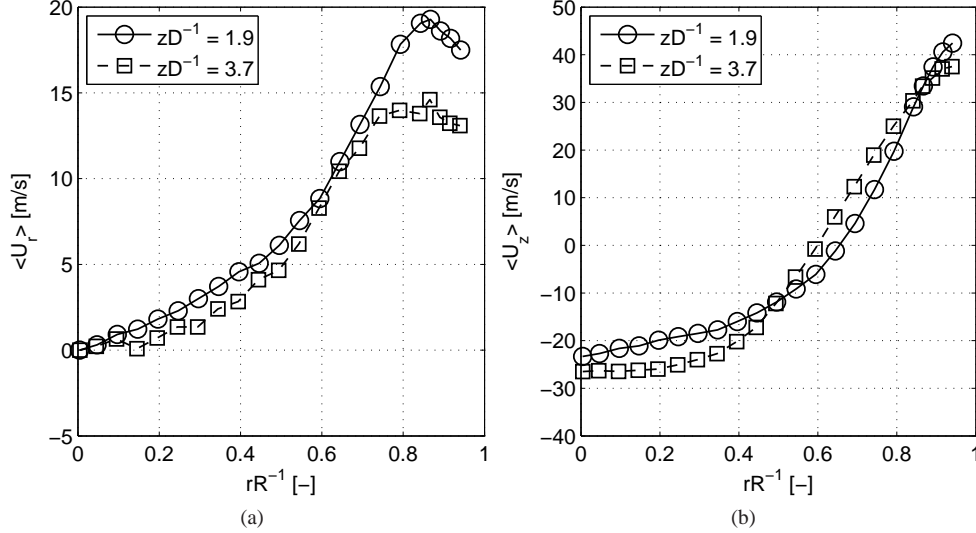


Figure 4.11: (a) Radial droplet velocity and (b) axial droplet velocity as a function of the radial coordinate at two axial positions for  $\varepsilon = 0.35$  and  $\dot{m} = 34.7$  g/s.

with the droplet size. The correlation will be provided in § 4.4.8.

Because of the small droplet size (this will be shown in § 4.4.8), the scattered light intensity was very low, which reduced the signal to noise ratio. This effect was mainly observed in the core region, at larger  $z$ , and resulted in a lower accuracy for  $\langle U_r \rangle$ .

The mean axial velocity  $\langle U_z \rangle$  is plotted in Fig. 4.11b. In the core region, the flow is directed towards the cold exit, and near the wall the axial velocity is directed towards the hot exit. This is an indication for the presence of a secondary circulation region in the RHVT, which is also observed by, among others, Ahlborn & Groves (1997) and Gao *et al.* (2005).

#### 4.4.2 Velocity fluctuations

Velocity fluctuations, especially those in radial direction, are the driving force of the energy separation process in the RHVT (Chapter 5). The magnitude of the velocity fluctuations is represented by the standard deviations (rms values) and the shear stresses of the velocity components.

The rms values of the three velocity components for  $\varepsilon = 0.35$  are shown in Fig. 4.12. The trend in the magnitude of the velocity fluctuations is similar for all velocity components in the region  $rR^{-1} < 0.5$ .

The corresponding shear stresses are shown in Fig. 4.13. The shear stress components  $\tau_{r\theta}$  and  $\tau_{rz}$  (Figs. 4.13a and 4.13b respectively) are the highest near the wall and are similar at the two axial positions. Surprisingly,  $\tau_{\theta z}$  at  $zD^{-1} = 3.7$  is larger than at  $zD^{-1} = 1.9$ , indicating that the flow is more unstable at larger axial positions.

Normalizing  $\sigma$  with the local absolute velocity magnitude (which is computed from the mean velocities shown in Figs. 4.10a, 4.11a, and 4.11b), we obtain the relative fluctuation intensity  $I \equiv \sigma/|U|$ , which is shown in Fig. 4.14. It shows very high values ( $> 30\%$ ) in the

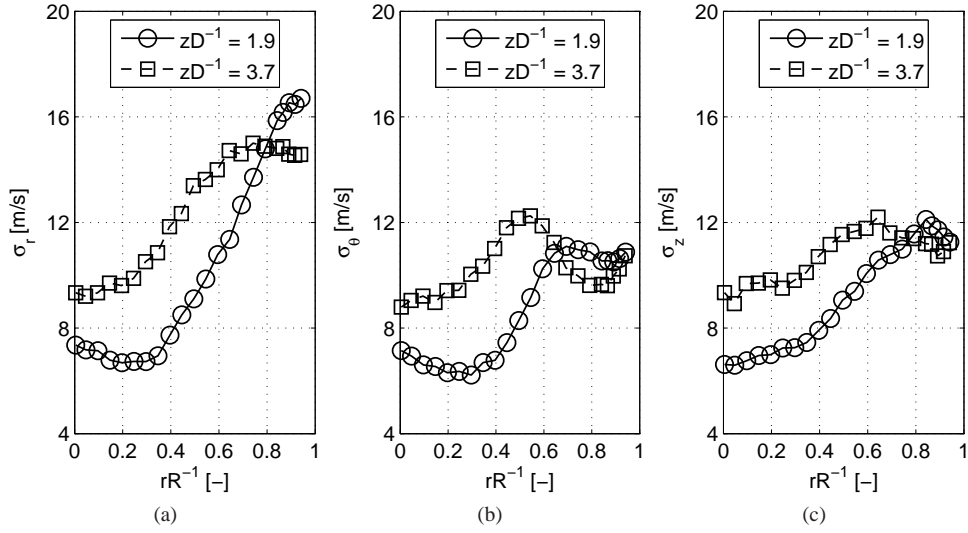


Figure 4.12: Standard deviation of the velocity fluctuations as a function of the radial coordinate for two axial positions for  $\varepsilon = 0.35$  and  $\dot{m} = 34.7$  g/s. (a) Radial component, (b) swirl component, and (c) axial component.

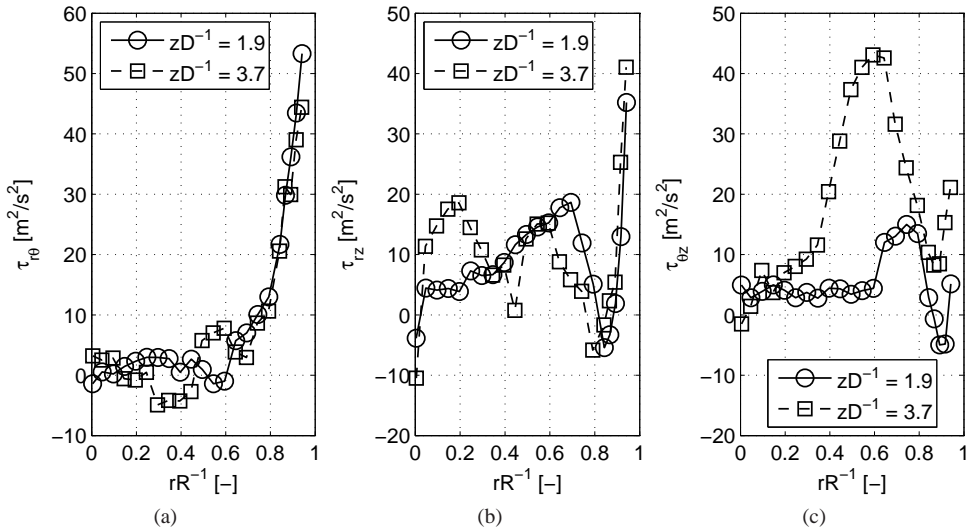


Figure 4.13: Shear stresses in the gas as a function of the radial coordinate for two axial positions for  $\varepsilon = 0.35$  and  $\dot{m} = 34.7$  g/s. (a)  $\tau_{r\theta}$ , (b)  $\tau_{rz}$ , and (c)  $\tau_{\theta z}$ .

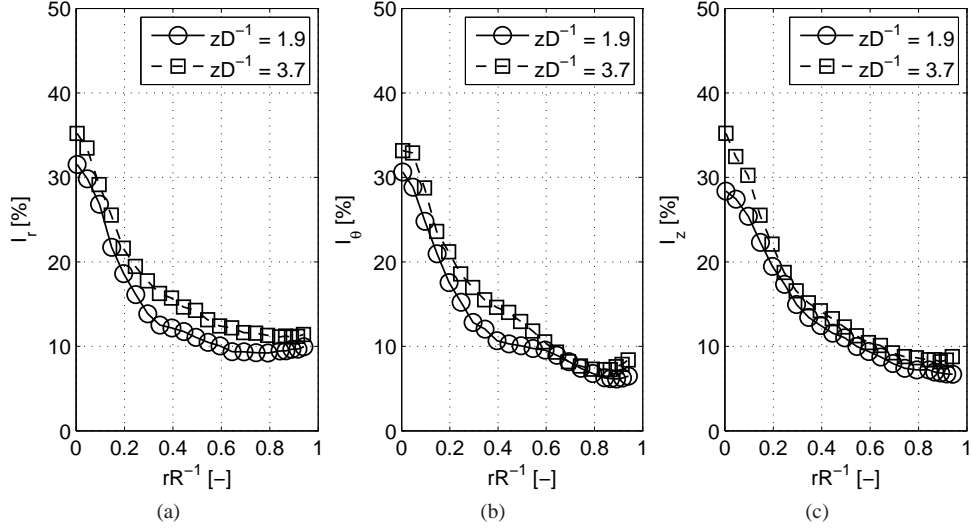


Figure 4.14: Relative fluctuation intensity as a function of the radial coordinate for two axial positions for  $\varepsilon = 0.35$  and  $\dot{m} = 34.7$  g/s. (a) Radial component, (b) swirl component, and (c) axial component.

core region for all velocity components.

#### 4.4.3 Influence of the cold fraction

Previously shown results were obtained for a cold fraction of  $\varepsilon = 0.35$ . Now, we will compare these results to the flow characteristics at  $\varepsilon = 0$  (measured at  $zD^{-1} = 1.3$ ) and  $\varepsilon = 0.65$  (measured at  $zD^{-1} = 1.9$ ).

When the cold fraction is set to zero, the flow in the RHVT is similar to in a uniflow (or parallel flow) vortex tube (see e.g. Yilmaz *et al.* (2009)). Measurements have been made possible by injecting small droplets, which were generated with the Six Jet Atomizer (as described in §4.3), directly into the vortex chamber through what used to be the cold exit (the flow rate of seeding was 5% of the total mass flow). In this way, it was possible to have good signal to noise ratio because the droplets are larger (the mean droplet size was approximately  $3 \mu\text{m}$ ) than when droplets are injected via the main inlet of the RHVT (see §4.4.8). The measurements for  $\varepsilon = 0.65$  were performed using the same operating conditions as those for  $\varepsilon = 0.35$ .

The mean swirl velocity and corresponding angular velocity are shown in Fig. 4.15. The most prominent feature, is that the mean swirl velocity and the angular velocity are much lower for  $\varepsilon = 0$  than for the other two cases, despite the fact that these measurements were performed closer to the vortex chamber. The reason for this is that the pressure in the core region of the vortex chamber decreases with  $\varepsilon$ . As will be shown in §5.3.2, the swirl Mach number is related to this pressure. The higher the pressure in the core, the lower the swirl Mach number and the swirl velocity. With increasing  $\varepsilon$ , the flow behaves more and more like a solid body rotation and the angular velocity increases (Fig. 4.15b). Because of the

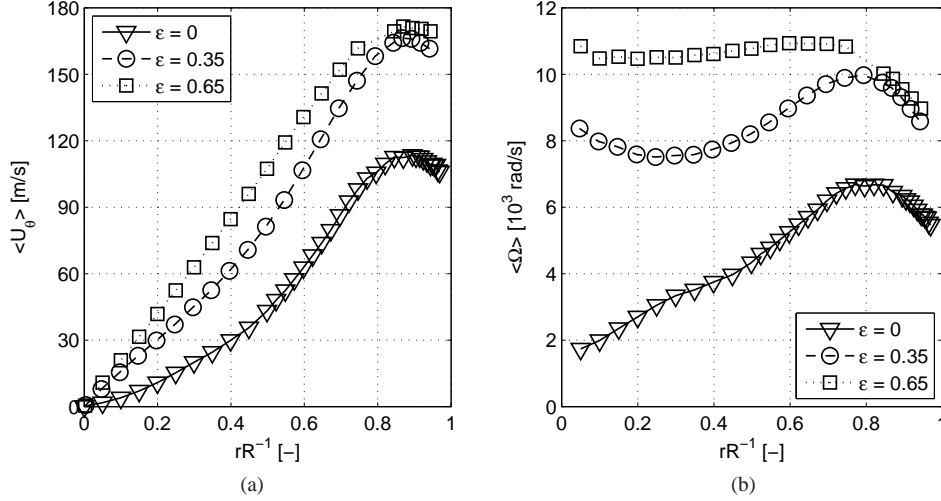


Figure 4.15: (a) Mean swirl velocity and (b) angular velocity as a function of the radial coordinate for 3 cold fractions at  $\dot{m} = 34.7$  g/s.  $zD^{-1} = 1.9$  for  $\varepsilon > 0$  and  $zD^{-1} = 1.3$  for  $\varepsilon = 0$ .

larger angular velocity, the radial droplet velocity increases with  $\varepsilon$ , as seen from Fig. 4.16a. Despite the low angular velocity for  $\varepsilon = 0$ , the radial droplet velocity is very similar to that of  $\varepsilon = 0.35$ .

A higher cold fraction means that more gas flows through the cold exit. Therefore, the axial velocity, shown in Fig. 4.16b, decreases in the core region with  $\varepsilon$ . For the case of  $\varepsilon = 0$ , interestingly, the axial velocity is positive at  $r = 0$ , just as in the periphery at  $r > 0.7R$ , but there is a small region ( $0.35 < rR^{-1} < 0.70$ ) where flow reversal is present and the axial velocity is negative. This indicates the existence of multiple re-circulations in that region.

The corresponding relative fluctuation intensities are shown in Fig. 4.17. For  $\varepsilon = 0$ , the maximum value of the fluctuation intensity is not located at the axis, but around  $rR^{-1} \approx 0.1$ , and is higher than for higher cold fractions. This might be a result of the flow reversal and re-circulation.

#### 4.4.4 Comparison between different mass flows

In this paragraph, we show results obtained with three different mass flows:  $\dot{m} = 8.7$  g/s,  $\dot{m} = 34.7$  g/s and  $\dot{m} = 69.4$  g/s. The cold fraction was kept constant at  $\varepsilon = 0.35$ , and the measurements took place at  $zD^{-1} = 1.9$ . During the experiment with the highest mass flow, the signal to noise ratio was so low, that measurements of the radial velocity component were impossible. The signal to noise ratio of the swirl and axial velocity components, however, was sufficient and the results are included.

The mean swirl velocity and angular velocity are plotted in Fig. 4.18. As to be expected, the swirl velocity (and thus the angular velocity) increases with increasing mass flow. The same is true for the radial velocity (Fig. 4.19a). The axial velocities, measured at different

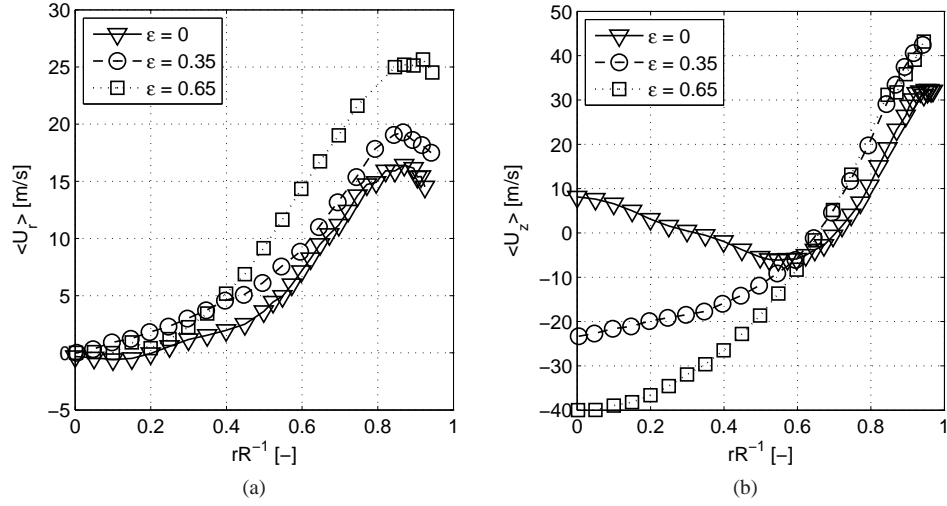


Figure 4.16: (a) Mean radial droplet velocity and (b) mean axial velocity as a function of the radial coordinate for two cold fractions at  $\dot{m} = 34.7$  g/s.  $zD^{-1} = 1.9$  for  $\epsilon > 0$  and  $zD^{-1} = 1.3$  for  $\epsilon = 0$ .

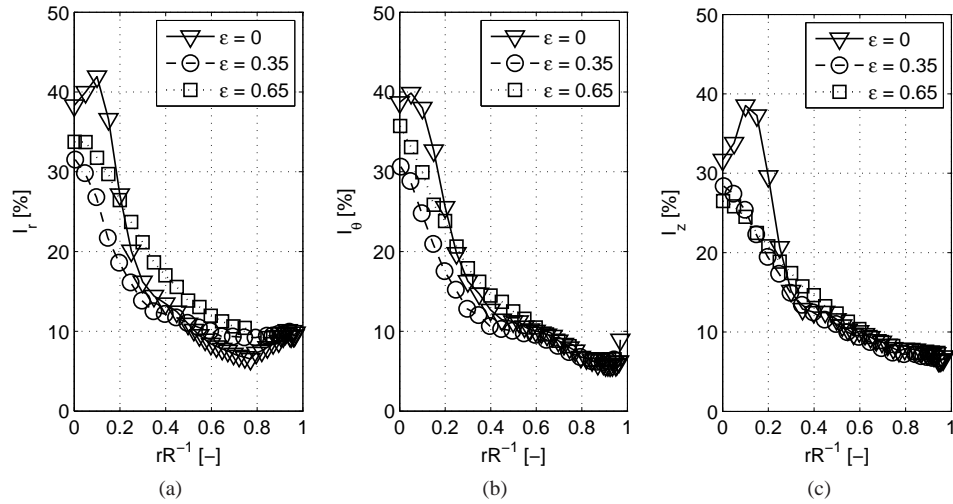


Figure 4.17: Relative fluctuation intensity as a function of the radial coordinate for two cold fractions at  $\dot{m} = 34.7$  g/s.  $zD^{-1} = 1.9$  for  $\epsilon > 0$  and  $zD^{-1} = 1.3$  for  $\epsilon = 0$ . (a) Radial component, (b) swirl component, and (c) axial component.

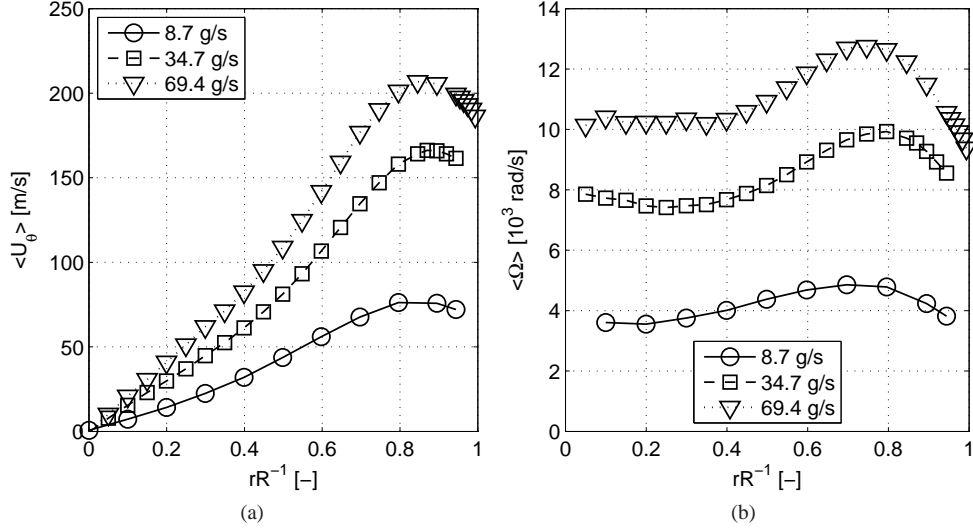


Figure 4.18: (a) Mean swirl velocity and (b) angular velocity as a function of the radial coordinate for different mass flows.  $zD^{-1} = 1.9$  and  $\varepsilon = 0.35$ .

mass flows, shown in Fig. 4.19b, are approximately equal at  $rR^{-1} \approx 0.7$ .

The measured swirl and axial velocities that show to have similar velocity profiles. This means that the velocities can be scaled. The obvious scaling factor would be the velocity that is proportional to the pressure difference over the RHVT  $\Delta p$  according to  $V \propto \sqrt{\Delta p / \rho}$ . The problem is, however, that the flow in the RHVT is compressible. The mass density is only known in the plenum and varies (significantly) through the device. We have found that a more suitable scaling factor is the square root of the mass flow  $\sqrt{\dot{m}}$ , which is also related to  $\Delta p$  and  $\rho$ .

In Fig. 4.20, the scaled velocities are shown. From these graphs, we observe that the scaled swirl and axial velocities almost collapse onto each other. The relative fluctuation intensities (not shown here), are already scaled by the velocity magnitude and are therefore not influenced by the mass flow.

#### 4.4.5 Influence of the type of swirl generator

Laser Doppler measurements have also been performed by using swirl generator type 2 (details are provided in §3.1.1). In this paragraph, the mean velocities of the type 1 and type 2 swirl generators are compared. The mass flow was  $\dot{m} = 34.7$  g/s, the cold fraction was  $\varepsilon = 0.35$ , and the measurements took place at  $zD^{-1} = 1.9$ .

The mean swirl velocity and angular velocity for two types of swirl generators are shown in Fig. 4.21. The swirl velocity for the type 2 nozzle is slightly lower than that of the type 1 nozzle. The radial and axial velocities (Fig. 4.22) are very similar for both the swirl generators as well. Apparently, the velocities are not really influenced by the type of swirl generators that are used. However, these results were obtained for a relative low mass flow, where the flow conditions were far below the limits of the nitrogen supply system. In principle (see

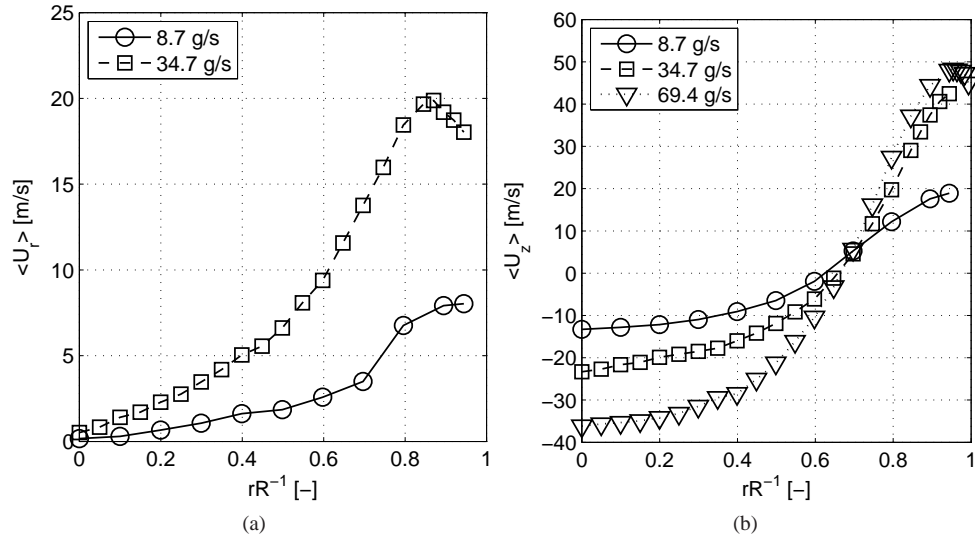


Figure 4.19: (a) Mean radial velocity and (b) axial velocity as a function of the radial coordinate for different mass flows.  $zD^{-1} = 1.9$  and  $\epsilon = 0.35$ .

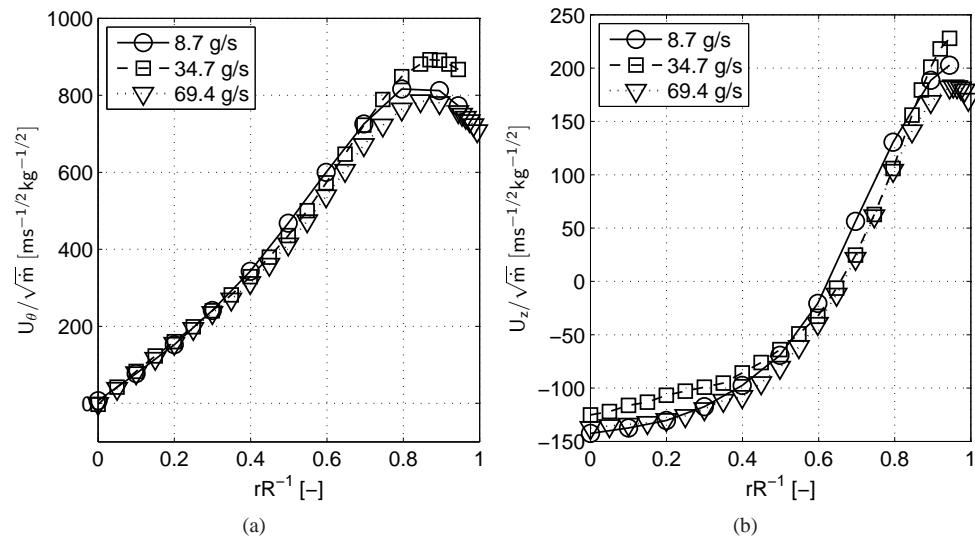


Figure 4.20: (a) Scaled mean swirl velocity and (b) scaled axial velocity as a function of the radial coordinate for different mass flows.  $zD^{-1} = 1.9$  and  $\epsilon = 0.35$ .



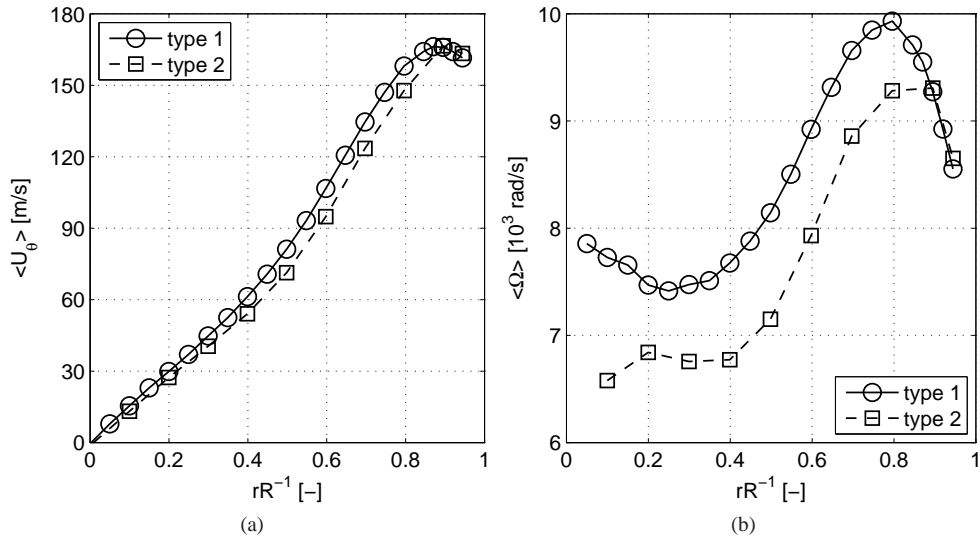


Figure 4.21: (a) Mean swirl velocity and (b) angular velocity as a function of the radial coordinate for different nozzles.  $zD^{-1} = 1.9$  and  $\varepsilon = 0.35$ .

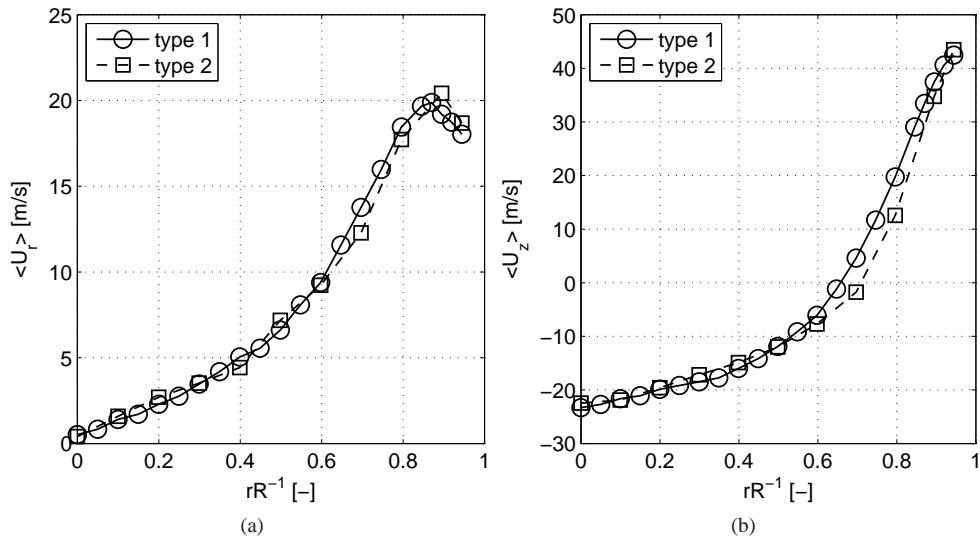


Figure 4.22: (a) Mean radial velocity and (b) axial velocity as a function of the radial coordinate for different nozzles.  $zD^{-1} = 1.9$  and  $\varepsilon = 0.35$ .

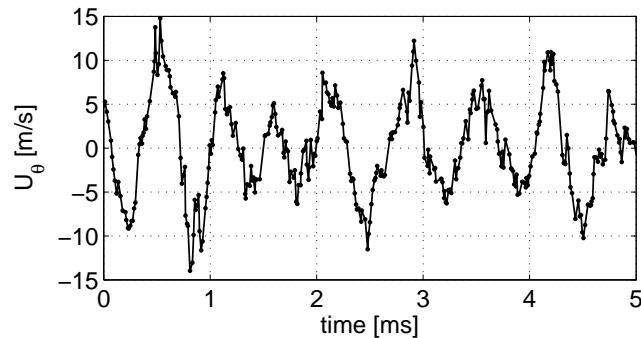


Figure 4.23: A sample of the swirl velocity as a function of time, measured at  $rR^{-1} = 0$  and  $zD^{-1} = 1.9$ .

§3.1.1), higher rotational velocities can be reached by using swirl generator type 2 when the plenum pressure and mass flow are high enough.

#### 4.4.6 Frequency analysis

To be able to explain the high relative fluctuation intensity in the core, the swirl velocity was measured at high data rates ( $\sim 70$  kHz, not to be confused with the frequency of the velocity fluctuations, described in §4.1). This allowed us to see the velocity behaviour in time. One of the results is shown in Fig. 4.23, where  $U_\theta$  at the axis is plotted as a function of time. It shows not only chaotic fluctuations, but also a high amplitude periodic behaviour. The frequency spectrum of this periodic behaviour contains additional information about the physics of the flow inside the RHVT.

The frequency spectrum was determined with a fast fourier transform (FFT) of the measured velocity in time. The velocities that are measured by PDPA are generally provided non-uniformly in time, because every single measurement is obtained from a droplet that passes through the measurement volume of PDPA. Therefore, the time interval between each individual measurement varies randomly. To be able to perform the FFT, the velocity data was first interpolated onto a discrete time vector (having a constant time interval between velocity samples).

The maximum frequency that can be determined with the FFT procedure is limited by the data rate. If the seeding concentration is homogeneous, and the signal quality constant, the data rate is a function of the velocity only. The absolute velocity magnitude increases with  $r$  (see § 4.4.1), so taking into account the above assumptions, the data rate ideally increases towards the tube wall. This means that the frequency range of the FFT analysis also increases with  $r$ . Therefore, the possibility exists that the measured amplitudes of high frequencies near the tube wall are higher than in the core region.

According to the above, the FFT results can be affected by the data rate. We have recorded the data rate during the experiments. The data rates as a function of  $r$  at several axial positions are shown in Fig. 4.24. The figure shows that the actual data rate remains approximately constant, what indicates that the seeding concentration decreases with  $r$ . From this, we may conclude that the results obtained with the FFT analysis are not influenced by the data rate, and that it is safe to neglect this effect.

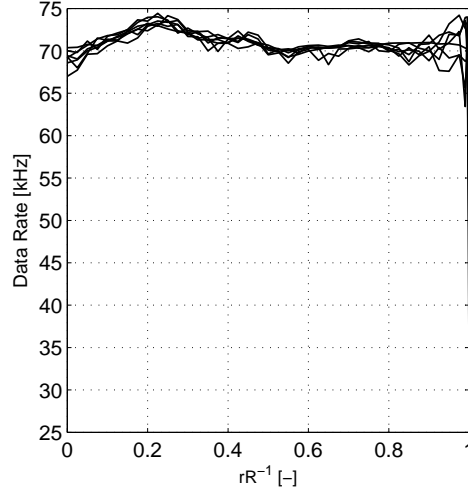


Figure 4.24: Data rate as a function of the radial coordinate, measured at several positions between  $1.825 \leq zD^{-1} \leq 5.425$ .

Results of the FFT are shown in Fig. 4.25 for four axial positions. The amplitudes are normalized with the maximum amplitude (for frequencies larger than 1000 Hz) found at the corresponding radial position. The graphs clearly show high amplitudes at distinct frequencies from which the first non-zero frequency is the fundamental frequency,  $f_0$ , which is present at all radii. As  $r$  increases, higher harmonics become visible. Remarkably, we were able to resolve up to seven harmonics. With increasing  $z$ , the amplitudes of the fundamental and higher order frequencies become more distinct.

The corresponding radially averaged frequency amplitudes are shown in Fig. 4.26, clearly showing the peaks at the fundamental frequency and its higher harmonics. The fundamental frequency was determined to be  $f_0 \approx 1250$  Hz and is approximately equal to the maximum angular frequency ( $\langle \Omega \rangle_{max} / 2\pi \approx 1260 \approx f_0$ ) of the main vortex. Kurosaka (1982) and Gao (2005) have found a similar agreement of the periodic behaviour and the angular velocity of the main vortex.

The frequency analysis was also applied to  $U_z$ , obtained from a different experiment. In this experiment, the data rate was approximately 30kHz, and the result is shown in Fig. 4.27. The figure shows that the fundamental frequency is also present in this velocity component. Because of the similarity in the three rms values of the velocity components (Fig. 4.12), we expect to find this as well in  $U_r$ . Unfortunately, it was impossible to have a sufficiently high data rate for  $U_r$  to proof this.

#### 4.4.7 Vortex wobbling

The existence of the high amplitude periodic behaviour can be explained by the following. The axis of the main vortex, i.e., the vortex filament, is typically not located exactly at the axis of the tube but is located off-axis. Due to the off-axis alignment and its confinement, the vortex filament precesses around the RHVT axis, indicated as vortex wobbling. This

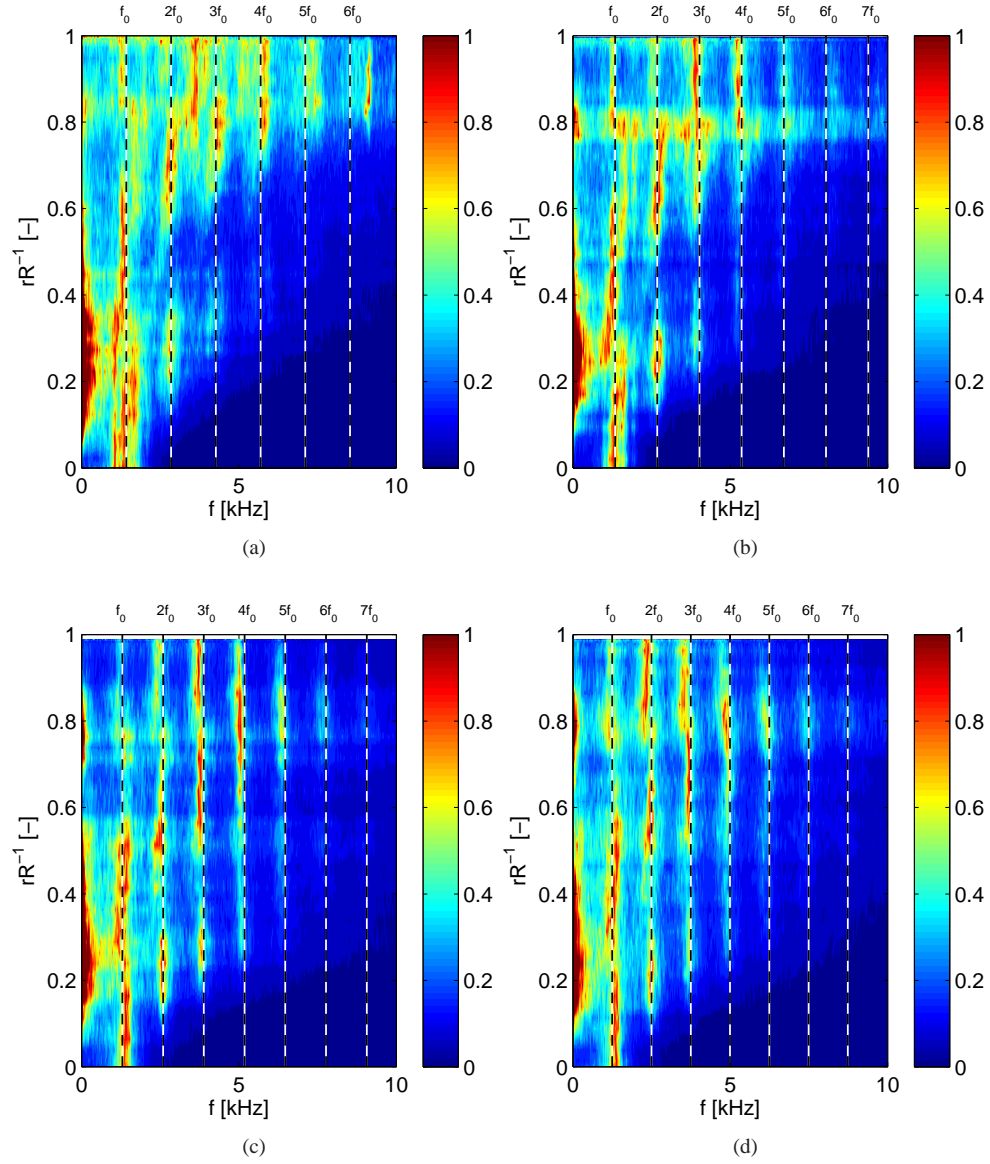


Figure 4.25: The normalized frequency amplitude of  $U_\theta$  as a function of the radial coordinate and the frequency for  $\varepsilon = 0.35$ . The dashed lines indicate the main and higher order frequencies. (a)  $zD^{-1} = 1.825$ , (b)  $zD^{-1} = 2.325$ , (c)  $zD^{-1} = 3.625$ , and (d)  $zD^{-1} = 4.125$ .

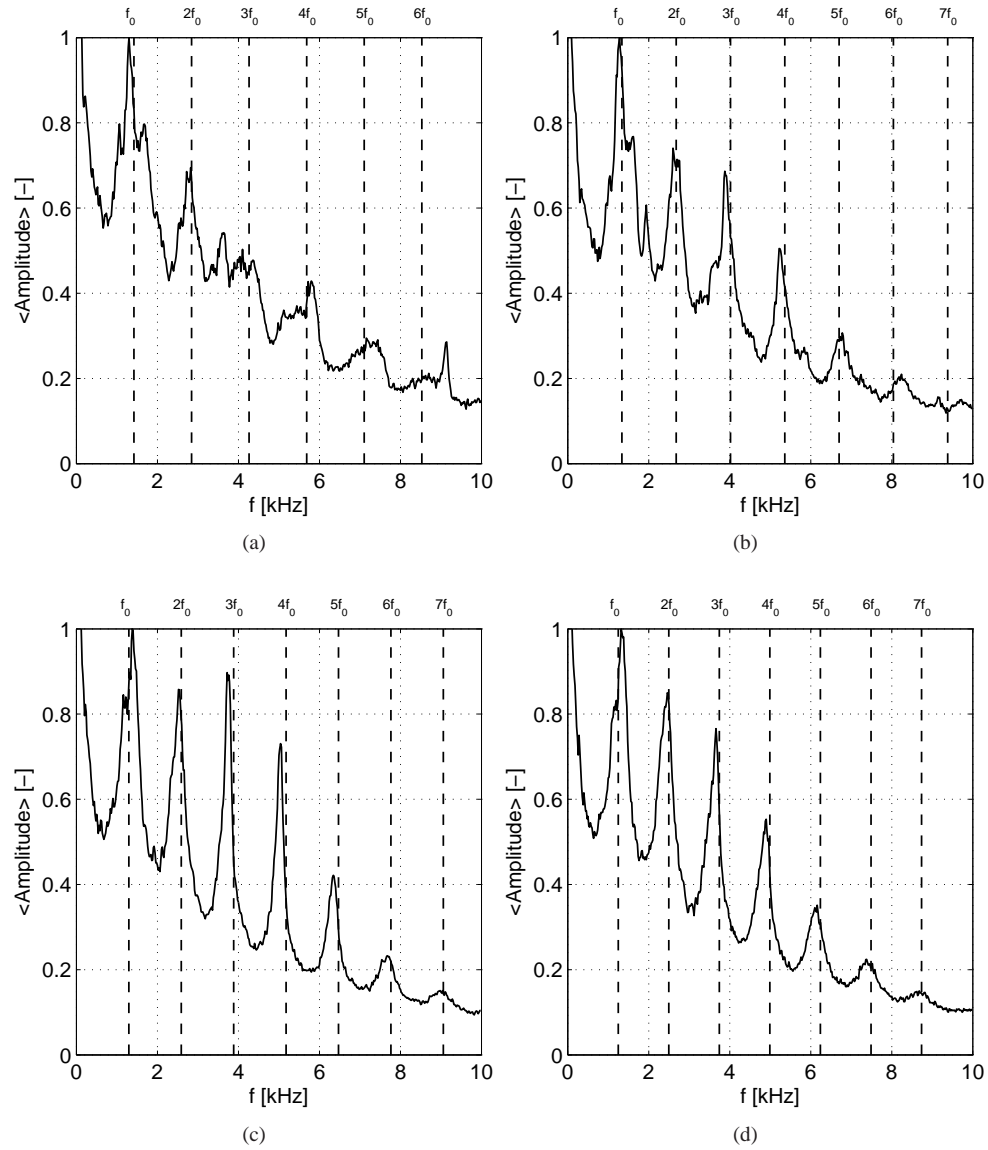


Figure 4.26: Radially averaged amplitude of  $U_\theta$  as a function of the frequency for  $\varepsilon = 0.35$  at several axial positions. The dashed lines indicate the main and higher order frequencies. (a)  $zD^{-1} = 1.825$ , (b)  $zD^{-1} = 2.325$ , (c)  $zD^{-1} = 3.625$ , and (d)  $zD^{-1} = 4.125$ .

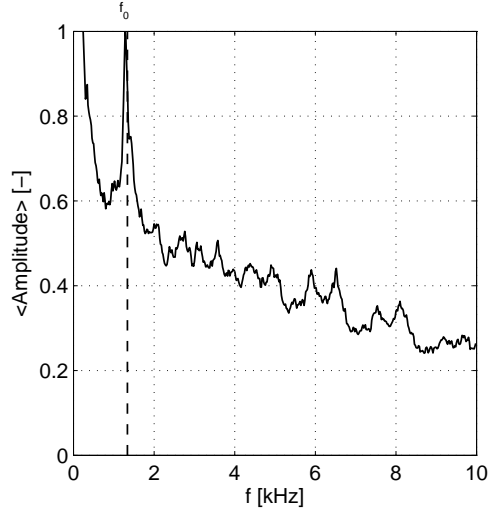


Figure 4.27: The normalized frequency amplitude of  $U_z$ , averaged in radial direction, measured at  $zD^{-1} = 1.825$ . The dashed line denotes the fundamental frequency.

motion of a vortex filament in a closed circular domain was already described by Lamb (1932, §155) and, more recently, by Fukumoto & Okulov (2005) and IJzermans *et al.* (2007). In the presence of a non-zero  $U_z$ , the vortex filament forms a helical curve, schematically represented in Fig. 4.28. Let point A be an instantaneous location of the vortex filament that has an angular velocity  $\Omega$ . Because of the location of point A in the cylinder, this point follows a circular pattern around the tube axis as time progresses (dashed lines). The angular velocity of this precession is  $\Omega_2 = \dot{\varphi}$ . If the radius of the circular pattern is much smaller than the tube radius, we can make the approximation  $\Omega_2 \approx \langle \Omega \rangle_{max}$ . This explains why  $f_0 \approx \langle \Omega \rangle_{max} / 2\pi$ .

The normalized amplitudes of the first four harmonics are plotted as a function of  $rR^{-1}$  and  $zD^{-1}$  in Fig. 4.29. The highest amplitude of  $f_0$  (Fig. 4.29a) is found in the core region and increases until  $zD^{-1} \approx 4$ . This indicates that the intensity of the wobbling is increasing in the first part of the main tube. For larger axial positions, the intensity of  $f_0$  in the core region decreases with  $z$ .  $f_0$  reappears at  $rR^{-1} \approx 0.5$ . The second until fourth harmonics,  $2f_0$ - $4f_0$ , are shown in Figs. 4.29b-4.29d. These frequencies are not found in the core region, but at  $rR^{-1} \approx 0.65$  and near the wall.

We have numerically computed the flow field in the RHVT with Fluent<sup>TM</sup> (compressible Reynolds Averaged Navier-Stokes (RANS) [ $k - \epsilon$  model], steady state, coupled pressure-based solver) to show the vortex wobbling. The computational domain for a vortex tube, which has a inner diameter of 40 mm and a length of 500 mm, contained 2.4 million nodes. The simulation was 3D to be able to capture non-axisymmetric behaviour, e.g., vortex wobbling. The results were obtained using the following boundary conditions: inlet mass flow 69.8 g/s; plenum pressure 4.70 bar; inlet temperature 295 K;  $\epsilon = 0.35$ . One of the results is shown in Fig. 4.30, which shows the absolute swirl velocity. Although it is a result from a steady state simulation, it clearly shows non-axisymmetric behaviour of the vortex.

As mentioned in §4.4.6, the intensity of the harmonics increase with  $z$ . A reason for this

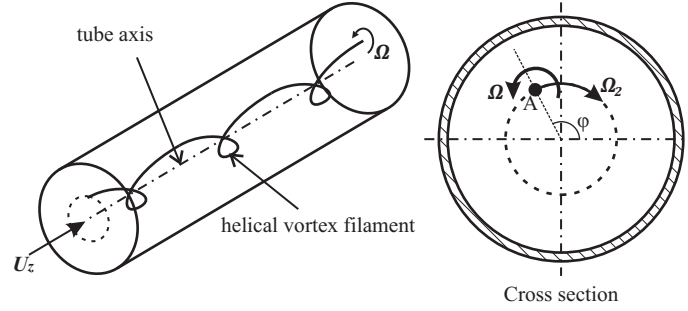


Figure 4.28: A confined vortex filament precessing around a tube axis. At a certain time, the center of the vortex filament is located in point A, which follows a circular pattern (dashed line) around the tube axis as time progresses.  $\Omega$  is the angular velocity of the vortex filament,  $\Omega_2 = \dot{\varphi}$  is the angular velocity of the precession around the axis, and  $\varphi$  is the angular position.

can be found from the RANS result. It is clear from Fig. 4.30 that the relative amplitude of the wobbling increases with  $z$ , what results in more clearly visible higher harmonics.

The quasi-periodic motion of a vortex in a cylindrical domain has also been observed in, among others, cyclone separators (Hoekstra *et al.*, 1999; O’Doherty *et al.*, 1999) and swirl combustors (Syred, 2006). It is known that the precessing vortex core has a strong impact on the level of measured velocity fluctuations and on the collection efficiency of cyclone separators (Derksen & Van Den Akker, 2000) while in swirl combustors, it enhances mixing and flame stability (Litvinov *et al.*, 2013). Derksen & Van Den Akker (2000) have performed numerical simulations of the turbulent flow in cyclone separators. They have shown that on average the vortex core spirals around the geometrical axis of the the cyclone body and that the amplitude of the precessing motion clearly depends on the axial coordinate, which is also observed from the measurements in the RHVT (Fig. 4.29). Hoekstra *et al.* (1998), as cited in Derksen & Van Den Akker (2000), have found that in cyclone separators, typically 80% of the kinetic energy of the fluctuations is contained in the precessing motion of the vortex core.

To see how large the contribution of velocity fluctuations that are caused by the vortex wobbling is to the rms values, the main and higher order frequencies were subtracted from the velocity signal. To do so, the velocity signal passed a high pass filter that had a cutoff frequency of 10 kHz. This filtered velocity was then subtracted from the initial signal. What remained, were the velocity fluctuations that were superimposed onto the wobbling motion of the vortex, i.e., the turbulence. The rms of this filtered signal,  $\tilde{\sigma}$ , was determined and compared to  $\sigma$  (the rms of the original velocity). The contribution of the wobbling to the velocity fluctuations,  $\psi$ , was found with

$$\psi = \left(1 - \frac{\tilde{\sigma}}{\sigma}\right) \times 100\%. \quad (4.11)$$

If  $\psi = 100\%$ , all the velocity fluctuations are due to the wobbling, and if  $\psi = 0\%$ , all the velocity fluctuations are due to turbulence.

In Fig. 4.31a, we show  $\sigma$  and  $\tilde{\sigma}$  as a function of the radial coordinate. The corresponding values for  $\psi_\theta$  are shown in Fig. 4.31b. This figure explains why the relative fluctuation intensity is so high at the axis, and decreases towards the wall: Approximately 75% of the measured fluctuation intensity at the axis and 20% near the wall is caused by the vortex

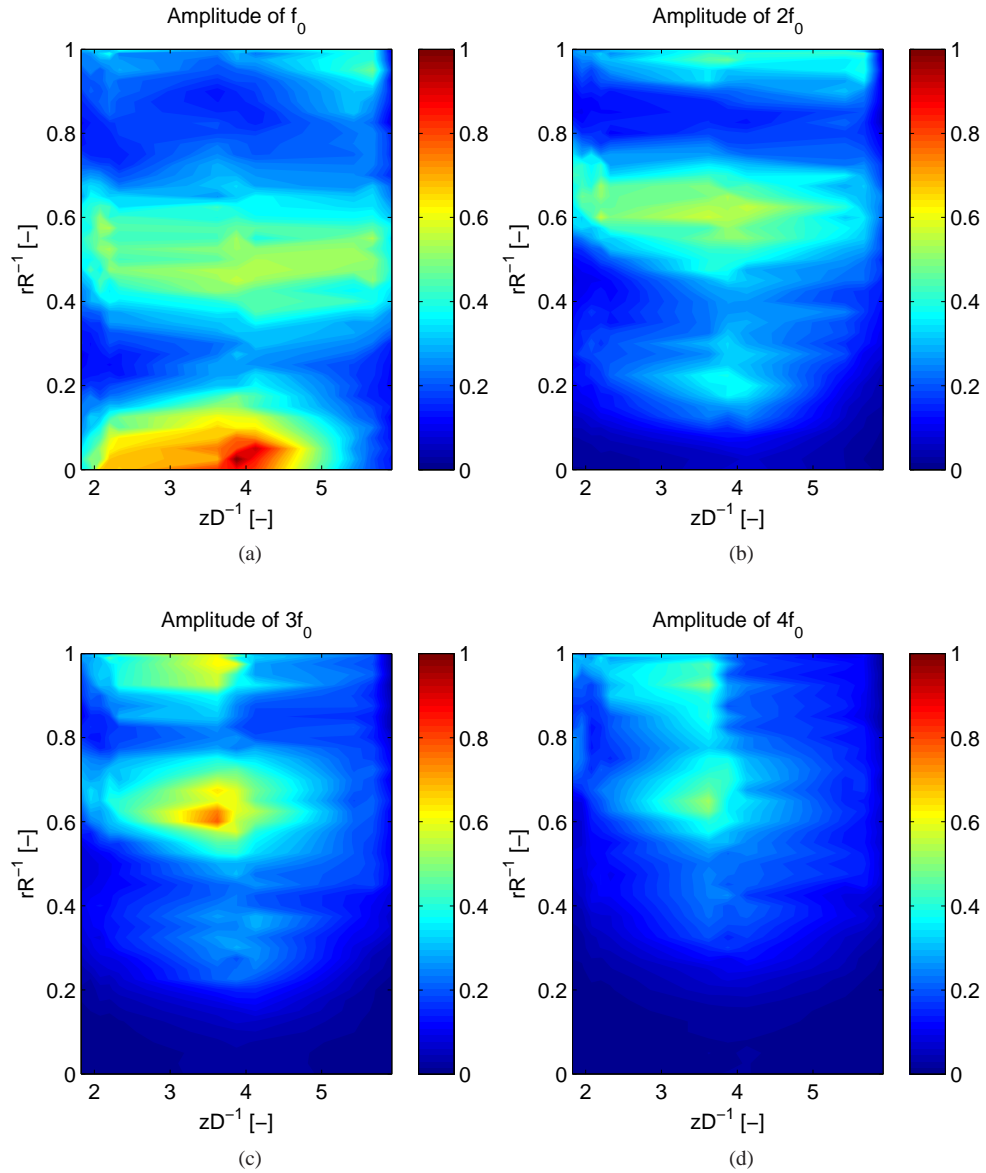


Figure 4.29: The normalized frequency amplitude for  $U_\theta$  as a function of the radial and axial coordinates. (a) Fundamental frequency  $f_0 \pm 40\text{Hz}$ ; (b) second harmonic  $2f_0 \pm 40\text{Hz}$ ; (c) third harmonic  $3f_0 \pm 40\text{Hz}$ ; (d) fourth harmonic  $4f_0 \pm 40\text{Hz}$ . The amplitudes are normalized with the maximum value found for  $f_0$ .



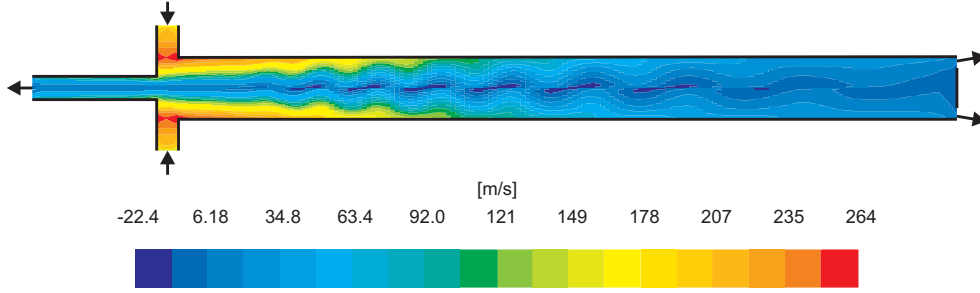


Figure 4.30: Contour plot of the absolute swirl velocity obtained from numerical simulation.

wobbling. This means that 56% at the axis and 4% near the wall of the kinetic energy of the fluctuations is contained in the vortex wobbling, which is somewhat less than the 80% at the axis observed by Hoekstra *et al.* (1998). The intensity of the actual turbulent (chaotic) velocity fluctuations, equal to  $I(1 - \psi)$ , is for all radii determined to be less than 10%.

#### 4.4.8 Droplet behaviour

Because of the positioning of the 1D probe (Fig. 3.14) the signal intensity of the third component is low compared to the other two components. The TSI FSA4000 processor discards bad quality signals, which are mostly from the smallest droplets. To prevent a size bias in the measured size distributions, the droplet size distributions were measured by using the 514.5 nm wavelength and the RV-probe (see Fig. 3.14), which gave the highest quality signals.

Two measured droplet size distributions are shown in Fig. 4.32. In this figure, we show normalized droplet size distributions (DSD) that are measured at two radial positions in the RHVT. Because the minimum droplet size that can be measured with PDPA is  $0.5 \mu\text{m}$ , there is no size data available for droplets smaller than  $0.5 \mu\text{m}$ . Fig. 4.32a shows the DSD that is measured at  $rR^{-1} = 0$ , and Fig. 4.32b shows the DSD near the wall at  $rR^{-1} = 0.95$ . The cumulative size distributions (CSD) are shown as the solid lines in the figures and show that 95% of the measured droplets are smaller than  $d_p < 2 \mu\text{m}$  at the axis and  $d_p < 3 \mu\text{m}$  near the wall.

The size distribution is weighted with the droplet volume in order to show how much water is contained by droplets in a certain size interval. The volume weighted droplet size distributions ( $\text{DSD}_v$ ) at the axis and near the wall are shown in Figs. 4.33a and 4.33b respectively. The corresponding cumulative volume distributions ( $\text{CSD}_v$ , solid lines in the figures) show that about 95% of the liquid water is contained by droplets that are smaller than  $4 \mu\text{m}$ .

There is not only a change in droplet size in radial direction, but also in axial direction. Figure 4.34 shows both the mean and volume mean diameter as a function of  $rR^{-1}$  for different values of  $zD^{-1}$ . The volume mean  $\langle d_p \rangle_v$  was computed according to

$$\langle d_p \rangle_v = \left( \frac{\sum_{i=1}^N d_p^3}{N} \right)^{1/3}, \quad (4.12)$$

where we have adopted  $N$  and  $i$  from § 4.2. The results show that the largest droplets can be found near the wall or close to the entrance and that the droplet size decreases with increasing  $z$ .

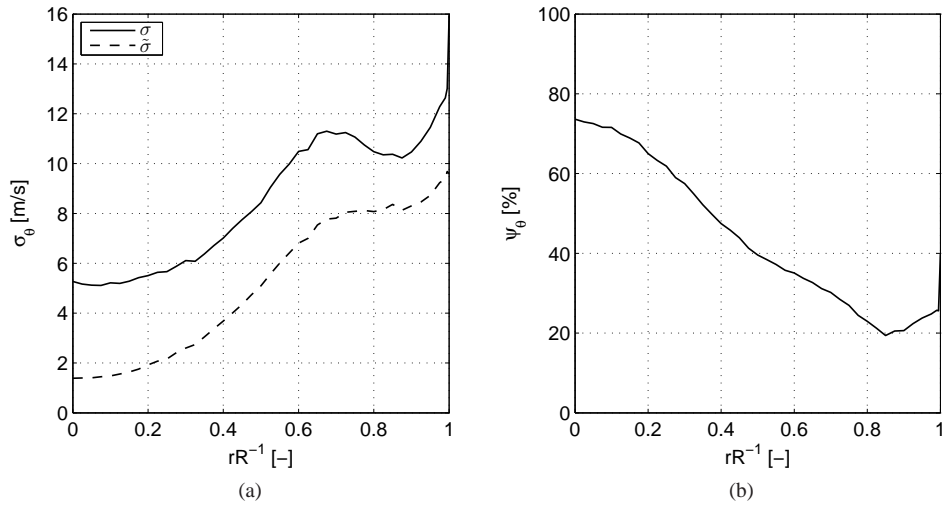


Figure 4.31: (a) The original ( $\sigma$ ) and filtered ( $\tilde{\sigma}$ ) standard deviations of  $U_\theta$ . (b) The contribution of the vortex wobbling in  $\sigma$  as a function of the radial coordinate, measured at  $zD^{-1} = 1.15$ .

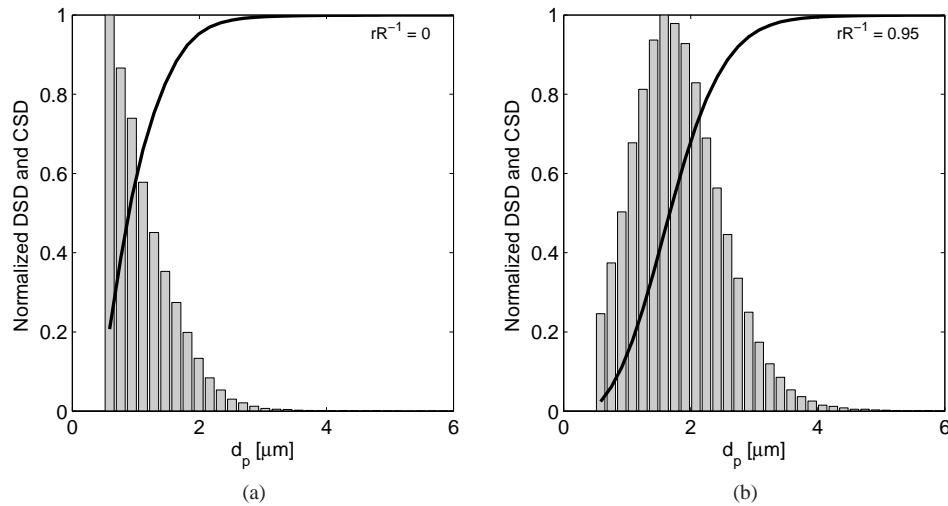


Figure 4.32: Normalized droplet size distributions (bars) and corresponding cumulative size distributions (solid line) at  $zD^{-1} = 2.325$ . (a)  $rR^{-1} = 0$  and (b)  $rR^{-1} = 0.95$ .

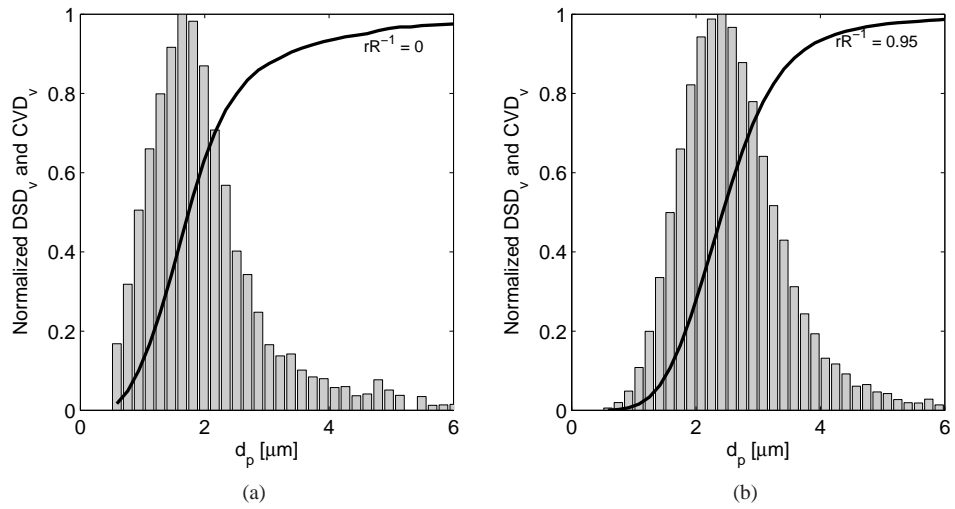


Figure 4.33: Normalized volume weighted droplet size distributions (bars) and corresponding cumulative size distributions (solid line) at  $zD^{-1} = 2.325$ . (a)  $rR^{-1} = 0$  and (b)  $rR^{-1} = 0.95$ .

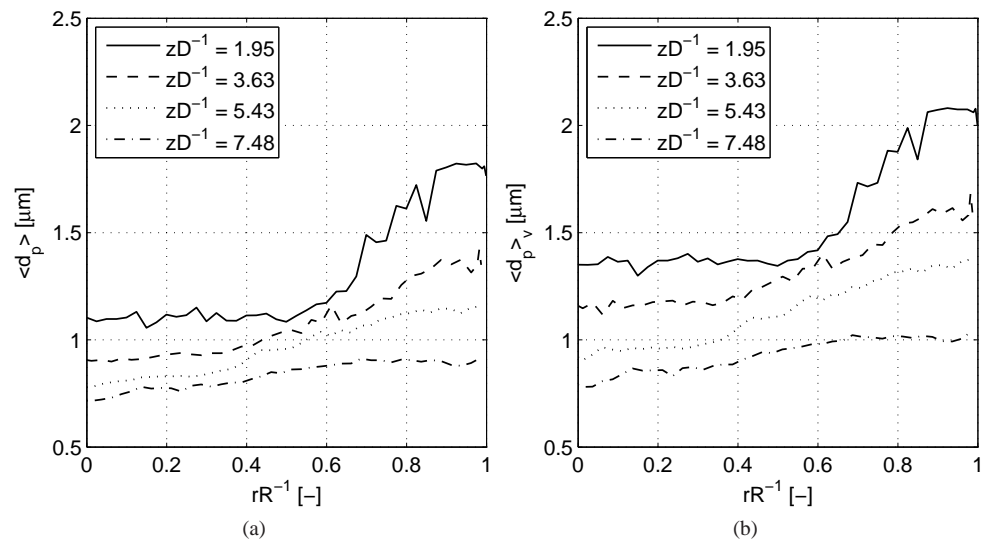


Figure 4.34: (a) Mean droplet diameter  $\langle d_p \rangle$  and (b) volume mean diameter  $\langle d_p \rangle_v$  as a function of  $rR^{-1}$  and  $zD^{-1}$ .

The radial velocity of the droplets is an important parameter for the design of the RHVT separator. This velocity can be used to predict the location in the RHVT at which the droplets hit the wall and form an - easy to separate - liquid film. If the swirl velocity of the fluid is known, the radial velocity of the droplets can be computed from a balance between the centrifugal force and the drag force (Bird *et al.*, 2007). For small droplets, the Stokes drag force can be applied

$$F_d = 3\pi\mu_f d_p (U - V), \quad (4.13)$$

where  $U$  and  $V$  are the droplet- and fluid velocity, respectively. The above equation is valid for a droplet Reynolds number  $\text{Re}_p = d_p |U - V| / \nu_f < 1$ . To be able to take into account the fact that the Reynolds number may exceed one, we use the correlation  $C = 1 + 0.15\text{Re}_p^{0.687}$ , which is valid for  $\text{Re}_p < 800$  and is the ratio of the actual drag force to the Stokes drag force (Schiller & Naumann, 1933). By equating the drag force to the centrifugal force  $F_c \approx \rho_p \frac{\pi}{6} d_p^3 \Omega^2 r$ , we find the terminal (radial) velocity of droplets with respect to the fluid, i.e., the radial drift velocity  $U_{drift} = U - V$ . Using the definition of the particle relaxation time  $\tau_p$  (§4.1) we obtain

$$U_{drift} = \Omega^2 r \frac{\tau_p}{C}. \quad (4.14)$$

Because  $\tau_p$  depends quadratically on the droplet size (§2.1), we would expect that the measured radial droplet velocity is higher for large droplets than for small droplets.

Fig. 4.35 shows the radial velocity for three droplet size intervals. The measured values are shown with symbols for  $0.5 < d_p < 0.55$ ,  $2 < d_p < 2.05$ , and  $d_p > 3 \mu\text{m}$ . For convenience, the theoretical predictions according to Eq. (4.14) for droplet sizes  $d_p = 0.5$ ,  $d_p = 2$ , and  $d_p = 3 \mu\text{m}$  are added. According to Eq. (4.14), the radial velocity for the larger droplets should be higher than that of the smaller droplets. The figure, however, shows that this is not the case. The smallest droplets have a significantly higher radial velocity than predicted by Eq. (4.14), while the larger droplets have a lower velocity. All droplet size intervals behave approximately the same as the  $d_p = 2 \mu\text{m}$  droplets.

Scatter plots of the instantaneous velocity fluctuations (defined in §4.2) as functions of the measured droplet size are shown in Fig. 4.36 for the three velocity components, at two radial coordinates. We have added bin averaged radial velocities to show the velocity-size dependence. The top graphs show the velocity fluctuations of droplets at the axis while the bottom graphs show the velocity fluctuations close to the wall. The bin averaged velocity shows that in both locations and for all velocity components, there is no noticeable correlation between droplet size and droplet velocity (only the swirl velocity seems to increase slightly with the droplet size).

That the droplet size and velocity are uncorrelated can be explained by taking a closer look into the behaviour of the vortex filament, as described in § 4.4.2. IJzermans *et al.* (2007) computed the velocity field and the motion of a vortex filament that was positioned off-axis in a cylindrical tube (Fig. 4.28). They have shown that there exists a non-zero radial velocity component due to the asymmetry of the vortex. The drag force, caused by this velocity component, reduces the effect of the centrifugal force on droplets, which is an undesired phenomenon for the efficiency at which droplets can be separated. Kuerten *et al.* (2007) and Van Esch & Kuerten (2008) have performed numerical simulations of centrifugal separation of particles in a rotating circular channel. Their results show that there is an asymmetric vortex and, consequently, a lower efficiency at which particles are collected at the channel wall.

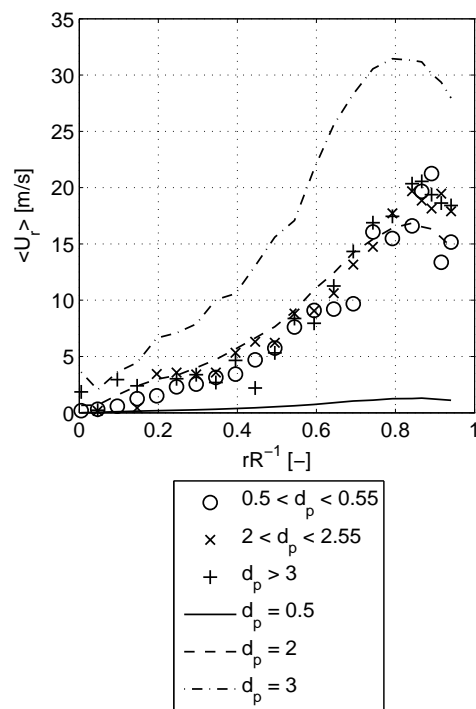


Figure 4.35: Radial velocity as function of the radial coordinate for droplet size intervals  $0.5 < d_p < 0.55$ ,  $2 < d_p < 2.05$ , and  $d_p > 3$   $\mu\text{m}$  compared to results of Eq. (4.14) for  $d_p = 0.5$ ,  $d_p = 2$ , and  $d_p = 3$   $\mu\text{m}$ . Symbols: experimental results; lines: Eq. (4.14) by using the measured  $\langle U_\theta \rangle$ .

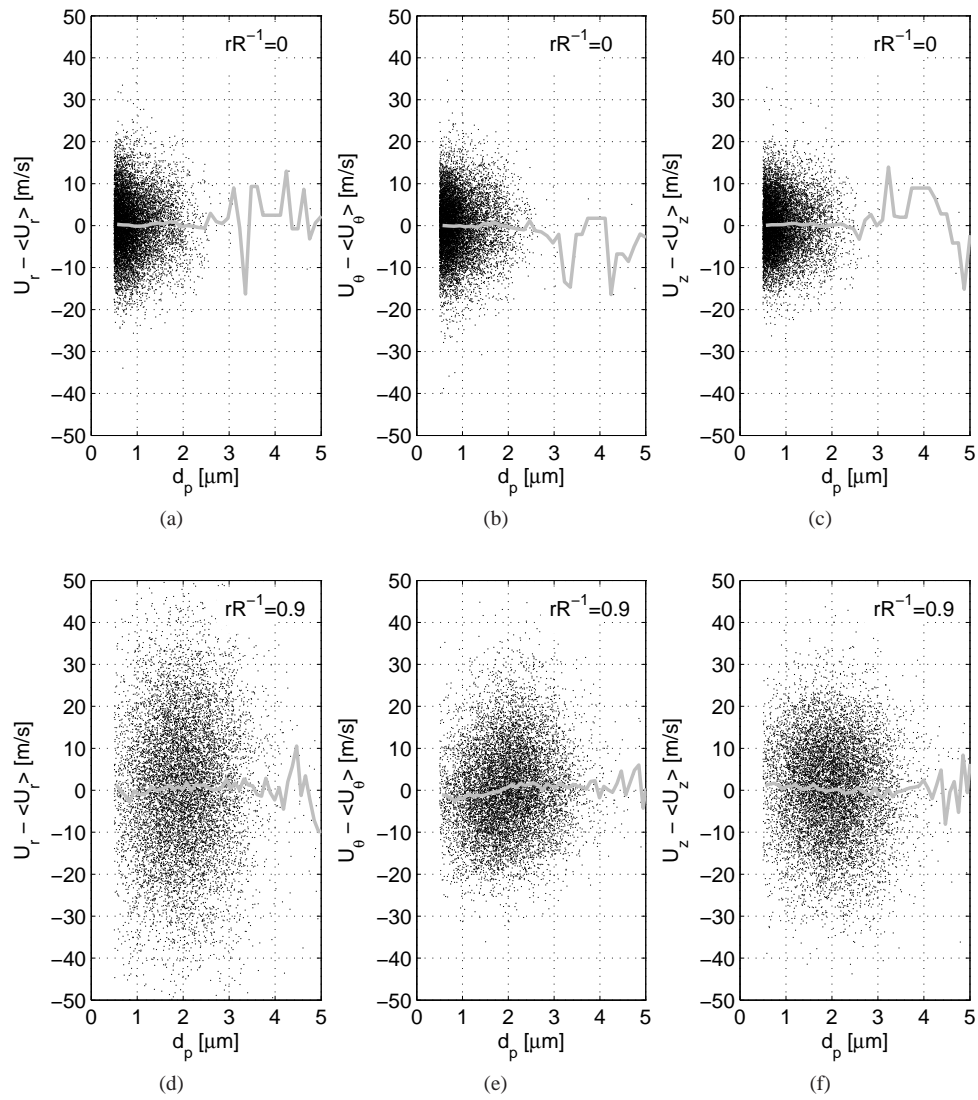


Figure 4.36: Instantaneous velocity fluctuations of droplets as a function of the droplet size at the axis (top) and near the wall (bottom). The solid lines are the bin average for a bin size of 0.05  $\mu\text{m}$ . (a, d) radial component, (b, e) swirl component, and (c, f) axial component.

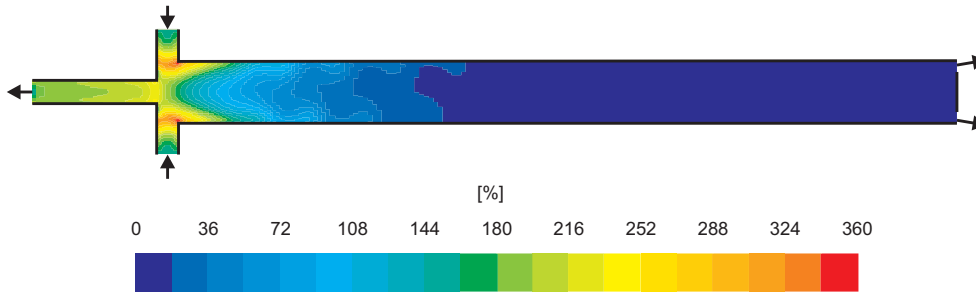


Figure 4.37: Contour plot of the relative humidity obtained from numerical simulation.

From the previous explanations, the following question is raised: Why do the size distributions change with  $r$ , as shown in Figs. 4.32 and 4.34, while the radial velocities are equal for all droplet sizes? A possible explanation for the change in size distributions is that the droplet size varies in the entrance region due to the way of injecting the droplets into the vortex chamber. In this region, there is no wobbling motion of the vortex and the centrifugal force is more important. Because the gas and the droplets are injected via the entrances of the RHVT, in combination with the centrifugal force, it is very plausible that larger droplets are found near the wall. In the peripheral region, the axial velocity is positive and the (relative large) droplets move towards the hot end. In the core region, the axial velocity is negative, and droplets, which are traveling back from the hot end towards the cold exit, have smaller sizes. These droplets are smaller because they partially evaporate during their travel. A measurement at one specific axial position shows, consequently, smaller droplets in the core and larger droplets near the wall.

On top of this, there is a second effect, which is caused by the pressure and temperature distribution inside the RHVT. Due to the centrifugal force, the pressure increases with  $r$  (Ahlborn *et al.*, 1994; Gao, 2005). As described in Chapter 2, the local humidity varies with the pressure and temperature. Assuming a constant mole fraction of water in the gas mixture, based on  $RH_{pl} = 0.99$ , (described in §2.2.1 and 6.1) and using the pressure and temperature obtained from the numerical simulation (see §4.4.7), we obtain an indication of the local relative humidity in the RHVT (without condensation or evaporation).

Fig. 4.37 shows the local relative humidity in the RHVT. In the region near the vortex chamber, the gas mixture is supersaturated ( $RH > 100\%$ ). In this region, droplets grow due to condensation. Here, the humidity increases with  $r$  due to an increasing pressure. Therefore, droplets that move with a positive  $U_r$  grow due to condensation, resulting in larger droplets near the wall than in the core region. Note that in the result shown in Fig. 4.37 evaporation and condensation are not taken into account.

On the other hand, the swirl velocity decreases and the temperature increases with  $z$ , resulting in lower humidities. Consequently, droplets evaporate at larger  $z$ . Both the droplet size increase with  $r$  and the decrease with  $z$  is clearly shown in Fig. 4.34. At  $zD^{-1} \approx 7.5$ , all droplets have evaporated. PDPA measurements were, therefore, not possible for larger  $z$ . This is a result that was already predicted by the simulation of droplet behaviour in Chapter 2. According to results from the simulation (e.g. Fig. 2.18), no droplets would be present for  $zD^{-1} > 7$ . This is now confirmed by the PDPA measurements.

## 4.5 Conclusions

Based on the Kolmogorov timescale in the RHVT, the Stokes number is  $\text{Stk} = \mathcal{O}(1)$  for  $\mathcal{O}(1)$   $\mu\text{m}$  droplets. Consequently, only the larger scale velocity fluctuations are resolved with the PDPA measurements. However, the maximum frequency that could be measured with the PDPA is approximately 10 kHz. It has been determined that at this frequency, the response amplitude of a  $d_p = 2$   $\mu\text{m}$  droplet is 76% and the corresponding Stokes number is  $\text{Stk} = 0.13$ . In the measurable frequency range, droplets of  $d_p \leq 2$   $\mu\text{m}$  can therefore be considered to be tracer particles.

The size of droplets that enter the RHVT is affected by the injection of the gas/droplet mixture through the swirl generator. Due to the inertia of the droplets, there is a difference in velocity between the droplets and the gas. If the Weber number, which is the ratio of kinetic energy and surface energy, exceeds  $\text{We}_{max} > 12$ , droplets break up. We have computed the maximum Weber number for various droplet sizes in the two types of swirl generators, assuming laminar flow. Two cases of plenum pressures and mass flows are used as operating conditions. Based on the results, droplets larger than  $d_p > 28$   $\mu\text{m}$  and  $d_p > 7$   $\mu\text{m}$  for the type 1 and type 2 nozzles, respectively, break up in the nozzle at a nitrogen mass flow of  $\dot{m} = 70$  g/s and a pressure of  $p_{pl} = 5.5$  bar. At a lower mass flow and pressure ( $\dot{m} = 35$  g/s,  $p_{pl} = 2.75$  bar), droplets break up if  $d_p > 50$   $\mu\text{m}$  and  $d_p > 11$   $\mu\text{m}$  for the type 1 and type 2 nozzles, respectively. Assuming that turbulence enhances droplet break up, and that droplets therefore break up if  $\text{We}_{max} > 1$ , the droplets that will enter the vortex chamber are generally not larger than  $d_p > 10$   $\mu\text{m}$ .

In a turbulent pipe flow experiment (Reynolds number of  $\text{Re} = 10300$ ), velocities have been measured as a test case for LDA. The measured velocities and turbulent fluctuations are in good agreement with DNS results, indicating that accurate measurements can be made by using the transparent measurement sections.

We have performed PDPA experiments in the entrance region of the vortex tube to give insight into the behaviour of water droplets in the device. The PDPA method provided detailed results, related to the three dimensional velocity field, its statistical properties, and droplet properties. Various flow configurations have been used during the experiments. The axial measurement position was varied to see how the flow changes with  $z$ . Results of different mass flows, cold fractions, and entrance nozzles were compared to each other to see their individual influences of the flow field. It has to be noted here that all velocities measured are that of the droplets.

The radial droplet velocity is affected by the swirl velocity. In general,  $U_r$  increases with increasing swirl velocity (angular velocity). It was expected that the radial velocity of droplets was influenced by the droplet size.

The results of the swirl velocity show that the type of vortex is similar as a solid body vortex at large cold fractions. The angular velocity in the core region increases with  $z$  and  $\varepsilon$ . For  $\varepsilon = 0.65$ , it seems that  $\Omega$  is constant with  $r$  for  $0 \leq rR^{-1} \leq 0.7$ . When  $\varepsilon = 0$ , the swirl velocity is (approximately) a quadratic function of the radial coordinate. The maximum value of the swirl velocity also increases with increasing cold fraction. This has to do with the pressure distribution in the vortex chamber. The pressure in the core decreases with increasing  $\varepsilon$ , resulting in higher rotational velocities (discussed in § 5.3.2).

The cold fraction also influences the axial velocity. For  $\varepsilon > 0$ , the axial velocity is negative in the core region and positive in the periphery. In the case that  $\varepsilon = 0$ , the axial velocity is positive at the axis.



Changing the mass flow, while maintaining  $\varepsilon$  and  $zD^{-1}$  constant, reveals that the shape of the velocity distributions remain the same. This implies that the velocities are scalable. We have found that a proper scaling factor is the square root of the mass flow.

The geometry of the swirl generator did not have noticeable influence on the measured droplet velocities. However, it is expected that significant differences are present when the mass flow is increased. Unfortunately, it was impossible to perform accurate PDPA at higher mass flows with the type 2 nozzle.

The standard deviations of the velocity fluctuations are similar to each other in the core region. The relative fluctuation intensity increases not only with  $z$ , but also with  $\varepsilon$  and is very high ( $> 30\%$ ) at the axis and decreases towards the wall. To explain the high intensity, we have analyzed the frequencies of the velocity signal. There is a high amplitude fundamental frequency that is strongly correlated to the angular velocity. This frequency has the highest amplitude at the axis of the RHVT. With increasing  $r$ , higher order (up to the seventh) frequencies were measured.

The fundamental frequency is not only found in the swirl velocity component, but also in the axial velocity component. Because of the similarity in the standard deviation of the velocity components, it is expected that the same fundamental frequency is present in the radial velocity component.

The strong correlation of the fundamental frequency to the angular velocity is due to the wobbling of the (helical) vortex around the tube axis. By subtracting the fundamental and higher order frequencies from the velocity signal, we have determined that 75% of the magnitude of the fluctuations at the axis, and 20% near the wall is caused by the wobbling of the vortex. According to this, the turbulence intensity is less than 10%.

The droplet sizes were determined with PDPA. Results show that the majority of the droplets is smaller than  $d_p = 2 \mu\text{m}$ . The largest droplets are found near the entrances and the tube wall of the RHVT, where the local humidity is the highest; smaller droplets are found at the axis, or at larger  $z$ . It was expected that larger droplets would have a higher radial velocity than smaller droplets due to the larger centrifugal force. The results show, unexpectedly, that there is no correlation between droplet size and  $U_r$ .

Due to the wobbling of the vortex axis, there is a non-zero radial velocity component. The drag force, resulting from this velocity, reduces the effect of the centrifugal force on the radial droplet velocity. Because of this, the droplet size has a minor influence on  $U_r$ .

The variation of droplet sizes inside the RHVT is mainly caused by the combination of two effects. First, the droplet size varies in the inlet region (vortex chamber) due to the centrifugal force and the axial velocity. Secondly, the humidity in the RHVT varies with the pressure and temperature and local condensation or evaporation causes the droplet size distributions to change.

As far as we have measured, there is no correlation between the droplet size and the radial droplet velocity. This is in disagreement with axisymmetric (and laminar) models of droplets in a rotating flow field and is caused by the wobbling of the vortex. The wobbling of the vortex can also be observed from numerical simulations, but only if the simulation is fully 3D, having no symmetry conditions. When the computational domain is axisymmetric, an axisymmetric flow is imposed, while in practice the flow is far from that. This results in simulated velocities, statistics, and temperatures that are not representing the flow in the RHVT (besides the difference in the quantities due to turbulence modeling).

A major disadvantage of vortex wobbling is that droplets are trapped in the vortex. During the experiments, we have observed that droplets are not reaching the main tube wall, but they

remain suspended in the gas. This makes it impossible to have a easy-to-remove liquid film. Therefore, it is expected that the vortex wobbling has a negative influence on the performance of the RHVT as a separator.

It remains unclear how large the contribution of the vortex wobbling is to the energy separation phenomenon. The main question is: is turbulence the cause for the existence of the temperature difference in the RHVT, or is it the vortex wobbling, or is it crucial to have a combination of both? This is a very interesting topic for future studies.

## 5 | Energy Separation in the RHVT

As already pointed out in the introductory chapter of this thesis, various attempts were made in literature to describe the energy separation process. In (Liew *et al.*, 2012), we have proposed a model that can be used to predict the energy separation in the RHVT with high accuracy. This chapter provides a detailed explanation of the model and its experimental validation.

First, we provide an overview of some of the existing theories that are available from literature. In §5.2, we continue with the theoretical background and the derivation of the energy separation model that we have developed. To compute the exit temperatures, it is required to know the maximum swirl Mach number. In §5.3, we show experimental results that were obtained with a cylindrical pitot tube and derive an equation that will be used to compute the maximum swirl Mach number as a function of the plenum pressure and the static pressure in the cold exit. In section 5.4, details of the experimental setup are provided and results from the model will be compared to experimental results. The conclusions are summarized in §5.5.

### 5.1 A selection of existing RHVT theories

Hilsch (1947) explained the energy separation by means of internal friction. For frictionless flow, the swirl velocity of the gas would increase to supersonic speed while it expands towards the axis, because of conservation of angular momentum. In the core region (close to the axis), however, viscous effects are more dominant and force the flow to establish a solid body rotation. By means of the viscous effects, kinetic energy is transported from the core region towards the peripheral region (which is close to the walls of the main tube), cooling the gas in the core region, while heating the gas present in the peripheral region. The smaller diameter of the cold exit only allows cold gas from the core region to leave, the remaining gas exits via the hot exit. Schultz-Grunow (1951) addressed theories of heat transfer in the atmosphere and explained that, because of the existence of a pressure gradient caused by the centrifugal force, there is a potential temperature difference between the core and peripheral region. When gas pockets move from the axis towards the wall and vice-versa, they transport energy from the core region towards the peripheral region, introducing the temperature difference between both regions. Van Deemter (1952) and Deissler & Perlmutter (1960) explained that turbulent eddies transport gas from the core region towards the peripheral region and vice-versa. The compression and expansion cycles of gas in these eddies, which are subjected to a radial pressure gradient, in combination with mechanical energy transfer are the cause for the energy transport. Linderstrøm-Lang (1971) computed the distribution of the

swirl velocity and the total temperature, assuming an incompressible gas, and showed that there is turbulent transport of both heat and kinetic energy. According to their results, transport of kinetic energy is more dominant in the peripheral region and transport of heat is more dominant in the core region. Kurosaka (1982) has measured frequency spectra of generated sound by the gas in the RHVT and found that the magnitude of the acoustic power is related to the difference in temperatures. He proposes that acoustic streaming is the main source for the energy separation. Ahlborn *et al.* (1994) also found that the radial pressure gradient inside the RHVT is important for the energy separation process. They have performed velocity measurements with a cylindrical pitot probe (Ahlborn & Groves, 1997) and measured secondary circulation (also found by, among others, Gao (2005), Aljuwayhel *et al.* (2005), and Shtern & Borissov (2010)). Later, Ahlborn *et al.* (1998) developed a semi-incompressible gas model that is based on a heat pump in the RHVT. Recently, a book was published (Shtern, 2012) in which the nature of the counterflow and secondary circulation in vortex tubes and other devices is explained. According to its author, the counterflow is a crucial feature in the RHVT.

Because of the complex flow in combination with an increasing computing power since the last decades, it became popular to study the flow field and the energy separation processes in the vortex tube by means of numerical simulations. Fröhlingsdorf & Unger (1999) published results that were computed using a 2D axisymmetric numerical simulation method. Their results indicate that there is a secondary circulation in the main tube. They concluded that energy separation is the result of mechanical energy transfer via friction in combination with cooling due to expansion of gas. Kazantseva *et al.* (2005) performed a 3D simulation and verified the existence of the secondary circulation. Their results show that multiple large scale vortices are present in the main tube, which were also observed by, among others, Farouk & Farouk (2007), Secchiaroli *et al.* (2009), and Xue *et al.* (2011). Numerous other numerical studies have focussed on simulation methods (Dutta *et al.*, 2010; Eiamsa-ard & Promvong, 2007, 2008a; Skye *et al.*, 2006), or were used as optimization tool (Behera *et al.*, 2005; Pourmahmoud *et al.*, 2012; Shamsoddini & Nezhad, 2010). Most numerical computations have shown to be able to capture the energy separation phenomenon, however, do not provide a full understanding of the energy separation processes inside the RHVT. More extensive reviews of the available literature are found in Eiamsa-ard & Promvong (2008b), Yilmaz *et al.* (2009), and Xue *et al.* (2010).

This survey of existing theories shows that there are strong correlations between most theories: energy transport caused by gas motions that are parallel to a pressure gradient and/or diffusion of kinetic energy through viscous effects. Although the theories give (possible) explanations of the processes inside the RHVT, none of the theories resulted so far in a model that quantitatively represents experimental results.

From the literature, we were able to develop a model that cover the most important energy transfer mechanisms in the RHVT. In contrast to models proposed in literature, it incorporates not only the pressures in the plenum and in the cold exit, but also the pressure in the hot exit. In this way, the model allows us to predict the energy separation based on the measured pressures.

## 5.2 Energy separation model

Pressurized gas is expanded through the nozzles in the swirl generator to create a high intensity vortex. The swirl velocity has the highest magnitude in the vortex chamber and decreases towards the hot exit due to viscous effects (Ahlborn *et al.*, 1998; Gao, 2005). The pressure in the periphery close to the hot exit is, therefore, lower than the pressure in the periphery near the inlet. Some of the gas moves towards the axis and flows back to the cold exit (Fröhlingsdorf & Unger, 1999).

While gas expands through the RHVT, no work and approximately no heat is extracted from it. According to the first law of thermodynamics, the total enthalpy is conserved, and by assuming that the specific heat capacity at constant pressure  $c_p$  is constant, the energy balance reduces to

$$T_{pl} = \varepsilon T_{t,c} + (1 - \varepsilon) T_{t,h}, \quad (5.1)$$

where  $T$  is the temperature. Subscripts  $pl$ ,  $h$ , and  $c$  represent plenum, hot stream, and cold stream conditions, respectively. Subscript  $t$  is used to indicate total (or stagnation) properties. The total temperatures in the exits can be computed with this formula as long as the ratio of both is known.

Based on available literature (e.g. Van Deemter (1952) and Deissler & Perlmutter (1960)), there are two main processes involved that are responsible for the existing total temperature difference between gas in the hot exit and gas in the cold exit.

### 5.2.1 Process I: Energy transfer

The first process is energy transfer due to fluid motion in a radial pressure gradient. The radial component of the steady state and inviscid momentum balance reads (by neglecting gravity)

$$V_r \frac{\partial V_r}{\partial r} + \frac{V_\theta}{r} \frac{\partial V_r}{\partial \theta} + V_z \frac{\partial V_r}{\partial z} - \frac{V_\theta^2}{r} = -\frac{1}{\rho_f} \frac{\partial p}{\partial r}, \quad (5.2)$$

where  $V$  is the velocity,  $r$ ,  $\theta$ , and  $z$  are the radial, tangential, and axial coordinates,  $p$  is the pressure,  $\rho_f$  is the mass density of the gas, and  $r$  is the radial coordinate. When gas rotates at an angular velocity  $\Omega(r) = V_\theta/r$ , and assuming that gravity and the radial and axial velocity components are negligible, the radial component of the equation of motion in cylindrical coordinates yields

$$\frac{dp}{dr} = \rho_f \Omega(r)^2 r, \quad (5.3)$$

In steady state and in absence of radial velocities, conduction causes the the static temperature in the vortex to be uniform. The flow in the RHVT, however, is known to be highly turbulent. On top of this, there are high intensity periodic motions of the vortex. All these features introduce velocity fluctuations and additional circulation in the main tube. Consequently, gas pockets move from the core region towards the peripheral region and back. The pressure in a gas pocket increases when it moves towards the wall, and when it moves back, the gas pocket expands and its pressure decreases. Because of the compression or expansion, the temperature of the gas pocket increases or decreases, respectively. Therefore, during the compression and expansion stages, there exists a temperature difference between the gas pocket and its surroundings (Schultz-Grunow, 1951; Van Deemter, 1952). Because of the temperature difference between the gas pocket and its surroundings, there is energy exchange between both (heat exchange by eddy conductivity). Therefore, each radial velocity

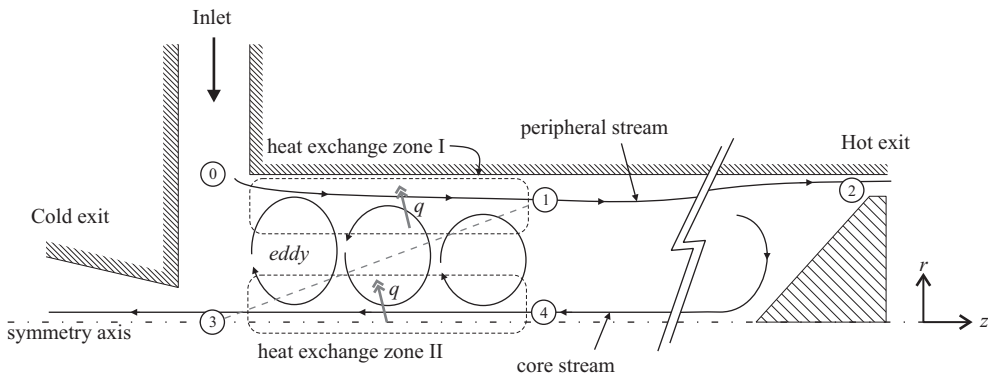


Figure 5.1: Schematic representation of turbulent eddies, flow in the core, and flow in the periphery. Heat is transferred from gas in the eddies towards the core stream or the peripheral stream in the heat exchange zones.

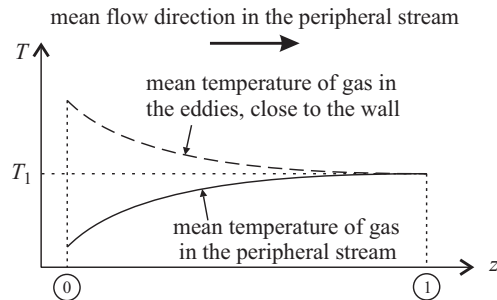


Figure 5.2: Schematic of the mean gas temperature in the peripheral stream and in the eddies, close to the wall (heat exchange zone I) as functions of the axial coordinate between points 0 and 1.

fluctuation causes transport of heat from the core region towards the peripheral region, and gas in the lower pressure region cools down, while gas in the high pressure region heats up (Deissler & Perlmutter, 1960; Van Deemter, 1952). This is similar to a heat pump, which is described by Ahlborn *et al.* (1998), however, instead of one large secondary circulation zone, each turbulent eddy acts as an individual heat pump.

The first process in the RHVT is illustrated in Fig. 5.1, in which turbulent eddies, a core stream, and a peripheral stream are schematically shown. In the turbulent eddies, gas pockets continuously move between a high pressure zone near the wall (heat exchange zone I), and a low pressure zone near the axis (heat exchange zone II). Close to the axis, the gas pockets have a low temperature due to expansion, and in the periphery their temperature is high due to compression.

Then one can distinguish gas that after injection remains in the periphery of the tube and exits the RHVT through the hot exit, referred to as the peripheral stream, flowing via points  $0 \rightarrow 1 \rightarrow 2$  (Fig. 5.1). The temperature of the gas in the peripheral stream and the temperature of the gas pockets in the eddies, which are in the heat exchange zone I, are shown in Fig. 5.2. In point 0, the temperature of the gas stream is lower than that of the gas pockets

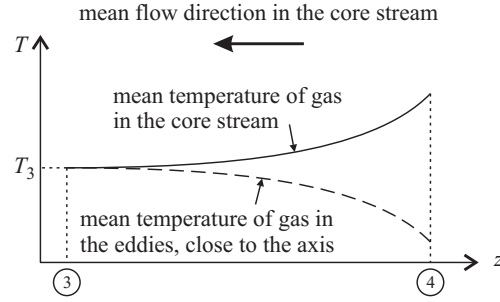


Figure 5.3: Schematic of the mean gas temperature in the core stream and in the eddies, close to the axis (heat exchange zone II) as functions of the axial coordinate between points 3 and 4.  $T_3$  is lower than  $T_1$  in Fig. 5.2

in the eddies, resulting in a positive flow of heat ( $q$  in the Fig. 5.1) from the gas in the eddies towards gas in the peripheral stream. Therefore, the temperature of the gas in the peripheral stream increases from point 0 to point 1.

Simultaneously, a fraction of the gas in the periphery close to the hot exit flows towards the centerline, forming a gas stream directed towards the cold exit. The pressure and temperature of this fraction of gas decreases while traveling to point 4. The temperature of the gas in this core stream and the temperature of the gas pockets in the eddies, which are in the heat exchange zone II, are shown in Fig. 5.3. In point 4, the core gas stream has a higher temperature than the gas pockets in the eddies. From  $4 \rightarrow 3$ , there is heat transfer from the gas stream towards the gas pockets in the eddies. Consequently, between points 4 and 3 the temperature of the gas in the core stream decreases.

During the heat exchange between the gas pockets in the eddies and gas in the peripheral or core streams in zone I and II, their difference in temperature diminishes (see Figs. 5.2 and 5.3). This means that in points 1 and 3 the gas in the peripheral or core streams, respectively, have the same temperature as gas pockets in the turbulent eddies. It is therefore not possible to exchange more heat between the gas in the eddies and gas in the core or peripheral streams (Van Deemter, 1952). In this case, the temperatures and pressures in points 1 and 3 are related via the adiabatic gas relation ( $T \sim p^{\gamma-1/\gamma}$ ), according to

$$\frac{T_1}{T_3} = \left( \frac{p_1}{p_3} \right)^{\frac{\gamma-1}{\gamma}}, \quad (5.4)$$

where subscripts refer to points 1 and 3 in Fig. 5.1 and  $\gamma \equiv c_p/c_v$  is the adiabatic exponent, which is the ratio of the specific heat capacities at constant pressure  $c_p$  and constant volume  $c_v$ .

It has to be noted, that the adiabatic law is not valid during transport from  $0 \rightarrow 1$  or  $0 \rightarrow 3$  due to the heat exchange, and that thermal diffusion, which transfers heat in opposite direction, is neglected because the time scale is much larger than the time scale at which heat is transported by the eddies (Van Deemter, 1952). Furthermore, only a minor part of the gas flows directly from point 1 to point 3. This has been observed from results of various numerical simulations (see, e.g., Aljuwayhel *et al.* (2005); Fröhlingdorf & Unger (1999), and Farouk & Farouk (2007)). Therefore, we assume that this can be neglected in the analysis.

To support Eq. (5.4) we have performed a numerical simulation in Fluent<sup>TM</sup> (3D domain,

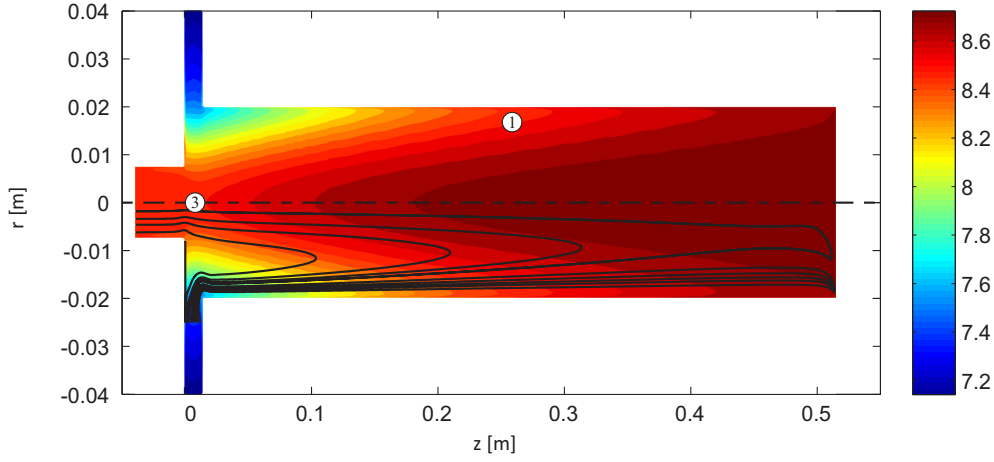


Figure 5.4: False colour plot of  $T/p^{\frac{\gamma-1}{\gamma}}$ , obtained from the RANS simulation. A projection of computed streamlines (solid black lines) are added in the lower half of the plot.

RANS steady state,  $k-\varepsilon$  turbulence model). The dimensions (including cold exit diameter; the number, width, and thickness of the entrance nozzles; the main tube and vortex chamber diameters) of the RHVT used in experiments *a*, *c*, and *d*, see § 5.4, were used in the simulation. The length of the main tube, however, was shorter compared to the experimental RHVT (0.5 m instead of 2.50 m). The computational mesh contained 1.9 million nodes and the compressible (density based) solver was used (Michalek, 2013). We are mainly interested to validate Eq. (5.4). From Fig. 5.4, we observe that, indeed, this quantity is approximately constant between points 1 and 3.

### 5.2.2 Process II: Decay of the vortex

The second process is present between points 1 and 2 and is related to the decay of the vortex. In the RHVT, the maximum swirl velocity depends on the axial coordinate  $z$  (decay of swirl). Close to the entrance region, the maximum swirl velocity is larger than close to the hot exit. Additionally, experimental results have shown (Gao, 2005, p. 113) that the radially averaged pressure is approximately independent of the axial position  $z$ . According to Eq. (5.3), where  $\Omega \equiv V_\theta/r$  and  $V_\theta$  is the swirl velocity, the pressure  $p_1$  at point 1 must therefore be higher than the pressure  $p_2$  in point 2. Between points 1 and 2 the velocity and pressure decrease simultaneously.

Between points 1 and 2, kinetic energy is converted into heat because of the deceleration of the vortex (Ahlborn *et al.*, 1998). If this process is adiabatic, the total enthalpy  $h_t$  of the gas is conserved, and the corresponding energy balance is

$$h_t = h + \frac{V^2}{2} = \text{Const.} \quad (5.5)$$

In compressible fluid dynamics, the Mach number is an important dimensionless velocity and is defined as the velocity  $V$  divided by the speed of sound  $c$

$$\text{Ma} \equiv \frac{V}{c}, \quad (5.6)$$



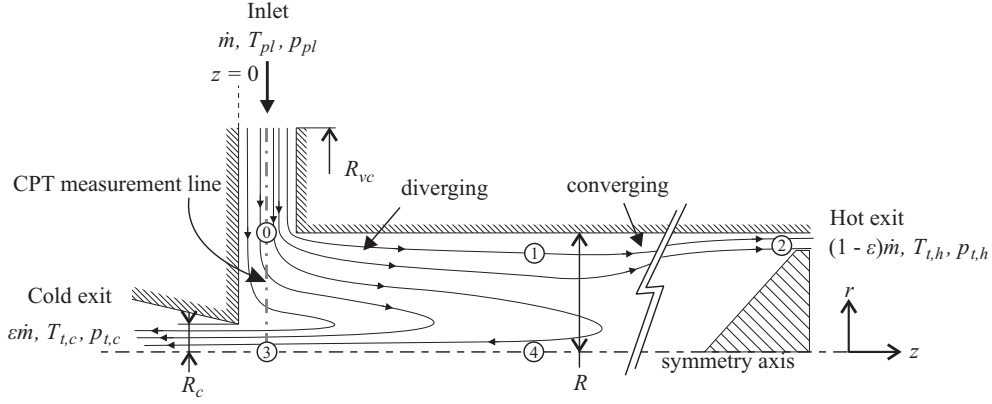


Figure 5.5: Projected streamlines of the time average axial and radial flow field in the RHVT. CPT measurements were performed along the grey dash-dotted line.

where the speed of sound in an ideal gas is  $c = \sqrt{\gamma \bar{\mathcal{R}} T}$  and  $\bar{\mathcal{R}}$  is the specific gas constant. With the enthalpy defined as  $h \equiv c_p T$ , where  $c_p$  can be written as  $c_p = \gamma \bar{\mathcal{R}} / (\gamma - 1)$ , we rewrite Eq. (5.5) to become

$$T_t = T \left( 1 + \frac{\gamma - 1}{2} \text{Ma}^2 \right) = \text{Const.} \quad (5.7)$$

We decompose  $\text{Ma}$  into a radial-, swirl-, and axial Mach number ( $\text{Ma}_r$ ,  $\text{Ma}_\theta$ , and  $\text{Ma}_z$ , respectively). The radial and axial Mach numbers are expected to be much smaller than  $\text{Ma}_\theta$  and are neglected. In points 0 and 1  $\text{Ma}_\theta$  has a significant value. To be able to say more about  $\text{Ma}_\theta$  in point 1, we have to focus on the streamlines in the RHVT. A projection of the streamlines of the time averaged axial and radial flow field are schematically shown in Fig. 5.5. As indicated in this figure, the streamlines are diverging in the peripheral region from  $0 \rightarrow 1$ . Although  $\text{Ma}_\theta$  close to the wall decreases with  $z$ , the kinetic energy of gas close to the wall is transferred to gas located at smaller radii (conservation of angular momentum). Because of this,  $\Omega$  close to the wall decreases with  $z$  while it increases at smaller radii. This spin-up was also observed from laser Doppler measurements (for the experimental details, see chapter 4). Fig. 5.6 shows the experimental values of the time averaged  $\Omega$  versus the radial coordinate at two axial positions in the main tube ( $zD^{-1} = 1.9$  and  $zD^{-1} = 3.7$ ). It shows that in the core region the angular velocity increases with  $z$  between the two axial positions. In the periphery in between points 0 and 1, the total kinetic energy remains approximately constant (neglecting friction at the wall), and the kinetic energy of the gas is not lost, but is ‘smoothed’ over a larger cross sectional area of the main tube. Therefore, we may use  $\text{Ma}_0 \equiv \text{Ma}_{\theta,0}$  as characteristic velocity that describes the kinetic energy of gas in the periphery between points 0 and 1. From points 1 to 2, the vortex decays due to viscous effects and its kinetic energy is converted into heat. This process is assumed to be adiabatic and according to Eq. (5.7), the resulting temperature ratio between points 1 and 2 becomes

$$\frac{T_2}{T_1} = 1 + \frac{\gamma - 1}{2} \text{Ma}_0^2. \quad (5.8)$$

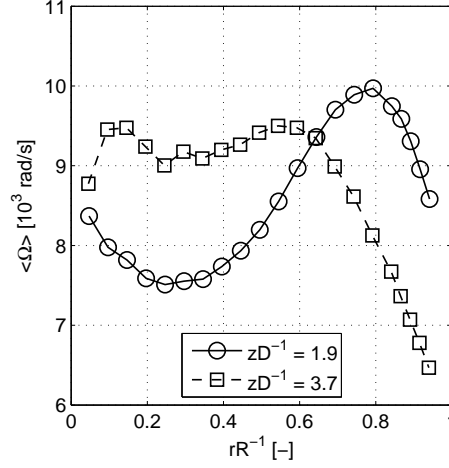


Figure 5.6: The time average angular velocity as a function of the radial coordinate at two axial positions.

### 5.2.3 The overall process

We combine the two described processes to compute the ratio between the static temperatures in points 2 and 3. For the first process, described by Eq. (5.4), the static pressure in point 1 is required. This pressure, however, is unknown a priori. The static pressures at the wall and at the axis, obtained from the RANS simulation, are plotted in Fig. 5.7. This graph clearly indicates that the pressure in point 2 is nearly the same as that in point 1, especially with respect to the difference between  $p_1$  and  $p_3$ . Therefore, we may assume that  $p_1 \approx p_2$ . The temperature ratio  $T_1/T_3$ , as provided in Eq. (5.4), is therefore approximated by

$$\frac{T_1}{T_3} = \left( \frac{p_1}{p_3} \right)^{\frac{\gamma-1}{\gamma}} \approx \left( \frac{p_2}{p_3} \right)^{\frac{\gamma-1}{\gamma}}. \quad (5.9)$$

Multiplying Eqs. (5.8) and (5.9) results in

$$\frac{T_2}{T_3} = \frac{T_1}{T_3} \frac{T_2}{T_1} = \left( \frac{p_2}{p_3} \right)^{\frac{\gamma-1}{\gamma}} \left( 1 + \frac{\gamma-1}{2} \text{Ma}_0^2 \right), \quad (5.10)$$

which is the ratio of static temperatures in the exits of the RHVT. The ratio of total temperatures is found by using

$$\frac{T_{t,h}}{T_2} = \left( \frac{p_{h,t}}{p_2} \right)^{\frac{\gamma-1}{\gamma}}; \quad (5.11a)$$

$$\frac{T_3}{T_{t,c}} = \left( \frac{p_3}{p_{c,t}} \right)^{\frac{\gamma-1}{\gamma}}, \quad (5.11b)$$

assuming isentropic flow in the hot and cold exits. Multiplying Eq. (5.10), (5.11a), and (5.11b) results in the ratio of total temperatures in the exits of the RHVT

$$\frac{T_{t,h}}{T_{t,c}} = \left( \frac{p_{t,h}}{p_{t,c}} \right)^{\frac{\gamma-1}{\gamma}} \left( 1 + \frac{\gamma-1}{2} \text{Ma}_0^2 \right), \quad (5.12)$$

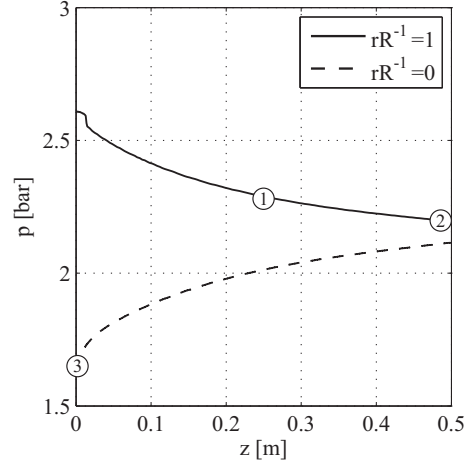


Figure 5.7: The static pressure at the axis and at the wall as functions of the axial coordinate obtained from the RANS simulation. The numbers in the graph correspond to the points indicated in Fig. 5.1

where  $p_{t,h}$  and  $p_{t,c}$  are the total pressures in the hot and cold exit, respectively. This expression, in combination with Eq. (5.1), is the model that is used to compute the exit temperatures, based on the measured exit pressures. It will be explained in § 5.3 how  $Ma_0$  is determined.

The analysis indicates that a certain minimum length of the main tube is required to be able to maximize the heat exchange between the eddies and the peripheral or core streams (process I). This process takes place between the axial coordinates of points 0 and 1 (or points 3 and 4), which is the first section of the main tube. Furthermore, there is a certain distance required between points 1 and 2, i.e. the second section of the main tube, for the decay of the vortex. These are the reasons why the RHVT has an optimum length. If the main tube is too short, not all the heat is transferred from core stream to the peripheral stream by the eddies, resulting in a smaller temperature difference. In practise, when the main tube is too long, heat losses to the surroundings (e.g. convective heat losses) are larger due to the larger surface area of the main tube, which also results in a smaller temperature difference. Based on literature, the optimum length to diameter ratio of the main tube is  $L/D \approx 20$  (Eiamsa-ard & Promvong, 2008b). The energy separation model is, therefore, valid as long as the main tube is sufficiently long ( $L/D > 20$ ).

### 5.3 Determination of $Ma_0$

In the previous section, a temperature model was developed that requires  $Ma_0$  to be known. The maximum swirl Mach number  $Ma_0$  is generally not known. Ahlborn *et al.* (1998) proposed a semi-incompressible model to determine  $Ma_0$ . The model requires the cold exit pressure and the pressure in the exit of the nozzle to be known. In their model, however, they assume that the mass density is constant while at the same time high Mach numbers can be reached in the RHVT, which is inconsistent.

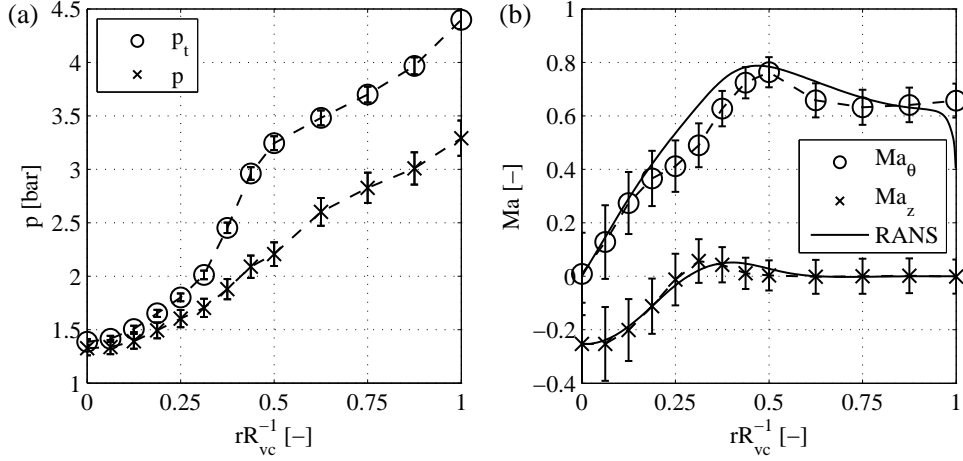


Figure 5.8: (a) Total and static pressures obtained from CPT measurements in the vortex chamber as functions of the dimensionless radial coordinate. The dotted lines are meant as guides to the eye. (b) Mach numbers determined from Eq.(3.22) (symbols) and results of the RANS simulation (solid lines) as functions of the dimensionless radial coordinate.

We have measured the Mach number as a function of the (dimensionless) radial coordinate  $rR_{vc}^{-1}$  in the vortex chamber in between the cold exit and main tube (indicated with the grey dash-dotted line in Fig. 5.5). This allowed us to develop a model for  $Ma_\theta$  as a function of the plenum- and cold exit pressures.

### 5.3.1 The Mach number in the vortex chamber

Mach numbers were measured in the vortex chamber with a cylindrical pitot tube (CPT), which is described in §3.3. The measurements were performed in a vortex tube having  $R_{vc}/R = 2$  (type 1 swirl generator, see §3.1.1).

Results were obtained for a nitrogen mass flow of 72.9 g/s and a cold fraction of  $\varepsilon = 0.40$  (details of the experimental setup are provided in § 5.4). The total and static pressures as functions of the dimensionless radial coordinate are shown in Fig. 5.8a. The resulting swirl and axial Mach numbers are shown in Fig. 5.8b. The axial Mach number has significant values in the core region only, where the flow is directed towards the cold exit. In the range  $0.25 < rR_{vc}^{-1} < 0.5$ ,  $Ma_z$  is positive. In this region, gas moves into the main tube. In addition to the CPT measurements, the numerical simulation (see §5.2) was used to determine the Mach number in the vortex chamber for the same flow conditions as in the experiment. The results of this simulation are shown as the solid lines in Fig. 5.8b and are in remarkably good agreement with the CPT results. From both the CPT measurements and the simulation results, we observe that  $Ma_\theta$  increases approximately linearly with  $r$  for  $rR_{vc}^{-1} < 0.5$  and remains approximately constant for larger radii. Close to the vortex chamber wall ( $rR_{vc}^{-1} = 1$ ) the numerical result shows the decrease in Mach number in the boundary layer.

### 5.3.2 A model for $\text{Ma}_0$

From the CPT and numerical results, we may approximate  $\text{Ma}_\theta(r)$  by

$$\text{Ma}_\theta(r) = \begin{cases} \text{Ma}_0 r/R & (0 \leq r \leq R); \\ \text{Ma}_0 & (R < r \leq R_{vc}), \end{cases} \quad (5.13)$$

where  $\text{Ma}_0$  is the maximum swirl Mach number found in the vortex chamber, as in Eq. (5.12). Using this approximation, we have developed a model for  $\text{Ma}_0$  as a function of the plenum pressure and the cold exit pressure.

Considering an ideal gas and assuming that the swirl velocity is the only significant velocity, the radial component of the momentum balance, Eq. (5.3), is rewritten using the definitions of angular velocity, the speed of sound defined in Eq. (3.3), and Eqs. (5.6) and (5.13) to become

$$\frac{dp}{dr} = \gamma \frac{p(r)}{r} \text{Ma}_\theta^2(r). \quad (5.14)$$

Substitution of  $\text{Ma}_\theta(r)$  with Eq. (5.13) and integration of this equation between  $r = 0$  and  $r = R_{vc}$ , which is the radius of the vortex chamber, yields

$$\frac{p_0}{p_c} = \exp\left(\frac{\gamma}{2} \text{Ma}_0^2\right) \left(\tau_R\right)^{\gamma \text{Ma}_0^2}, \quad (5.15)$$

where  $p_0$  is the static pressure in the exit of a nozzle and  $\tau_R = R_{vc}/R$ . Here we have used the boundary condition  $p(r=0) = p_c$  ( $z=0$ ), i.e. the static cold exit pressure. Assuming frictionless expansion through the nozzles, the plenum pressure  $p_{pl}$  and  $p_0$  are related to each other via isentropic gas relations, which results in

$$\frac{p_{pl}}{p_c} = \exp\left(\frac{\gamma}{2} \text{Ma}_0^2\right) \left(\tau_R\right)^{\gamma \text{Ma}_0^2} \left(1 + \frac{\gamma-1}{2} \text{Ma}_0^2\right)^{\frac{\gamma}{\gamma-1}}. \quad (5.16)$$

The maximum swirl Mach number is shown in Fig. 5.9 as a function of  $p_{pl}/p_c$  for  $\tau_R = 1$  and  $\tau_R = 2$  ( $\gamma = 1.4$ ). To have a maximum temperature ratio, it is desired to have  $\text{Ma}_0 = 1$ , meaning that for  $\tau_R = 2$ , a pressure ratio of approximately 10 is required. In general, a pressure ratio of 10 is rather high (conventional air supply compressor systems work at 8 bars); the condition  $\text{Ma}_0 = 1$  would never be achieved. The required pressure ratio is significantly reduced by lowering  $\tau_R$ . For example,  $\tau_R = 1$  (i.e., no vortex chamber) requires a pressure ratio of less than 4 to achieve  $\text{Ma}_0 = 1$ . Note that the absolute diameter of the main tube has no influence on  $\text{Ma}_0$  and hence on the temperature ratio. In our experimental study, we have used two swirl generators with different  $\tau_R$  (see §3.1.1) and have used a vacuum pump to be able to vary the pressure ratio over a wide range.

Note that the above equations are valid for the measured velocity profile. A different geometry of vortex chamber may result in a different type of vortex, e.g. a wall jet (Steenbergen, 1995). This means that the integral of Eq. 5.14 has a different solution and Eq. 5.16 changes accordingly.

### 5.3.3 The static cold exit pressure

The static cold exit pressure  $p_c$  can be measured directly via a static pressure port (small hole) in the cold exit wall, or by using a static pressure probe. Another method, which we have

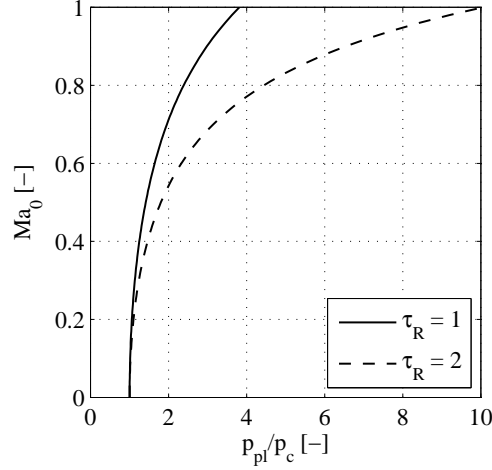


Figure 5.9: The maximum swirl Mach number as a function of the ratio of plenum and cold exit pressures according to Eq. 5.16 for  $\tau_R = 1$  and  $\tau_R = 2$  ( $\gamma = 1.4$ ).

addressed, is to use 1D compressible gas dynamics equations (provided in § 3.1.1) to compute  $p_c$ , however, this requires  $T_{t,c}$  to be known as well. Assuming that the flow through the cold exit is isentropic, we can compute  $p_c$  with

$$p_c = p_{t,c} \left( 1 + \frac{\gamma - 1}{2} Ma_c^2 \right)^{\frac{\gamma}{1-\gamma}}. \quad (5.17)$$

The cold exit Mach number  $Ma_c$  is related to, among others, the total temperature and the total pressure in the cold exit (see § 3.1.1.1) via

$$Ma_c \left( 1 + \frac{\gamma - 1}{2} Ma_c^2 \right)^{\frac{1+\gamma}{2(1-\gamma)}} = \frac{\varepsilon \dot{m}}{p_{t,c} \pi R_c^2} \sqrt{\frac{\mathcal{R} T_{t,c}}{\gamma}}. \quad (5.18)$$

It is expected that shock waves will be present in the cold exit if  $Ma_c > 1$ . Eq. (5.18) is, therefore, valid for  $Ma_c \leq 1$ .

In an experiment, we can relatively easily measure  $T_{t,c}$ , which is required in Eq. (5.18), however, the aim of the model is to predict this temperature based only on the measured pressures and mass flows.  $T_{t,c}$  can be found iteratively by using the proposed energy separation model. In that case, we first estimate  $T_{t,c}$  and compute  $Ma_c$  according to Eq. (5.18). Then,  $p_c$  and  $Ma_0$  are computed with Eqs. (5.16) and (5.17) and we use the model that is described in § 5.2 to find  $T_{t,c}$  and  $T_{t,h}$  based on  $Ma_0$  and the measured  $p_{t,c}$  and  $p_{t,h}$ . The resulting  $T_{t,c}$  is again used in Eq. (5.18) and the iterative cycle is repeated. Only three iterations are required to have a converged solution (the residual is  $\delta Ma_0 \leq 10^{-4}$ ).

We have compared the iterative method to the method where we have directly inserted the measured cold exit temperature in Eq. (5.18). The two methods agree in general within 0.4% for  $Ma_0$ .

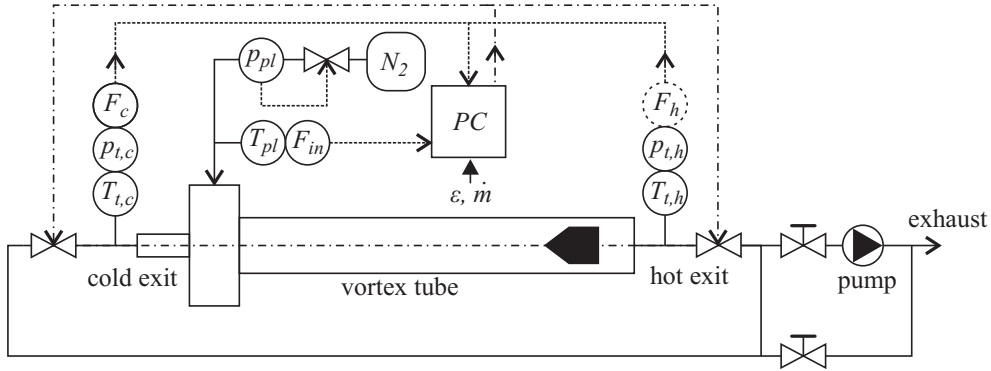


Figure 5.10: Schematic overview of the experimental setup.

## 5.4 Experimental Study

The presented energy separation model is validated by experiments. The vortex tube that was used in the experiments is shown in Fig. 3.1, where the main components are indicated. Pressurized gas (in this study nitrogen gas) enters the RHVT via two main inlets, which are attached to an outer ring. The gas expands and accelerates through slots in the swirl generator and enters the vortex chamber at a high velocity. The diameter of the main tube was  $2R = 40$  mm and it had a length up to  $L = 2.50$  m. The diameter of the cold exit was  $2R_c = 15.75$  mm. To accelerate the gas, two types of swirl generators were used, which are described in §3.1.1. The first type swirl generator contained 8 rectangular slot nozzles ( $1 \times 14$  mm). The inner diameter of the swirl generator, i.e., the vortex chamber was  $2R_{vc} = 80$  mm ( $\tau_R = 2$ ). The second type contained 12 nozzles ( $0.7 \times 7$  mm) and had an inner diameter of  $2R_{vc} = 40$  mm ( $\tau_R = 1$ ).

A schematic overview of the experimental setup is provided in Fig. 5.10. The plenum pressure  $p_{pl}$  was controlled via a pressure controller that was connected to a nitrogen tank,  $N_2$ .  $\varepsilon$  was controlled by means of two exit valves and mass flow meters at the cold exit ( $F_c$ ) and inlet ( $F_{in}$ ). A third mass flow sensor located in the hot exit tube,  $F_h$ , was used to estimate the uncertainty in the mass flow and cold fraction. In the range  $0.2 < \varepsilon < 0.8$ , the relative uncertainty in the mass flow was determined to be less than 2%. For other cold fractions, the uncertainty in mass flow was less than 3%. The absolute uncertainty in  $\varepsilon$  was less than 0.01 for all  $\varepsilon$ . Inlet and exit temperatures were measured with pt1000 temperature probes (calibrated to have an accuracy of 0.01K). Care has been taken to ensure that the velocity of the nitrogen passing the temperature probes was low enough in order to accurately measure the total temperatures. The pressures were measured with digital pressure sensors (accuracy of 0.02% FS (0 – 21 bar)). Pressure losses, which are due to friction in the main inlet and the swirl generator, were measured (for  $\tau_R = 2$ ) with the CPT method (§5.3) and increase linearly with  $\dot{m}$ . At  $\dot{m} = 70$  g/s, the measured pressure loss was 0.4 bar. For the swirl generator having  $\tau_R = 1$ , we have simulated the flow through the nozzle and determined that the pressure drop at the same mass flow is 0.45 bar. The measured and simulated pressure losses were used to correct the measured plenum pressure. A vacuum pump was utilized to be able to lower the overall pressure in the system. The pump (Gardner Denver™ Liquid-Ring 2SVG.161 pump) had a suction capacity of  $480 \text{ Nm}^3/\text{h}$  (167 g/s) at 1 bar absolute. At

experiment	$\tau_R$	$\dot{m}$ [g/s]	$p_{pl}/p_c$ [-]	$\varepsilon_0$ [-]	pump?
<i>a</i>	2	70	3.27	0.40	no
<i>b</i>	1	54	3.67	0.41	no
<i>c</i>	2	53	7.43	0.40	yes
<i>d</i>	2	14	8.50	0.55	yes

Table 5.1: Experimental settings that were used in the experiments. The data represent flow conditions when the control valves are fully opened.

low pressure (0.15 bar absolute) the capacity was approximately 113 Nm<sup>3</sup>/h (39 g/s). All the temperatures, pressures and mass flows were recorded simultaneously.

Four experiments were carried out, the corresponding flow configurations are listed in Table 5.1. The data in this table represent flow conditions for the case that the control valves are fully opened, which corresponds to the maximum flow rate at the set value of the plenum pressure. The corresponding cold fraction is  $\varepsilon_0$ . Three experiments, *a*, *c*, and *d*, were performed with a swirl generator having  $\tau_R = 2$ . The RHVT used in experiment *b* had a swirl generator with  $\tau_R = 1$ . During experiments *c* and *d*, the vacuum pump was used to lower the overall pressure in the system. The measured pressures and mass flows were used as input for the model.

The absolute temperature differences scale with the plenum temperature. Therefore, the temperatures are made dimensionless with  $T_{pl}$  according to

$$\Theta = \frac{T_t - T_{pl}}{T_{pl}}. \quad (5.19)$$

In a similar way, the dimensionless pressure drop is

$$\Pi = \frac{p_{pl} - p_t}{p_{pl}}. \quad (5.20)$$

Other characteristic parameters are the dimensionless heating and cooling powers of the RHVT, defined by

$$\Phi_h = (1 - \varepsilon) \Theta_h, \quad \Phi_c = -\varepsilon \Theta_c, \quad (5.21)$$

which represent the heating or cooling power ( $= \varepsilon \dot{m} c_p (T_{pl} - T_{t,c})$  or  $(1 - \varepsilon) \dot{m} c_p (T_{t,h} - T_{pl})$ , respectively) divided by the total thermal energy going into the system per second ( $= \dot{m} c_p T_{pl}$ ). This allows us to compare experiments with different mass flows to each other.

### 5.4.1 Results

The graphs shown in Fig. 5.11 represent the normalized total pressures  $\Pi_c$  and  $\Pi_h$ . The pressures are non-differentiable functions of the cold fraction because of the way of controlling  $\varepsilon$ . The cold fraction at which the control valves at the exits are fully opened is  $\varepsilon_0$ . When  $\varepsilon < \varepsilon_0$  only the control valve at the hot exit was fully opened and the cold exit valve was partially closed. For  $\varepsilon > \varepsilon_0$  the cold valve was fully opened and the hot exit valve was partially closed. Because of this, the mass flow also varied with  $\varepsilon$  (typically a few percent). The maximum total pressure drop is for all experiments found at  $\varepsilon = \varepsilon_0$ . Obviously,  $\Pi$  is higher for experiments where the vacuum pump was used.



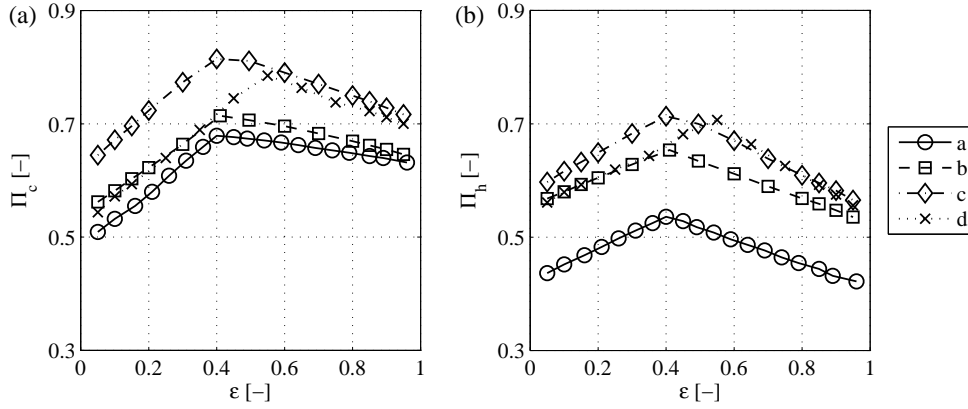


Figure 5.11: Normalized total pressure drop as functions of the cold fraction at the cold exit (a) and at the hot exit (b).

The corresponding  $Ma_0$ -numbers are shown in Fig. 5.12. As expected,  $Ma_0$  is higher for smaller  $\tau_R$  or for relatively lower cold exit pressures. As can be seen from Fig. 5.11a,  $\Pi_c$  is quite similar for experiments *a* and *b*. However, because of the smaller  $\tau_R$ , a higher  $Ma_0$  was reached during experiment *b*. The axial Mach number in the cold exit (not shown here), which is used to determine  $p_c$  and eventually  $Ma_0$ , reached  $Ma_c = 1$  (choking) during experiment *c*, for  $\varepsilon > 0.8$ . For higher Mach numbers shock waves would be present and we cannot relate  $p_{pl}/p_c$  to  $Ma_0$  by means of Eqs. (5.16), (5.17), and (5.18). Therefore, the modeled values of experiment *c* are only shown for  $\varepsilon \leq 0.8$ .

The measured pressures are now used to predict the exit temperatures using Eqs.(5.1), (5.12), and (5.16). The measured and modeled temperature differences are shown in Fig. 5.13. The modeled values are shown as the solid lines and are generally in very good agreement with the experimental values (symbols). The uncertainty in the measured temperatures is so small, that error bars are smaller than the symbols and are therefore not plotted. For all the experiments, the lowest temperatures are reached at  $\varepsilon = \varepsilon_0$ . Results of experiments *a* and *b*, Figs. 5.13a and 5.13b, show no major difference in measured exit temperatures. Apparently, changing the dimensions of the nozzle from  $\tau_R = 2$  to  $\tau_R = 1$  does not affect the energy separation. Figures 5.13c and 5.13d show the temperature differences for the low pressure experiments *c* and *d*. During experiment *c*, the largest temperature differences were reached. As already concluded by Ahlborn *et al.* (1996), temperature differences occur for both the high and low pressure experiments, which means that the energy separation phenomenon depends only on the pressure ratio, and not on the absolute plenum pressure nor the mass flow.

Discrepancies between the modeled and measured temperatures are generally small. However, at large  $\varepsilon$  the differences become larger and the measured hot exit temperatures are consistently smaller than predicted by the model. Especially, the theoretical  $\Theta_h$  of experiment *d* starts to deviate significantly from the experimental values, while  $\Theta_c$  remains in good agreement. The reason for these deviations becomes clear by studying the heating and cooling powers.

The specific heating and cooling powers are shown in Fig. 5.14. The highest specific cooling or heating power was measured during experiment *c*. Ideally  $\Phi_h = \Phi_c \equiv \Phi_{ideal}$ ,

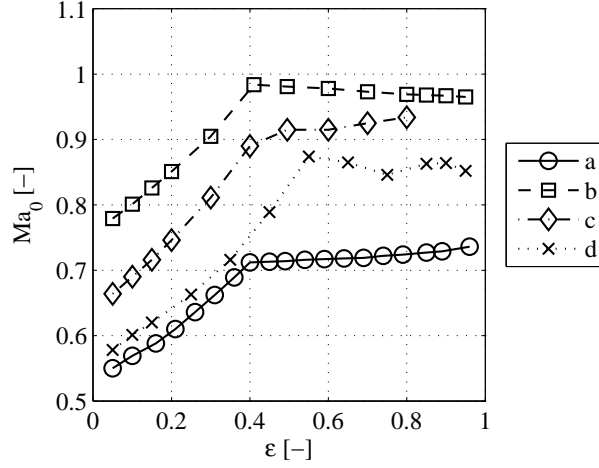


Figure 5.12: The maximum swirl Mach number  $Ma_0$  as a function of the cold fraction, computed with Eq. (5.16). For experiment *c*, the calculated values for  $\varepsilon \leq 0.8$  are shown only. The model is invalid for larger  $\varepsilon$  because of choking in the cold exit.

which would be the case if there are no heat losses, i.e., the RHVT is perfectly insulated. The wall temperature of the RHVT may reach temperatures well above  $120^\circ\text{C}$ . Despite the insulation, there are losses to the surroundings. Convective heat losses from the main tube to the surroundings are relatively small, but, conductive losses are more significant. Conductive heat losses occur via supports to which the hot tube is mounted and via the main tube itself, which is connected to the vortex chamber. Increasing  $\varepsilon$  leads to higher temperatures of the hot gas and, consequently, an increasing heat loss via the main tube wall to the surroundings. The cold gas temperature is below ambient and there will be a negative heat loss through the cold exit tube. Therefore, we observe  $\Phi_h > \Phi_c$  for low cold fractions and  $\Phi_h < \Phi_c$  for high cold fractions. The results show that for high mass flow rates (experiments *a-c*), the difference between  $\Phi_h$  and  $\Phi_c$ , which is a measure for the heat loss  $\Delta\Phi = \Phi_c - \Phi_h$ , is smaller than those of the low mass flow (experiment *d*).

The heat loss depends on, among others, the difference between the tube wall temperature and room temperature, but not on the mass flow through the vortex tube. So, for low mass flow experiments, the heat loss is relatively large compared to the available heating power. For small  $\dot{m}$ , the hot exit temperature and heating power are, therefore, significantly lower compared to experiments with a higher mass flow.

The heat loss  $\Delta\Phi$  is now compared to the ideal heating power  $\Phi_{ideal}$  assuming that there are no losses. The surface area of the cold exit tube is much smaller than the surface area of the main tube. Therefore, we consider the losses through the main tube only, while losses through the cold exit tube are considered to be negligibly small. In that case,  $\Phi_{ideal}$  can be approximated by  $\Phi_c$  and the relative heat loss is

$$\phi \equiv \frac{\Delta\Phi}{\Phi_{ideal}} \approx \frac{\Delta\Phi}{\Phi_c}. \quad (5.22)$$

If  $\phi = 1$ , the heating power of the RHVT and the heat losses are equal. In that case, the hot exit temperature equals the plenum temperature as all generated heat is lost. In Fig. 5.15,

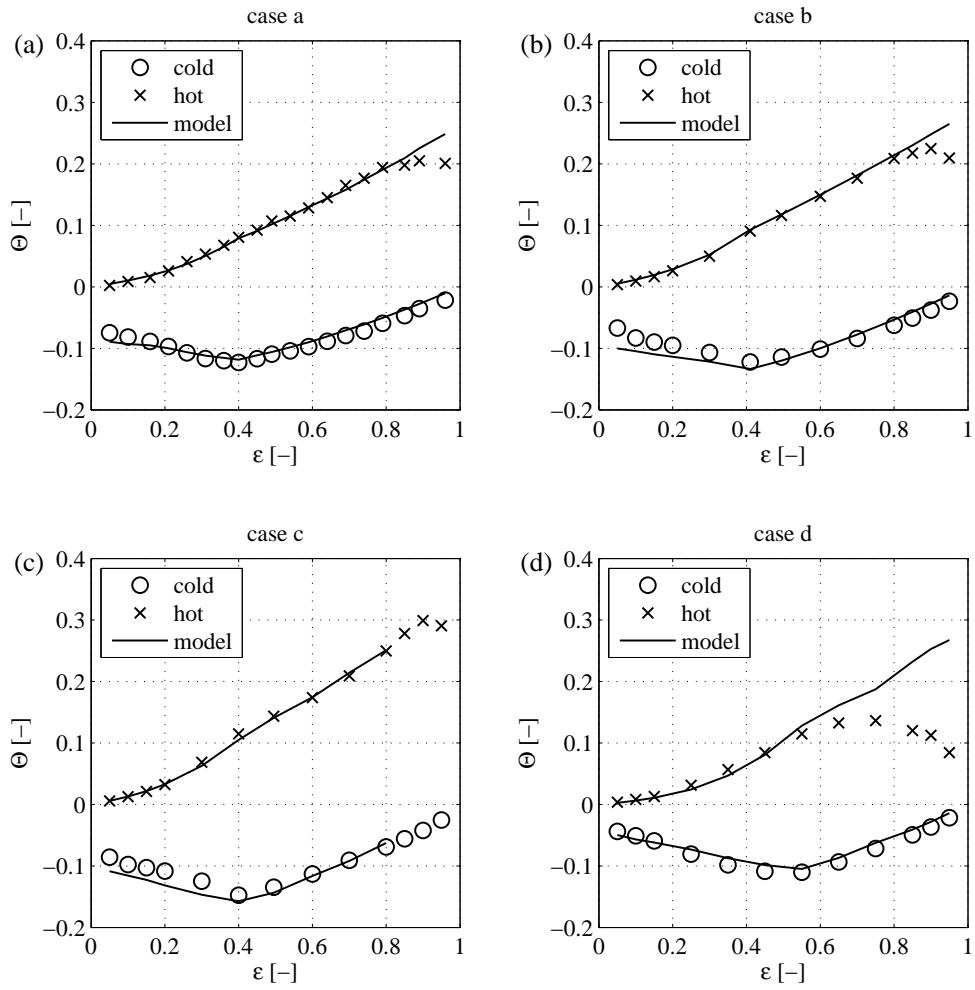


Figure 5.13: Dimensionless exit temperatures as functions of the cold fraction for experiments *a* – *d*. Symbols are experimental values, solid lines are computed using the model. For experiment *c*, the modeled values for  $\epsilon \leq 0.8$  are shown only. The model is invalid for larger  $\epsilon$  because of choking in the cold exit.

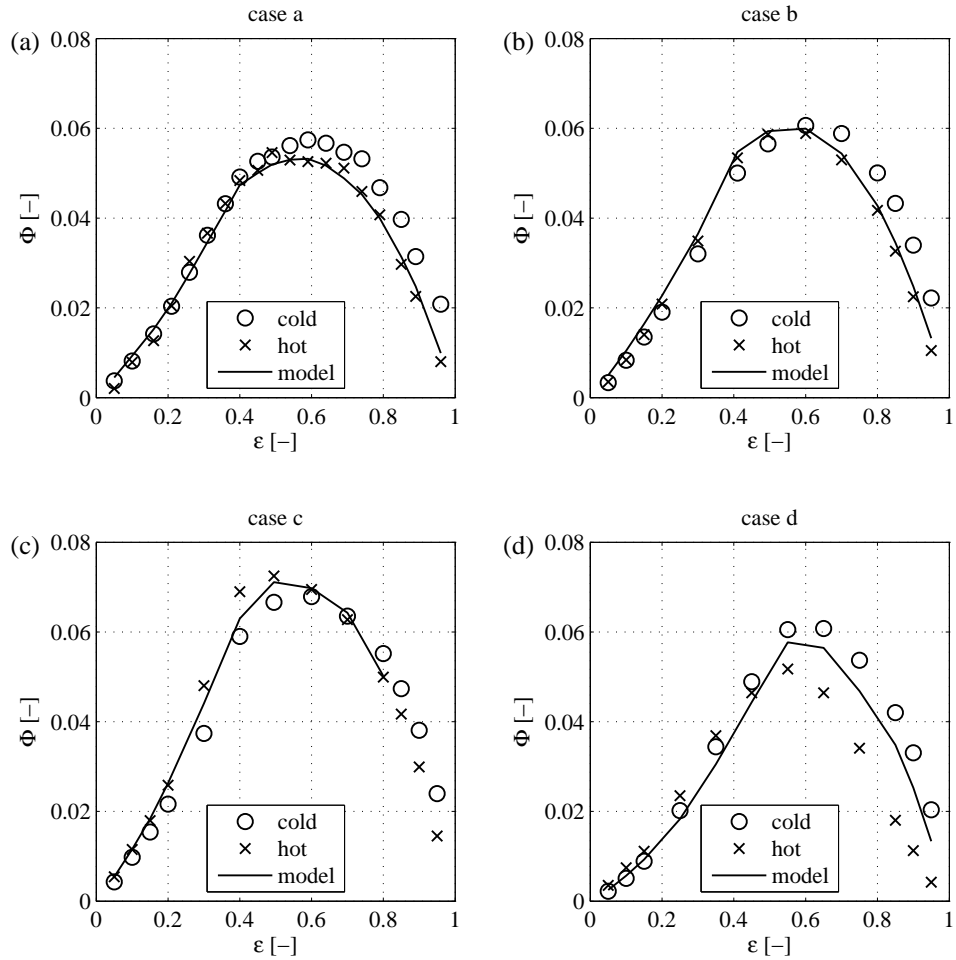


Figure 5.14: Dimensionless cooling and heating powers as functions of the cold fraction for experiments *a* – *d*. Symbols are experimental values, solid lines are computed using Eqs.(5.1),(5.12), and (5.16). For experiment *c*, the modeled values for  $\epsilon \leq 0.8$  are shown only. The model is invalid for larger  $\epsilon$  because of choking in the cold exit.

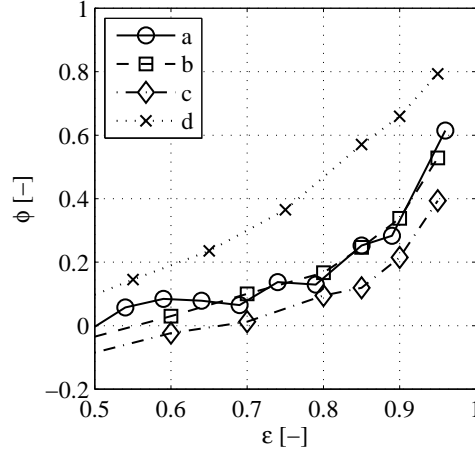


Figure 5.15: Relative heat loss in the experiments as a function of the cold fraction for  $\varepsilon > 0.5$ .

the relative heat loss is plotted for  $\varepsilon > 0.5$ . For experiment *d*, the relative heat loss is significantly larger than for the other experiments, and at  $\varepsilon = 0.95$ ,  $\phi = 0.8$ , meaning that 80% of the heating power is lost. This explains the large discrepancies between the measured and modeled temperatures as observed from Fig. 5.13d.

The lowest temperature and the highest specific cooling power was reached during experiment *c*. However, the efficiency of the vortex tube as a cooling device appears to be lower compared to that of the high pressure experiments. The thermodynamic efficiency of the vortex tube is defined as the ratio of cooling power and the isentropic work that is required to bring the cold exit pressure back to the plenum pressure. Using the dimensionless temperature and pressure, the efficiency is

$$\eta_c = \frac{\varepsilon \Theta_c}{1 - (1 - \Pi_c)^{\frac{\gamma-1}{\gamma}}}. \quad (5.23)$$

Fig. 5.16 represents the thermodynamic efficiencies of the vortex tube for the different experiments. As can be seen from the figure, the efficiency is very poor compared to that of a conventional refrigerator (typically  $\eta_c > 100\%$ ) and has its maximum around  $\varepsilon = 0.6$ . The efficiency of the RVHT during the low pressure experiments is approximately 10% lower than that of the high pressure experiments. Also interesting to note is that the efficiency is not really affected by the total mass flow, reconfirming that the energy separation process does not depend on the mass flow, but depends mainly on the pressures.

## 5.5 Summary and conclusions

Since its invention in 1933, many scientist have studied the Ranque-Hilsch vortex tube in order to explain and model the energy separation processes that take place in the device. In this chapter, we provide the derivation of a relatively simple model that we have used to

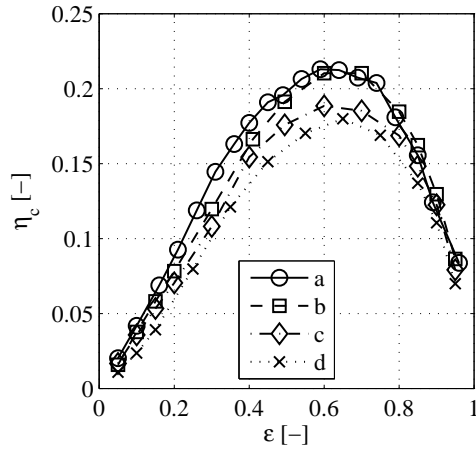


Figure 5.16: Isentropic efficiency as function of the cold fraction for experiments *a* – *d*.

predict the temperatures of the cold and hot gas at the exits of the RHVT, provided that the main tube of the RHVT is sufficiently long ( $L/D > 20$ ).

The model is based on two main processes. The first process is energy transport between the core and the periphery of the vortex due to the presence of a large radial pressure gradient. The radial position of gas pockets fluctuates due to turbulence and periodic motions. A gas pocket is thereby compressed or expanded and transports energy from the core towards the periphery. The second process involves the kinetic energy distribution of the vortex. Gas in the periphery has a higher kinetic energy than gas in the core region. The angular velocity decreases towards the hot end side due to viscous effects, and the kinetic energy of the gas in the periphery is converted into heat. Because of these two processes, the gas in the periphery has a higher total temperature than gas in the core region close to the cold exit.

The first process is modeled by using the adiabatic gas equation, which is valid between two points in the RHVT. The second process is modeled with adiabatic deceleration in combination with isentropic expansion of gas. The maximum swirl Mach number,  $Ma_0$ , is required to be known in the model. With a cylindrical pitot tube, the distribution of the swirl Mach number was measured. Based on these results, we have derived an equation that relates  $Ma_0$  to the plenum- and cold exit pressures. In this way, the temperature model only requires the pressures in the plenum and exits to be known.

Experiments were conducted to validate the model. Temperatures, pressures and mass flows were simultaneously measured. Results show that modeled quantities, like temperature and heating or cooling power, are in very good agreement with the experimental results, except for high cold fractions and/or low mass flows. At high cold fractions or low mass flows, heat losses, which are not taken into account in the model, are relatively large compared to the heating power of the RHVT and cause the model to deviate from the experiment.

The velocity distribution of the vortex in the vortex chamber that was measured with the CPT method may change when other swirl generators are used. The model for  $Ma_0$  is, therefore, not unconditionally valid. For the examined cases however, the model predictions are in good agreement with the experimental results.

Ideally, an RHVT is perfectly insulated and the cooling and heating powers are inde-

pendent of the mass flow. The theory, the resulting model, and experiments show that the pressures are the only relevant parameters for the energy separation process. To have an optimum cooling power, a high  $Ma_0$  (high  $p_{pl}$  and low  $p_c$ ) in combination with a high hot- to cold exit pressure ratio is necessary. The latter, however, is difficult to achieve in practice, because changing one of the pressures directly leads to a change in  $\varepsilon$  and, consequently, in the cooling power.





# 6 | Preliminary study of the RHVT as a separator

In this chapter, we provide experimental and theoretical results regarding separation of gases with the RHVT. The experimental results are obtained from a mixture of water vapour and nitrogen gas. The theoretical predictions are made for a methane - carbon dioxide mixture. In §6.1 we will explain how to measure the water content in a mixture of gas and droplets. Some preliminary results of water vapour separation are provided in § 6.2. Simulation results of a RHVT operating with the methane - carbon dioxide mixture are presented in § 6.3.

## 6.1 Measuring the water content in a gas/droplet mixture

To be able to determine the quantitative separation performance of the RHVT, it is required to know the total mass flows of water in the inlet and in the two exits of the vortex tube. The relative humidity can directly be measured with sensors. However, the relative humidity is the ratio of the water vapour pressure and the saturation vapour pressure of water and does not contain quantitative information of the water content in the gas mixture unless the temperature and pressure are known.

The water vapour mole fraction  $\Gamma$  (in mol H<sub>2</sub>O per mol of gas mixture), which was already defined in §2.2.1, can be used to quantify the amount of water that is present in the gas mixture. The advantage of this quantity is that it is independent of pressure and temperature and therefore allows us to compare inlet and outlet quantities. Another quantity, often used in humidity studies, is the mixing ratio<sup>1</sup> (mass ratio) MR (in kg H<sub>2</sub>O per kg N<sub>2</sub>), which has the same advantages. The mixing ratio is related to  $\Gamma$  and the molar masses of nitrogen and water via

$$\text{MR} = \frac{\Gamma}{1 - \Gamma} \frac{M_{\text{H}_2\text{O}}}{M_{\text{N}_2}}, \quad (6.1)$$

where the water vapour mole fraction is

$$\Gamma = \frac{p_{\text{H}_2\text{O}}}{p} = \frac{p_{\text{sat}}(T)}{p} \text{RH}. \quad (6.2)$$

As long as all the water is in the gaseous state, and the pressure, temperature, and humidity are simultaneously measured, the mixing ratio can be computed. When the mixture contains

---

<sup>1</sup>Other units that are used are parts per million by volume (PPMv =  $10^6 \cdot \Gamma$ ) or parts per million by weight (PPMw =  $10^6 \cdot Y$ ).

droplets, however, it is difficult to determine the total water content, because the relative humidity sensor will be wet and will give an erroneous value. It depends on the plenum conditions and the cold fraction whether droplets will be present in the inlet and the exits of the RHVT. Droplets present in the hot stream will quickly evaporate (see §2.5.2), and it is therefore not expected to find droplets in the hot exit. In the inlet of the RHVT, there are small droplets present if more water is injected in the humidifier vessel than is required to saturate the gas (which will be the case when  $\phi_{\text{H}_2\text{O}} > \chi$ , see §3.4). For specific operating conditions (lower cold fractions, lower cold exit pressures), the cold exit temperature is so low that the gas is saturated and droplets will be suspended in the cold stream. Under these circumstances, the mixing ratio can not be determined directly. A way to overcome this problem, is to take a small sample of the gas/droplet mixture and heat the sample until all droplets are evaporated. In that way, all water is in the vapour phase and the method described above can be used to determine MR.

We have studied two methods of sampling. The first is a discrete method, taking a small sample from the main stream and heat it in a closed container while monitoring the pressure, temperature and relative humidity. The second method is a continuous method, where a sample stream of the gas/droplet mixture is extracted from the main stream via a sampling tube, followed by a heated tube (the evaporator, see the process scheme in §3.5.3) and a sensing section where all required quantities are measured. The main reason to take only a sample stream from the cold stream is that less heating power is required to heat up the sample stream and evaporate droplets that are present in the cold exit stream.

Wolf (2011) and Liefkens (2012) have compared both methods and have shown that the first method is very sensitive to tiny amounts of liquid water that is present from a previous experiment, making it unreliable. The second method is more accurate and provides continuous monitoring of the humidity in time. The latter method is therefore used to determine the mixing ratio in the cold exit,  $\text{MR}_c$ .

The mixing ratio in the plenum can be determined in two ways as well. If the plenum humidity is  $\text{RH}_{pl} < 1$ , the mixing ratio in the plenum,  $\text{MR}_{pl}$ , can be computed if the plenum humidity, temperature, and pressure are measured. In the case that  $\text{RH}_{pl} > 1$ ,  $\text{MR}_{pl}$  can be found as follows: water is supplied from a water reservoir via a pump to the high pressure water nozzles. The water reservoir is placed onto an accurate scale (§3.5.2), and by logging the weight of the water reservoir in time, the amount of water that is suspended in the nitrogen gas per unit time  $\dot{m}_{\text{H}_2\text{O}}$  is known. Together with the mass flow of the nitrogen  $\dot{m}$ , the mixing ratio in the plenum is

$$\text{MR}_{pl,sc} = \frac{\dot{m}_{\text{H}_2\text{O}}}{\dot{m}}, \quad (6.3)$$

where subscript  $sc$  stands for ‘determined with the scale’. The mixing ratio that is determined with the humidity sensor is indicated as  $\text{MR}_{pl,RH}$ . The input of water per unit time,  $\dot{m}_{\text{H}_2\text{O}}$ , is determined by first differentiating the measured weight with respect to time and then determine the moving average of a half hour time interval (smoothing).

The amount of water that is injected into the RHVT should be equal to the amount of water leaving the device. The steady state mass balance of water in the RHVT is

$$\text{MR}_{pl} = \varepsilon\text{MR}_c + (1 - \varepsilon)\text{MR}_h + \delta\text{MR} = \text{MR}_e + \delta\text{MR}, \quad (6.4)$$

where  $\text{MR}_c$  and  $\text{MR}_h$  are the mixing ratios in the cold and hot exit streams, respectively,  $\text{MR}_e$  is the combined mixing ratio in the exits of the RHVT, and  $\delta\text{MR}$  is the absolute error in the

measurement. Ideally,  $MR_e$  and  $MR_{pl}$  are equal. The relative uncertainty in the mixing ratio is defined as

$$\frac{\delta MR}{MR} = \left| \frac{MR_{pl} - MR_e}{MR_{pl}} \right|. \quad (6.5)$$

Based on the specifications of the humidity sensors (which state that the accuracy in the measured relative humidity is 2% absolute, see §3.5.3), the uncertainty in MR can be very high (> 50%) at low relative humidities (the derivation is provided in Appendix C). However, the actual uncertainty depends on the calibrations of the individual humidity sensors. This means that the uncertainty can be much smaller than the uncertainty based on the sensor specifications. Therefore, we have measured the temperatures, pressures, and relative humidities in the inlet and exit streams, and the weight of the water reservoir in time in order to measure  $\delta MR/MR$  more accurately.

The sample stream that was taken from the cold outlet was heated in the evaporator in order to evaporate the droplets. During the experiment, all parameters (such as the nitrogen pressure, nitrogen mass flow, cold fraction, nitrogen temperature, water pressure, and mean evaporator temperature) were kept constant. The mass flow of water was small enough to ensure that the gas in the plenum remained unsaturated ( $RH_{pl} < 1$ ). In this way, the mixing ratios determined with the scale and the relative humidity sensor could be compared to each other.

Figure 6.1 shows measured values of the relative humidities, pressures, temperatures, and the weight of the water reservoir as functions of time over a period of 6 hours. Subscripts  $pl$ ,  $s$ , and  $h$  are used to distinguish between plenum, sampled from the cold exit, and hot exit properties, respectively. The values shown in the graphs are averaged (smoothed) over 10 minutes.

The relative humidities and pressures (Figs. 6.1a and 6.1b) remain approximately constant over time. The corresponding temperatures (Fig. 6.1c), however, increase during the experimental time. The cause for this is that the high pressure water pump slowly increases the temperature of the water that is partially injected in the vessel, and partially recirculated, thereby heating up the pressure vessel. The temperature of the sample stream,  $T_s$ , is controlled by the evaporator and is higher than the cold exit temperature (in this case almost equal to the plenum temperature). Because of the large system size, it took more than 6 hours to reach a steady state. The weight of the water reservoir decreases approximately linearly in time, as seen from Fig. 6.1d.

The computed mixing ratios are shown in Fig. 6.2. The mixing ratios increase over time due to the increasing temperature. According to the results, the mixing ratio in the plenum is higher than in both the cold and hot exit, indicating that there are uncertainties involved.

The mixing ratio in the plenum has also been determined with the scale according to Eq. (6.3), and additionally by combining the mixing ratios in the exits according to Eq. (6.4). These are compared with  $MR_{pl,RH}$  in Fig. 6.3a, showing that  $MR_{pl,RH}$  is higher than that obtained with the scale ( $MR_{pl,sc}$ ). The combined mixing ratio in the exits,  $MR_e$ , is in between both.

The relative uncertainties in the mixing ratio, described by Eq. (6.5), of  $MR_{pl,RH}$  and  $MR_{pl,sc}$  are shown in Fig. 6.3b. The relative uncertainty in  $MR_{pl,RH}$  is approximately 6%. The relative uncertainty of the mixing ratio determined with the scale is smaller, and is approximately 4%.

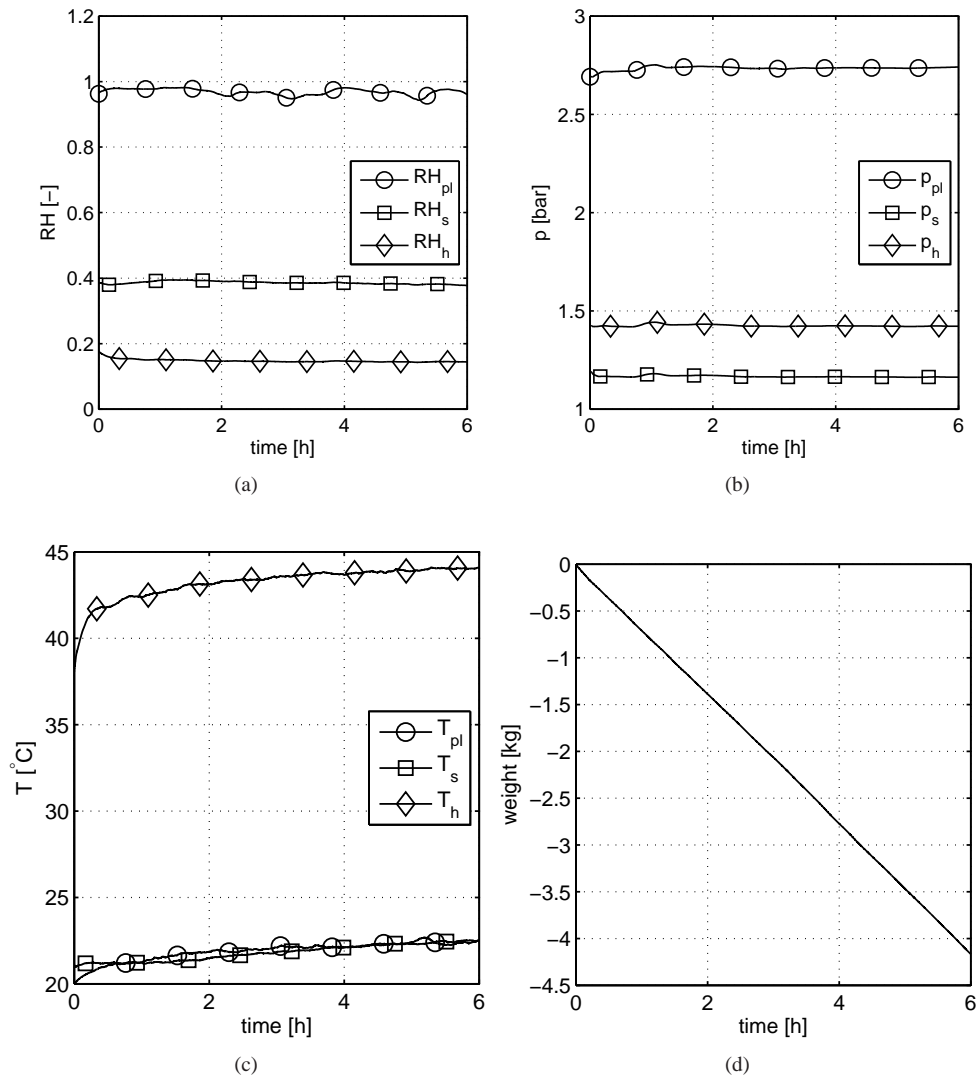


Figure 6.1: (a) Relative humidities, (b) pressures, (c) temperatures, and (d) the weight of the water reservoir as functions of time for a nitrogen mass flow of 34.7 g/s and  $\varepsilon = 0.61$ . Subscripts  $pl$ ,  $s$ , and  $h$  are used to distinguish between plenum, sampling, and hot exit properties, respectively.

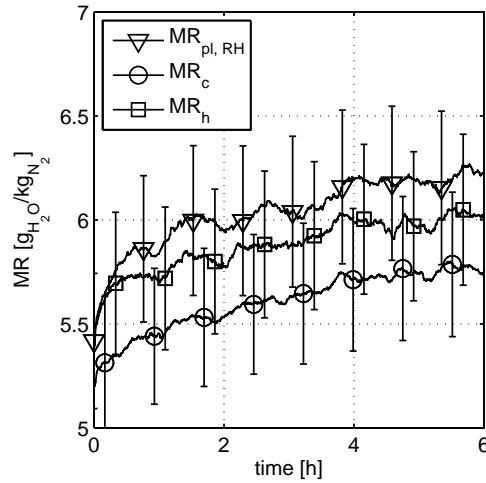


Figure 6.2: Mixing ratios in the plenum, cold exit, and hot exit that are measured as a function of time.

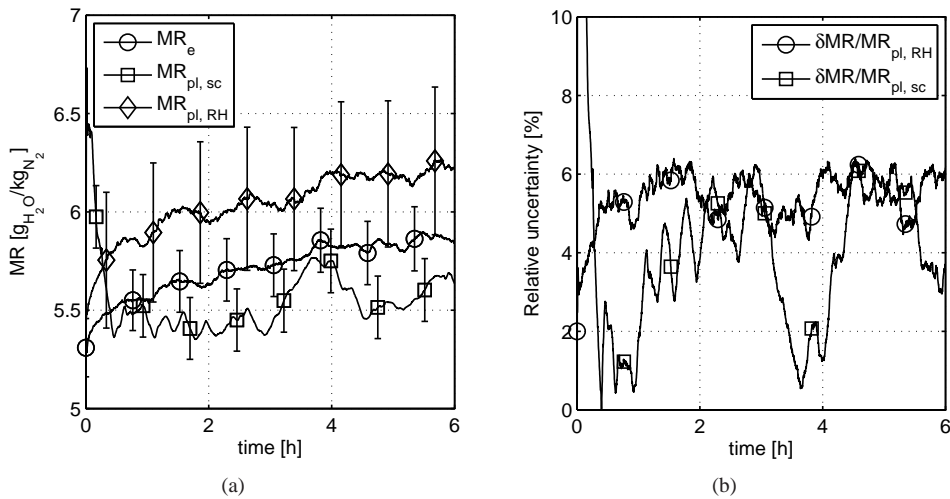


Figure 6.3: (a) Mixing ratios and (b) relative uncertainty in mixing ratio according to Eq. ( 6.5) as functions of time for a nitrogen mass flow of 34.7 g/s and  $\varepsilon = 0.61$ .

## 6.2 Preliminary results of water vapour separation

Experiments have been performed to study the separation of water vapour from nitrogen gas by using the RHVT. At the time of the experiments presented here, we were unable to determine the mixing ratio in the cold exit. Therefore, it was not possible to compute uncertainties based on the mass balance. Also, the automated draining on the pressure vessel (see §3.5.2) did not work properly, so the mixing ratio determined with the scale was unreliable. The available reference that was reliable enough was the mixing ratio determined with the plenum humidity. Based on the experiment above, the relative uncertainty in the mixing ratio is 6%.

During the separation studies, the RHVT was operated at high plenum pressures. Due to the cooling inside the RHVT, ice was formed that clogged the cold exit. This made the separation experiments very difficult, or sometimes impossible. To overcome this problem, we have installed a heater that is used to increase the nitrogen temperature before it enters the pressure vessel, where the humidification takes place. Another advantage of a higher nitrogen temperature is that higher mixing ratios can be reached in the plenum, while maintaining  $RH_{pl} < 1$ , thereby increasing the accuracy of the measurements.

The dry nitrogen gas was supplied from a liquid nitrogen tank via the  $LN_2$  evaporator and a 100 m long pipeline, which was exposed to the outside temperature, to the laboratory (§3.5.2). During summer, the nitrogen entering the laboratory has a higher temperature than during winter, and the heater allowed us to increase the nitrogen temperature to 60 °C before it entered the humidifier vessel. After humidification of the nitrogen in the vessel, the gas mixture was fed to the RHVT, having a plenum temperature that varied between  $T_{pl} = 28 - 32^\circ\text{C}$ , and a plenum humidity that varied between  $RH = 0.7 - 0.9$ . The mass flow of nitrogen was 70 g/s and the plenum pressure was 5.00 – 5.30 bar, dependent on  $\varepsilon$ . Because of the high plenum temperature, the cold exit temperature remained for most cold fractions above or around 0°C, and ice formation was prevented.

The mixing ratios in the plenum and hot exit as functions of the cold fraction are shown in Fig. 6.4a. The plenum mixing ratio is not constant, caused by the temperature increase of the vessel during the time of the experiment (the experiment started at high  $\varepsilon$ ). At low  $\varepsilon$ , the mixing ratios in the plenum and hot exit are nearly the same, indicating that there is no water vapour separation. Increasing the cold fraction leads to larger differences between the plenum and hot exit mixing ratio.

The enrichment of water vapour in the hot exit is defined as

$$\eta_v = \left( \frac{MR_h}{MR_{pl}} - 1 \right) \times 100\% \quad (6.6)$$

and is shown as a function of the cold fraction in Fig. 6.4b. It is clear from the graph that the largest separation of water vapour takes place at  $\varepsilon = 0.65$ . The corresponding water vapour enrichment is 37%.

## 6.3 A theoretical example of the RHVT as a gas cleaner

In order to predict the thermodynamics of the RHVT when mixtures of real gases (methane,  $CH_4$ , and carbon dioxide,  $CO_2$ ) are injected, the energy separation model (chapter 5) is utilized. Because the energy separation model is valid for an ideal gas (not a real gas) some

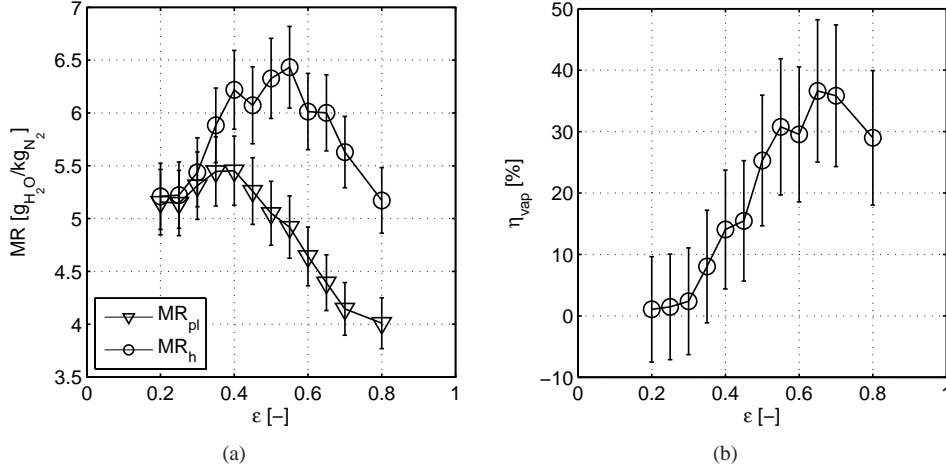


Figure 6.4: (a) Mixing ratios in the plenum and hot exit (b) enrichment of water vapour in the hot exit at 70 g/s, RH = 0.7 – 0.9, and  $T_{pl} = 28 - 32^\circ\text{C}$

modifications have been made. By incorporating Joule-Thomson cooling and heating due to enthalpy changes caused by condensation of components, the model can be utilized to predict the compositions of gas (and possibly liquid) mixtures in the exit streams of the RHVT. When  $T_{t,h}/T_{t,c}$  is known from the (ideal gas) model described by Eq. (5.12), the accompanying energy balance, where condensation and Joule-Thomson effects are incorporated, is

$$T_{pl} = \varepsilon \left( T_{t,c} - \frac{x h_{fg}}{c_p} \right) + (1 - \varepsilon) T_{t,h} + \mu_{JT} \Delta p, \quad (6.7)$$

where  $x_l$  is the liquid mass fraction in the mixture in the cold stream,  $h_{fg}$  is the heat of vaporization,  $\mu_{JT} = \left( \frac{\partial T}{\partial p} \right)_h$  is the Joule-Thomson coefficient, and  $\Delta p$  is the pressure difference between inlet and outlets of the RHVT.

The temperatures of the exit streams are computed by combining Eqs. (5.12) and (6.7), where the plenum pressure and cold exit pressure are the control parameters.  $Ma_0$  is given by Eq. (5.16). The hot exit pressure, which is unknown a priori, can be estimated by assuming that the radially averaged pressure is independent of the axial coordinate in the RHVT. Therefore, the radially averaged pressure can be computed based on the velocity profile in the vortex chamber (see §5.3.2). Assuming that the radial pressure gradient is negligible close to the hot exit (because of an insignificant swirl velocity due to the decay of the vortex), and assuming that pressure losses due to friction are marginal, the radially averaged pressure in the vortex chamber is equal to the hot exit pressure. The hot exit pressure can, therefore, be approximated by

$$p_h = \frac{1}{\pi R^2} \int_0^R 2\pi r p(r) dr. \quad (6.8)$$

Assuming a solid body type of rotation in the vortex chamber, the solution of the radial

component of the momentum balance, Eq. (5.14), is

$$p(r) = p_c \exp\left(\frac{\gamma}{2} \text{Ma}_0^2 \frac{r^2}{R^2}\right), \quad (6.9)$$

where the boundary condition  $p(r = 0) = p_c$  has been used. It has been assumed here that the pressure variation in the cold exit, due to its finite size, is negligible. Resultantly, the hot exit pressure is

$$p_h = \frac{2p_c}{\gamma \text{Ma}_0^2} \left[ \exp\left(\frac{\gamma}{2} \text{Ma}_0^2\right) - 1 \right]. \quad (6.10)$$

It has to be noted, that the kinetic energy of gas in the exits of the RHVT is neglected in this analysis assuming that the Mach number in the cold and hot exits are less than 0.3. This means that  $p_c = p_{t,c}$  and  $p_h = p_{t,h}$ .

Properties of the gas mixture at a given temperature and pressure (e.g.  $x_l$ ,  $c_p$ ,  $c_v$ ,  $\gamma (= c_p/c_v)$ ,  $h_{fg}$ , and  $\mu_{JT}$ ) are provided by the commercial package Prode Properties (Prode, 2013), which is able to compute properties of gas mixtures consisting of several different chemical components. The method that is used in the software is based on flash calculations (see, e.g., Appendix D in Willems (2009), and references therein). Because the liquid fraction in the cold exit depends, among others, on the cold exit temperature, an iterative procedure is required to obtain a solution for  $x_l$  and the exit temperatures. An initial guess for the cold exit temperature is found by initializing  $x_l$  to zero. The solution was accepted to be converged if the enthalpy of the inlet stream equals the sum of the enthalpy of the cold and hot exit streams within 0.001 kJ/kg.

The assumptions that are made in this model are:

- There is no liquid phase present in the plenum and hot exit;
- The latent heat of vaporization is absorbed by all the gas in the RHVT (both the hot and cold gas);
- Droplets remain in the cold stream (no centrifugal effects on droplets);
- All the liquid can successfully be removed from the cold gas stream;
- The gas mixture is treated as an ideal gas (except for the energy balance, which is replaced by Eq. (6.7));
- The volume flow and cold fraction are not affected by phase changes;
- Only gas and liquid phases (or their mixture) are computed by the model;
- The kinetic energy of gas in the exits is negligibly small.

The computed phase envelope of a 50%<sub>mol</sub>CO<sub>2</sub> + 50%<sub>mol</sub>CH<sub>4</sub> mixture is shown in Fig. 6.5. Unfortunately, the Prode program did not allow us to compute solid-liquid and solid-liquid-water vapour lines. Therefore, solid phases are not shown by the results.

The operating conditions of the RHVT are  $T_{pl} = 0^\circ\text{C}$ ,  $p_{pl} = 70$  bar, and  $p_c = 30$  bar. The computed Mach number is  $\text{Ma}_0 = 0.54$  in a RHVT with  $\tau_R = 2$ , and the hot exit pressure is  $p_h = 35.17$  bar ( $\gamma = 2.13$ ,  $\mu_{JT} = 0.8863$ ). For a cold fraction of  $\varepsilon = 0.30$ , the exit temperatures are  $T_{t,c} = -51.3^\circ\text{C}$  and  $T_{t,h} = 7.80^\circ\text{C}$ , which are indicated in the phase envelope, showing that the conditions of the mixture in the cold exit is in the gas-liquid



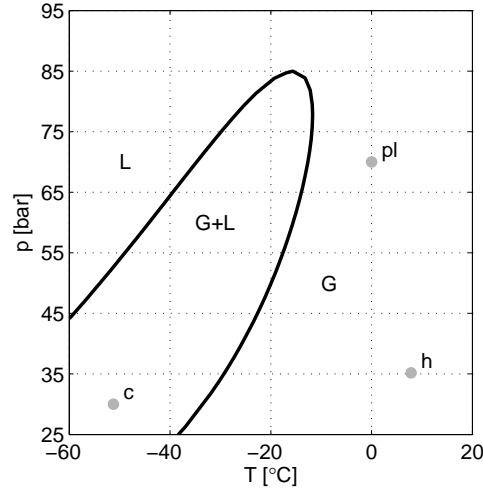


Figure 6.5: Phase envelope of a 50%<sub>mol</sub>CO<sub>2</sub> + 50%<sub>mol</sub>CH<sub>4</sub> mixture. L and G indicate liquid and gas states. Points *pl*, *c* and *h* indicate the conditions in the plenum, cold, and hot exit of the RHVT for  $\varepsilon = 0.30$ . The plenum temperature is  $T_{pl} = 0^\circ\text{C}$ , the plenum, cold, and hot exit pressures are  $p_{pl} = 70$  bar,  $p_c = 30$  bar, and  $p_h = 35.17$  bar, respectively.

phase. The mixture in the hot exit is in the gas phase. When all the liquid is removed from the cold gas (obviously an ideal situation), the mole fraction of methane is different from that in the plenum. The plenum methane mole fraction is 50%, while in the cold stream the methane mole fraction is increased to 72%. The enrichment of gaseous methane in the cold gas mixture is defined as

$$\eta_{\text{CH}_4,c} = \left( \frac{Y_{\text{CH}_4,c}}{Y_{\text{CH}_4,pl}} - 1 \right) \times 100\%, \quad (6.11)$$

where  $Y_{\text{CH}_4}$  is the mass fraction (mole fraction can also be used here) of methane. The computed enrichment in the cold gas is  $\eta_{\text{CH}_4,c} = 44.8\%$ .

The above analysis is repeated for different cold fractions. The operating conditions remain the same ( $T_{pl} = 0^\circ\text{C}$ ,  $p_{pl} = 70$  bar, and  $p_c = 30$  bar) and the RHVT has a vortex chamber with  $\tau_R = 2$ . The dimensionless exit temperatures, Eq. (5.19), as functions of  $\varepsilon$  are shown in Fig. 6.6a. The temperatures that are reached if there is no condensation (Joule-Thomson cooling remains to be present) are added to the graph, and are indicated with  $\Theta^*$ , to show that the exit temperatures are higher when condensation takes place. The computed enrichment of gaseous methane in the cold gas is shown in Fig. 6.6b. For  $\varepsilon < 0.1$ , all the matter in the cold exit is in the liquid phase and  $\Theta$  and  $\eta_{\text{CH}_4,c}$  are undefined.

High methane enrichment in the cold exit can be achieved at low cold fractions. The enrichment decreases rapidly with  $\varepsilon$ . After recombining the cold and hot streams, the overall enrichment ( $= \varepsilon \times \eta_{\text{CH}_4,c}$ ) is much lower. The overall enrichment has its maximum value at  $\varepsilon = 0.30$  and is  $\eta_{\text{CH}_4} = 13.4\%$ .

A RHVT with a different vortex chamber geometry, having smaller  $\tau_R$ , has also been simulated. The operating conditions are the same ( $T_{pl} = 0^\circ\text{C}$ ,  $p_{pl} = 70$  bar, and  $p_c = 30$  bar),

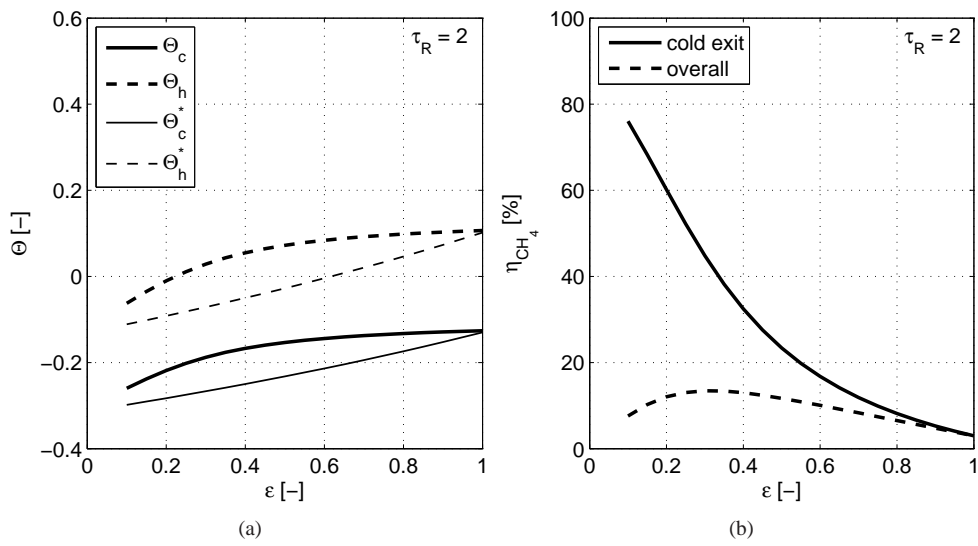


Figure 6.6: (a) Dimensionless exit temperatures as functions of the cold fraction for a  $50\%_{mol}CO_2 + 50\%_{mol}CH_4$  mixture. (b) The enrichment of gaseous methane in the cold exit and overall as functions of the cold fraction. The swirl generator in the simulated RHVT has a vortex chamber with  $\tau_R = 2$ . The plenum temperature is  $T_{pl} = 0^\circ C$ , the plenum, cold, and hot exit pressures are  $p_{pl} = 70$  bar,  $p_c = 30$  bar, and  $p_h = 35.17$  bar ( $Ma_0 = 0.54$ ), respectively.

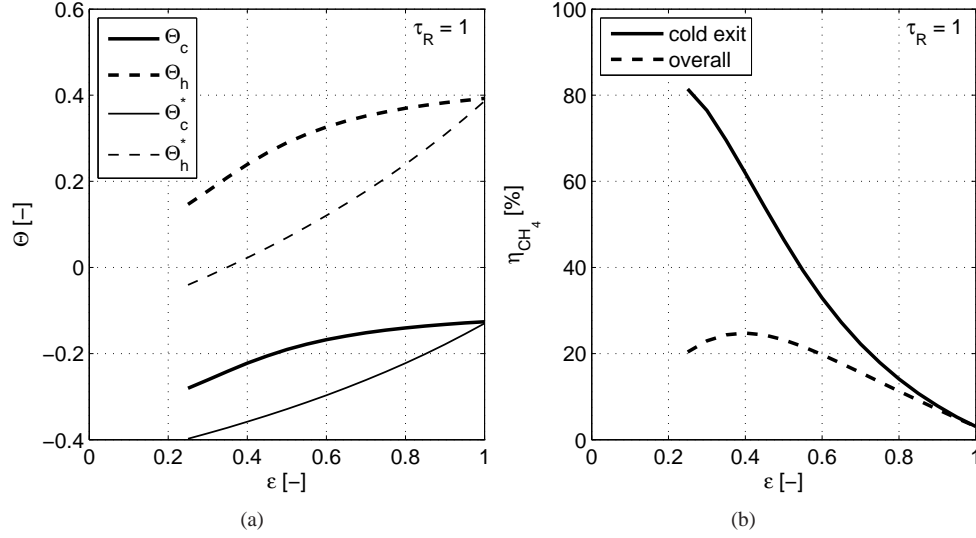


Figure 6.7: (a) Dimensionless exit temperatures as functions of the cold fraction for a  $50\%_{mol}CO_2 + 50\%_{mol}CH_4$  mixture. (b) The enrichment of gaseous methane in the cold exit and overall as functions of the cold fraction. The swirl generator in the simulated RHVT has a vortex chamber with  $\tau_R = 1$ . The plenum temperature is  $T_{pl} = 0^\circ C$ , the plenum, cold, and hot exit pressures are  $p_{pl} = 70$  bar,  $p_c = 30$  bar, and  $p_h = 41.87$  bar ( $Ma_0 = 0.77$ ), respectively.

but the RHVT has a vortex chamber with  $\tau_R = 1$ . The results are shown in Fig. 6.7. The computed Mach number is  $Ma_0 = 0.77$ , resulting in  $p_h = 41.87$ . Therefore, there is a significantly larger temperature separation than in the previous case, and the cold stream is completely liquid for  $\varepsilon < 0.25$ . The optimum overall enrichment is obtained at  $\varepsilon = 0.40$  and the corresponding temperature of the cold exit stream is  $T_{t,c} = -60.7^\circ C$ . At this temperature, the methane enrichment in the cold exit is  $\eta_{CH_4} = 62\%$ . The optimum overall enrichment is  $\eta_{CH_4} = 24.8\%$ , which is 85% higher compared to a RHVT with  $\tau_R = 2$ . This is achieved for the same pressure drop over the RHVT, indicating that a proper design of the RHVT has a major influence on its separation performance.

## 6.4 Conclusions

This chapter describes a method to determine the total water content in a gas-droplet mixture. Experimental results show that the uncertainty in the mixing ratio is 4 – 6%. Preliminary experimental results of water vapour separation with the RHVT are presented, indicating that a water vapour enrichment of 37% can be achieved in the hot exit stream.

The energy separation model is utilized in order to predict the thermodynamics of the RHVT when it is operated with real gases. The energy balance is modified by incorporating the Joule-Thomson effect and condensation of components. An example for a plenum gas

mixture  $50\%_{mol}CO_2 + 50\%_{mol}CH_4$  is provided. Although the model is not a model suitable for real gases, the results provide a first indication how well the RHVT performs as a gas separator (by considering the thermodynamics only). According to the results, a maximum overall gaseous methane enrichment of 13% can be achieved in a RHVT with  $\tau_R = 2$  at a plenum pressure of 70 bar, a cold exit pressure of 30 bar, and a cold fraction of  $\varepsilon = 0.30$ . The corresponding enrichment of gaseous methane in the cold stream is  $\eta_{CH_4} = 45\%$ . For a RHVT with  $\tau_R = 1$ , the optimum cold fraction is  $\varepsilon = 0.40$ . The corresponding methane enrichment in the cold exit is  $\eta_{CH_4} = 62\%$ , and the overall enrichment is  $\eta_{CH_4} = 25\%$ , which is 85% higher compared to a RHVT with  $\tau_R = 2$ . These results reveal that the RHVT is suitable to condense undesired components in the cold stream, thereby increasing the mass fraction of the gaseous product.

The developed model can be used as a design tool that simulates various types of gas mixtures. Based on a specified gas mixture, it can be used to optimize the operating conditions of the RHVT and to make predictions, from a thermodynamic point of view, of the overall separation efficiency.

# 7 | Conclusions & recommendations

In this study, we have investigated the behaviour of micron-sized water droplets that are injected, together with nitrogen gas and water vapour, into a Ranque-Hilsch Vortex Tube. Additionally, we have developed a model that describes the thermodynamics in the RHVT. This model has been utilized to make estimations regarding the separation performance of the RHVT as separator.

Based on the experimental and theoretical studies of the Ranque-Hilsch Vortex Tube, the following main conclusions and recommendations are made.

## 7.1 Conclusions

### 7.1.1 Theoretical analysis of droplet behaviour in the RHVT

Droplet velocities, trajectories, and sizes were computed by solving the equation of motion for small droplets in a flow field from which the temperature, pressure, and velocities are based on experimental data. Dependent on the local relative humidity, the change in droplet size due to condensation and evaporation is computed during each time step of the time dependent simulation.

Based on the flow characteristics, we have computed that droplets smaller than  $d_p < 1.1 \mu\text{m}$  are able to enter the main tube when they are injected, together with the gas, through the swirl generator. Larger droplets, having sizes between  $1.1 \leq d_p \leq 2.3 \mu\text{m}$ , are trapped in the vortex chamber. Droplets larger than  $d_p > 2.3 \mu\text{m}$  will be swirled towards the outer walls of the vortex chamber, immediately after they are injected into the vortex chamber.

The trajectories of droplets in the main tube depend on the initial droplet size and the positions at which droplets are released. Droplets larger than approximately  $1 \mu\text{m}$  are able to reach the main tube wall due to the centrifugal force. Smaller droplets, however, evaporate before they reach the tube wall. The evaporation and condensation processes are related to the local relative humidity, which can be adjusted by changing the water vapour content in the plenum gas.

From the droplet trajectories, we have computed liquid concentrations. According to the model, droplets are found in the region  $zD^{-1} < 7$ , dependent on the relative humidity of the plenum gas. Droplets that are released in the core region are transported directly towards the cold exit and do not enter the main tube. Droplets that are able to enter the main tube,

are swirled towards the wall or evaporate. Because of these effects, the experimental domain where PDPA measurements can be performed is very limited in size.

### 7.1.2 Experimental methods and equipment

A new laboratory has been set up for the experimental studies of the RHVT. The mass flows and cold fraction can be controlled via a mass flow control system, while pressures, temperatures, and relative humidities can simultaneously be recorded.

Details of the experimental RHVT are provided. Two types of swirl generators can be mounted into the vortex chamber to investigate their influences on the flow and temperatures. The first swirl generator was already available from a previous study. A new version of the swirl generator was designed and fabricated to maximize the injection velocity, based on 1D compressible gas dynamics and the properties of the nitrogen supply system.

3D PDPA equipment has been purchased to measure the velocities and sizes of the water droplets in the RHVT. The system is mounted onto a fully automated translation system to be able to move and position the measurement volume in the RHVT. Specially designed optically transparent measurement sections were produced through which the PDPA measurements can take place. The optical distortion is negligible because of the very small thickness (0.35 mm) of the window material. By means of a ray tracing analysis, we have computed that there is sufficient overlap of the laser beams to perform the PDPA measurements inside the RHVT.

A gas conditioning system has been developed in order to humidify the nitrogen gas. In a pressure vessel, water is injected via high pressure spray nozzles, creating numerous droplets. The droplets evaporate, thereby humidifying the nitrogen gas. The humidity of the plenum gas can be varied by changing the mass flow of water, the nitrogen temperature, and the nitrogen mass flow.

### 7.1.3 Experimental study of flow and droplet behaviour in the RHVT

The influence of the acceleration of the gas through the nozzles in the swirl generator on the sizes of droplets that are injected was investigated. Assuming that droplets break up if the Weber number  $We > 1$ , the droplets that will enter the vortex chamber are generally not larger than 10  $\mu\text{m}$ .

The Stokes number is determined to be  $Stk = \mathcal{O}(1)$  for 1  $\mu\text{m}$  droplets. This means that only the larger scale velocity fluctuations are resolved with the PDPA measurements.

In a turbulent pipe flow experiment (Reynolds number of  $Re = 10300$ ), velocities have been measured as a test case for LDA. The measured velocities and turbulent fluctuations are in good agreement with DNS results, indicating that accurate measurements can be made by using the transparent measurement sections.

Various PDPA experiments have been performed. The main results of the velocity measurements are:

- The radial velocity component is  $U_r < 0.1U_\theta$  and increases with  $r$ ;
- The swirl velocity shows that the vortex is similar to a solid body vortex and increases with increasing cold fraction;
- The axial velocity is positive (directed towards the hot exit) near the wall and negative at the tube axis for  $\varepsilon > 0$ . For the case that  $\varepsilon = 0$ , the axial velocity is positive at the axis;

- The standard deviations of the velocity fluctuations are similar to each other in the core region. The relative fluctuation intensity reaches values of more than 30% at the axis and decreases towards the wall;
- The cold fraction has a major influence on the velocities in the RHVT. Not only the magnitude of the velocities, but also the velocity profiles are affected by changing  $\varepsilon$ ;
- The mass flow has only little influence on the shape of the velocity profiles. The velocity profiles are scalable with the square root of the mass flow;
- The geometry of the swirl generator has no significant influence on the velocities for the operating conditions used;

The velocity exhibits a high amplitude fundamental frequency that is approximately equal to the angular velocity of the mean flow. This frequency has the highest amplitude at the axis of the RHVT and is the cause for the high fluctuation intensity. The fundamental frequency is found in both the swirl and axial velocity components. It is expected that it is present in the radial velocity component as well. With increasing  $r$ , higher orders (up to the seventh) of the fundamental frequency are present in the flow. The reason that these high magnitude frequencies exist is that the vortex is not axisymmetric, but wobbles around the main tube axis (vortex wobbling or precession of the vortex). It has been determined that 75% of the magnitude of the fluctuations at the axis, and 20% near the wall is caused by the wobbling of the vortex. Consequently, the turbulence intensity is less than 10%.

The majority of the measured droplets in the RHVT are smaller than 2  $\mu\text{m}$ . Because of vortex wobbling, droplets are trapped in the vortex and there is no correlation between droplet size and radial droplet velocity. Furthermore, droplets do not reach the main tube wall, but remain suspended in the gas, making it impossible to have an easy-to-remove liquid film. It is expected that the vortex wobbling has, consequently, a negative influence on the performance of the RHVT as a separator. However, the vortex wobbling might be a key mechanism for the thermal performance of the vortex tube.

#### 7.1.4 Energy separation in the RHVT

A relatively simple, but accurate analytical energy separation model has been developed that can be used to predict the thermodynamics in the RHVT, provided that the main tube is sufficiently long ( $L/D > 20$ ). The exit temperatures, heating/cooling powers, and isentropic efficiencies, can be computed if the geometry of the swirl generator, properties of the gas, and the pressures in the plenum and exits are known.

Various experiments were conducted to validate the model. Temperatures, pressures and mass flows were simultaneously measured. Results show that modeled quantities are in good agreement with the experimental results (the error in the predicted temperatures is typically less than 1%). The computed quantities are made dimensionless with the plenum temperature, mass flow and heat capacity of the gas, making comparison between experiments under different operating conditions possible.

The energy separation model forms a basis for an engineering (design) tool that can be used to optimize the RHVT geometry, or make thermodynamical predictions of the RHVT as gas separator.

### 7.1.5 Preliminary study of the RHVT as separator

The water content of the gas mixtures in the plenum and exits of the RHVT can be determined experimentally, with a relative uncertainty of less than 10%. Experimental results of a preliminary water vapour separation experiment indicate that a water vapour enrichment of 37% can be achieved in the hot exit stream of the RHVT.

The energy separation model is coupled to a commercial program that is able to compute various properties of gas mixtures. This allows us to predict the thermodynamics of the RHVT when it is operated with real gases. It is possible to have various gas mixtures, such as  $\text{CO}_2$  and  $\text{CH}_4$  or  $\text{CO}_2$  and  $\text{N}_2$ , as working medium. The model accounts for the possibility that phase changes occur.

An example computation of a plenum gas mixture  $50\%_{mol}\text{CO}_2 + 50\%_{mol}\text{CH}_4$  is provided. According to the results, a maximum overall gaseous methane enrichment of 13% can be achieved in a RHVT with  $\tau_R = 2$  at a plenum pressure of 70 bar, a cold exit pressure of 30 bar, and a cold fraction of  $\varepsilon = 0.30$ . The overall enrichment is larger for a RHVT with  $\tau_R = 1$  and is  $\eta_{\text{CH}_4} = 25\%$  at  $\varepsilon = 0.40$ . These results reveal that the RHVT is suitable to condense undesired components in the cold stream, thereby increasing the mass fraction of the gaseous product.

## 7.2 Recommendations

Based on the conclusions and experiences that I gained during my study on the RHVT, I have the following recommendations for further studies:

- The wobbling of the vortex in the main tube reduces the effect of the centrifugal force on the motion of droplets. Therefore, it has a major influence on the efficiency of the RHVT as a droplet separator. Stabilizing the vortex to prevent wobbling might be an option to enhance the centrifugal separation of droplets. Stabilization may be achieved by inserting an inner body in the RHVT or by reducing the precession of the vortex axis, by introducing asymmetry in the flow (by means of, for example, an asymmetric nozzle configuration in the swirl generator).
- It remains unclear how large the contribution of the vortex wobbling is to the energy separation phenomenon. The main question is: is turbulence the cause for the existence of the temperature difference in the RHVT, or is it the vortex wobbling, or is it crucial to have a combination of both? This is a very interesting topic for future studies.
- More experiments should be performed to study the separation of a mixture of nitrogen, water vapour, and water droplets. In the case of the formation of a liquid film on the wall, the water must be removed via slot separators and the amount of water that is removed must be measured in order to determine the separation efficiency;
- Based on the specifications of the humidity sensors, the uncertainty in the measured relative humidity is very high at low relative humidities, which is mostly the case for the hot gas. A way to overcome this problem is to cool the gas in order to increase the humidity and thus the accuracy, which is based on the sensor specifications. To cool the hot gas, we may use the cold gas that is produced by the RHVT. The cold gas and hot gas could be fed through a heat exchanger, thereby lowering the temperature of the hot gas while increasing the temperature of the cold gas. The humidity in the hot exit



is thereby increased and humidity measurements become more accurate. An additional advantage might be that the droplets that are present in the cold gas will evaporate, thereby enabling relative humidity measurements directly in the cold stream (cold gas sampling and heating is not required anymore);

- The energy separation model should be tested by using different (commercial) vortex tubes. In this way, we are able to study the validity of the model over a wider range of geometries. Based on the model, optimum geometries of the swirl generator, main tube, and cold exit can be found. These optima should be validated by comparing them with geometries of commercial vortex tubes.
- Ice formation in the cold exit when water is injected together with the nitrogen gas is a major problem. Because of the ice, the cold exit gets clogged and the mass flow and cold fraction cannot be controlled anymore. Heating the plenum gas to significant temperatures will result in higher cold stream temperatures. If the plenum temperature is high enough, the cold stream temperature is above the freezing point, and ice formation is prevented.



# A | Properties of water and nitrogen

## Properties of water

- The **saturation vapour pressure of water** was computed as a function of the temperature,  $T$  (Hardy, 1998). Enhancement factors, which need to be incorporated for high pressures in the presence of other gases than water vapour, are neglected. For example, the increase in saturation vapour pressure of water in nitrogen is 3% when the pressure is 10 bar.

$$\ln \left( \frac{p_{sat}}{p_{ref}} \right) = \sum_{i=0}^6 a_i \left( \frac{T}{T_{ref}} \right)^{i-2} + a_7 \ln \left( \frac{T}{T_{ref}} \right), \quad (\text{A.1})$$

where  $p_{sat}$  is the saturation vapour pressure of water in Pascals, and  $T$  is the absolute temperature in Kelvin. The reference pressure and temperature are  $p_{ref} = 1$  Pa and  $T_{ref} = 1$  K, respectively. The coefficients in Eq. (A.1) are

$$\begin{aligned} a_0 &= -2.8365744 \cdot 10^3 \\ a_1 &= -6.028076559 \cdot 10^3 \\ a_2 &= 1.954263612 \cdot 10^1 \\ a_3 &= -2.737830188 \cdot 10^{-2} \\ a_4 &= 1.6261698 \cdot 10^{-5} \\ a_5 &= 7.0229056 \cdot 10^{-10} \\ a_6 &= -1.8680009 \cdot 10^{-13} \\ a_7 &= 2.7150305 \end{aligned}$$

- The **diffusion coefficient for water vapour in nitrogen gas** was approximated by the diffusion coefficient of water vapour in air (see Montgomery (1947) and references therein). For gases, the dependence of diffusivity on pressure and temperature is

$$\frac{\mathcal{D}}{\mathcal{D}_0} = \left( \frac{T}{T_0} \right)^{1.75} \frac{p_0}{p}, \quad (\text{A.2})$$

where  $T_0 = 273.15$  K and  $p_0 = 10^5$  Pa are the reference temperature and pressure, respectively. The diffusion coefficient at the reference condition is  $\mathcal{D}_0 = 2.26 \cdot 10^{-5}$  m<sup>2</sup>/s.

- The **latent heat of vaporization of water** as a function of temperature was approximated by a linear function that was fitted to tabulated data (NIST, 2013) between  $275 \text{ K} \leq T \leq 350 \text{ K}$ , reading

$$h_{fg} = 3.1575 \cdot 10^6 - 2.4012 \cdot 10^3 T. \quad (\text{A.3})$$

- Other properties are (NIST, 2013):
  - The specific heat capacity of water is  $c_w = 4.18 \cdot 10^3 \text{ J/(kg}\cdot\text{K)}$ ;
  - The molar mass is taken to be  $M_{\text{H}_2\text{O}} = 0.018 \text{ kg/mol}$ ;
  - The mass density of water  $\rho_p = 998 \text{ kg/m}^3$ .
  - The surface tension  $\gamma_p = 0.0728 \text{ N/m}$ .

### Properties of nitrogen

The universal gas constant is given by  $\mathcal{R} = 8.314 \text{ J/(mol}\cdot\text{K)}$ . The ratio of specific heat capacities at constant pressure and constant volume is  $\gamma = \frac{c_p}{c_v} = 1.4$ .

- Molar mass:  $M_{\text{N}_2} = 0.028 \text{ kg/mol}$ .
- Density  $\rho_f = \frac{p}{\mathcal{R}T}$ , where  $\overline{\mathcal{R}} = \frac{\mathcal{R}}{M_{\text{N}_2}}$ .
- Dynamic viscosity is
 
$$\mu_f = -3.228 \cdot 10^{-11} T^2 + 6.548 \cdot 10^{-8} T + 1.159 \cdot 10^{-6} \text{ Pa}\cdot\text{s}.$$
- Specific heat capacity at constant pressure  $c_p = 1.05 \cdot 10^3 \text{ J/(kg}\cdot\text{K)}$  (at  $p = 6 \text{ bar}$ ).

## B | Ray tracing analysis

This ray tracing analysis is used to model the refraction of laser beams through an cylindrical window with an inner radius  $R_i$  and outer radius  $R_o$ . In Fig. B.1 it is shown how a ray is refracted trough a cylindrical window and the most important variables are indicated. We are interested to compute the actual position of the measurement volume as a function of the displacement of the LDA probe. In the figure,  $x$  is the coordinate along the optical axis of the LDA probe and  $y$  is the vertical coordinate. Because the optical axis of the LDA probe is normal to the axis of the cylindrical tube, the domain is symmetrical to the  $x$ -axis and only the upper half of the domain is plotted here. The coordinate at which the laser beam crosses the  $x$ -axis, is the crossing point of the laser beams, i.e.  $x_{MV}$ . The displacement of the LDA probe with respect to the axis of the cylindrical window, which is located at  $x = 0$ , is  $x_{LDA}$ .

The origin of the ray (the laser beam) is located in point  $\mathbf{p}_0 = [x_0, y_0]^T$ . Its  $x$ -coordinate is found according to

$$x_0 = \frac{y_0}{d_0} + x_{LDA}, \quad (\text{B.1})$$

where  $y_0$  is the half of the initial beam spacing,  $d_0 = \tan(\alpha_0)$  is the slope of the ray, and  $\alpha_0 = \kappa$  is the half of the beam angle. The direction of the ray is  $\mathbf{v}_1 = [-\cos(\alpha_0), -\sin(\alpha_0)]^T$ , and the point at which the ray hits the window is point  $\mathbf{p}_1 = [x_1, y_1]^T$ . After some math, we find the coordinates of this point to be

$$\begin{aligned} x_1 &= \frac{x_0 d_0^2 + \left( R_o^2 (d_0^2 + 1) - (x_0 d_0 - y_0)^2 \right)^{0.5} - y_0 d_0}{d_0^2 + 1}; \\ y_1 &= \sqrt{R_o^2 - x_1^2}. \end{aligned} \quad (\text{B.2})$$

The outer interface normal  $\mathbf{n}_1$  at point  $\mathbf{p}_1$  is

$$\mathbf{n}_1 = \frac{\mathbf{p}_1}{R_o}, \quad (\text{B.3})$$

and with the direction of the ray, the incident angle with respect to the outer interface normal, i.e.  $\theta_{i,1}$ , is given by

$$\cos(\theta_{i,1}) = \frac{\mathbf{v}_1 \cdot \mathbf{n}_1}{|\mathbf{v}_1| |\mathbf{n}_1|} = \mathbf{v}_1 \cdot \mathbf{n}_1. \quad (\text{B.4})$$

According to Snell's law of refraction, Eq. (3.16), the refracted angle  $\theta_{r,1}$  is

$$\theta_{r,1} = \arcsin \left( \frac{n_a}{n_b} \sin(\theta_{i,1}) \right), \quad (\text{B.5})$$

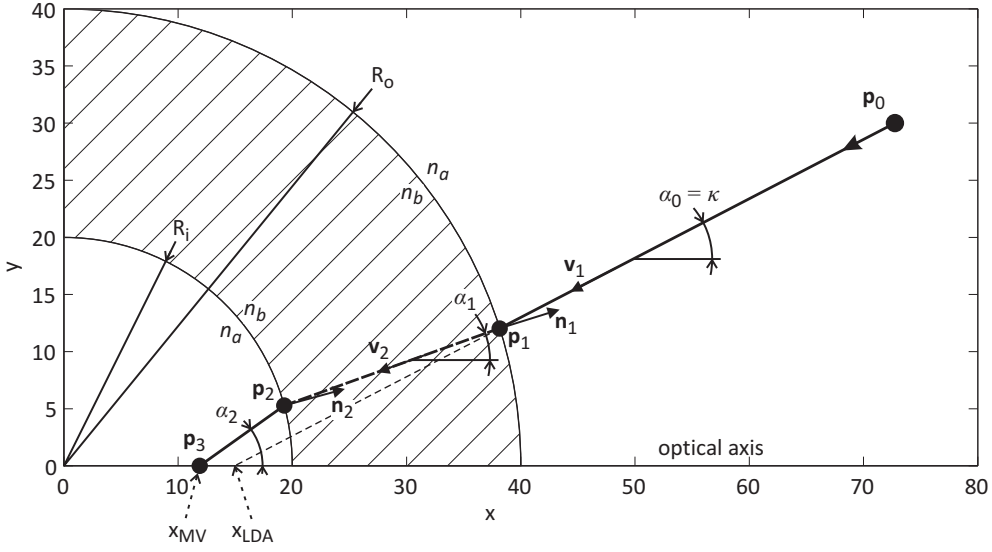


Figure B.1: A laser beam refracting through an cylindrical window. The solid lines are the parts of the ray that is present in air, the thick dashed line is the part of the ray that is present in the window material. The thin dashed line indicates the path of the ray if there was no window present.

where  $n_a$  and  $n_b$  are the refractive indices of air and the window material, respectively. This angle represents the angle of the refracted ray (the thick dashed line) with respect to the interface normal. With respect to the optical axis of the LDA, the angle becomes

$$\alpha_1 = \arctan\left(\frac{y_1}{x_1}\right) + \theta_{r,1}. \quad (\text{B.6})$$

Using the computed  $\mathbf{p}_1$  and  $\alpha_1$ , we repeat the same analysis as above. In short:  $d_1 = \tan(\alpha_1)$  and  $\mathbf{p}_2 = [x_2, y_2]^T$ , with

$$\begin{aligned} x_2 &= \frac{x_1 d_1^2 + \left(R_i^2 (d_1^2 + 1) - (x_1 d_1 - y_1)^2\right)^{0.5} - y_1 d_1}{d_1^2 + 1}; \\ y_2 &= \sqrt{R_i^2 - x_2^2}. \end{aligned} \quad (\text{B.7})$$

The second interface normal is

$$\mathbf{n}_2 = \frac{\mathbf{p}_2}{R_i}, \quad (\text{B.8})$$

and the incident angle becomes

$$\cos(\theta_{i,2}) = \mathbf{v}_2 \cdot \mathbf{n}_2, \quad (\text{B.9})$$

where  $\mathbf{v}_2 = [-\cos(\alpha_1), -\sin(\alpha_1)]^T$ . The refracted angle becomes

$$\theta_{r,2} = \arcsin\left(\frac{n_b}{n_a} \sin(\theta_{i,2})\right), \quad (\text{B.10})$$

and

$$\alpha_2 = \arctan\left(\frac{y_2}{x_2}\right) + \theta_{r,2}. \quad (\text{B.11})$$

Finally, the  $x$ -coordinate of the measurement volume  $x_{MV}$  is found with

$$x_{MV} = x_2 - \frac{y_2}{d_2}, \quad (\text{B.12})$$

where  $d_2 = \tan(\alpha_2)$ . The discrepancy between refracted and non-refracted locations of the the measurement volume is

$$\delta_{cyl} = x_{LDA} - x_{MV}. \quad (\text{B.13})$$

The half crossing angle of the refracted laser beams is

$$\kappa' = \alpha_2, \quad (\text{B.14})$$

and the relative difference in crossing angle is

$$\Delta\kappa = \left(\frac{\kappa'}{\kappa} - 1\right) \times 100\%. \quad (\text{B.15})$$





## C | Uncertainty analysis mixing ratio

The mixing ratio is computed according to

$$\text{MR} = \frac{\Gamma}{1 - \Gamma} \frac{M_{\text{H}_2\text{O}}}{M_{\text{N}_2}} = \frac{M_{\text{H}_2\text{O}}}{M_{\text{N}_2}} \left( \frac{p}{p_{\text{sat}}(T)\text{RH}} - 1 \right)^{-1}, \quad (\text{C.1})$$

where,  $M_{\text{H}_2\text{O}}$  and  $M_{\text{N}_2}$  are the molar masses of water and nitrogen, respectively,  $p$  is the pressure,  $p_{\text{sat}}$  is the saturation vapour pressure of water, and RH is the relative humidity.

The absolute uncertainty in the mixing ratio due to the accuracy of the sensors,  $\delta\text{MR}$ , is given by

$$\delta\text{MR} = \sqrt{\left( \frac{\partial\text{MR}}{\partial p} \delta p \right)^2 + \left( \frac{\partial\text{MR}}{\partial p_{\text{sat}}} \delta p_{\text{sat}} \right)^2 + \left( \frac{\partial\text{MR}}{\partial \text{RH}} \delta \text{RH} \right)^2}, \quad (\text{C.2})$$

where  $\delta p = 420$  Pa and  $\delta \text{RH} = 0.02$  are the absolute uncertainties in pressure and relative humidity. The values for these are provided known from calibration reports (details are provided in §3.5.3). The uncertainty in saturation vapour pressure of water,  $\delta p_{\text{sat}}$ , is

$$\delta p_{\text{sat}} = \frac{\partial p_{\text{sat}}}{\partial T} \delta T, \quad (\text{C.3})$$

from which  $\delta T = 0.5$  K is also known from the calibration reports. The partial derivative of the saturation vapour pressure of water over temperature is approximated by

$$\delta p_{\text{sat}} \simeq \frac{p_{\text{sat}}(T + e) - p_{\text{sat}}(T - e)}{2e} \delta T, \quad (\text{C.4})$$

where  $e \ll T$  is a small number and  $p_{\text{sat}}$  is computed with Eq. (A.1). The partial derivatives of the mixing ratio are

$$\frac{\partial\text{MR}}{\partial p} = -\frac{M_{\text{H}_2\text{O}}}{M_{\text{N}_2}} \frac{p_{\text{sat}}\text{RH}}{(p - p_{\text{sat}}\text{RH})^2} \quad (\text{C.5a})$$

$$\frac{\partial\text{MR}}{\partial p_{\text{sat}}} = \frac{M_{\text{H}_2\text{O}}}{M_{\text{N}_2}} \left( \frac{\text{RH}}{p - p_{\text{sat}}\text{RH}} + \frac{p_{\text{sat}}\text{RH}^2}{(p - p_{\text{sat}}\text{RH})^2} \right) \quad (\text{C.5b})$$

$$\frac{\partial\text{MR}}{\partial \text{RH}} = \frac{M_{\text{H}_2\text{O}}}{M_{\text{N}_2}} \left( \frac{p_{\text{sat}}}{p - p_{\text{sat}}\text{RH}} + \frac{p_{\text{sat}}^2\text{RH}}{(p - p_{\text{sat}}\text{RH})^2} \right) \quad (\text{C.5c})$$

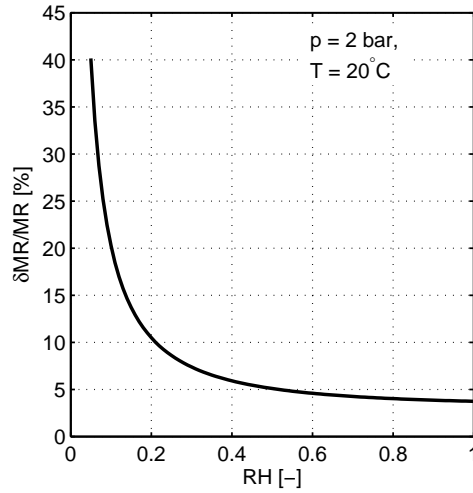


Figure C.1: Relative uncertainty as a function of the relative humidity are  $p = 2 \text{ bar}$  and  $T = 20^\circ \text{C}$

Using Eq. (C.2), we have computed the relative uncertainty  $\delta MR/MR$  as a function of the relative humidity. The resulting relative uncertainty is plotted in Fig. C.1 as a function of the relative humidity, and shows very high uncertainties at low relative humidities. The uncertainty of the humidity sensor, which is 2%, has the largest contribution in the uncertainty of the mixing ratio. The relative uncertainty shown in Fig. C.1 will therefore not change significantly by changing the temperature or pressure.

## References

- AHLBORN, B.K. & GROVES, S. (1997). Secondary flow in a vortex tube. *Fluid. Dyn. Res.*, **21**, 73–86. 60, 62, 86, 112
- AHLBORN, B.K., KELLER, J.U., STAUDT, R., TREITZ, G. & REBHAN, E. (1994). Limits of temperature separation in a vortex tube. *J. Phys. D: Appl. Phys.*, **27**, 480–488. 6, 107, 112
- AHLBORN, B.K., CAMIRE, J. & KELLER, J.U. (1996). Low pressure vortex tubes. *J. Phys. D: Appl. Phys.*, **29**, 1469–1472. 125
- AHLBORN, B.K., KELLER, J.U. & REBHAN, E. (1998). The heat pump in a vortex tube. *J. Non-Equil. Thermodyn.*, **23**, 159–165. 6, 112, 113, 114, 116, 119
- AIRTX (2013). <http://www.airtx.com/vortex-tubes>. 6
- ALBRECHT, H.E. (2003). *Laser doppler and phase doppler measurement techniques*. Springer. 48
- ALJUWAYHEL, N.F., NELLIS, G.F. & KLEIN, S.A. (2005). Parametric and internal study of the vortex tube using a CDF model. *Int. J. Refrig.*, **28**, 442–450. 112, 115
- AVVARU, B., PATIL, M.N., GOGATE, P.R. & PANDIT, A.B. (2005). Ultrasonic atomization: Effect of liquid phase properties. *Ultrasonics*, **44**, 146–158. 67
- BACHALO, W.D. & HOUSER, M.J. (1984). Phase/Doppler spray analyzer for simultaneous measurements of drop size and velocity distributions. *Opt. Eng.*, **23**, 583–591. 48, 50
- BANSAL, G.D., GOLOMBOK, M., BROUWERS, J.J.H. & TESSELAAR, G. (2011). CO<sub>2</sub> droplets condensed from natural gas. *Ind. Eng. Chem. Res.*, **50**, 3011–3020. 3
- BARNETT, D.O. & BENTLEY, H.T. (1974). Statistical bias of individual realization laser velocimeters. *Proc. Second Int. Workshop on Laser Velocimetry*, **1**, 428–444. 82
- BEHERA, U., PAUL, P.J., KASTHURIRENGAN, S., KARUNANITHI, R., RAM, S.N., DINESH, K. & JACOB, S. (2005). CDF analysis and experimental investigations towards optimizing the parameters of Ranque-Hilsch vortex tube. *Int. J. Heat Mass Tran.*, **48**, 1961–1973. 112
- BIRD, B.R., STEWART, W.E. & LIGHTFOOT, E.N. (2007). *Transport Phenomena*. John Wiley & Sons, Inc., 2nd edn. 12, 104

- BP (2012). Statistical review of world energy. Tech. rep., British Petroleum. 1
- BRADLEY, D. (1965). *The Hydrocyclone*. Pergamon Press, 1st edn. 2, 3
- BROUWERS, J.J.H. (1996). Rotational particle separator: A new method for separating fine particles and mists from gases. *Chem. Eng. Technol.*, **19**, 1–10. 3
- BROUWERS, J.J.H. (1997). Particle collection efficiency of the rotational particle separator. *Powder Technol.*, **92**, 89–99. 3
- CHAKER, M.A., MEHER-HOMJI, C.B. & MEE, T. (2002). Inlet fogging of gas turbine engines - Part B: Fog droplet sizing analysis, nozzle types, measurement and testing. *Proc. ASME Turbo Expo*. 64
- CIA (2012). The world factbook. 1
- CORTES, C. & GIL, A. (2007). Modeling the gas and particle flow inside cyclone separators. *Prog. Energy Combust. Sci.*, **33**, 409–452. 7
- CRANK, J. & NICOLSON, P. (1947). A practical method for numerical evaluation of solutions of partial differential equations of the heat-conduction type. *Proc. Camb. Phil. Soc.*, **43**, 50–67. 19
- CROWE, C.T., SCHWARZKOPF, J.D., SOMMERFELD, M. & TSUJI, Y. (2012). *Multiphase Flows With Droplets and Particles*. CRC Press. 12
- CUNNINGHAM, E. (1910). On the velocity of steady fall of spherical particles through fluid medium. *Proc. R. Soc. Lond. A*, **83**, 357–365. 12
- DAVIES, C.N. (1945). Definitive equations for the fluid resistance of spheres. *Proc. Phys. Soc.*, **57**, 259–270. 12
- DEISSLER, R.G. & PERLMUTTER, M. (1960). Analysis of the flow and energy separation in a turbulent vortex. *Int. J. Heat Mass Tran.*, **1**, 173–191. 6, 111, 113, 114
- DEN TOONDER, J.M.J. & NIEUWSTADT, F.T.M. (1997). Reynolds number effects in a turbulent pipe flow for low to moderate Re. *Phys. Fluids*, **9**, 3398–3409. 83
- DERKSEN, J.J. & VAN DEN AKKER, H.E.A. (2000). Simulation of vortex core precession in a reverse-flow cyclone. *A.I.Ch.E. Journal*, **46**, 1317–1331. 99
- DEUSS, K.R.M. (2012). LDA measurements in the vortex tube. Tech. rep., Eindhoven University of Technology. 54
- DURST, F., KIKURA, H., LEKAKIS, I., JOVANOVIĆ, J. & YE, Q. (1996). Wall shear stress determination from near-wall mean velocity data in turbulent pipe and channel flows. *Exp. Fluids*, **20**, 417–428. 82
- DUTTA, T., SINHAMAHAPATRA, K.P. & BANDYOPDHYAY, S.S. (2010). Comparison of different turbulence models in predicting the temperature separation in a Ranque-Hilsch vortex tube. *Int. J. Refrig.*, **33**, 783–792. 112

- 
- EGGELS, J.G.M., UNGER, F., WEISS, M.H., WESTERWEEL, J., ADRIAN, R.J., FRIEDRICH, R. & NIEUWSTADT, F.T.M. (1994). Fully developed turbulent pipe flow: a comparison between direct numerical simulation and experiment. *J. Fluid. Mech.*, **268**, 175–209. 83
- EIAMSAR-ARD, S. & PROMVONGE, P. (2007). Numerical investigation of the thermal separation in a Ranque-Hilsch vortex tube. *Int. J. Heat Mass Tran.*, **50**, 821–832. 112
- EIAMSAR-ARD, S. & PROMVONGE, P. (2008a). Numerical simulation of flow field and temperature separation in a vortex tube. *Int. Commun. Heat Mass*, **35**, 937–947. 112
- EIAMSAR-ARD, S. & PROMVONGE, P. (2008b). Review of Ranque-Hilsch effects in vortex tubes. *Renew. Sust. Energ. Rev.*, **12**, 1822–1842. 7, 112, 119
- ELGHOBASHI, S. (1994). On predicting particle-laden turbulent flows. *Appl. Sci. Res.*, **52**, 309–329. 11, 77
- EXAIR (2013). <http://www.exair.com>. 6
- FAETH, G.M. (1977). Current status of droplet and liquid combustion. *Prog. Energy Combust. Sci.*, **3**, 191–224. 13, 15
- FAROUK, T. & FAROUK, B. (2007). Large eddy simulations of the flow field and temperature separation in the Ranque-Hilsch vortex tube. *Int. J. Heat Mass Tran.*, **50**, 4724–4735. 6, 112, 115
- FERRON, G.A. & SODERHOLM, S.C. (1990). Estimation of the times for evaporation of pure water droplets and for stabilization of salt solution particles. *J. Aerosol Sci.*, **21**, 415–429. 18
- FILTAN (2013). <http://www.filtan-gas.com/ingles/indexen.html>. 8
- FRÖHLINGS DORF, W. & UNGER, H. (1999). Numerical investigations of the compressible flow and the energy separation in the Ranque-Hilsch vortex tube. *Int. J. Heat Mass Tran.*, **42**, 415–422. 6, 112, 113, 115
- FUKUMOTO, Y. & OKULOV, V.L. (2005). The velocity field induced by a helical vortex tube. *Phys. Fluids*, **17**, 107101. 98
- GAO, C.M. (2005). *Experimental Study on the Ranque-Hilsch Vortex Tube*. Ph.D. thesis, Eindhoven University of Technology. 9, 12, 19, 23, 24, 26, 27, 28, 29, 46, 95, 107, 112, 113, 116
- GAO, C.M., BOSSCHAART, K.J., ZEEGERS, J.C.H. & DE WAELE, A.T.A.M. (2005). Experimental study on a simple Ranque-Hilsch vortex tube. *Cryogenics*, **45**, 173–183. 60, 62, 86
- HAJDIK, B., MANFRED, L., JURGEN, S. & KEITH, T. (1997). Vortex tube can increase liquid hydrocarbon recovery at plant inlet. *Oil and Gas Journal*, **95**, 76–83. 7
- HARDY, B. (1998). ITS-90 Formulations for vapor pressure, frostpoint temperature, dew-point temperature, and enhancement factors in the range -100 to +100 C. *Int. Symp. Hum. Moist.*. 151

- HEIST, R.H. & REISS, H. (1973). Investigation of the homogeneous nucleation of water vapor using a diffusion cloud chamber. *J. Chem. Phys.*, **59**, 665–671. 17
- HELLYAR, K.G. (1979). *Gas Liquefaction using a Ranque-Hilsch vortex tube: Design criteria and bibliography*. Master's thesis, Massachusetts Institute of Technology. 7
- HERRIN, J.L. & DUTTON, J.C. (1993). An investigation of LDV velocity bias correction techniques for high speed separated flows. *Exp. Fluids*, **14**, 354–363. 82
- HILSCH, R. (1947). The use of the expansion of gases in a centrifugal field as cooling process. *Rev. Sci. Instr.*, **18**, 108–113. 4, 6, 111
- HOEKSTRA, A.J., ISRAEL, A.T., DERKSEN, J.J. & VAN DEN AKKER, H.E.A. (1998). The application of laser diagnostics to cyclonic flow with vortex precession. *9th Int. Symp.: Appl. Laser Techn. Fluid Mech.* 99, 101
- HOEKSTRA, A.J., DERKSEN, J.J. & VAN DEN AKKER, H.E.A. (1999). An experimental and numerical study of turbulent swirling flow in gas cyclones. *Chem. Eng. Sci.*, **54**, 2055–2065. 2, 99
- HOESEL, W. & RODI, W. (1977). New biasing elimination method for laser doppler velocimeter counter processing. *Rev. Sci. Instr.*, **48**, 910–919. 82
- HOLTERMAN, H.J. (2003). Kinetics and evaporation of water drops in air. Tech. rep., IMAG Wageningen. 18, 19
- IJZERMANS, R.H.A., HAGMEIJER, R. & VAN LANGEN, P.J. (2007). Accumulation of heavy particles around a helical vortex filament. *Phys. Fluids*, **19**, 107102. 98, 104
- ITW-VORTEC (2013). <http://www.vortec.nl>. 6
- JANNA, W.S. (2000). *Engineering Heat Transfer*. CRC Press, 2nd edn. 18
- KAZANTSEVA, O.V., PIRALISHVILI, S.A. & FUZEEVA, A.A. (2005). Numerical simulation of swirling flows in vortex tubes. *High Temp.*, **43**, 608–613. 6, 112
- KROES, J.P. (2012). *Droplet collection in a scaled-up rotating separator*. Ph.D. thesis, Eindhoven University of Technology. 3
- KUERTEN, J.G.M., VAN ESCH, B.P.M., VAN KEMENADE, H.P. & BROUWERS, J.J.H. (2007). The effect of turbulence on the efficiency of the rotational phase separator. *Int. J. Heat Fluid Fl.*, **28**, 630–637. 104
- KUNDU, P.K. & COHEN, I.M. (2008). *Fluid Mechanics*. Elsevier Inc., 4th edn. 12, 23, 43
- KUO, K.K. (2005). *Principles of Combustion*. John Wiley & Sons, Inc., 2nd edn. 13
- KUROSAKA, M. (1982). Acoustic streaming in swirling flow and the Ranque Hilsch (vortex - tube) effect. *J. Fluid. Mech.*, **124**, 139–172. 6, 95, 112
- LAMB, H. (1932). *Hydrodynamics*. Cambridge University Press, 6th edn. 98
- LANG, R.J. (1962). Ultrasonic atomization of liquids. *J. Acoust. Soc. Am.*, **34**, 6–8. 63, 67

- 
- LIEFKENS, B.N.J. (2012). Ranque-Hilsch vortex tube humidity measurements. Tech. rep., Eindhoven University of Technology. 134
- LIEW, R., ZEEGERS, J.C.H., KUERTEN, J.G.M. & MICHAŁEK, W.R. (2012). Maxwell's Demon in the Ranque-Hilsch Vortex Tube. *Phys. Rev. Lett.*, **109**, 054503. 111
- LIEW, R., ZEEGERS, J.C.H., KUERTEN, J.G.M. & MICHAŁEK, W.R. (2013). 3D Velocimetry and droplet sizing in the Ranque-Hilsch vortex tube. *Exp. Fluids*, **54**, 1416. 75
- LINDERSTRØM-LANG, C.U. (1964). Gas separation in the Ranque-Hilsch vortex tube. *Int. J. Heat Mass Tran.*, **7**, 1195–1206. 7
- LINDERSTRØM-LANG, C.U. (1971). The three-dimensional distributions of tangential velocity and total-temperature in vortex tubes. *J. Fluid. Mech.*, **45**, 161–187. 6, 111
- LITVINOV, I.V., SHTORK, S.I., KUIBIN, P.A., ALEKSEENKO, S.V. & HANJALIC, K. (2013). Experimental study and analytical reconstruction of precessing vortex in a tangential swirler. *Int. J. Heat Fluid Fl.* 99
- MATBASE (2012). <http://www.matbase.com/material/polymers/commodity/pmma>. 58
- MAXEY, M.R. & RILEY, J.J. (1983). Equation of motion for a small rigid sphere in a nonuniform flow. *Phys. Fluids*, **26**, 883–839. 12, 76
- MCLAUGHLIN, D.K. & TIEDERMAN, W.G. (1973). Biasing correction for individual realization of laser anemometer measurements in turbulent flows. *Phys. Fluids*, **16**, 2082–2088. 82
- MICHAŁEK, W.R. (2013). *To be submitted*. Ph.D. thesis, Eindhoven University of Technology. 116
- MILLER, R.C., ANDERSON, R.J., KASSNER, JR, J.L. & HAGEN, D.E. (1983). Homogeneous nucleation rate measurements for water over a wide range of temperature and nucleation rate. *J. Chem. Phys.*, **6**, 3204–3211. 17
- MONDT, E. (2005). *Compact centrifugal separator of dispersed phases*. Ph.D. thesis, Eindhoven University of Technology. 1
- MONTGOMERY, R.B. (1947). Viscosity and thermal conductivity of air and diffusivity of water vapor in air. *J. Meteorology*, **4**, 193–196. 151
- NIMBALKAR, S.U. & MULLER, M.R. (2009). An experimental investigation of the optimum geometry for the cold end orifice of a vortex tube. *Appl. Therm. Eng.*, **29**, 509–514. 7
- NIST (2013). <http://webbook.nist.gov/chemistry/>. 152
- O'DOHERTY, T., GRIFFITHS, A.J., SYRED, N., BOWEN, P.J. & FICK, W. (1999). Experimental analysis of rotating instabilities in swirling and cyclonic flows. *Dev. Chem. Eng. Mineral Process*, **7**, 245–267. 99
- OERTEL, H. (2010). *Prandtl - Essentials of Fluid Mechanics*. Springer Science, 3rd edn. 78

- OLAJIRE, A.A. (2010). CO<sub>2</sub> capture and separation technologies for end of pipe applications - A review. *Energy*, **35**, 2610–2628. 3
- PENG, W., HOFFMANN, A.C., BOOT, P.J.A.J., UDDING, A., DRIES, H.W.A., EKKER, A. & KATER, J. (2002). Flow pattern in reverse-flow centrifugal separators. *Powder Technol.*, **127**, 212–222. 2
- PILCH, M. & ERDMAN, C.A. (1987). Use of breakup time data and velocity history data to predict the maximum size of stable fragments for acceleration-induced breakup of a liquid drop. *Int. J. Multiphas Flow*, **13**, 741–757. 79
- POLING, B.E., PRAUSNITZ, J.M. & REID, R.C. (2001). *The Properties of Gases and Liquids*. McGraw-Hill Book Company, Inc., 5th edn. 12
- POURMAHMOUD, N., ZADEH, A.H., MOUTABY, O. & BRAMO, A. (2012). CFD analysis of helical nozzles effects on the energy separation in a vortex tube. *Therm. Sci.*, **16**, 151–166. 112
- PRODE (2013). www.prode.com. 140
- RAJAN, R. & PANDIT, A.B. (2001). Correlations to predict droplet size in ultrasonic atomisation. *Ultrasonics*, **39**, 235–255. 67
- RANQUE, G.J. (1933). Experiences sur la detente avec production simultanees d'un echappement d'air chaud et echappement d'air froid. *J. Phys. Rad.*, **7**, 112–4–S–115. 4
- RANQUE, G.J. (1934). Method and apparatus for obtaining from a fluid under pressure two currents of fluid at different temperatures. *US Patent*, **1952281**. 4
- RANZ, W.E. & MARSHALL, W.R. (1952). Evaporation from drops. parts I & II. *Chem. Eng. Progr.*, **48**, 141–146; 173–180. 18
- SAZHIN, S.S. (2005). Modeling of heating, evaporation and ignition of fuel dropltes: Combined analytical, asymptotic and numerical analysis. *J. Phys.: Conf. Ser.*, **22**, 174–193. 14
- SCHILLER, L. & NAUMANN, A.Z. (1933). über die grundlegenden berechnungen bei der schwerkraftaufbereitung. *Ver. Deut. Ing.*, **77**, 318–320. 12, 104
- SCHULTZ-GRUNOW, F. (1951). Turbulenter wärmedurchgang im zentrifugalfeld. *Forsch. Ing. Wes.*, **17**, 65–76. 6, 111, 113
- SECCHIAROLI, A., RICCI, R., MONTELPARE, S. & D'ALESSANDRO, V. (2009). Numerical simulation of turbulent flow in a Ranque-Hilsch vortex tube. *Int. J. Heat Mass Tran.*, **52**, 5496–5511. 6, 112
- SHAMSODDINI, R. & NEZHAD, A.H. (2010). Numerical analysis of the effects of nozzles number on the flow and power of cooling of a vortex tube. *Int. J. Refrig.*, **33**, 774–782. 112
- SHTERN, V. (2012). *Counterflows*. Cambridge University Press. 112
- SHTERN, V.N. & BORISSOV, A.A. (2010). Nature of counterflow and circulation in vortex separators. *Phys. Fluids*, **22**, 083601. 112



- 
- SKYE, H.M., NELLIS, G.F. & KLEIN, S.A. (2006). Comparison of CDF analysis to empirical data in a commercial vortex tube. *Int. J. Refrig.*, **29**, 71–80. 112
- SPALDING, D.B. (1953). The combustion of liquid fuels. *Int. Symp. Combustion*, **4**, 847–864. 13
- SPIEGELMAN, M. & KATZ, R.F. (2006). A semi-Lagrangian Crank-Nicolson algorithm for the numerical solution of advection-diffusion problems. *Geochem. Geophys. Geosyst.*, **7**. 21
- SQUIRES, K.D. & EATON, J.K. (1991). Preferential concentration of particles by turbulence. *Phys. Fluids A*, **3**, 1169–1178. 82
- STEENBERGEN, W. (1995). *Turbulent pipe flow with swirl*. Ph.D. thesis, Eindhoven University of Technology. 121
- SVAROVSKY, L. (1984). *Hydrocyclones*. Holt, Rinehart & Winston. 2
- SYRED, N. (2006). A review of oscillation mechanisms and the role of the precessing vortex core (PVC) in swirl combustion systems. *Prog. Energy Combust. Sci.*, **32**, 93–161. 99
- TAKAHAMA, H. & YOKOSAWA, H. (1981). Energy separation in vortex tubes with a divergent chamber. *J. Heat Tran.*, **103**, 196–203. 7
- TSI (2013). [www.tsi.com](http://www.tsi.com). 50
- TWISTER (2013). <http://twisterbv.com/>. 4
- VAN DEEMTER, J.J. (1952). On the theory of the Ranque-Hilsch cooling effect. *Appl. Sci. Res.*, **3**, 174–196. 6, 111, 113, 114, 115
- VAN ESCH, B.P.M. & KUERTEN, J.G.M. (2008). DNS of the flow of particles in rotating pipe flow. *J. Turbulence*, **9**, 1–17. 104
- VAN WISSEN, R.J.E., BROUWERS, J.J.H. & GOLOMBOK, M. (2007). In-line centrifugal separation of dispersed phases. *A.I.Ch.E. Journal*, **53**, 374–380. 3
- WALPOT, R.J.E., VAN DER GELD, C.W.M. & KUERTEN, J.G.M. (2007). Determination of the coefficients of Langevin models for inhomogeneous turbulent flows by 3D PTV and DNS. *Phys. Fluids*, **19**, 045102. 82, 83, 84
- WESTERWEEL, J., DRAAD, A.A., VAN DER HOEVEN, J.G.T. & VAN OORD, J. (1996). Measurement of fully-developed turbulent pipe flow with digital particle image velocimetry. *Exp. Fluids*, **20**, 165–177. 83
- WILLEMS, G.P. (2009). *Condensed rotational cleaning of natural gas*. Ph.D. thesis, Eindhoven University of Technology. 1, 140
- WOLF, B. (2011). Humidity measurements in moist gas conditions. Tech. rep., Eindhoven University of Technology. 134
- XUE, Y., ARJOMANDI, M. & KELSO, R. (2010). A critical review of temperature separation in a vortex tube. *Exp. Therm. Fluid Sci.*, **34**, 1367–1374. 7, 112

- XUE, Y., ARJOMANDI, M. & KELSO, R. (2011). Visualization of the flow structure in a vortex tube. *Exp. Therm. Fluid Sci.*, **35**, 1514–1521. 7, 112
- YILMAZ, M., KAYA, M. & KARAGOZ, S. (2009). A review on design criteria for vortex tubes. *Heat Mass Trans.*, **45**, 613–632. 7, 88, 112
- ZEEGERS, J.C.H., KUERTEN, J.G.M. & BAJLEKOV, G.I. (2011). Mach and Reynolds number dependencies, and literature review on the static pressure of flow around a circular cylinder. Tech. rep., Eindhoven University of Technology. 60
- ZHANG, Z. & EISELE, K. (1996). The effect of astigmatism due to beam refractions on the formation of the measurement volume in LDA measurements. *Exp. Fluids*, **20**, 466–471. 55





# Nomenclature

$A$	surface area of a droplet	$[\text{m}^2]$
$A$	cross sectional area of a nozzle	$[\text{m}^2]$
$A_f$	velocity amplitude	$[\text{m s}^{-1}]$
$A_p$	droplet response amplitude	$[\text{m s}^{-1}]$
$b$	dimensionless mass fraction	$[-]$
$B_M$	Spalding mass transfer number	$[-]$
$C$	liquid concentration	$[-]$
$C_c$	slip factor	$[-]$
$c$	speed of sound	$[\text{m s}^{-1}]$
$c_p$	specific heat capacity at constant pressure	$[\text{J kg}^{-1} \text{K}^{-1}]$
$c_v$	specific heat capacity at constant volume	$[\text{J kg}^{-1} \text{K}^{-1}]$
$c_w$	specific heat capacity of liquid water	$[\text{J kg}^{-1} \text{K}^{-1}]$
$D$	diffusion coefficient water vapour in nitrogen gas	$[\text{m}^2 \text{s}^{-1}]$
$D$	main tube diameter	$[\text{m}]$
$d$	distance between two laser spots	$[\text{m}]$
$d_m$	molecular collision diameter	$[\text{m}]$
$d_p$	droplet diameter	$[\text{m}]$
$E$	Young's modulus	$[\text{Pa}]$
$f_c$	centrifugal acceleration	$[\text{m s}^{-2}]$
$f$	frequency	$[\text{s}^{-1}]$
$f_0$	fundamental frequency	$[\text{s}^{-1}]$
$F_c$	centrifugal force	$[\text{N}]$
$f_D$	Doppler frequency	$[\text{s}^{-1}]$
$F_d$	drag force	$[\text{N}]$
$h$	specific enthalpy	$[\text{J kg}^{-1}]$
$\bar{h}$	overall heat transfer coefficient	$[\text{W m}^{-2} \text{K}^{-1}]$
$h_{fg}$	specific enthalpy of vaporization	$[\text{J kg}^{-1}]$
$I$	relative fluctuation intensity	$[-]$
$k$	Boltzmann constant = $1.38 \cdot 10^{-23} \text{ J K}^{-1}$	$[\text{J K}^{-1}]$
$\mathcal{L}$	characteristic length scale	$[\text{m}]$
$L$	main tube length	$[\text{m}]$
$l$	thickness of the window material	$[\text{m}]$
$L_N$	length of a nozzle	$[\text{m}]$
$M$	molar mass	$[\text{kg mol}^{-1}]$
$\text{Ma}$	Mach number	$[-]$

$Ma_0$	maximum swirl Mach number	[-]
MR	Mixing Ratio	[-]
$\dot{m}$	mass flow	[kg s <sup>-1</sup> ]
$m_p$	mass of a droplet	[kg]
$\Delta m$	total mass transfer from droplets in a certain size interval during a time interval	[kg]
$N$	number of nozzles in the swirl generator	[1]
$N_p$	number of droplets present in a computational cell	[1]
$n$	refractive index	[-]
$n$	number of droplet size intervals	[1]
Nu	Nusselt number	[-]
On	Ohnesorge number	[-]
$p$	pressure	[Pa]
Pr	Prandtl number	[-]
$p_{sat}$	saturation vapour pressure	[Pa]
$p_0$	static pressure in the exit of a nozzle	[Pa]
$p_s$	static pressure	[Pa]
$\Delta p$	pressure difference	[Pa]
$Q$	heat transfer	[W]
$Q_{fg}$	energy required for phase changes	[W]
$\mathcal{R}$	universal gas constant = 8.314 J mol <sup>-1</sup> K <sup>-1</sup>	[J mol <sup>-1</sup> K <sup>-1</sup> ]
$\bar{\mathcal{R}}$	specific gas constant	[J kg <sup>-1</sup> K <sup>-1</sup> ]
$R$	inner radius of the main tube	[m]
$r$	radial coordinate	[m]
$r_{cell}$	radial coordinate of a computational cell	[m]
$\Delta r$	size of a computational cell in radial direction	[m]
Re	Reynolds number	[-]
RH	relative humidity	[-]
$R_{vc}$	inner radius of the vortex chamber	[m]
$R_c$	cold exit diameter	[m]
$R_w$	inner radius window	[m]
$s$	shape parameter in the radial velocity distribution of gas	[m]
Stk	Stokes number	[-]
$T$	temperature	[K]
$\Delta T$	temperature difference	[K]
$t$	time	[s]
$t$	thickness of a nozzle exit	[m]
$t_{life}$	lifetime of a droplet	[s]
$t_0$	thickness of a nozzle entrance	[m]
$\Delta t$	length of a time interval	[s]
$U$	droplet velocity	[m s <sup>-1</sup> ]
$u$	velocity fluctuation of a droplet	[m s <sup>-1</sup> ]
$U^{\parallel}$	velocity parallel to the LDA fringes	[m s <sup>-1</sup> ]
$U^{\perp}$	velocity perpendicular to the LDA fringes	[m s <sup>-1</sup> ]
$U_{drift}$	drift velocity of a droplet	[m s <sup>-1</sup> ]
$U_c$	centerline velocity	[m s <sup>-1</sup> ]

$\mathcal{V}$	volume	[m <sup>3</sup> ]
$V$	gas velocity	[m s <sup>-1</sup> ]
$v$	normal velocity of gas to droplet surface	[m s <sup>-1</sup> ]
$w$	thickness of the vortex chamber (width of a nozzle)	[m]
We	Weber number	[-]
$x$	x-coordinate	[m]
$x$	position along optical axis	[m]
$x_v$	absolute humidity	[kg m <sup>-3</sup> ]
$x_l$	liquid mass fraction	[-]
$Y$	water vapour mass fraction	[-]
$y$	y-coordinate	[m]
$z$	axial coordinate	[m]
$\Delta z$	size of a computational cell in axial direction	[m]

### Greek

$\alpha$	inclination angle CPT	[rad]
$\alpha_p$	relative droplet response amplitude	[-]
$\alpha_f$	thermal diffusivity	[m <sup>2</sup> s <sup>-1</sup> ]
$\alpha_s$	static pressure angle	[rad]
$\beta$	flow angle	[rad]
$\Gamma$	water vapour mole fraction	[-]
$\gamma$	adiabatic exponent = $c_p/c_v$	[-]
$\gamma_p$	surface tension of water	[N m <sup>-1</sup> ]
$\delta$	difference between position of the MV and the focal point of the LDA lens	[m]
$\delta_f$	fringe spacing	[m]
$\epsilon$	strain	[-]
$\varepsilon$	cold fraction = $\dot{m}_c/\dot{m}$	[-]
$\varepsilon_m$	uncertainty in the mean	[-]
$\varepsilon_\sigma$	uncertainty in the standard deviation	[-]
$\eta$	enrichment	[%]
$\eta_c$	thermodynamic efficiency	[-]
$\Theta$	dimensionless temperature difference	[rad]
$\theta$	angular coordinate	[rad]
$\theta_i$	incident beam angle	[rad]
$\theta_r$	refracted beam angle	[rad]
$\kappa$	half of the beam crossing angle	[rad]
$\Delta\kappa$	variation in beam crossing angle	[rad]
$\lambda$	wavelength laser	[m]
$\lambda_f$	thermal conductivity of the gas phase	[W m <sup>-1</sup> K <sup>-1</sup> ]
$\lambda_m$	molecular mean free path length	[m]
$\mu_f$	dynamic viscosity of the gas phase	[Pa s]
$\mu_{JT}$	Joule-Thomson coefficient	[K Pa <sup>-1</sup> ]
$\nu$	kinematic viscosity	[m <sup>2</sup> s <sup>-1</sup> ]
$\Omega$	angular velocity	[rad s <sup>-1</sup> ]
$\Pi$	dimensionless pressure difference	[-]

$\varpi$	weighting factor liquid concentration	[-]
$\varpi_{d_p}$	probability to have a droplet with a certain size	[-]
$\dot{\varphi}$	angular velocity of the precession motion	[rad s <sup>-1</sup> ]
$\Delta\varphi$	phase difference PDPA	[rad]
$\rho$	mass density	[kg m <sup>-3</sup> ]
$\sigma$	material stress	[Pa]
$\sigma$	standard deviation of the velocity (rms)	[m s <sup>-1</sup> ]
$\tilde{\sigma}$	standard deviation of a filtered velocity signal	[m s <sup>-1</sup> ]
$\sigma_{d_p}$	standard deviation of droplet size distribution	[m]
$\tau$	residence time	[s]
$\tau$	specific shear stress	[m <sup>2</sup> s <sup>-2</sup> ]
$\tau_\kappa$	kolmogorov timescale	[s]
$\tau_f$	time scale of the flow	[s]
$\tau_p$	particle relaxation time	[s]
$\tau_R$	ratio between the vortex chamber radius and the main tube radius	[-]
$\Phi$	dimensionless heating or cooling power	[-]
$\Delta\Phi$	dimensionless heat loss	[-]
$\phi$	relative heat loss	[-]
$\phi_{\text{H}_2\text{O}}$	liquid water content per unit volume	[kg m <sup>-3</sup> ]
$\chi$	maximum absolute humidity	[kg m <sup>-3</sup> ]
$\Psi$	mass flux	[kg s <sup>-1</sup> m <sup>-2</sup> ]
$\psi$	the contribution of vortex wobbling to the velocity fluctuations	[-]
$\omega$	angular frequency	[rad s <sup>-1</sup> ]

### Subscript

$\infty$	quantity far away from the droplet surface
$\alpha$	as a function of the inclination angle
$\theta$	angular coordinate
0	initial condition
1, 2, 3	PDPA velocity component indices
$a, b$	material indices
$a, b$	position indices
$c$	cold stream
$cyl$	cylindrical window
$e$	estimated
$e$	equilibrium
$e$	exit
$f$	gas (fluid)
$flat$	flat window
$h$	hot stream
$\text{H}_2\text{O}$	water (water vapour)
$i$	index of species
$i$	time step
$i$	axial index of a computational cell



<i>i</i>	index of size interval
<i>j</i>	radial index of a computational cell
<i>LDA</i>	focal point LDA
<i>max</i>	maximum
<i>min</i>	minimum
<i>MV</i>	measurement volume
<i>n</i>	droplet index
<i>N<sub>2</sub></i>	nitrogen gas
<i>new</i>	new time step
<i>p</i>	droplet (particle)
<i>pl</i>	plenum condition
<i>r</i>	radial coordinate
<i>RH</i>	measured with RH probe
<i>s</i>	droplet surface
<i>s</i>	sampling conditions
<i>sc</i>	measured with the scale
<i>t</i>	total or stagnation property
<i>tot</i>	total
<i>v</i>	vapour phase
<i>v</i>	volume weighted
<i>vc</i>	vortex chamber
<i>z</i>	axial coordinate in the vortex tube

### Acronyms

CPT	Cylindrical Pitot Tube
CSD	Cumulative Size Distribution
CSD <sub>v</sub>	Volume weighted Cumulative Size Distribution
DNS	Direct Numerical Simulation
DSD	Droplet Size Distribution
DSD <sub>v</sub>	Volume weighted Droplet Size Distribution
FFT	Fast Fourier Transform
LDA	Laser Doppler Anemometry
LES	Large Eddy Simulation
MV	Measurement Volume
PDPA	Phase Doppler Particle Analysis
PMMA	Polymethyl-Methacrylate
PMT	Photomultiplier Tube
RANS	Reynolds Averaged Navier-Stokes
RHVT	Ranque-Hilsch Vortex Tube

### Vectors

<b>f</b>	acceleration force vector
<b>u</b>	droplet velocity vector
<b>v</b>	gas velocity vector
<b>x</b>	droplet position vector



# Abstract

## **Droplet behaviour and thermal separation in Ranque-Hilsch vortex tubes**

The Ranque-Hilsch Vortex Tube is a device by which compressed gas is converted into two lower pressure gas streams, having lower and higher temperatures compared to the temperature at the inlet. The gas is tangentially injected into a cylindrical tube, thereby forming a strong vortex. In the vortex there is energy transfer between the gas streams, resulting in cold gas in the core of the vortex and hot gas near the wall. In this way cold and hot gas are simultaneously produced without having moving components.

Vortex tubes are mostly used for low temperature applications, for example, to cool electronics or for solvent free cooling of cutting tools. The aim of the project is to investigate if the vortex tube can also be used to clean contaminated gases. If a gas mixture of, e.g.,  $\text{CO}_2$  and  $\text{CH}_4$  (where  $\text{CO}_2$  is considered to be the contaminant) is injected into the device, condensation of  $\text{CO}_2$  can, under suitable circumstances, occur. The droplets that are thereby created are subjected to a large centrifugal acceleration. Ideally, they will move towards the walls where they can be removed from the gas.

In this thesis, we focus on the behaviour (e.g. trajectories, sizes, velocities) of small droplets (water), which are suspended in a carrier gas (nitrogen), in the vortex tube. Dependent on local conditions, like temperature, pressure, and gas composition, the droplets change in size due to condensation or evaporation. We have theoretically investigated the droplet behaviour in the vortex tube by solving the equation of motion of droplets and by computing the change in droplet size due to condensation or evaporation. Experimental data of the flow field inside a vortex tube, available from literature, were used as gas conditions. It appeared that droplets evaporate in a few milliseconds, sometimes before they have reached the tube wall. Based on the results, droplets are present only in a small region that is close to the entrances. From the computed droplet trajectories, velocities, and sizes, we have determined criteria and specifications for the laboratory equipment.

A new laboratory, where all experiments have been performed, has been realized. By means of Laser Doppler Anemometry (LDA), we have measured droplet velocities in an experimental vortex tube. Various experiments have been performed under different operating conditions. Simultaneously, droplet sizes were measured by means of Phase Doppler Particle Analysis. There exists a correlation between the centrifugal force and the radial droplet velocity in a rotating flow field as long as (turbulent) radial gas velocities are negligibly small. The experimental results show, however, that this correlation is nearly absent, indicating that there are significant radial velocity fluctuations of the gas. It has been confirmed by the LDA measurements that these high intensity velocity fluctuations are present.

From frequency spectra, which were computed from the measured velocity data, we have

obtained detailed information on the movement of the main vortex in the vortex tube. Apparently, the vortex is not stationary, but precesses in the vortex tube, thereby forming a helical shape. This motion, i.e. vortex wobbling, is the cause for the high intensity (radial) velocity fluctuations. A drawback of vortex wobbling is that droplets can be trapped in the vortex, which makes it more difficult to separate them from the gas.

Despite the vortex wobbling, we have measured separation of water content. Because of condensation and evaporation of water droplets in the vortex tube, water vapor is transported from the cold to the hot gas stream. First experimental results have shown that water vapour enrichments of 37% in the hot stream can be achieved.

By understanding the thermodynamics of the vortex tube and how the energy transfer is related to the dimensions of the vortex tube and its operating conditions, one is able to optimize the geometry of the vortex tube. Since its invention in 1933, many scientists have analyzed processes in the vortex tube in order to explain or model the existing temperature differences. Most of the proposed models cannot be proven or have poor agreement with experimental results. An important result of our study is the development of a relatively simple and analytical model that describes the energy separation process at high accuracy. Various experiments have been performed that validate the model.

The developed model has been utilized to predict the thermal behaviour of the vortex tube when it is operated with a gas mixture of 50%<sub>mol</sub>CO<sub>2</sub> and 50%<sub>mol</sub>CH<sub>4</sub>. Based on a modified energy balance, we have computed the enrichment of CH<sub>4</sub> in the exit streams. The results indicate that, from thermodynamics point of view, the vortex tube should be suitable to condense gaseous components in the cold stream, thereby enriching the gas with CH<sub>4</sub>.

# Samenvatting

## **Druppelgedrag en thermische separatie in Ranque-Hilsch wervelbuizen**

De Ranque-Hilsch wervelbuis is een apparaat waarin gecomprimeerd gas wordt opgesplitst in twee lage druk stromen met een verschil in temperatuur. Het gas wordt in een rotatie gebracht en vormt daarbij een sterke wervel. In de wervel vindt energietransport plaats waardoor de kern van de wervel afkoelt terwijl het gas aan de wand opwarmt. Hiermee kan zonder bewegende delen tegelijkertijd koud en warm gas worden geproduceerd voor diverse toepassingen.

De meest voorkomende toepassing van de wervelbuis is het leveren van koele lucht voor bijvoorbeeld het koelen van gereedschappen of elektronica. In dit project onderzoeken we of de wervelbuis ook kan worden gebruikt om vervuilde gassen te reinigen. Als er bijvoorbeeld een mengsel van  $\text{CO}_2$  en  $\text{CH}_4$  (waar  $\text{CO}_2$  als verontreiniging wordt beschouwd) wordt geïnjecteerd, dan kan onder de juiste condities een deel van de  $\text{CO}_2$  condenseren. Door de sterke rotatie van het gas werkt er een centrifugaalkracht op de druppeltjes. In het ideale geval worden deze daardoor naar de buiswand geslingerd en kunnen daar worden afgescheiden van het gas.

In dit proefschrift wordt gefocuseerd op het gedrag (waaronder trajecten, groottes, en snelheden) van water druppels (samen met stikstofgas) in de wervelbuis. Lokale opwarming en koeling van het gas in de wervelbuis beïnvloedt het druppelgedrag. Afhankelijk van de temperatuur, de druk, en de compositie van het gas, veranderen de druppels van grootte door condensatie of verdamping. We hebben het druppelgedrag in de wervelbuis theoretisch bestudeerd door de beweging en de verandering in grootte van de waterdruppels te berekenen. Om deze berekeningen te kunnen doen hebben we een uit de literatuur bekend stromingsveld in de wervelbuis aangenomen. De resultaten laten zien dat druppels verdampen in een paar milliseconden, soms zelfs voordat ze de buiswand bereiken. Het blijkt dat er maar een klein gebied is waar druppels zich bevinden. Deze resultaten zijn gebruikt om specificaties voor de meetapparatuur te bepalen.

Een nieuw laboratorium, waarin alle experimenten zijn uitgevoerd, is opgebouwd. Druppelsnelheden in een experimentele wervelbuis zijn gemeten met behulp van Laser Doppler Anemometrie (LDA). Verscheidene metingen zijn uitgevoerd om te zien hoe het stromingsveld afhangt van de experimentele condities. Tegelijkertijd werden de groottes van de druppeltjes gemeten door middel van phase Doppler particle analysis. Er bestaat een duidelijke correlatie tussen de centrifugale kracht en de (turbulente) radiale snelheid van druppels in een roterende stroming als de radiale snelheidsfluctuaties verwaarloosbaar klein zijn. Uit de experimentele resultaten blijkt echter dat er nagenoeg geen correlatie is, wat aangeeft dat er aanzienlijke radiale snelheidsfluctuaties in het gas aanwezig moeten zijn. Resultaten van de LDA metingen bevestigen de aanwezigheid van deze snelheidsfluctuaties.

Uit de gemeten snelheden zijn frequentiespectra bepaald. Deze geven gedetailleerde informatie over de beweging van de wervel in de wervelbuis. Het blijkt dat de wervel niet stationair is, maar beweegt in de vortex buis. Deze beweging, het wiebelen van de wervel, is de oorzaak voor de hoge intensiteit radiale) snelheidsfluctuaties. Door dit verschijnsel kunnen druppels worden gevangen in de wervel, wat het scheiden van druppels uit het gas bemoeilijkt.

Ondanks het wiebelen van de wervel blijkt er toch scheiding van waterdamp op te treden. Door condensatie en verdamping van waterdruppels in de wervelbuis wordt er waterdamp van de koude naar de warme gasstroom getransporteerd. Experimentele resultaten hebben aangetoond dat als gevolg hiervan een verrijking van 37% in de waterconcentratie in de warme gasstroom mogelijk is.

Als we begrijpen hoe de thermodynamica in de wervelbuis werkt en hoe deze afhangt van de afmetingen en werkcondities van de wervelbuis, dan kunnen we de wervelbuis optimaliseren. Vele wetenschappers hebben sinds de uitvinding in 1933 de processen in de wervelbuis geanalyseerd om het verschil in temperaturen (thermische separatie) te kunnen verklaren en/of te modelleren. De meeste van de voorgestelde modellen kunnen lastig worden getoetst of komen slecht overeen met experimentele resultaten. Een belangrijk resultaat van deze studie is de ontwikkeling van een relatief simpel en analytisch model dat het energietransport met hoge nauwkeurigheid beschrijft. Verschillende experimenten zijn uitgevoerd die het model valideren.

Het ontwikkelde model is gebruikt om het thermische gedrag van de wervelbuis te voorspellen wanneer een gasmengsel van 50%<sub>mol</sub> CO<sub>2</sub> en 50%<sub>mol</sub> CH<sub>4</sub> wordt geïnjecteerd. Op basis van een aangepaste energiebalans is de verrijking van CH<sub>4</sub> in de uitgangsstromen berekend. De resultaten geven aan dat, vanuit thermodynamisch oogpunt, de wervelbuis geschikt zou moeten zijn om gasvormige componenten in de koude stroom te condenseren en daarmee het gas te verrijken met CH<sub>4</sub>.

# List of publications

## Journal publications

**Liew, R.**, Saha, D., Zeegers, J.C.H., Kuerten, J.G.M. & Michalek, W.R.  
Vortex core precession in Ranque-Hilsch vortex tubes  
*In preparation for publication*

**Liew, R.**, Zeegers, J.C.H., Kuerten, J.G.M. & Michalek, W.R.  
Energy separation in Ranque-Hilsch vortex tubes  
*Submitted for publication in Int. J. Heat Mass Trans.*

Michalek, W.R., Kuerten, J.G.M., Zeegers, J.C.H., **Liew, R.**, Pozorski, J. & Geurts, B.J.  
(2013).  
A hybrid stochastic-deconvolution model for LES of particle-laden flow  
*Submitted for publication in Phys. Fluids.*

**Liew, R.** (2013).  
Mysterie van de Ranque-Hilsch vortexbuis  
*Nederlands Tijdschrift voor Natuurkunde*, **79**(2), 58 – 61.

**Liew, R.**, Zeegers, J.C.H., Kuerten, J.G.M. & Michalek, W.R. (2013).  
3D Velocimetry and droplet sizing in the Ranque-Hilsch vortex tube  
*Exp. Fluids*, **54**, 1416.

**Liew, R.**, Zeegers, J.C.H., Kuerten, J.G.M. & Michalek, W.R. (2012).  
Maxwell's Demon in the Ranque-Hilsch Vortex Tube  
*Phys. Rev. Lett.*, **109**, 054503.

Clerx, N., Van Deurzen, L.G.M., Pecenko, A., **Liew, R.**, Van der Geld, C.W.M. & Kuerten, J.G.M. (2011).  
Temperature fields induced by direct contact condensation of steam in a cross-flow in a channel  
*Int. J. Heat Mass Trans.*, **47**, 981 – 990.

## Conference proceedings

Michałek, W.R., Kuerten, J.G.M., **Liew, R.**, Zeegers, J.C.H., & Geurts, B.J. (2013).  
A hybrid stochastic-deconvolution model for particle-laden LES  
*ICNAAM, AIP Conference Series (submitted)*

Michałek, W.R., Kuerten, J.G.M., **Liew, R.**, & Zeegers, J.C.H. (2013).  
LES of the particle laden Ranque-Hilsch Vortex Tube  
*Direct and Large Eddy Simulation 9, ERCOFTAC (submitted)*

Michałek, W.R., Kuerten, J.G.M., **Liew, R.**, Zeegers, J.C.H., Pozorski, J., & Geurts, B.J. (2013).  
A hybrid deconvolution-stochastic model for LES of particle-laden flow  
*Direct and Large Eddy Simulation 9, ERCOFTAC (submitted)*

**Liew, R.**, Zeegers, J.C.H., Kuerten, J.G.M. & Michałek, W.R. (2012).  
Temperature, pressure and velocity measurements on the Ranque-Hilsch vortex tube  
*Journal of Physics: Conference Series*, **395**, 012066.

**Liew, R.**, Zeegers, J.C.H., Kuerten, J.G.M. & Michałek, W.R. (2011).  
Droplet behaviour in a Ranque-Hilsch Vortex Tube  
*Journal of Physics: Conference Series*, **318**, 052013.

Michałek, W.R., **Liew, R.**, Kuerten, J.G.M. & Zeegers, J.C.H. (2011).  
LES of droplet-laden non-isothermal channel flow  
*Journal of Physics: Conference Series*, **318**, 042056.

**Liew, R.**, Zeegers, J.C.H., Kuerten, J.G.M. & Michałek, W.R. (2010).  
Droplet behaviour in a Ranque-Hilsch Vortex Tube  
*Proceedings of the 5<sup>th</sup> International Conference on Vortex Flow Modeling (ICVFM2010)*



# Acknowledgements

Finally, after years of designing, computing, experimenting, analyzing, and writing, my PhD time at the department of Applied Physics at the Eindhoven University of Technology has come to an end. The results: this thesis, a few papers, a beautiful new laboratory, and a great experience; all has been achieved with the support of many people.

Professor Anton Darhuber, our group leader and my first promotor, provided a comfortable work environment and the required space for a laboratory. I thank him for his valuable comments on the thesis, which are highly appreciated.

Professor Hans Kuerten, my second promotor, was closely involved in the project. His invaluable input and feedback during the many meetings we had resulted very often in a better understanding of the physics and a higher quality of work. Also the non-work related talks and his, sometimes unexpected, humorous comments created a pleasant and informal atmosphere.

Besides the initiator of the research and my co-promotor, Jos Zeegers was my daily supervisor and motivator. I cannot express how grateful I am that he has offered me the opportunity to work on the intriguing subjects described in this thesis. Because of his expert input and structured approach, the (almost) four years of PhD were very productive and pleasant. Our visit to the USA, where we have visited the APS in San Diego, California Institute of Technology, University of California, and Arizona State University, was a great experience. I really appreciate the ability of both Jos and Hans to find compromises between the demands of the companies involved in the project, the TU/e, and myself.

Furthermore, I thank the other members of the core committee, Prof. Henrik Alfredsson, Prof. Jerry Westerweel, Prof. Bert Brouwers, and Prof. Gertjan van Heijst, for their enthusiasm to be part of the committee and the time and energy they have spent for reading my thesis. Henrik, I highly appreciate your kind invite to KTH Stockholm; it was a great visit. Bert, I would like to thank you for your inspiring feedback on the thesis and for the invite to join the study trip to Switzerland, which was informative and enjoyable.

This project would not be successful without the support of STW and the companies involved: Shell, RWE, Twister, KEMA, and Vortex Engineering.

I am grateful to the technical staff for their technical support: Henny Manders, Jørgen van der Veen, Freek van Uitert, Jos Bremmers; and Brigitte van de Wijdeven for her administrative support. Special thanks go to Henny, who has designed many critical components of the experimental setup and helped me setting up the laboratory (sorry voor de vallende moersleutel). Jørgen as well helped me in the laboratory, and his knowledge of optics was very useful. Freek's expertise of Labview was invaluable. He has taught me the basics of Labview and developed control software for the laboratory. Jos had no issues to open, close, or clean the nitrogen evaporators, sometimes every day of the week, no matter the weather. I

have experienced working (or drinking coffee during the 10 O'clock coffee break) with the staff members to be very pleasant.

Bas van de Wiel and Rudie Kunnen, thanks for your encouragement to submit a manuscript to a high ranked journal. Also, the discussion about 'the most suitable title for a PRL article' during the ETC13 conference appeared to be very fruitful.

Professor Mico Hirschberg, who has expert knowledge (it seems in almost all fields), often provided clever questions or suggestions during presentations or during lunch and coffee; something what I can appreciate.

Wiktor Michałek worked on the numerical counterpart of this project. We shared our numerically and experimentally encountered problems in order to find solutions for both of us, what resulted in good agreements between experiments and numerics. Without the results of his numerical studies, many questions would remain unanswered. Besides the work related talks, we had many nice conversations about life, the tax system of the Netherlands, and Poland vs. the Netherlands in general.

A part of the work has been delivered by Bram Wolf and Bjorn Liefkens, who worked on methods to measure absolute humidity content, and Koen Deuss, who investigated various LDA configurations.

I am very grateful to my colleagues Christian, David, Güneş, Humberto, Jorge, Oleksii, and Valentina. I was always welcome to have a talk and share my opinions, thoughts, and problems with them. I thank all the people in Cascade who were responsible for a nice working environment, among others: Aniruddah, Ariel, Badr, Ber, Berend, Davis, Debashish, Dennis, Florian G., Florian J., Jemil, Jens, Judith, Kees, Margit, Sebastian, Stefan, Sudhir, and Theo. Furthermore, I want to thank my friends Guus, Edwin, Patric, Bart, and Peter for their friendship and support.

Mijn ouders hebben mij altijd gesteund en aangemoedigd in alles wat ik doe. Dankzij hen heb ik een tot dusver zorgeloos leven geleid en heb dit alles kunnen bereiken. Daarvoor ben ik ze zeer dankbaar. Finally, last but not least, my dear Laura, you are there for me, you support me, and you encourage me to look beyond my own boundaries...

Raoul Liew  
July 2013

# Curriculum vitae

Raoul Liew was born on October 24, 1985, in 's-Hertogenbosch, The Netherlands. He started his study mechanical engineering at the AVANS Hogeschool 's-Hertogenbosch in 2002 where he received his Bachelor of Science degree in 2006 (Cum Laude). In the same year, he continued with the Master's study mechanical engineering at the Eindhoven University of Technology. During this study, he was assistant lecturer for the courses 'Thermodynamica' and 'Procestechnische Constructies'. In 2009, he received his Master of Science degree under the supervision of prof.dr. J.G.M. Kuerten and dr. C.W.M. van der Geld. The topic of his Master's thesis was 'Phosphor thermometry and simulation of direct steam injection'.

In October 2009, he started working his PhD project in the group of prof.dr. A.A. Darhuber (Applied Physics, Eindhoven University of Technology) under the supervision of dr.ir. J.C.H. Zeegers and prof.dr. J.G.M. Kuerten. The title of the project was 'The Vortex Tube as a Tool in Sustainable Energy Production'. The project was (financially) supported by STW, Shell, Twister, KEMA, RWE, and Vortex Engineering. Results of the project, which are provided in this thesis, have been presented during the International Conference on Vortex Flow Modeling (8 – 10 November 2010, Napoli, Italy), the 13<sup>th</sup> International Turbulence Conference (12 – 15 September 2011, Warsaw, Poland), the 6<sup>th</sup> Eurotherm (4 – 9 September 2012, Poitiers, France), and the 65<sup>th</sup> APS/DFD (18 – 20 November 2012, San Diego, United States of America).